Collective Excitations and Emergent Quantum Phases in Spin-Orbit Coupled Spin-1 Bose-Einstein Condensates

A Thesis Submitted
in partial fulfilment of the requirements
for the degree of
Doctor of Philosophy

by

Sanu Kumar Gangwar
206121026

under the supervision of

Dr. Pankaj Kumar Mishra



to the

DEPARTMENT OF PHYSICS
INDIAN INSTITUTE OF TECHNOLOGY Guwahati
March, 2026

TH-4102_206121026

TH-4102_206121026

Declaration



This is to certify that the work contained in this thesis entitled **"Collective Excitations and Emergent Quantum Phases in Spin-Orbit Coupled Spin-1 Bose-Einstein Condensates"** submitted by me to the Indian Institute of Technology, Guwahati, for the award of the degree of PhD, is a bonafide work carried out by me under the supervision of Dr. Pankaj Kumar Mishra and that this work has not been submitted elsewhere for a degree of diploma. I also wish to state that to the best of my knowledge and understanding nothing in this report amounts to plagiarism.



June 23, 2026

Sanu Kumar Gangwar
Department of Physics
Indian Institute of Technology
Guwahati

TH-4102_206121026

TH-4102_206121026

Certificate



It is certified that the work contained in this thesis entitled **"Collective Excitations and Emergent Quantum Phases in Spin-Orbit Coupled Spin-1 Bose-Einstein Condensates"** by **Sanu Kumar Gangwar**, has been carried out under my supervision, and this work has not been submitted elsewhere for a PhD. degree.

Pankaj Kumar Mishra

June 23, 2026

Dr. Pankaj Kumar Mishra
Associate Professor
Department of Physics
Indian Institute of Technology
Guwahati

TH-4102_206121026

TH-4102_206121026

Preface



Spin–orbit (SO) coupling, which couples a particle's internal spin degree of freedom with its center-of-mass motion, is a key mechanism underlying many important phenomena in condensed matter physics, including topological insulators, the quantum Hall effect, and spintronics. The realization of synthetic SO coupling in ultracold atomic gases has opened a new avenue for exploring such effects in highly controllable quantum systems. Raman-induced SO coupling was first realized in a spin-1/2 Bose-Einstein condensate (BEC) by Lin *et al.* in 2011, using two hyperfine states of Rubidium to generate equal strength Rashba-Dresselhaus coupling. This scheme was later extended to spin-1 condensates by employing all three hyperfine states by Campbell *et al.* and Luo *et al.* in 2016, enabling the realization of SO coupled spin-1 BECs. These advances established ultracold atoms as a versatile platform for studying the interplay between the synthetic gauge fields and interactions.

The equilibrium and dynamical properties of SO coupled condensates are well described within the framework of coupled Gross-Pitaevskii equations (GPEs). This mean-field approach helps to determine ground-state phases through energy minimization and to analyze the competition between SO coupling, Rabi coupling, detuning, and interatomic interactions. Depending on the system parameters, a variety of phases, such as plane-wave (PW), zero-momentum (ZM), and stripe-wave (SW) phases, can emerge. Collective excitations are low-lying excitations, which provide essential insight into the stability and dynamical response of these phases. Linearization around the stationary state leads to the Bogoliubov-de Gennes (BdG) equations, whose quasiparticle spectrum reveals key features such as phonon modes, roton-maxon modes, and instability regions. In SO coupled condensates, the softening of ro-

TH-4102_206121026

ton modes is closely linked to the emergence of stripe and supersolid-like phases. For spin-1 SO coupled condensates, the additional spin degree of freedom significantly enriches both the ground-state phase diagram and excitation spectrum. Although various works have reported different ground-state phases in ferromagnetic and antiferromagnetic regimes, a systematic and unified understanding of ground-state phase diagrams and their stability remains incomplete. In particular, detailed investigations of collective excitations and associated instabilities in homogeneous quasi-one- and quasi-two-dimensional SO coupled spin-1 condensates remain unexplored.

This thesis addresses these open questions through a comprehensive study of ground-state phases, collective excitations, and dynamical instabilities in SO coupled spin-1 condensates. Using mean-field GPEs, we map the ground-state phases in ferromagnetic and antiferromagnetic regimes. Employing BdG theory, we identify the phonon-maxon-roton modes, unstable avoided crossings, and the mechanisms by which these instabilities lead to complex pattern formation. Below, we present a brief summary of the key results of this thesis, organized into seven chapters.

Chapter 1 begins with a brief overview of single-component BECs, introducing the mean-field description and the GPE. The discussion then extends to multicomponent and spinor condensates, highlighting the role of spin degrees of freedom and interatomic interactions. Building on this foundation, SO coupling in ultracold atomic gases is introduced, together with its significance for realizing novel quantum phases and collective excitations. The BdG formalism is outlined as the primary tool for analyzing excitation spectra and stability. The chapter concludes with a concise review of theoretical and experimental progress in SO coupled spinor BECs and identifies open problems that motivate the work of the present thesis.

In **Chapter 2**, we present the numerical scheme employed to solve the mean-field GPEs for SO coupled spin-1 BECs. We outline the split-step Crank-Nicolson (CN) method for solving coupled GPEs, using imaginary-time propagation to obtain the condensate ground state and real-time propagation to study its dynamical evolution. The numerical scheme is formulated for multicomponent systems and is applied to SO coupled GPEs in both quasi-one-dimensional (quasi-1D) and quasi-two-dimensional (quasi-2D) geometries. We present the grid-independence test for spatial and temporal step sizes in both quasi-1D and quasi-2D geometries. Finally, we discuss the quench protocols to study the nonequilibrium dynamics of SO coupled spin-1 condensates.

In **Chapter 3**, we investigate the ground-state phases and quench dynamics of SO-coupled spin-1 BECs with both ferromagnetic and antiferromagnetic interactions. For ferromagnetic interactions at very weak Rabi coupling ($\Omega \approx 0$), we identify the zero-

TH-4102_206121026

momentum (ZM) phase, elongated zero-momentum phase of type I (EZM I), stripe-wave (SW) phase, and superstripe-wave (SSW) phase, while the SSW phase disappears at finite Rabi coupling. In contrast, for antiferromagnetic interactions, the ZM, EZM I, and SW phases appear at finite Rabi coupling, whereas at very weak Rabi coupling, the EZM I and SW phases vanish, giving rise to the elongated zero-momentum type II (EZM II) and SSW phases. Quantum phase transitions are characterized using spin-density vectors, miscibility, and the root-mean-square size of the condensate. Furthermore, in the SW and SSW phases, tuning the attractive density–density and spin-exchange interactions drives transitions to the EZM I and EZM II phases, respectively. Quench-dynamics studies reveal that Rabi coupling stabilizes the condensate, whereas quenches of the SO coupling induce strong fluctuations and complex pattern formation, accompanied by the disappearance of the zeroth spin component in the SW phase.

Building on the previous chapter, **Chapter 4** focuses on uncovering the microscopic origins of the observed instabilities by analyzing the collective excitation spectrum. We compute the Bogoliubov excitation spectrum of a quasi-1D ferromagnetic spin-1 BEC with both SO and Rabi couplings using BdG theory. The eigenspectrum reveals distinct stability regimes in the SO–Rabi coupling parameter space, including regions of phononlike stable excitations, multiband instabilities, and a particularly intriguing regime characterized by unstable avoided crossings (UACs) between low-lying and first-excited branches. These avoided crossings give rise to I_o-type dynamical instabilities that drive pattern formation. Numerical simulations of the coupled GPEs, initiated via trap quenches, corroborate the BdG predictions, showing the disappearance of the zeroth spin component and fragmentation of stripe-wave density profiles. Eigenvector analysis further identifies the spin-dipole and mixed spin–density modes responsible for these instabilities.

In **Chapter 5**, we extend the analysis to antiferromagnetic interactions to elucidate how the sign of spin-dependent interactions affects stability and instability growth over a broad parameter range. Using BdG theory in conjunction with numerical simulations of the coupled GPEs, we demonstrate that ferromagnetic and antiferromagnetic condensates exhibit qualitatively distinct modulational instability (MI) regimes. Notably, for antiferromagnetic interactions, the excitation spectrum displays double unstable avoided crossings between excitation branches—a feature absent in the ferromagnetic case—leading to enhanced and more complex domain formation during dynamical evolution. We find that SO coupling amplifies instability growth, whereas Rabi coupling plays a stabilizing role. This work highlights how avoided crossings be-

TH-4102_206121026

tween excitation modes act as a universal mechanism driving I_o-type instabilities and spatial pattern formation in multicomponent quantum gases.

In **Chapter 6**, we extend our investigation to quasi-2D SO coupled spin-1 condensates. In this work, we perform a detailed analysis of collective excitations and dynamics within a mean-field framework for Rashba-type SO coupling. Employing the BdG formalism, we compute excitation spectra over a wide range of interaction strengths and coupling parameters. By systematically varying the SO and Rabi couplings, we construct the corresponding stability phase diagram and identify the emergence of phonon, maxon, and roton modes in the excitation spectrum. The softening of these modes signals the onset of dynamical instabilities, which lead to fragmentation of the ground-state density profile and complex pattern formation during time evolution.

In **Chapter 7**, we summarize the main findings of this thesis, emphasizing the interplay of SO coupling, Rabi coupling, and interaction in determining the ground-state phases, collective excitations, and dynamical instabilities of spin-1 BECs. We highlight the physical origins of avoided crossings, roton softening, modulational instabilities, and condensate dynamics across different geometries and interaction regimes. Finally, we discuss possible future directions, including extensions to finite-temperature systems, the inclusion of disorder, and beyond-mean-field effects.

This thesis offers novel insights into ground-state phases and collective excitation spectra of SO coupled spin-1 BECs in quasi-one- and two-dimensional geometries. Given ongoing experimental progress in realizing and probing multicomponent SO coupled condensates, the findings of this thesis are expected to serve as a useful theoretical reference for future investigations of excitation spectra, stability, and emergent phases in such condensates.

TH-4102_206121026

TH-4102_206121026

Acknowledgements

My PhD journey, which began in 2020, has now reached its conclusion. It has been one of the most enriching and transformative phases of my life. At this moment, I would like to express my heartfelt gratitude to all those who have supported and accompanied me throughout this journey.

First and foremost, I would like to express my sincere gratitude to my PhD supervisor, Dr. Pankaj Kumar Mishra, under whose guidance I had the privilege of conducting my doctoral research. From the very beginning, his confidence in my abilities and constant encouragement played a defining role in shaping my academic journey. Although I began this journey with limited experience in numerical methods and programming, he never wavered in his faith in my potential or determination. His constant encouragement, along with a thoughtful balance of freedom and guidance, allowed me to explore diverse and exciting research directions with confidence. For this trust and enduring support, I remain profoundly grateful. I also deeply appreciate his continued cooperation and support throughout this journey, both in academic matters and beyond. Working under his mentorship has been an enriching and inspiring experience, and I will always carry these memories with warmth and gratitude.

I am sincerely thankful to my Doctoral Committee members, Prof. Saurabh Basu, Prof. Padma Kumar Padmanabhan, and Prof. Jiten Chandra Kalita, for their constructive suggestions, encouragement, and continuous evaluation of my progress. I would also like to acknowledge the support and guidance of the former Heads of the Department, Prof. Subhradip Ghosh and Prof. Perumal Alagarsamy, and the current Head, Prof. Bosanta Ranjan Boruah, for providing a conducive academic and research environment. I am specially thankful to Prof. Subhradip Ghosh (former Head of the Department) for his guidance and support at the beginning of my PhD tenure during the challenging COVID period.

TH-4102_206121026

It is my pleasure to express my gratitude to my collaborators. I greatly benefited from their expertise, discussions, and insights during my research. I would like to acknowledge Prof. Paulsamy Muruganandam (Bharathidasan University) for fruitful discussions on numerical techniques for simulating the mean-field models of Bose-Einstein condensates. I acknowledge him for sharing his experience in diverse fields of ultracold gases. I acknowledge Dr. Rajamanickam Ravisankar for introducing me to several software packages and for helping me understand the analytical aspects at the beginning of my PhD tenure, which have been used in this thesis. I would also like to acknowledge Dr. Henrique Fabrelli for his support in developing the numerical technique for the eigenspectrum solver.

I acknowledge all the faculty members of the department from whom I received rigorous training during my PhD coursework. Their teaching laid a strong foundation for my research. Specifically, I would like to thank Prof. Padma Kumar Padmanabhan, Dr. Pankaj Kumar Mishra, and Prof. Sitangshu Bikas Santra for enhancing my understanding of Basic Physics during the coursework at IIT Guwahati. I would like to thank Prof. Saurabh Basu, whose course on Advanced Condensed Matter Physics I had the opportunity to audit. I would like to make a special mention of my middle school teacher, Mr. Poshaki Lal Gangwar, whose teaching and guidance played a crucial role in shaping my academic interests. His belief in the importance of education and constant motivation laid the foundation for my journey in science.

I extend my thanks to my current lab mates–Dr. Rony Boral, Shawan, Joya, Nalinikant, Sumit, Prembrata, and Sayan and to former members Dr. Sonali Gangwar and Dr. Swarup Kanti Sarkar– for their cooperation and fruitful discussions.

I would like to acknowledge the staff members of the department for their assistance and support with administrative and technical matters. I sincerely thank Monojit Bhattacharjee and Ambrish Biswas for helping me with administrative work and ensuring the smooth completion of different PhD-related formalities. I would also like to thank Basab Bijoy Purkayastha for the technical support he provided at various stages.

The completion of my PhD thesis would not have been possible without the supercomputing facilities provided by IIT Guwahati. I would like to acknowledge our supercomputing resources, including PARAM ISHAN and PARAM KAMRUPA. I also acknowledge the departmental cluster “Newton” for computational work. I am grateful to the Ministry of Education (formerly MHRD), Government of India, for providing financial support through the institute fellowship.

During my time at IIT Guwahati, I had the privilege of being surrounded by a wonderful group of friends who made this journey truly memorable. I am deeply grateful to Himanshu, Soumya, Bhagwat, Sanju, Sirsendu, Debraj, Madan, Samten,

TH-4102_206121026

Dipendu, Nayan, Ankan, Sanjib, Likun, Pranjal, Lwithwsa, and many others for their constant support, meaningful tea-time discussions, and the countless moments of joy and laughter we shared. Their companionship made even the most challenging phases of my PhD much easier and more enjoyable.

Beyond academics, I would also like to acknowledge the role of sports in keeping me balanced and motivated throughout this journey. I am thankful for the excellent sports facilities at IIT Guwahati, which allowed me to actively pursue my interests in cricket and running. I extend my sincere thanks to all my teammates from the department team, specially Suchit Kumar Jena, Rajnandan Choudhury Das, Debabrata Paul, Vishal, Sahilesh, Debabrata Sahu, as well as my teammates from the state cricket team, including Shashi Bhusan Singh, Abhimanyu Singh, and many others, for their camaraderie, encouragement, and many memorable moments on and off the field. Their support played an important role in maintaining both my physical and mental well-being during my PhD years.

I am specially thankful to my close friend, Swati Shaw, for being a constant source of strength and encouragement throughout this journey. Her understanding, patience, and unwavering support helped me navigate both academic challenges and personal ups and downs during this period.

Finally, I express my deepest gratitude to my family for their unconditional love, constant support, and unwavering belief in me. Their encouragement and sacrifices have been the foundation of this journey. I am grateful to my Mummy and Papa for their constant guidance, patience, and for always motivating me to pursue my goals with sincerity and determination. A special mention and sincere gratitude to my uncle, Mr. Rambahadur Gangwar (Tauji), for always standing by me in every situation. I would also like to thank my siblings for their support, understanding, and encouragement throughout my journey. Their presence has been a constant source of strength; without them, this achievement would not have been possible.

TH-4102_206121026

TH-4102_206121026

To my family . . .

TH-4102_206121026

TH-4102_206121026

Publications

1. **S. K. Gangwar**, R. Ravisankar, P. Muruganandam, and P. K. Mishra, *Emergence of spin-mixed superstripe phases in spin-orbit coupled spin-1 condensate*, Phys. Rev. A **113**, 023311 (2026).

2. **S. K. Gangwar**, R. Ravisankar, H. Fabrelli, P. Muruganandam, and P. K. Mishra, *Emergence of unstable avoided crossing in the collective excitations of spin-1 spin-orbit-coupled Bose-Einstein condensates*, Phys. Rev. A **109**, 043306 (2024).

3. **S. K. Gangwar**, R. Ravisankar, H. Fabrelli, P. Muruganandam, and P. K. Mishra, *Double unstable avoided crossings and complex-domain-pattern formation in spin-orbit-coupled spin-1 condensates*, Phys. Rev. A **111**, 063303 (2025).

4. **S. K. Gangwar**, S. Chatterjee, R. Ravisankar, H. Fabrelli, P. Muruganandam, and P. K. Mishra, *Supersolid phases and Collective excitations in two-dimensional Rashba spin-orbit coupled spin-1 condensates*, arXiv:2601.18568 (2026)[submitted to Phys. Rev. A].

Journal publication outside thesis

1. R. Ravisankar, **S. K. Gangwar**, H. Fabrelli, Y. Zhang, P. Muruganandam, P. K. Mishra, E. Kengne, G. Xianlong, and B A Malomed, *Stable supersolids and boselets in spin-orbit-coupled Bose-Einstein condensates with three-body interactions*, Physical Review Research **7**, 023317 (2025).

Conference publication

1. **S. K. Gangwar**, R. Ravisankar, and P. K. Mishra, *Excitation Spectrum of Repulsive Spin-Orbit Coupled Bose-Einstein Condensates in Quasi-one Dimension: Effect of Interactions and Coupling Parameters*, Nonlinear Dynamics and Applications: Proceedings of the ICNDA 2022 (Springer International Publishing), **1287–1297** (2022).

TH-4102_206121026

Contents

Declaration iii

Certificate v

Preface vii

Acknowledgement xii

Publications xviii

List of figures xxiii

1 Introduction 1

1.1 Bose-Einstein Condensates . . . 3

1.1.1 Mean-field Gross-Pitaevskii equation . . . 6

1.2 Spinor Bose-Einstein condensates . . . 9

1.2.1 Microscopic picture . . . 10

1.2.2 Second Quantized Hamiltonian . . . 12

1.2.3 Coupled Gross-Pitaevskii Equations for spin-1 condensates . . . 13

1.3 Spin-orbit coupled Bose-Einstein condensates . . . 14

1.3.1 Spin-orbit interaction in atomic systems . . . 14

1.3.2 Different types of spin-orbit couplings . . . 15

1.3.3 Synthetic spin-orbit coupled Bose-Einstein condensates . . . 17

1.3.4 Gross-Pitaevskii Equations for spin-orbit coupled spin-1 condensates . . . 21

1.4 Collective Excitation spectrum . . . 24

1.4.1 Bogoliubov-de Gennes spectrum . . . 24

1.4.2 Experimental measurement of collective excitations in spin-orbit coupled condensates . . . 26

1.5 Progress in spin-orbit coupled Bose-Einstein condensates . . . 28

1.6 Layout of this thesis . . . 31

TH-4102_206121026

2 Numerical method to solve the coupled mean-field equations 34
2.1 Split-step Crank-Nicolson scheme . . . 34
2.1.1 Real-time propagation . . . 38
2.1.2 Imaginary-time propagation . . . 45
2.1.3 Numerical extension to the quasi-two-dimensional condensates . 47
2.1.4 Convergence of ground state . . . 50
2.1.5 Quench dynamics of the spin-orbit coupled condensate . . . 53
2.2 Summary . . . 53

3 Emergence of spin-mixed superstripe phases in spin-orbit coupled spin-1 condensate 54
3.1 Introduction . . . 54
3.2 Mean-Field Model . . . 57
3.3 Simulation results . . . 60
3.3.1 Ground state phases for ferromagnetic interactions . . . 60
3.3.1.1 Different ground state phases . . . 60
3.3.1.2 Effect of SO coupling and Rabi coupling on the miscibility and ground state phase transformation . . . 65
3.3.2 Ground state phases and spin texture for antiferromagnetic interactions . . . 68
3.3.2.1 Different ground state phases . . . 68
3.3.2.2 Effect of SO and Rabi coupling on miscibility and ground state phase transformation . . . 71
3.3.3 Effect of spin-independent (c_0) and spin-exchange (c_2) interactions on the ground state phases . . . 75
3.3.3.1 Impact on the ZM phase . . . 75
3.3.3.2 Impact on the SW phase . . . 76
3.3.3.3 Impact on the SSW phase . . . 81
3.3.4 Quench dynamics of the ground state phases . . . 87
3.3.4.1 ZM phase: $k_L \sim 0.0$, and $\Omega \sim 0.0$ . . . 88
3.3.4.2 SW phase: $k_L = 3.0$, $\Omega = 1.0$ . . . 89
3.3.4.3 SSW phase: $k_L = 3.0$, $\Omega \sim 0.0$ . . . 90
3.4 Summary and Conclusions . . . 91

4 Emergence of unstable avoided crossing in the collective excitations of spin-1 spin-orbit coupled Bose-Einstein condensates 93
4.1 Introduction . . . 94
4.2 Mean-Field Model . . . 97
4.3 Single-particle spectrum . . . 99
4.4 Collective Excitation spectrum: Bogoliubov-de-Gennes Analysis . . . 101
4.5 Effect of Rabi and SO coupling on the excitation spectrum . . . 103
4.5.1 Excitation spectrum in region I . . . 106
4.5.1.1 Excitation spectrum . . . 106
4.5.1.2 Dynamical stability . . . 107
4.5.2 Excitation spectrum in region IIa . . . 109

4.5.2.1 Excitation spectrum . . . 109
4.5.2.2 Dynamical stability . . . 110
4.5.3 Excitation spectrum in region IIb . . . 113
4.5.3.1 Excitation spectrum: . . . 113
4.5.3.2 Dynamical stability . . . 116
4.5.4 Excitation spectrum in region-III . . . 118
4.5.4.1 Excitation spectrum . . . 118
4.5.4.2 Dynamical stability . . . 120
4.5.5 Effect of coupling strength on the Band gap . . . 121
4.6 Summary and Conclusions . . . 122

5 Double unstable avoided crossings and complex domain patterns formation in spin-orbit coupled spin-1 condensates 126
5.1 Introduction . . . 127
5.2 Mean-field model . . . 130
5.3 Collective Excitation spectrum . . . 132
5.3.1 Collective excitation spectrum of ferromagnetic SO coupled BECs ($c_0 > 0, c_2 < 0$) . . . 133
5.3.2 Collective excitation spectrum of antiferromagnetic SO coupled BECs ($c_0 > 0, c_2 > 0$) . . . 139
5.4 Impact of density-density interaction and spin-exchange interaction on the MI . . . 145
5.5 Characterization of double unavoided crossings using the band gap Δ_{g1}, and Δ_{g2} of the eigen-spectrum . . . 149
5.6 Numerical Simulation . . . 150
5.6.1 Dynamics of ferromagnetic SO coupled BECs . . . 151
5.6.2 Dynamics of anti-ferromagnetic SO coupled BECs . . . 152
5.7 Summary and Conclusions . . . 153

6 Supersolid phases and collective excitations in two-dimensional Rashba spin-orbit coupled spin-1 condensates 156
6.1 Introduction . . . 157
6.2 Mean-Field Model . . . 159
6.3 Single-particle spectrum . . . 161
6.4 Collective Excitation spectrum . . . 164
6.5 Stability phases based on collective excitation for Ferromagnetic interactions . . . 165
6.5.1 Effect of finite SO and Rabi coupling on collective excitation spectrum . . . 167
6.5.1.1 Region I . . . 167
6.5.1.2 Region IIa . . . 170
6.5.1.3 Region IIb . . . 177
6.5.2 Collective excitation spectrum in absence of Rabi coupling (Ω): Region III . . . 179
6.6 Collective Excitations for Anti-ferromagnetic interactions . . . 183

6.6.1 Case (ii): $k_L = 4.0, \Omega = 0.0$ 189
6.7 Summary and Conclusions 194

7 Conclusion and future work **196**
7.1 Main conclusions of the thesis 196
7.2 Future outlook 199

A Appendix related to Chapters 4 and 5 **201**
A.1 Relevant terms of the BdG matrix of collective excitations 201

B Appendix related to Chapter 6 **204**
B.1 Relevant terms of the BdG matrix of collective excitations 204

Indian Institute of Technology Guwahati

List of Figures

1.1 (a) Depicts particles at high temperature. (b) As the temperature decreases, the characteristic de Broglie wave length λ_{dB} emerges. (c) At $T = T_c$ wavefunctions begin to overlap, and (d) Near $T \approx 0$, a macroscopic wave function forms, indicating the Bose-Einstein condensate. The figure is taken from the Ref. [28]. 5

1.2 False color images depict the cloud's velocity distribution at three stages: (A) immediately before the condensate forms, (B) just after it appears, and (C) after additional evaporation produces nearly a pure condensate. The round shape of the non-condensate fraction (mostly yellow and green) reflects an isotropic velocity distribution, consistent with thermal equilibrium. In contrast, the condensate fraction (mostly blue and white) has an elliptical shape, indicating a strongly non-thermal distribution. The figure is taken from Ref. [14]. 6

1.3 Magnetic phases of spin-1 Bose-Einstein condensates (a) $c_2 < 0$: ferromagnetic phase, and (b) $c_2 > 0$: antiferromagnetic phase. The figure is adopted from the Ref. [35]. 9

1.4 Intuitive picture showing the process of atomic interactions in spin-1 bosons. (a) Two bosons of hyperfine spin $f = 1$ approach each other. (b) They couple together and form a total spin $F = 0, 2$; precess around the total spin F during the collision. (c) Two bosons are separated from each other after the collision is finished. The figure is adopted from the Ref. [35]. 10

1.5 Spin textures associated with different spin-orbit coupling configurations. Panels (a) and (b) illustrate two-dimensional spin-orientations. (a) Rashba coupling, propotional to $\lambda_R \times (k_y\sigma_x - k_x\sigma_y)$ arising from structural inversion symmetry (b) Dresselhaus coupling, propotional to $\lambda_D \times (-k_y\sigma_x - k_x\sigma_y)$, originating from bulk inversion symmetry. Panels (c) and (d) depict effective one-dimensional SO couplings obtained when Rashba and Dresselhaus couplings contribute equally, producing two distinct unidirectional forms: (c) -$\lambda_{RD}k_x\sigma_y$ and (d) $\lambda_{RD}k_y\sigma_x$. The red and blue colors represent the different spins. This figure is adopted from Ref. [43] 16

1.6 A two-photon Raman transition couples the hyperfine states $|F = 1, m_F = -1\rangle$ and $|F = 1, m_F = 0\rangle$ within the $F = 1$ ground state manifold of ^{87}Rb. The energy difference between these two states is measured by the Zeeman splitting as $\hbar\omega_Z$. The Raman lasers have frequency shift as $\Delta\omega_L = \hbar(\omega_Z + \delta)$, where δ denotes detuning from Raman resonance. The state $|F = 1, m_F = +1\rangle$ is shifted away in energy due to a large quadratic Zeeman shift ω_q, effectively decoupling it from the Raman transition. This figure is adopted from Ref. [4]. 18

1.7 (a) Schematic and level diagram. The $|-1\rangle \leftrightarrow |0\rangle$ and $|0\rangle \leftrightarrow |+1\rangle$ transitions of the $F = 1$ ground state of ^{87}Rb were independently Raman coupled, giving experimental control of Ω_1 and Ω_2. (b) Phase diagram. The ferromagnetic order parameter is plotted against Ω_2 and Ω_1. The dashed (solid) red curve denotes the first-order (second-order) transition from the magnetized phase. This figure is taken from Ref. [10]. . . . 21

1.8 Bragg spectroscopy of a spin-orbit coupled Bose-Einstein condensate. (a) Measured Bragg response showing three resonance peaks labeled α, β, and γ. (b) Schematic representation of the corresponding transitions in the Bogoliubov excitation spectrum. The β transition probes the finite momentum roton-like minimum. The figure is take from Ref. [22]. 28

2.1 (a) Temporal evolution of the total energy and (b) temporal evolution of the root mean square size during imaginary time propagation as the system converges to the ground state. The parameters are the same as those considered in Table 2.1. 51

2.2 Stability of the condensate density profile during real-time propagation for (a) $|\psi_{+1}|^2$, (b) $|\psi_{+1}|^2$, and (c) $|\psi_{+1}|^2$. To obtain the ground state, we consider $k_L = 0.5$, $\Omega = 1.0$, $c_0 = 10$, and $c_2 = -5.0$. The density profile remains unchanged in both shape and amplitude during time evolution, indicating the stable nature of its ground state. 52

3.1 Different ground state phases of the SO coupled spin-1 BECs with ferromagnetic interaction. Real-space (top) and momentum-space (bottom) density profiles of spin components $|\psi_{+1}(x)|^2$ (solid red), $|\psi_0(x)|^2$ (dashed blue), and $|\psi_{-1}(x)|^2$ (dotted black), along with their corresponding momentum-space densities $|\psi_{+1}(k)|^2$ (solid coral), $|\psi_0(k)|^2$ (dashed purple), and $|\psi_{-1}(k)|^2$ (dotted green), under varying Rabi coupling Ω and spin-orbit coupling k_L. Interaction strengths are fixed at $c_0 = 10$ and $c_2 = -5.0$. Panels (a–d) correspond to $\Omega \sim 0$ and panels (e–h) to $\Omega = 1.0$, with $k_L = 0.0, 1.0, 1.5, 3.0$ increasing from left to right in each set. For $\Omega \sim 0$, increasing k_L induces transitions through ZM, EZM I, SW, and SSW ground state phases. At finite Ω, the SSW phase is absent. 61

3.2 Spin-density vector (SDV) components S_x (solid red line), S_y (dashed blue line), and S_z (thin black line) shown in panels (a) and (b), corresponding to Fig. 3.1, using the same interaction and coupling parameters. The S_y component remains zero across all phases. In the ZM phase, S_x shows a single peak while S_z vanishes. The EZM I phase features a single-peak S_x accompanied by finite S_z. The SSW phase is characterized by vanishing SDV components, whereas the SW phase displays a multipeak structure in S_x and oscillations in S_z, indicating density modulation. 64

3.3 Miscibility parameters (a) η_{np} and (b) η for interaction strengths $c_0 = 10$ and $c_2 = -5.0$. The top rows of (a) and (b) show pseudo color representation of η_{np} and η as a function of k_L in the range [0,5] and Ω varies from small but finite values up to 5. The green line with white dots marks the critical relation $k_L^2 \approx \Omega$, beyond which both η_{np} and η begin to decrease. η_{np} shows decreasing trend for intermediate values of k_L and then rises again. (a ii) and (b ii) show the η_{np} and η as a function of k_L for $\Omega \sim 0.0$ (dashed-dotted red line), and 1.0 (dashed green line). Panels (c i) and (c ii) show the root mean square size (x_{rms}) as a function of k_L for $\Omega \sim 0.0$ and $\Omega = 1.0$, respectively. Background color shading indicates distinct quantum phases: red (ZM), green (EZM I), blue (SW), and coral (SSW). 66

3.4 Different ground state phases of the SO coupled spin-1 BECs with antiferromagnetic interaction. Ground state density profile of the spin-component $|\psi_{+1}|^2$ (solid red line), $|\psi_0|^2$ (dashed blue line), and $|\psi_{-1}|^2$ (dotted black line) for (a1-a4) $\Omega \sim 0.0$ and (b1-b4) $\Omega = 1.0$, with interaction strengths $c_0 = 10$ and $c_2 = 5$. In each panel, k_L varies from left to right: 0.0, 0.5, 1.5, and 3.0. For $\Omega \sim 0$, the ZM phase, EZM II phase, and SSW phase are observed. For finite Ω, the SSW phase disappears, giving rise to the appearance of EZM I and SW phases. 69

3.5 SDV component S_x, S_y, and S_z in panels (a), and (b) corresponding to the Fig. 3.4. The lines representation is the same as in Fig. 3.2. Almost zero of S_y across all phases and a single peak S_x with zero (finite) S_z, confirms the ZM (EZM I) phase for finite Ω. All SDVs remain zero in the ZM polar phase, EZM II phase, and SSW phase for $\Omega \sim 0$. Multi-peak S_x along with oscillating S_z confirms the SW phase. 70

3.6 Miscibility parameters (a) η_{np} and (b) η for interaction strengths $c_0 = 10$ and $c_2 = 5.0$. (a i) and (b i) show η_{np} and η as functions of spin-orbit coupling strength k_L in the range $[0, 5]$ and Rabi coupling varies from small but finite values up to 5. The green line with white dots marks the critical relation $k_L^2 \approx \Omega$. Beyond this boundary ($k_L^2 > \Omega$), both η_{np} and η decrease. However, η_{np} exhibits a non-monotonic behavior—decreasing initially and rising again to near-maximum values. (a ii) and (b ii) display η_{np} and η as functions of k_L for fixed $\Omega \sim 0.0$ (dash-dotted red line) and $\Omega = 1.0$ (dashed green line). Panels (c i) and (c ii) show the root-mean-square condensate size $x_{\rm rms}$ versus k_L for $\Omega \sim 0.0$ and $\Omega = 1.0$, respectively. The background color represents distinct quantum phases: red (ZM), green (EZM I), limegreen (EZM II), blue (SW), and coral (SSW). 72

3.7 Ground state density profiles of $|\psi_{+1}|^2$ (solid red line), $|\psi_0|^2$ (dashed blue line), and $|\psi_{-1}|^2$ (dotted black line) in panels (a) and (c), and corresponding spin-density vector components S_x (solid red line), S_y (dashed blue line), and S_z (thin black line) in panels (b) and (d), for $k_L = 3.0$ and $\Omega = 1.0$. Panels (a, b) correspond to $c_2 = -5.0$, and panels (c, d) to $c_2 = 5.0$. In each case, the density-density interaction c_0 varies as -0.25, -0.50, -1.0, and -5.0 from left to right. The appearance of multipeak structures in S_x and oscillations in S_z indicates the SW phase, while a single peak in S_x with finite S_z signifies the EZM I phase. A transition from the SW to EZM I phase occurs with increasing $|c_0|$, for both $c_2 < 0$ and $c_2 > 0$. As $c_0 < 0$ in all cases, no external trapping potential is applied. 74

3.8 Ground state phase diagram in the c_0-c_2 plane for fixed $k_L = 3.0$ and $\Omega = 1.0$. The black dotted line separates the trapless ($c_0 < 0$) and trapped ($c_0 \gtrsim 0$) regimes. Different quantum phases are indicated by color: green denotes the EZM I phase and blue denotes the SW phase. For considered parameter (k_L, Ω) = (3.0, 1.0), the system resides in the SW phase under weak or repulsive interaction strengths, while the higher attractive strength of both c_0 and c_2 drives a transition into the EZM I phase. 77

3.9 Miscibility parameters (a) η_{np} and (b) η as functions of interaction strengths c_0 and c_2, for fixed $k_L = 3.0$ and $\Omega = 1.0$. In (a i), and (b i), both c_0 and c_2 are varied within the range $[-5, 5]$. (a ii), and (b ii) show η_{np} and η as functions of c_0 for fixed values of $c_2 = -5.0$ (dash-dotted red line), -2.5 (solid blue line), and 5.0 (dashed magenta line). Panels (c i) and (c ii) depict the root-mean-square size $x_{\rm rms}$ of the condensate for $c_2 = -5.0$ and $c_2 = 5.0$, respectively, as c_0 is varied. The background color shading represents distinct quantum phases: green indicates the EZM I phase and blue indicates the SW phase, highlighting the phase transition of the condensate. The black dotted line indicates the boundary separating trapped regime ($c_0 \gtrsim 0$) and untrapped regime ($c_0 < 0$) condensates. . . 79

3.10 Ground state density profile $|\psi_{+1}|^2$ (solid red line), $|\psi_0|^2$ (dashed blue line), and $|\psi_{-1}|^2$ (dotted black line) upon varying c_0, keeping $k_L = 3.0$ and $\Omega \sim 0.0$ with (a) $c_2 = -5.0$, and (b) $c_2 = 5.0$. The density-density interaction strength varies as $c_0 = -1.0, -3.0, -4.0$, and -5.0 in columns from top to bottom. A phase transition takes place from the SSW phase to the EZM I phase and EZM II phase upon increasing the magnitude of c_0 for $c_2 < 0$ and $c_2 > 0$, respectively. Since $c_0 < 0$, no external trapping is required. 82

3.11 Ground state phase diagram in the c_0-c_2 plane for fixed $k_L = 3.0$, and $\Omega \sim 0$. The black dotted line separates the trapless ($c_0 < 0$) and trapped ($c_0 \gtrsim 0$) regimes. Different quantum phases are indicated by color: green denotes the EZM I phase, lime green denotes EZM II, and coral denotes the SSW phase. For considered parameter ($k_L = 3.0, \Omega \sim 0.0$), the system resides in the SSW phase under weak or repulsive interaction strengths, while the higher attractive strength of both c_0 and c_2 drives a transition into the EZM's phase. 83

3.12 Miscibility parameters (a) η_{np}, and (b) η upon varying c_0 and keeping $k_L = 3.0$ and $\Omega \sim 0$. In (a i) and (b i), c_0 and c_2 vary within the range [-5,5]. (a ii) and (b ii) exhibit the η_{np} and η upon varying c_0 for $c_2 = -5.0$ (dashed-dotted red line), -2.5 (solid blue line), and 5.0 (dashed magenta line). In the bottom row, panels (c i) and (c ii) represent the root mean square (x_{rms}) size of the condensate for $c_2 = -5.0$ and 5.0, respectively, which indicate different phases of the condensate. The color code represents different quantum phases: green represents the EZM I phase, limegreen represents the EZM II phase, and coral represents the SSW phase. The black dotted line separates untrapped ($c_0 < 0$) and trapped ($c_0 \gtrsim 0$) regimes of the condensate. 85

3.13 Ground state density profile (a1-a3) for $m_F = +1, 0, -1$, respectively, with $c_0 = -1.0$, and $c_2 = 5.0$, in absence of the k_L, and Ω. The condensate is in the ZM phase. Panels (b1-b3) and (c1-c3) depict the time evolution of the initially prepared density profile upon quenching the SO coupling from $k_L \sim 0 \to 0.20$ and $k_L \sim 0.0 \to 1.0$, respectively. For a small quench of the SO coupling strength, periodic high-density peaks appear along the propagation direction, whereas a complex pattern emerges for stronger quench. Panels (d1-d3) and (e1-e3) exhibit the dynamics of the condensate density upon quenching the Rabi coupling $\Omega \sim 0.0 \to 0.20$ and $\Omega \sim 0.0 \to 0.50$, respectively. In both cases, the quench of the Rabi coupling leads to the stabilization of the condensate. The SO and Rabi coupling is quenched at $t = 0$ units. 86

3.14 Ground state density profile (a1-a3) for $m_F = +1, 0, -1$, respectively, with $(k_L, \Omega) = (3.0, 1.0)$. The interaction strengths are $c_0 = -1.0$, and $c_2 = 5.0$. The condensate is in the SW phase. Panels (b1-b3) and (c1-c3) depict the time evolution of the initially prepared density profile in the $x - t$ plane upon quenching the SO coupling strength $k_L = 3.0 \to 3.20$ and $k_L = 3.0 \to 4.0$, respectively. The SO coupling is quenched at $t = 0$ units. For a stronger quench of the Rabi coupling strength, the condensate fragments into small domains, forming a complex pattern, and the zeroth component disappears at a later time unit. 89

3.15 Ground state density profile (a1-a3) for $m_F = +1, 0, -1$, respectively, with $(k_L = 3.0, \Omega \sim 0.0)$. The interaction strengths are $c_0 = -1.0$, and $c_2 = 5.0$. The condensate is in the SSW phase. Panels (b1-b3) and (c1-c3) exhibit dynamics of the ground state profile in the $x - t$ plane upon quenching the SO coupling strength $k_L = 3.0 \to 3.20$ and $k_L = 3.0 \to 4.0$, respectively. The SO coupling is quenched at $t = 0$ units. The strong quench of the SO coupling strength leads to the emergence of complex patterns. 90

4.1 Single-particle energy spectrum in momentum space for the different set of SO and Rabi coupling strengths (k_L, Ω): (a)-(f): $(0, 0)$, $(0.7, 0)$, $(0, 0.5)$, $(0.7, 0.5)$, $(0.7, 0.7)$, $(1.0, 0.5)$. The thick-solid-red, dash-dotted green line and thin-solid-blue line represent the energy eigenspectrum for $\{-1, 0, +1\}$ components of the spin, respectively. Varying the coupling parameters lead to the changes in the eigenspectrum of different components, where ω_-, only having the lowest minimum for $\Omega > k_L^2$, whereas $\Omega < k_L^2$, the ω_- exhibits double minima appearance of plane-wave phase, indicating the presence of stripe phase. 100

4.2 Stability phase diagram in the k_L- Ω plane for the interaction parameter $c_0 = 0.5, c_2 = -0.1$ which is being considered for all the simulation runs. Based on the different characteristics of the eigenspectrum and ground state, the phase diagram is divided into regions I, IIa, IIb, and III. While Region I is stable, regions IIa, IIb, and III are unstable. The dotted white line along with green dots represent the $\Omega = k_L^2$ curve that separates region I from IIa. Blue dots with a white solid line representing $\Omega \approx 0.1365 k_L^2 - 0.0686$ separates the regions IIa and IIb. The horizontal line with a filled half square for $\Omega \sim 0$ denotes the region III after the cutoff, $k_L^c = 0.68$, which is a tricritical point for regions IIa-IIb-III, indicated as a red triangle. 103

4.3 Excitation spectrum (a) and eigenvectors (b) and (c) for the coupling parameters $k_L = 0.5$, $\Omega = 2.0$. (a) solid magenta line represents $\mathrm{Re}(\omega_-)$, and dashed-dotted green line represents the $|\mathrm{Im}(\omega_-)|$, here solid and dash-dotted lines are the analytical results of BdG Eq. 4.12 and open circles are numerical results obtained by solving Eq. 4.9. In the eigenvectors, $|u_{+1}|^2$(red open circles), $|u_{-1}|^2$ (black diamonds), $|u_0|^2$ (magenta open hexagons), $|v_0|^2$ (cyan open stars), $|v_{+1}|^2$ (green open squares), and $|v_{-1}|^2$ (magenta triangles), (b-c) the eigenvectors corresponding to eigenspectrum has shown, which we obtained by solving Eq. 4.9 numerically. The first column of the figure shows the presence of phonon mode in the eigenspectrum. Also, it has no negative or complex eigenfrequency thus, it is energetically and dynamically stable. 104

4.4 Time evolution of initially prepared stationary state density profiles illustrating dynamical stability of (a) $+1$, (b) 0, and (c) -1 components of the condensate, where the parameters are similar to Fig. 4.3. All three components $|\psi_{+1}|^2$, $|\psi_0|^2$, and $|\psi_{-1}|^2$ depict stable breather-like dynamics, which validate the dynamical stability of the condensate. 106

4.5 Energy variation in the time evolution for the stable region I. The parameter values considered in this figure are similar to Fig. 4.3. During time evolution, the condensate exhibits temporal variation of the energy and further shows stable behaviour. 107

4.6 Stability excitation spectrum eigenvalues and eigenvectors: The SO and Rabi coupling strength are $(k_L, \Omega) = (2.0, 2.0)$ (top row), and $(2.35, 4.0)$ (bottom row), respectively. (a1), (a2) shows eigenenergy, (b1), (c1), and (b2), (c2) corresponding eigenvectors, figure labels are as like Fig. 4.3. The eigenenergy spectrum shows the presence of complex eigenfrequencies in terms of two (one) bands in the top (bottom) row, which indicates the system is dynamically unstable. Whereas the eigenvectors display the spin-dipole along with spin-like mode along the q_x momentum direction, also symmetric along the axis. 108

4.7 Dynamics: (a-c) and (d-f) depict temporal evolution of stationary state density profile of $|\psi_{+1}|^2$, $|\psi_0|^2$, and $|\psi_{-1}|^2$ for (k_L, Ω): top row $(2.0, 2.0)$ and bottom row $(2.35, 4.0)$, respectively. The density profile holds stripe wave behavior in both cases for $t < 150$, and $t < 180$ for the top and bottom row, respectively. Further, it gets fragmented into several small domains. This behavior signifies the change in shape and amplitude of the density profile, where the bottom row 0-th component gets diminished, whereas the ± 1 components gained the density. 110

4.8 (a) and (b) represent the total energy of the condensate for the density evolution in Fig. 4.7. In both cases, the energy of the condensate increases at the beginning of dynamical evolution, but finally shows well-settled stable behavior; such a sudden change happened due to the external perturbation. 111

4.9 Excitation spectrum (a), and (b) for the coupling strengths, $(k_L, \Omega) = (3.1, 1.17)$ and $(5.0, 2.5)$ depict the low-lying and first-excited branches of the spectrum. The solid magenta line represents the $\mathrm{Re}(\omega_-)$ and the dashed green line represents the $|\mathrm{Im}(\omega_-)|$ which is low-lying branch of the spectrum, while the blue dash-dotted line represents $\mathrm{Re}(\omega_+)$ and black dotted line represents $|\mathrm{Im}(\omega_+)|$ corresponding to the first-excited branch of the spectrum, which obtained from Eq. 4.12. The eigenspectrum in (a, b) shows multiple instability bands as we obtained in 4.6(a1), however, (a) and (b) show one and two mode corresponding to no gap exists between the lower branch and first excited branch. Insets are for the better visualization of no gap mode between the lower and first excited state branch, the secondary y-axis scale is for representing the imaginary eigenfrequencies magnitudes. 113

4.10 The eigenvectors top and bottom rows corresponding to Fig. 4.9(a), and Fig. 4.9(b), respectively. The eigenvectors represents as $|u_{+1}|^2_{ll}$ (red dot), $|u_{-1}|^2_{ll}$ (black hexagons), $|u_0|^2_{ll}$ (magenta hexagons), $|v_0|^2_{ll}$ (cyan open stars), $|v_{+1}|^2_{ll}$ (green open squares), and $|v_{-1}|^2_{ll}$ (magenta triangles). Whereas, $|u_{+1}|^2_{fe}$ (blue open pentagon), $|u_{-1}|^2_{fe}$ (orange stars), $|u_0|^2_{fe}$ (olive open plus), $|v_0|^2_{fe}$ (red open x with the dotted line), $|v_{+1}|^2_{fe}$ (cyan open diamond), and $|v_{-1}|^2_{fe}$ (maroon dots). We depict the $+q_x$, however, the eigenfrequencies and eigenvectors are symmetric about the axis. Here we found that the eigenvectors show the spin-like mode when the complex-frequency exhibits, the density-like mode when it is only real. 114

4.11 Dynamics: (a)-(c) and (d)-(f) represent the dynamics of the condensate density profile of $|\psi_{+1}|^2$, $|\psi_0|^2$, and $|\psi_{-1}|^2$ components for (k_L, Ω) top row $(3.1, 1.17)$, and bottom row $(5.0, 2.5)$. The density profile holds stripe wave behavior in both cases for $t < 100$ and $t < 50$ units for the top and bottom row, respectively. Top row: $t > 100$, it shows non-periodic oscillation and non-uniform density in space-time, whereas the 0-th component gets disappeared. Bottom row: $t > 50$, it further gets fragmented into several small domains. This behaviour signifies the change in shape and amplitude of the density profile, along with the disappearance of the 0-th component, which confirms the dynamical instability. 115

4.12 (a) and (b) depict the total energy of the condensate for the dynamical evolution for the Fig. 4.11. Following the quenching of trap strength, the condensate exhibits temporal variation in the energy during the evolution, followed by a steady behaviour at later times. 117

4.13 Excitation spectrum (a) low-lying and (b) first-excited branches, for the coupling strengths $k_L = 5.0$, $\Omega = 0.0$. The label representation is similar to the Fig. 4.9. Insets are maximized for the visualization of the complex frequency mode. Whereas the mode corresponding to the no gap between the low-lying and first excited state branch also appeared along with the symmetric roton mode. 119

4.14 Eigenvectors top and bottom rows are corresponding to the Fig. 4.13(a) and, Fig. 4.13(b) respectively. The label representation is similar to the Fig. 4.10. In this region, both low-lying and the first excited state assume the value $\omega = 0$ for $q_x = 0$ with eigenvectors are in-phase with the low-lying and first-excited states, which indicates the existence of the phonon mode for these branches. 120

4.15 Dynamics: (a)-(c) represent the time evolution of super-stripe phase density profiles of $|\psi_{+1}|^2$, $|\psi_0|^2$, and $|\psi_{-1}|^2$ components of the condensate. The coupling strengths are $k_L = 5.0$, $\Omega = 0.0$ with interaction parameters $c_0 = 0.5$ and $c_2 = -0.1$. During dynamics, the unpolarized super-stripe wave holds its behavior for $t < 30$. Further, it breaks into two domains and oscillated either sides of the condensates of ± 1 components, and the 0-th component disappears, where ± 1 components densities are obtaining the gain, which shows the change in the density profile confirms the dynamical instability. 121

4.16 Variation of band gap Δ_g between negative and positive branches of the spectrum. (a1) For the fixed value SO coupling strength upon variation of Rabi coupling strength, vice versa in (b1). In (a1), the dash-dotted green and the dashed red lines represent gap calculation for $k_L = 1.14$ and $k_L = 3.10$, respectively. In (b1), the dash-dotted blue and the dashed black lines represent gap calculation for $\Omega = 1.3$ and $\Omega = 3.1$, respectively. The interaction parameter strength are $c_0 = 0.5$, and $c_2 = -0.1$. (a2) and (b2) are the logarithmic scale plots corresponding to (a1) and (b1), respectively. Further, in (a2) and (b2) the maroon (orange) dotted lines represent the fitting curve $\Delta_g = a\Omega^b$ with the parameters $a = 0.9811, b = 0.9974$, ($a = 1.0825, b = 1.0258$), and $a = 126.2992, b = -4.9568$, ($a = 46.4438, b = -2.2146$), respectively. 123

5.1 Eigenvalue and corresponding eigenvectors for (a) $(k_L, \Omega) = (0.5, 1.0)$ showing real eigenfrequencies and (b) $(k_L, \Omega) = (4.5, 1.0)$ showing the multiband instability for ferromagnetic interaction $c_0 = 5$, $c_2 = -2.0$. The dashed magenta line represents $\mathrm{Re}(\omega_{ll})$, the thick green line represents $|\mathrm{Im}(\omega_{ll})|$, dash-dotted blue line represents $\mathrm{Re}(\omega_{fe})$, the solid black line represents $|\mathrm{Im}(\omega_{fe})|$, dotted cyan line represents $\mathrm{Re}(\omega_{se})$, and the solid orange line represents $|\mathrm{Im}(\omega_{se})|$, here solid and dash-dotted lines are the analytical results of BdG Eq. 5.8 and open circles are numerical results obtained by solving Eq. 5.5. Eigenvectors of low-lying branch are $|u_{+1}|^2_{ll}$ (red dot), $|u_{-1}|^2_{ll}$ (black hexagons), $|u_0|^2_{ll}$ (magenta hexagons), $|v_0|^2_{ll}$ (cyan open stars), $|v_{+1}|^2_{ll}$ (green open squares), and $|v_{-1}|^2_{ll}$ (magenta triangles). For the first-excited branch, $|u_{+1}|^2_{fe}$ (blue open pentagon), $|u_{-1}|^2_{fe}$ (orange stars), $|u_0|^2_{fe}$ (olive open plus), $|v_0|^2_{fe}$ (red open x with the dotted line), $|v_{+1}|^2_{fe}$ (cyan open diamond), and $|v_{-1}|^2_{fe}$ (maroon dots). (a i) exhibits only real eigenfrequencies, and (b i) depicts multi-band instability, which is symmetric in the quasi-momentum direction. Corresponding eigenvectors depict density-like mode and spin-like mode, respectively. The UAC among branches results in I_o type instability band in the eigenspectrum. The vertical scale on the right represents the magnitude of imaginary eigenfrequencies. 134

5.2 Pseudo color plot of modulational instability gain for the ferromagnetic phase ($c_0 = 5$, $c_2 = -2$) in $k_L - q_x$ plane for (a, b) $\Omega = 1$ and (c, d) $\Omega = -1$. Left column panel corresponds to $\Sigma_{ll} \equiv |\mathrm{Im}(\omega_{ll})|$ and right column panel corresponds to $\Sigma_{fe} \equiv |\mathrm{Im}(\omega_{fe})|$. In (a), multi-band instability gain appears at $k_L = 1$, and in (b) a single-band instability appears at $k_L \approx 4.0$. In (c) and (d) double and single band instabilities appear at $k_L > 0.25$, respectively. The second-excited branch of the eigenspectrum shows the absence of instability gain for both sets of parameters. The instability gain is symmetric about k_L and q_x. 136

5.3 Pseudo color plot of the Modulational instability gain in $\Omega - q_x$ phase plane for ferromagnetic interactions ($c_0 = 5.0$, and $c_2 = -2.0$) with (a-c) for $k_L = 1$, and (d-f) for $k_L = 4.0$. (a,d) represents $\Sigma_{ll} \equiv |\mathrm{Im}(\omega_{ll})|$, (b,e) represents $\Sigma_{fe} \equiv |\mathrm{Im}(\omega_{fe})|$ and (c,f) for $\Sigma_{se} \equiv |\mathrm{Im}(\omega_{se})|$ low-lying, first-excited, and second-excited branches of the excitation spectrum. In (a), the primary band appears for $\Omega > 0$ following the relation $k_L^2 = \Omega$, while in (b) and (c), it appears only for $\Omega < 0$, with a cutoff in (c), $\Omega \approx -1.66$. Similar to the top row, the primary instability band in (d) appears for $\Omega > 0$. In (d) and (e), the secondary and primary bands appear for $\Omega > 0$ different than the top row. In (f), single band instability appears for $\Omega < 0$, following a cutoff value $\Omega \approx -1.44$. The instability gain appears is not symmetric about Ω and increases upon decreasing the Ω. However, it shows symmetric behaviour about q_x. 138

5.4 Eigenspectrum with antiferromagnetic interaction ($c_0 = 5.0$, $c_2 = 5.0$) for (a) $(k_L, \Omega) = (0.5, 1.0)$, and (b) $(k_L, \Omega) = (4.5, 1.0)$. The lines and symbols representation is same as in Fig. 5.1(a i) and (b i). In panel (a), a stable avoided crossing appears between first-excited (ω_{fe}) and second-excited (ω_{se}) as well as low-lying (ω_{ll}) and ω_{fe} branches. As SO coupling is increased in panel (b) multi-band instability emerges in the eigenspectrum accompanied by the appearance of UAC between ω_{fe}- ω_{se} and ω_{ll}- ω_{fe} branches. The first-excited branch exhibits the double UAC. The right vertical axis represents the imaginary eigenfrequencies. 140

5.5 Eigenvectors corresponding to Figs. 5.4(a) and (b), in (a) and (b), respectively. (a i, a ii), and (b i, b ii) represents eigenvectors of the low-lying and first-excited branch, while (a iii, a iv) and (b iii, biv) for the second-excited and first-excited branch of the eigenspectrum. The eigenvectors of the low-lying branch are given as $|u_{+1}|^2_{ll}$ (red dot), $|u_{-1}|^2_{ll}$ (black hexagons), $|u_0|^2_{ll}$ (magenta hexagons), $|v_0|^2_{ll}$ (cyan open stars), $|v_{+1}|^2_{ll}$ (green open squares), and $|v_{-1}|^2_{ll}$ (magenta triangles). For the first-excited branch, $|u_{+1}|^2_{fe}$ (blue open pentagon), $|u_{-1}|^2_{fe}$ (orange stars), $|u_0|^2_{fe}$ (olive open plus), $|v_0|^2_{fe}$ (red open x with the dotted line), $|v_{+1}|^2_{fe}$ (cyan open diamond), and $|v_{-1}|^2_{fe}$ (maroon dots). The eigenvectors of the second-excited branch are given as $|u_{+1}|^2_{se}$ (indigo dot), $|u_{-1}|^2_{se}$ (red hexagons), $|u_0|^2_{se}$ (black hexagons), $|v_0|^2_{se}$ (cyan triangle left), $|v_{+1}|^2_{se}$ (green open triangle down), and $|v_{-1}|^2_{se}$ (violet dots). (a i - a iv) depict in-phase behaviour (density-like mode) with the occurrence of flip at the point of stable avoided crossing between $\omega_{ll} - \omega_{fe}$, and $\omega_{se} - \omega_{fe}$. (b i, b iii) exhibit the out-of-phase behaviour (spin-like mode). At the point of UAC, eigenvectors are out-of-phase among the branches. However, (b ii, b iv) only depict density-like mode. 141

5.6 MI gain in the $k_L - q_x$ phase plane for (a-c) $\Omega = 1$ and (d-f) $\Omega = -1$. The interaction strengths are $c_0 = c_2 = 5.0$. In the panel, the pseudo color represents similar denotations as Fig. 5.3. In the top row, we obtain the instability bands at $k_L = 1.0$, following the critical relation $k_L^2 = \Omega$, while in the bottom row, it appears for $k_L > 0.25$. Symmetry arguments are similar to Fig.5.2. 142

5.7 MI gain in $\Omega - q_x$ phase diagram for (a-c) $k_L = 1$, and (d-f) $k_L = 4.0$. Here, the density-density interaction, $c_0 = 5.0$, and spin-dependent interaction $c_2 = 5.0$. The pseudo-color bar in the figure is similar to Fig. 5.3. Multi-band instability appears for the low-lying and first-excited branches of the spectrum, while the second-excited branch shows single-band instability. The instability gain appears is not symmetric about Ω and increases upon decreasing the Ω. However, it shows symmetric behaviour about q_x. 143

5.8 Pseudo color representation of the MI gain for $\Sigma_{ll} \equiv |\mathrm{Im}(\omega_{ll})|$ in $k_L - \Omega$ phase plane for (a) $(c_0, c_2) = (5, 5)$ and (b) $(c_0, c_2) = (5, -2)$ at quasi-momentum $q_x = 1$. Multi-band instability appears in each case, which increases upon increasing the k_L. The instability bands show symmetric behaviour about k_L, however, it is not symmetric with the variation in Ω. 145

5.9 (a) Pseudo color representation of MI gain for low-lying mode $\Sigma_{ll} \equiv |\mathrm{Im}(\omega_{ll})|$ in $c_0 - q_x$ phase plane with $(k_L, \Omega) = (0.5, 1.0)$. (b) and (c) represent the pseudo color representation of MI gain for low-lying mode $\Sigma_{ll} \equiv |\mathrm{Im}(\omega_{ll})|$ and first excited mode $\Sigma_{fe} \equiv |\mathrm{Im}(\omega_{fe})|$ respectively in the $c_0 - q_x$ phase plane for $(k_L, \Omega) = (4.5, 1.0)$. The spin-exchange interaction is $c_2 = -2.0$. In (a), the instability gain appears only in the low-lying branch, while in (b, c), it appears in a low-lying and first-excited branch of the excitation spectrum. In the panel, the instability gain increases upon decreasing the c_0, showing symmetric behaviour about q_x. However, it is not symmetric about c_0. 146

5.10 MI of antiferromagnetic interaction ($c_2 = 5.0$) in $c_0 - q_x$ phase for (a-c) $k_L = 4.5, \Omega = 1.0$. The pseudo color bar is similar to Fig. 5.3. Multi-band instability in low-lying and first-excited branches and single-band instability in the second-excited branch of eigenspectrum increases upon increasing the c_0 and symmetry arguments are similar to figure 5.9. . . . 147

5.11 MI in $c_2 - q_x$ phase plane for (a-c) $k_L = 4.0, \Omega = 1.0$, with $c_0 = 5.0$. The pseudo color bar is similar to Fig. 5.3. The instability gain of the spectrum increases upon increasing c_2, showing the symmetric behaviour about q_x. However, it is not symmetric about c_2. 148

5.12 The pseudo color representation of MI gain of lowest eigen mode $\Sigma_{ll} \equiv |\mathrm{Im}(\omega_{ll})|$ in $c_0 - c_2$ phase plane for (a) $(k_L, \Omega) = (0.5, 1.0)$ and (b) $(k_L, \Omega) = (4.0, 1.0)$. The quasi-momentum strength is fixed at $q_x = 1$. In (a) the instability gain appears only in the low-lying branch when the total interaction strength is attractive $c_0 + c_2 < 0$, while in (b) the spectrum exhibits multi-band instability. The instability gain in the eigenspectrum is neither symmetric about c_0 nor about c_2. 148

5.13 Pseudo color representation of the change in band gap $\Delta_{g1} = \mathrm{Re}(\omega_{fe}) - \mathrm{Re}(\omega_{ll})$ and $\Delta_{g2} = \mathrm{Re}(\omega_{se}) - \mathrm{Re}(\omega_{fe})$ for different k_L in $c_2 - q_x$ plane by keeping $\Omega = 1.0$, and $c_0 = 5.0$. (a i, a ii) for $k_L = 0.5$, (b i, b ii) for $k_L = 2.0$ and (c i, c ii) for $k_L = 4.5$. For (a i, b i), the band gap Δ_{g1} closes for positive $c_2 > 0$ (antiferromagnetic interaction). However, in (c i), it closes for both antiferromagnetic ($c_2 > 0$) and ferromagnetic ($c_2 < 0$) interactions. In (a ii - c ii), the band gap Δ_{g2} closes for antiferromagnetic interactions only ($c_2 > 0$). 149

5.14 Time evolution of the condensate in $x-t$ plane for $|\psi_{+1}|^2$, $|\psi_0|^2$, $|\psi_{-1}|^2$ components of the condensate for (top row) (k_L, Ω) = (0.5, 1.0), and (bottom row) (k_L, Ω) = (4.5, 1.0), upon quenching the trap strength to one-third of its initial value. The interaction strengths are $c_0 = 5.0$ and $c_2 = -2.0$. In the top row, the density profile shows stable behaviour throughout, showing the dynamical stability of the condensate. In the bottom row, the density profile holds its SW nature for a while; at a later time, $|\psi_{\pm1}|^2$ fragments in small domains and show decay in amplitude while the zeroth component diminishes at first, further gains the amplitude. 151

5.15 Dynamical evolution of the condensate in $x-t$ plane for $|\psi_{+1}|^2$, $|\psi_0|^2$, $|\psi_{-1}|^2$ components of the condensate for (top row) $k_L = 0.5, \Omega = 1.0$ and (bottom row) $k_L = 4.5, \Omega = 1.0$, by quenching the trap strength to one-third of its initial value. The interaction strengths are $c_0 = 5.0$, and $c_2 = 5.0$. In the PW phase, the density of the condensate shows stable breather-like dynamics. The SW phase holds its shape in the beginning, further $|\psi_{\pm1}|^2$ components fragments in several small domains, and zeroth components start diminishing, confirming the dynamical instability of the condensate. 153

6.1 Single-particle energy spectrum top row along q_x direction and bottom row along q_y direction for the different set of SO and Rabi coupling strengths (k_L, Ω): (a)-(f): $(0,0)$, $(0.7,0)$, $(0,0.5)$, $(0.7,0.5)$, $(0.5,1.0)$, $(1.0,0.5)$. The thick solid red, thin solid blue line, and dash-dotted green line represent the energy eigenspectrum for $\{-1, 0, +1\}$ components of the spin, respectively. Along q_x direction, the double minimum appears in the eigenvalue dispersion, following the relation $k_L^2 > \Omega$, indicating the emergence of finite momentum minima, whereas for $k_L^2 < \Omega$ the spectrum retains a single minimum at zero momentum. Along the q_y direction, the combined presence of SO and Rabi couplings produces an anisotropic dispersion with shifted minima due to symmetry breaking. 161

6.2 Stability phase diagram in the k_L–Ω plane for ferromagnetic interactions ($c_0 = 50.0$ and $c_2 = -2.5$) for full range of q_x with $q_y = 0$. The dash–dotted white line with green dots ($k_L^2 \simeq \Omega$) separates stable (I) and unstable (II) regions. Within region II, the solid white line with blue dots ($\Omega = -1.6329 + 0.13k_L^2$) distinguishes gapped (IIa) and gapless (IIb) spectra. The case $\Omega \sim 0$ lies in the unstable regime. The markers in different regions represent the coupling parameter points for which detailed collective excitation analysis is reported in the paper. 166

6.3 Eigenvalue spectrum and eigenvectors along the quasi-momentum directions q_x and q_y for $k_L = 0.5$, $\Omega = 1.0$, $c_0 = 50$, and $c_2 = -2.5$. Top row: low-lying branch. (a i) Eigenvalue spectrum, with $\mathrm{Re}(\omega_{ll})$ (solid magenta) and $|\mathrm{Im}(\omega_{ll})|$ (dashed dotted green). (a ii, a iii)Corresponding eigenvector components $|u_m|^2_{ll}$ and $|v_m|^2_{ll}$ for $m = 0, \pm 1$. Bottom row: first excited branch. (b i) Eigenvalue spectrum with $\mathrm{Re}(\omega_{fe})$ (solid blue). (b ii, b iii) Corresponding eigenvector components $|u_m|^2_{fe}$ and $|u_m|^2_{fe}$. All eigenvalues are real and positive, and the low-lying branch exhibits a phonon mode, indicating both dynamical and energetic stability. 168

6.4 Pseudocolor density plots showing the time evolution of the condensate following a quench of the harmonic trap strength from $\lambda = 1$ to $\lambda = 0.5$. Panel (a) shows the ground-state density profile, while panels (b-d) correspond to the evolution at $t = 200$, 500, and 1000, respectively, for coupling parameters $(k_L, \Omega) = (0.5, 1.0)$ and interaction strengths $c_0 = 50$, $c_2 = -2.5$. Columns (i-iii) represent the $j = +1, 0, -1$ components of the spinor condensate. The persistence of the density profiles over long times demonstrates the dynamical stability of the condensate under the trap quench. 170

6.5 Eigenvalue spectra [(a i), (b i)] and corresponding eigenvectors [(a ii, a iii) and (b ii, b iii)] for $k_L = 4.0$ and $\Omega = 1.0$ with interaction strengths $c_0 = 50.0$ and $c_2 = -2.5$, shown along the quasi-momentum directions q_x and q_y, respectively. Line styles and symbols follow the conventions of Fig. 6.3. A multiband instability develops along the q_x direction, leading to spin–density–spin mixed modes in the eigenvector components, while the low-lying branch exhibits negative-energy excitations along the q_y direction. 171

6.6 Eigenvalue spectra [(a i), (b i)] and corresponding eigenvectors [(a ii, a iii) and (b ii, b iii)] for $k_L = 4.0$ and $\Omega = 3.0$ with interaction strengths $c_0 = 50.0$ and $c_2 = -2.5$, shown along the quasi-momentum directions q_x and q_y, respectively. Line styles and symbols follow the conventions of Fig. 6.3. A single-band instability appears in the low-lying branch along the q_x direction, while a roton-maxon-like feature develops in the low-lying branch along the q_y direction. 172

6.7 Variation of roton-maxon modes for ferromagnetic interaction ($c_0 = 50$, $c_2 = -2.5$). Panels (a-c) show the results obtained for $k_L = 4.0$ as the Rabi coupling is varied. Panel (a) displays the evolution of the maxon (red open right triangles) and roton (green open diamonds) modes, while panel (b) shows the corresponding decay of the roton depth Δ_{RD} (blue open hexagons). Panel (c) illustrates quasi-momentum positions of the maxon (red open pentagon) and roton (green open hexagons) modes along the q_y direction. Panel (d) presents the phase diagram in the $k_L - \Omega$ plane at $q_x = 0.0$, with gray, blue, and red regions indicating the absence of maxon–roton modes n(M–R), the presence of maxon–roton modes (M–R), and energetic instability (Ener.-U), respectively, along the q_y direction. 174

6.8 Pseudocolor density plots showing the time evolution of the condensate following a quench of the harmonic trap strength from $\lambda = 1$ to $\lambda = 0.5$. (a) Stationary state density profile. (b-d) snapshots during time evolution at t = 200, 500, 1000, respectively, for coupling parameters (k_L, Ω) = (4.0, 1.0), with interaction strengths $c_0 = 50$, $c_2 = -2.5$. Each column represents the spinor components, with $j = +1$ (top) , 0 (middle), and -1 (bottom). 175

6.9 Eigenspectra and corresponding eigenvectors for the spinor condensate are shown, with the top (bottom) row corresponding to quasi-momentum along q_x (q_y) for $(k_L, \Omega) = (4.5, 0.5)$, and interaction strengths $c_0 = 50.0$, $c_2 = -2.5$. Panels (a i) and (b i) display the eigenspectra, with $\mathrm{Re}(\omega)$ shown as solid lines and $|\mathrm{Im}(\omega)|$ as dashed or dotted lines. The eigenvector components for the low-lying and first-excited branches are shown in panels (a ii, a iii) and (b ii, b iii), respectively. Multi-band instability appears in the low-lying branch, single-band instability in the first-excited branch arises from avoided crossings along q_x, and negative eigenfrequencies are observed along q_y. 176

6.10 Pseudocolor plots in panel represent (a) stationary state density and (b-d) density profile during time evolution at times $t = 200, 500, 100$, respectively, for coupling parameters (k_L, Ω) = (4.5, 0.5) with interaction strengths $c_0 = 50$, $c_2 = -2.5$. Each column (i–iii) corresponds to the density of the spinor components $|\psi_{+1}|^2$, $|\psi_0|^2$, and $|\psi_{-1}|^2$, respectively. During the time evolution, the trap strength is suddenly reduced to half of its original value. 178

6.11 Collective excitation spectrum (a i) and (b i) with the corresponding eigenvectors (a ii, a iii) and (b ii, b iii) for $k_L = 2.0$, $\Omega \sim 0.0$, using interaction strengths $c_0 = 50.0$ and $c_2 = -2.5$ along with quasi-momentum directions q_x and q_y, respectively. The line styles and symbols in the top and bottom rows follow the same convention as in Fig. 6.3. 180

6.12 (a i, b i) Eigenvalue spectrum and (a ii, a iii, b ii, b iii) corresponding eigenvectors for $k_L = 4.0$ in the static limit ($\Omega = 0$), with interaction strengths $c_0 = 50.0$ and $c_2 = -2.5$. The spectra and eigenvectors are plotted as functions of the quasi-momenta q_x and q_y, respectively. The line styles and symbols in the top and bottom rows follow the same convention as in Fig. 6.9. 180

6.13 Pseudocolor plots of the stationary state and time-evolved densities. (a) The circularly asymmetric density profile of the ground state. (b–d) The density evolution at times $t = 200, 500$, and 1000, respectively. Columns (i)–(iii) correspond to the spinor components $j = +1, 0$, and -1, respectively. Parameters: lattice coupling $(k_L, \Omega) = (2.0, 0.0)$ and interaction strengths $c_0 = 50$, $c_2 = -2.5$. 183

6.14 Collective excitation spectrum as a function of (a) quasi-momentum q_x and (b) quasi-momentum q_y. Parameters are SO coupling strength $k_L = 2.0$, Rabi frequency $\Omega = 0.0$, and interaction strengths $c_0 = 50$, $c_2 = 2.5$. Solid magenta, solid blue, and thin red lines represent $\mathrm{Re}(\omega_{ll})$, $\mathrm{Re}(\omega_{fe})$, and $\mathrm{Re}(\omega_{se})$, respectively; dashed green, dotted orange, and dash-dotted black lines show the corresponding magnitude of the imaginary part $|\mathrm{Im}(\omega)|$. A multiband instability with a roton minimum appears along q_x, while negative excitation frequencies are observed along q_y. 184

6.15 Eigenvector components for the excitation branches along the quasi-momentum directions (a i–a iv) q_x and (b i–b iv) q_y, corresponding to the eigenvalues in Fig. 6.14. For each branch, squared amplitudes $|u_m|^2$ and $|v_m|^2$ (with $m = 0, \pm 1$) are shown using distinct markers. Low-lying branch: $|u_{+1}|^2_{ll}$ (red open circles), $|u_{-1}|^2_{ll}$ (black diamonds), $|u_0|^2_{ll}$ (magenta open hexagons), $|v_0|^2_{ll}$ (cyan open stars), $|v_{+1}|^2_{ll}$ (green open squares), $|v_{-1}|^2_{ll}$ (magenta triangles). First-excited branch: $|u_{+1}|^2_{fe}$ (blue open pentagons), $|u_{-1}|^2_{fe}$ (orange stars), $|u_0|^2_{fe}$ (olive open pluses), $|v_0|^2_{fe}$ (red open crosses, dotted line), $|v_{+1}|^2_{fe}$ (cyan open diamonds), $|v_{-1}|^2_{fe}$ (maroon dots). Second-excited branch: $|u_{+1}|^2_{se}$ (indigo dots), $|u_{-1}|^2_{se}$ (red hexagons), $|u_0|^2_{se}$ (black hexagons), $|v_0|^2_{se}$ (cyan left-pointing triangles), $|v_{+1}|^2_{se}$ (green open downward triangles), $|v_{-1}|^2_{se}$ (violet dots). 185

6.16 Pseudocolor plots of the condensate density for the spin-1 system. Plot of (a) the stationary state density profile exhibiting a superstripe phase and (b–d) density profiles during dynamical evolution at times $t = 200$, 500, and 1000 (in arbitrary units), respectively. In each subfigure, columns (i), (ii), and (iii) correspond to the $m_F = +1$, 0, and -1 spinor components. The system parameters are fixed at $k_L = 2.0$, $\Omega = 0.0$, and interaction strengths $c_0 = 50$, $c_2 = 2.5$. 187

6.17 (a1, b1) Stationary state density profiles. (a2–a4, b2–b4) Density profiles at evolution times $t = 200, 500$, and 1000 (arb. units). The top row shows the density along the spatial x-direction at $y = 0$, and the bottom row shows the density along the y-direction at $x = 0$. Coupling parameters and interaction strengths are the same as in Fig. 6.16. The solid red line represents $|\psi_{+1}|^2$, the dashed blue line $|\psi_0|^2$, and the dotted black line $|\psi_{-1}|^2$. 188
6.18 Eigenvalue spectrum along the quasi-momentum directions (a) q_x and (b) q_y. The coupling parameters are $k_L = 4.0$ and $\Omega = 0.0$, with interaction strengths $c_0 = 50$ and $c_2 = 2.5$. Line styles and symbols have the same meaning as in Fig. 6.14. 189
6.19 Eigenvectors corresponding to Fig. 6.18; (a i-a iv) along the quasi-momentum direction q_x, and (b i-b iv) along the quasi-momentum direction q_y. The lines and symbols have the similar meaning as in Fig. 6.15. 190
6.20 Density profiles of a spin-1 condensate. (a) The initial stationary state profile, showing the superstripe phase. (b–d) Dynamical density profiles at evolution times $t = 200$, 500, and 1000 (in simulation units), respectively. For each state (a–d), the three columns (i), (ii), and (iii) correspond to the spinor components $m_F = +1, 0$, and -1. The system parameters are $k_L = 4.0$, $\Omega = 0.0$, $c_0 = 50$, and $c_2 = 2.5$. 192
6.21 (a) shows the ground-state density profile, while (b–d) display the density profiles during time evolution at $t = 200, 500$, and 1000 units, respectively. The top row shows densities along the x-direction at $y = 0$, and the bottom row along the y-direction at $x = 0$. The coupling parameters and interaction strengths are the same as in Fig. 6.20. Line styles indicate the spinor components: solid red for $|\psi_{+1}|^2$, dashed blue for $|\psi_0|^2$, and dotted black for $|\psi_{-1}|^2$. 193

Indian Institute of Technology Guwahati

TH-4102_206121026

TH-4102_206121026

Chapter 1

Introduction

Spin-orbit (SO) coupling, which links a particle's spin to its orbital angular momentum, is a central concept in condensed matter physics and plays a crucial role in understanding many quantum phenomena, including, topological insulators [1], the spin Hall effect [2], and spintronics [3]. In the context of ultracold atomic gases, the SO coupling has been realized by Lin *et al.* in 2011 [4], employing two of the three $F = 1$ hyperfine states of ^{87}Rb to engineer an effective coupling analogous to equal-strength Rashba [5] and Dresselhaus [6] couplings. Prior to this experimental breakthrough, most studies focused on theoretical proposals for implementing SO coupling in ultracold atoms and on exploring its effects at the single-particle level. Notable examples include the realization of Rashba SO coupling using an atomic tripod scheme [7] and proposals employing SO coupled atoms to simulate spin-Hall physics [8, 9]. These works established the framework for synthetic SO coupling; comparatively few investigations addressed the role in many-body systems, which are essential for understanding collective behaviour in Bose-Einstein condensates (BECs). Recently, Campbell *et al.* [10], and Luo *et al.* [11] have extended it to spin-1 BECs by employing all three $F = 1$ hyperfine states, enabling the formation of SO coupled spin-1 condensates. Spin-1 condensates possess additional internal degrees of freedom and spin-dependent interactions, leading to a substantially richer landscape of ground states and dynamical phenomena. The interplay between SO coupling and interactions gives rise to novel phases, complex spin textures, and unconventional symmetry-breaking mechanisms.

The study of ground-state properties offers valuable insight into the phase structure of the SO coupled spinor condensates. A comprehensive understanding of these condensates, however, necessitates an analysis of their collective excitations. The collective excitation spectrum provides detailed information about phase stability, fluc-

TH-4102_206121026

tuations around the ground-state phases, and superfluidity. In 1941, Landau coined the term elementary excitations and introduced a phenomenological description of superfluids in terms of collective modes such as rotons and phonons [12]. For weakly interacting Bose gases, the microscopic theory of these excitations was developed by Bogoliubov in 1947 [13]. By diagonalizing the interacting bosonic Hamiltonian, Bogoliubov showed that the low-momentum excitation spectrum is linear, corresponding to phonon-like modes, thereby providing a microscopic foundation for Landau's phenomenological picture. The experimental realization of dilute, weakly interacting BECs (weakly interacting limit refers to the regime $na_s^3 << 1$, which is satisfied by dilute atomic Bose-Einstein condensates.) in 1995 [14, 15] enabled direct probe of collective excitations in quantum gases. Soon after this breakthrough, low-lying Bogoliubov modes were observed in the laboratory through controlled perturbations of the trapping potential, confirming the theoretical picture of phonon-like excitations and superfluid behaviour [16, 17]. Bragg spectroscopy further allowed access to higher-momentum excitations, providing a direct measurement of the excitation spectrum and validating Bogoliubov theory in the weakly interacting regime [18, 19].

These early studies established collective excitations, an essential tool to diagnose the stability of the condensate and superfluidity. Extending this framework beyond single-component condensates revealed qualitatively new physics. In multicomponent condensates, coupling between internal degrees of freedom can modify the quasiparticle spectrum and even induce dynamical instabilities for repulsive interactions. A seminal theoretical analysis by Goldstein and Meystre demonstrated that the mode coupling in multicomponent condensates can lead to complex excitation frequencies, signaling the onset of dynamical instabilities [20]. The introduction of synthetic gauge fields and SO coupling has further enriched this landscape. In SO coupled BECs, the excitation spectrum is strongly modified due to the lack of Galilean invariance, giving rise to anisotropic sound modes, roton-like features, and novel instability mechanisms. In particular, studies of homogeneous SO coupled condensates have shown that dynamical and energetic instabilities can emerge due to the interplay between Raman coupling and interactions, as demonstrated by Ozawa [21]. More recently, collective excitations in SO coupled binary BECs have been experimentally probed by Khamehchi et al. [22] using Bragg spectroscopy, providing direct measurements of the roton modes in the excitation spectrum.

Recent theoretical works have explored the ground-state phase diagrams and collective excitation spectrum of SO coupled spin-1 condensates in both ferromagnetic and antiferromagnetic regimes [23–25], revealing a wide variety of magnetic phases

and a modified quasiparticle spectrum. These studies demonstrate that the SO coupling fundamentally alters the excitation spectrum of spin-1 condensates. Despite this progress, a comprehensive and unified understanding of the ground-state phases, collective excitations, and associated instability mechanisms in SO coupled spin-1 BECs remains incomplete. In particular, a systematic comparison of ferromagnetic and antiferromagnetic interaction regimes, as well as a detailed analysis of how dimensionality influences stability and condensate dynamics, is still lacking.

Motivated by these gaps, this thesis presents a systematic investigation of SO coupled spin-1 BECs, focusing on ground-state phase diagrams, collective excitation spectra, and dynamical instabilities. The analysis is carried out for homogeneous quasi-one-dimensional (quasi-1D) and quasi-two-dimensional (quasi-2D) geometries, with particular emphasis on contrasting ferromagnetic and antiferromagnetic interactions. This approach provides a coherent framework for understanding the roles of SO coupling, dimensionality, and spin-dependent interactions in determining the stability and dynamics of spin-1 condensates.

The outline of the chapter is as follows. We begin by presenting the theoretical framework for scalar BECs, including the derivation of the single-component Gross-Pitaevskii equation. We then extend the discussion to spinor condensates, with particular emphasis on spin-1 BECs, and introduce the corresponding three-component coupled Gross-Pitaevskii equations (GPEs). Subsequently, we discuss the realization of synthetic SO coupling in spin-1 condensates, building on earlier developments in binary condensates. The concept of collective excitations and their physical significance in BECs is then introduced. We first outline the derivation of the excitation spectrum for single-component condensates and subsequently discuss its extension to spin-1 condensates. Finally, we review recent progress in the field, identify open questions in the existing literature, and motivate the scope and objectives of the present thesis.

1.1 Bose-Einstein Condensates

A Bose-Einstein condensate (BEC) is a state of matter in which a macroscopic number of particles occupy the lowest quantum state of the system. More precisely, Bose-Einstein condensation is a quantum phenomenon in which indistinguishable bosonic particles lose their individual identities and behave collectively as a single coherent quantum entity. This phase is fundamentally distinct from classical phases of matter

TH-4102_206121026

such as solids, liquids, and gases. The particles that form a BEC are bosons, which possess integer spin, obey Bose-Einstein statistics, and have wave functions that are symmetric under the exchange of particle coordinates.

For a system of non-interacting bosons in thermal equilibrium, the mean occupation number of a single-particle state with energy ϵ_j is given by the Bose-Einstein distribution [26],

$$f(\epsilon_j) = \frac{1}{e^{\beta(\epsilon_j - \mu)} - 1}\,, \tag{1.1}$$

where μ is the chemical potential, $\beta = 1/(k_B T)$, k_B is the Boltzmann constant, and T is the temperature. Since bosons do not obey the Pauli exclusion principle, there is no upper bound on the number of particles occupying a single quantum state. As a result, below a critical temperature, a macroscopic population accumulates in the ground state, signaling the onset of Bose-Einstein condensation.

The condition for BEC can be estimated for a uniform gas of noninteracting bosons characterized by particle density n and mass m. Dimensional analysis shows that the characteristic energy scale of the system is set by $\hbar^2 n^{2/3}/m$, which can be associated with the thermal energy $k_B T_c$. The critical temperature for Bose-Einstein condensation is therefore given by

$$T_c = A\frac{\hbar^2 n^{2/3}}{k_B m}\,, \tag{1.2}$$

where A is a numerical constant determined from an exact calculation and has the value $A \approx 3.3$ [27].

An equivalent condition for condensation can be expressed in terms of the thermal de Broglie wavelength,

$$\lambda_T = \left(\frac{2\pi\hbar^2}{m k_B T}\right)^{1/2}\,. \tag{1.3}$$

At the transition temperature $T = T_c$, the thermal wavelength becomes comparable to the mean interparticle spacing, yielding,

$$\lambda_T \sim n^{-1/3}\,. \tag{1.4}$$

The physical significance of this result is illustrated schematically in Fig. 1.1. At high temperatures, the thermal wavelength is much smaller than the interparticle spacing, so the particles behave like a classical gas. As the temperature decreases, the wavelength increases and eventually becomes comparable to the interparticle separation. Near the critical temperature, matter waves begin to overlap, and below this point, they merge into a single macroscopic wave function, signaling the onset of con-

TH-4102_206121026

densation.

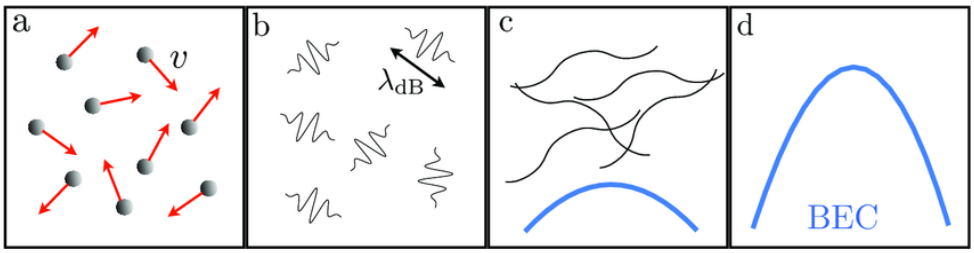


Figure 1.1: (a) Depicts particles at high temperature. (b) As the temperature decreases, the characteristic de Broglie wave length λ_{dB} emerges. (c) At $T = T_c$ wavefunctions begin to overlap, and (d) Near $T \approx 0$, a macroscopic wave function forms, indicating the Bose-Einstein condensate. The figure is taken from the Ref. [28].

In experimental situations, atomic gases are confined in trapping potentials, making the system spatially inhomogeneous. Such confinement is usually well approximated by a harmonic oscillator potential. For a gas containing N particles, the characteristic size (r) of the thermal cloud is of the order $(k_B T/m\omega_0^2)^{1/2}$, where ω_0 is the trapping frequency. Using this estimate, the density can be approximated as $n \approx N/r^3$.

Substitute this value of density in Eq. 1.2, and we get,

$$k_B T_c = A_1 \hbar N^{1/3} \omega_0 \,, \tag{1.5}$$

where A_1 is another constant which can be fixed by the calculation, and its value is 0.94 [27].

The schematic shown in Fig. 1.1 illustrates how the wavelength changes with temperature. In practice, achieving a BEC requires extremely low temperatures, typically in the nanokelvin range, together with sufficiently dilute atomic densities. Although Bose and Einstein predicted the phenomenon in 1924-25, it took several decades before it was realized experimentally. The first successful observation was achieved in 1995 using a dilute vapor of ^{87}Rb atoms. The formation of a condensate was confirmed from the measurements of the velocity distribution of the expanding atomic cloud, as shown in Fig. 1.2. Above the transition temperature, the distribution is broad and isotropic, characteristic of a thermal gas. Just below the transition, a narrow peak appears at the center, indicating the emergence of the condensate fraction. With further cooling, this peak becomes dominant, demonstrating the formation of a nearly pure condensate.

After outlining the basic picture of Bose-Einstein condensation, we now turn to its theoretical description. In the weakly interacting limit, the behaviour of a condensate can be captured by mean-field theory, leading to the Gross-Pitaevskii equation. In the following subsection, we derive the Gross-Pitaevskii equation for a single-component

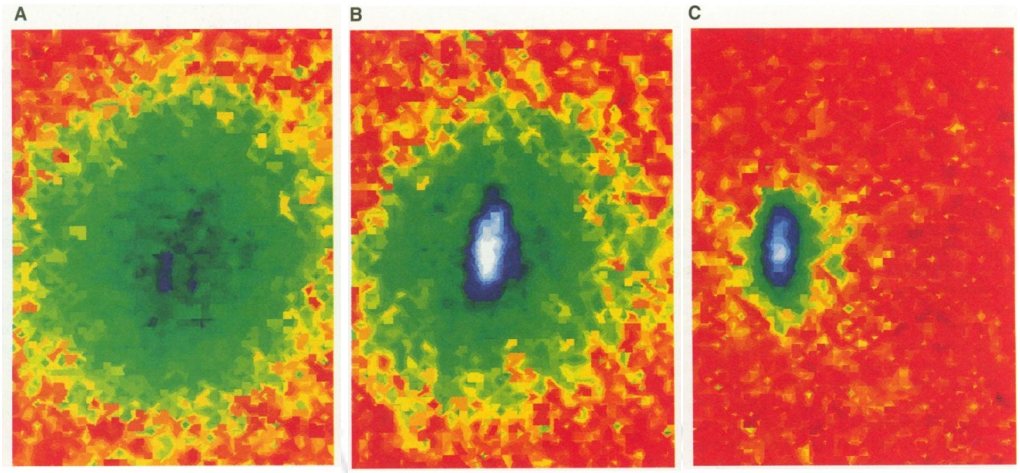


Figure 1.2: False color images depict the cloud's velocity distribution at three stages: (A) immediately before the condensate forms, (B) just after it appears, and (C) after additional evaporation produces nearly a pure condensate. The round shape of the non-condensate fraction (mostly yellow and green) reflects an isotropic velocity distribution, consistent with thermal equilibrium. In contrast, the condensate fraction (mostly blue and white) has an elliptical shape, indicating a strongly non-thermal distribution. The figure is taken from Ref. [14].

or scalar condensate.

1.1.1 Mean-field Gross-Pitaevskii equation

The second quantized Hamiltonian of a BEC can be written as the sum of a single-particle term and an interaction term,

$$\hat{\mathcal{H}} = \hat{H}_0 + \hat{H}_I \, . \tag{1.6}$$

The non-interacting part describes particles moving in an external potential and is given by

$$\hat{H}_0 = \int \hat{\psi}'^{\dagger} \left[-\frac{\hbar^2}{2m} \nabla'^2 + V' \right] \hat{\psi}' dr', \tag{1.7}$$

while the interaction term accounts for two-body interactions,

$$\hat{H}_I = \frac{1}{2} \int \int \hat{\psi}'^{\dagger} \hat{\psi}''^{\dagger} V_I(|r' - r''|) \hat{\psi}'' \hat{\psi}' dr'' dr' \, . \tag{1.8}$$

Substituting Eqs. 1.7 and 1.8 into Eq. 1.6, we get the Hamiltonian for the BECs,

TH-4102_206121026

$$\hat{\mathcal{H}} = \int \hat{\psi}'^{\dagger}\left[-\frac{\hbar^2}{2m}\nabla'^2 + V'\right]\hat{\psi}'dr' + \frac{1}{2}\int\int \hat{\psi}'^{\dagger}\hat{\psi}''^{\dagger}V_I(|r'-r''|)\hat{\psi}''\hat{\psi}'dr''dr' \,. \tag{1.9}$$

Here, $\hat{\psi}^{\dagger}(r',t) \equiv \hat{\psi}'^{\dagger}$ and $\hat{\psi}(r',t) \equiv \hat{\psi}'$ are the field operators that create and annihilate a boson, respectively, at position r' and time t. Kinetic energy operator is a function of prime co-ordinates, trap potential $V(r',t) = V'$, and $V_I(|r'-r''|)$ two-body interaction potential.

The bosonic field operators satisfy equal-time commutation relations

$$[\hat{\psi}', \hat{\psi}''] = [\hat{\psi}'^{\dagger}, \hat{\psi}''^{\dagger}] = 0 \,, \tag{1.10a}$$

$$[\hat{\psi}', \hat{\psi}''^{\dagger}] = \delta(r'-r'') \,. \tag{1.10b}$$

In dilute ultracold gases, the interparticle spacing is much larger than the range of the interatomic interaction, and collisions are dominated by s-wave scattering. Under these conditions, the interaction potential can be replaced by a contact pseudopotential valid in the low-energy limit where only s-wave scattering contributes.

$$V_I(r'-r'') = \frac{4\pi\hbar^2 a}{m}\delta(r'-r'') \,, \tag{1.11}$$

where a is the s-wave scattering length. Substituting this form into the interaction Hamiltonian removes one spatial integration using the defining property of the Dirac-delta function,

$$\int f(r'')\delta(r'-r'')dr'' = f(r') \,. \tag{1.12}$$

The Hamiltonian then becomes

$$\hat{\mathcal{H}} = \int \hat{\psi}'^{\dagger}\left[-\frac{\hbar^2}{2m}\nabla'^2 + V'\right]\hat{\psi}'dr' + \frac{U_0}{2}\int \hat{\psi}'^{\dagger}\hat{\psi}'^{\dagger}\hat{\psi}'\hat{\psi}'dr' \,, \tag{1.13}$$

where $U_0 = \frac{4\pi\hbar^2 a}{m}$. The factor $1/2$, already present in the two-body interaction Hamiltonian, prevents double counting of interacting particle pairs. To obtain the dynamical equation of motion for the field operator, we use the Heisenberg equation,

$$\frac{\partial}{\partial t}\hat{\psi} = \frac{1}{i\hbar}[\hat{\psi}, \hat{\mathcal{H}}] \,,$$

TH-4102_206121026

or,

$$\frac{\partial}{\partial t}\hat{\psi} = \frac{1}{i\hbar}(\hat{\psi}\hat{\mathcal{H}} - \hat{\mathcal{H}}\hat{\psi}) \, . \tag{1.14}$$

Evaluating the commutator yields,

$$i\hbar\frac{\partial\hat{\psi}}{\partial t} = \left[-\frac{\hbar^2}{2m}\nabla^2 + V' + U_0\hat{\psi}^\dagger\hat{\psi}\right]\hat{\psi} \, . \tag{1.15}$$

This operator equation describes the dynamics of an interacting Bose field within the contact interaction approximation. The nonlinear term contains the density operator $\hat{\psi}^\dagger\hat{\psi}$, which reflects the role of interactions. The particle number operator $\hat{N} = \int \hat{\psi}^\dagger\hat{\psi}dr$ commutes with the Hamiltonian, showing that the total particle number is conserved.

To obtain a closed equation for the condensate wave function, we now use the key physical assumption that a single quantum state is macroscopically occupied. Under this condition, the field operator can be decomposed into a condensate part and a fluctuation operator,

$$\hat{\psi}(r,t) = \sqrt{N}\psi(\mathbf{r},t) + \hat{\delta} \, , \tag{1.16}$$

where $\psi(\mathbf{r},t)$ is the condensate wave function normalized to unity and $\hat{\delta}$ represents fluctuation with zero expectation value. Hence, $\langle\hat{\psi}(r,t)\rangle = \sqrt{N}\psi(\mathbf{r},t)$. Taking the expectation value of the operator equation and neglecting fluctuations yields,

$$i\hbar\frac{\partial}{\partial t}\psi(\mathbf{r},t) = \left[-\frac{\hbar^2}{2m}\nabla^2 + V_{trap}(\mathbf{r},t) + U_0N|\psi(\mathbf{r},t)|^2\right]\psi(\mathbf{r},t) \, . \tag{1.17}$$

This nonlinear Schrödinger equation is known as the time-dependent Gross-Pitaevskii equation, where we now explicitly denote the external potential as $V_{trap}(\mathbf{r},t)$. The nonlinear term represents the mean-field interaction energy arising from atom-atom collisions and underlies theoretical descriptions of dilute BECs.

After establishing the mean-field description of scalar BECs, we extend the discussion to condensates with internal degrees of freedom in the next section. In such systems, the condensate order parameter becomes multicomponent, giving rise to spinor BECs. Unlike scalar condensates, spinor BECs support spin-dependent interactions, magnetic phases, and richer excitation spectra. These additional degrees of freedom lead to qualitatively new ground-state phases and dynamical behaviour, which form

TH-4102_206121026

the basis of the following discussion.

1.2 Spinor Bose-Einstein condensates

In the previous section, we focused on single-component BECs, which formed the primary subject of research immediately following the first experimental realization of BEC in 1995 [14, 15]. Such condensates, often called scalar BECs, are typically produced in magnetic traps that confine atoms to a single Zeeman sublevel within a hyperfine manifold. Progress in the field accelerated once multi-component condensates were realized, enabling the exploration of coupled quantum fluids with internal structure. In particular, condensates possessing spin degrees of freedom, known as spinor condensates, represent a richer form of coherent matter with nontrivial internal quantum dynamics.

Firstly, two-component condensates were realized using two hyperfine states of ^{87}Rb, where phenomena such as phase separation [29] and Rabi oscillations [30] were observed. Subsequently, experiments with sodium atoms at MIT demonstrated two-component condensates in optical traps that released the spin degrees of freedom [31]. This enabled systematic investigations of spinor physics, including ground-state structure, metastability, and quantum spin tunneling [32–34].

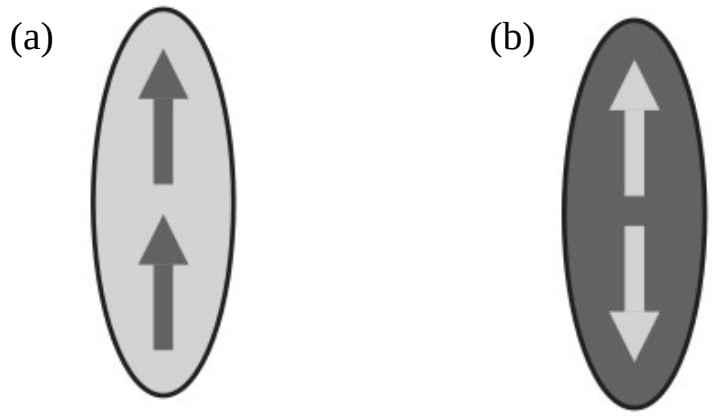


Figure 1.3: Magnetic phases of spin-1 Bose-Einstein condensates (a) $c_2 < 0$: ferromagnetic phase, and (b) $c_2 > 0$: antiferromagnetic phase. The figure is adopted from the Ref. [35].

Earlier, we noted that a scalar condensate can be described by a single order parameter ψ, whose dynamics follow Eq. 1.17. In contrast, a spinor condensate requires a multicomponent order parameter $\vec{\psi} = [\psi_F, \psi_{F-1}, ..., \psi_{-F}]$, which contains $2F + 1$ spin components and transforms under rotations in spin space [36–38]. For spin-1 conden-

sates, the two body interaction that incorporates spin dependence can be written as $V(r) = \delta(r)(c_0 + c_2\vec{F}_1 \cdot \vec{F}_2)$, where r is the interparticle separation and c_2 characterizes the spin-dependent interaction strength. The sign of c_2 determines the magnetic phase: positive c_2 corresponds to antiferromagnetic condensates, whereas negative c_2 gives ferromagnetic condensates [39] as shown in Fig. 1.3. Experiments confirm that dilute atomic gas sodium exhibits antiferromagnetic behaviour while rubidium shows ferromagnetic nature [40, 41].

1.2.1 Microscopic picture

Atomic interactions in spinor condensates arise from the low-energy s-wave collisions. At the microscopic level, consider two atoms with hyperfine spins f_1 and f_2. As they approach each other, their spins couple to form a total spin F, which can in principle take values $f_1 + f_2$ to $|f_1 - f_2|$. For identical particles with $f_1 = f_2 = f$, this reduces to $F = 2f, 2f-1, ..., 0$. However, the symmetry requirement under particle exchange imposes additional constraints: for identical bosons with a symmetric spatial wavefunction, only even values of F are allowed, whereas for fermions only odd values are permitted [39]. During the collision, the system evolves in this coupled spin channel, effectively precessing about F, after which the atoms separate.

For the spin-1 case, two identical bosons each with $f = 1$ combine into total spin channels $F = 0$ or $F = 2$. During the interaction, the pair evolves in this coupled spin state before separating again [Fig. 1.4].

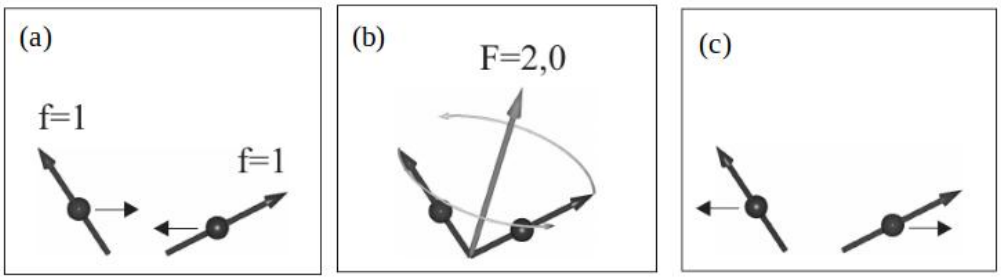


Figure 1.4: Intuitive picture showing the process of atomic interactions in spin-1 bosons. (a) Two bosons of hyperfine spin $f = 1$ approach each other. (b) They couple together and form a total spin $F = 0, 2$; precess around the total spin F during the collision. (c) Two bosons are separated from each other after the collision is finished. The figure is adopted from the Ref. [35].

Mathematically, the combined spin space of two spin-1 particles can be expressed either in the product basis $\sum_{m_f} \langle f = 1, m_f| \otimes \sum_{m_f} |f = 1, m_f\rangle$ or decomposed into irreducible total spin subspaces $\sum_{m_F} \langle F = 0, m_F| \otimes \sum_{m_F} |F = 2, m_F\rangle$. Projecting onto these

TH-4102_206121026

subspaces allows the interaction to be written as a sum over scattering channels,

$$V(\vec{r_1} - \vec{r_2}) = \delta(\vec{r_1} - \vec{r_2}) \sum_{F=0}^{2f} g_F P_F \,, \tag{1.18}$$

where, $\delta(\vec{r_1} - \vec{r_2})$ is the Dirac-delta function, g_F is the coupling strength, given in terms of scattering length a_F, mass term m and define as, $g_F = \frac{4\pi\hbar^2 a_F}{m}$, and P_F is the projection operator onto total spin F,

$$P_F \equiv \sum_{m_F=-F}^{F} |F, m_F\rangle \langle F, m_F| \,. \tag{1.19}$$

We know that the symmetry constraint on the total wavefunction of the identical bosons (fermions) should be symmetric (anti-symmetric). Since the spatial wavefunction is symmetric in both cases, the total spin part is even (odd) for bosons (fermions). As a result, only even F channels contribute for identical bosons.

$$1 = \sum_{F=0,even}^{2f} P_F = P_0 + P_2 + ... \,. \tag{1.20}$$

The spin-spin coupling operator can be written as,

$$\vec{f_1} \cdot \vec{f_2} = \frac{\vec{F}^2 - \vec{f_1}^2 - \vec{f_2}^2}{2} = \frac{F(F+1) - 2f(f+1)}{2} \,,$$

where, $\vec{f_1}$, $\vec{f_2}$, and $\vec{F}$ are dimensionless. Using identity operator defined in Eq. 1.20, we can write,

$$\vec{f_1} \cdot \vec{f_2} = (\vec{f_1} \cdot \vec{f_2})1 = \sum_F \vec{f_1} \cdot \vec{f_2} P_F = \sum_F \lambda_F P_F \,, \tag{1.21}$$

where $\lambda_F = \frac{F(F+1)-2f(f+1)}{2}$. For spin-1 particles, only F = 0 and F = 2 occur, so

$$1 = P_0 + P_2 \,. \tag{1.22}$$

And using Eq. 1.21, we can write,

$$\vec{f_1} \cdot \vec{f_2} = P_2 - P_0 \,. \tag{1.23}$$

Substituting these relations into the interaction term [Eq. 1.18] gives

$$V(\vec{r_1}-\vec{r_2}) = \delta(\vec{r_1}-\vec{r_2})(g_0P_0 + g_2P_2)\ . \tag{1.24}$$

Defining $c_0 = \frac{g_0+2g_2}{3}$ and $c_2 = \frac{g_2-g_0}{3}$, the interaction reduces to

$$V(\vec{r_1}-\vec{r_2}) = \delta(\vec{r_1}-\vec{r_2})[c_0 + c_2(\vec{f_1}\cdot\vec{f_2})]\ . \tag{1.25}$$

which is the standard spin-1 contact interaction.

After deriving the binary collision term, we can write the full Hamiltonian for N spin-1 atoms

$$H = \sum_{i=1}^{N}\frac{p_i^2}{2m} + U(r_i) + \sum_{i<j}\delta(\vec{r_i}-\vec{r_j})[c_0 + c_2(\vec{f_i}\cdot\vec{f_j})]\ , \tag{1.26}$$

where the first term is kinetic energy and the second term includes trapping and Zeeman potentials.

1.2.2 Second Quantized Hamiltonian

In second quantization, using field operators for Zeeman states ($\psi_{+1}, \psi_0, \psi_{-1}$), the Hamiltonian becomes

$$\begin{aligned} H = &\int d^3r\psi_i^\dagger(\vec{r})\left[-\frac{\hbar^2\nabla^2}{2m}\delta_{ij} + U_{ij}(\vec{r})\right]\psi_j(\vec{r}) \\ &+ \frac{g_{ij,kl}}{2}\int d^3r_1 d^3r_2\psi_i^\dagger(\vec{r_1})\psi_j^\dagger(\vec{r_2})\psi_k(\vec{r_2})\psi_l(\vec{r_1})\delta(\vec{r_1}-\vec{r_2})\ . \end{aligned} \tag{1.27}$$

Symmetry under particle exchange and time reversal reduces the large set of coupling constant $g_{ij,kl}$ to only two independent parameters, corresponding to scattering lengths in the $F = 0$ and $F = 2$ channels. In terms of c_0 and c_2,

$$\begin{aligned} H = &\int d^3r\psi_i^\dagger(\vec{r})\left[-\frac{\hbar^2\nabla^2}{2m}\delta_{ij} + U_{ij}(\vec{r})\right]\psi_j(\vec{r}) + \frac{c_0}{2}\int d^3r\psi_i^\dagger(\vec{r})\psi_j^\dagger(\vec{r})\psi_j(\vec{r})\psi_i(\vec{r}) \\ &+ \frac{c_2}{2}\int d^3r\psi_i^\dagger(\vec{r})\psi_j^\dagger(\vec{r})\vec{f}_{jk}\cdot\vec{f}_{il}\psi_k(\vec{r})\psi_l(\vec{r})\ , \end{aligned} \tag{1.28}$$

TH-4102_206121026

where, $\vec{f}_{jk} \cdot \vec{f}_{il} = (f_\alpha)_{jk}(f_\alpha)_{il}$, with $(f_\alpha)_{jk}$ are the matrix element of spin-1 Pauli matrices,

$$f_x = \frac{1}{\sqrt{2}} \begin{pmatrix} 0 & 1 & 0 \\ 1 & 0 & 1 \\ 0 & 1 & 0 \end{pmatrix}, f_y = \frac{i}{\sqrt{2}} \begin{pmatrix} 0 & -1 & 0 \\ 1 & 0 & -1 \\ 0 & 1 & 0 \end{pmatrix}, f_z = \begin{pmatrix} 1 & 0 & 0 \\ 0 & 0 & 0 \\ 0 & 0 & -1 \end{pmatrix}.$$

Interaction term of the Hamiltonian,

$$H_{int} = \frac{1}{2} \int d^3r \{ c_0(\psi_i^\dagger \psi_j^\dagger \psi_j \psi_i) + c_2(\psi_i^\dagger \psi_j^\dagger (\vec{f}_{jk} \cdot \vec{f}_{il}) \psi_k \psi_l) \} . \tag{1.29}$$

After expanding, we can write,

$$\begin{aligned} H_{int} = \frac{1}{2} \int d^3r \{ & (c_0 + c_2)\psi_{+1}^\dagger \psi_{+1}^\dagger \psi_{+1}\psi_{+1} + c_0 \psi_0^\dagger \psi_0^\dagger \psi_0 \psi_0 + (c_0 + c_2)\psi_{-1}^\dagger \psi_{-1}^\dagger \psi_{-1}\psi_{-1} \\ & 2(c_0 + c_2)\psi_{+1}^\dagger \psi_0^\dagger \psi_0 \psi_{+1} + 2(c_0 - c_2)\psi_{+1}^\dagger \psi_{-1}^\dagger \psi_{-1}\psi_{+1} + 2(c_0 + c_2)\psi_0^\dagger \psi_{-1}^\dagger \psi_{-1}\psi_0 \\ & 2c_2 \psi_{-1}^\dagger \psi_{+1}^\dagger \psi_0 \psi_0 + 2c_2 \psi_0^\dagger \psi_0^\dagger \psi_{-1}\psi_{+1} \} . \end{aligned} \tag{1.30}$$

1.2.3 Coupled Gross-Pitaevskii Equations for spin-1 condensates

After deriving the second quantized Hamiltonian for a spin-1 Bose gas, we now derive the dynamical equations governing the evolution of the spinor order parameter. The time evolution of each field operator component is determined from the Heisenberg equation of motion

$$i\hbar \frac{\partial \psi_\alpha}{\partial t} = [\psi_\alpha, H] , \tag{1.31}$$

where $\alpha = +1, 0, -1$ labels the Zeeman components. Substituting the Hamiltonian obtained in the previous section and evaluating the commutators gives the operator equation of motion

$$i\hbar \frac{\partial \psi_\alpha}{\partial t} = \left[-\frac{\hbar^2}{2m}\nabla^2 + U_\alpha \right] \psi_\alpha + c_0 \psi_i^\dagger \psi_i \psi_\alpha + c_2 \psi_j^\dagger \vec{F}_{\alpha k} \cdot \vec{F}_{jl} \psi_l \psi_k . \tag{1.32}$$

In the mean-field theory limit, we can replace the field operators with the vectorial order parameters,

$$(\psi_{+1}, \psi_0, \psi_{-1})^T = \langle (\psi_{+1}, \psi_0, \psi_{-1})^T \rangle, \tag{1.33a}$$

$$(\psi_{+1}^*, \psi_0^*, \psi_{-1}^*)^T = \langle (\psi_{+1}^\dagger, \psi_0^\dagger, \psi_{-1}^\dagger)^T \rangle. \tag{1.33b}$$

This approximation neglects quantum fluctuations and retains only the coherent condensate contribution. Defining component densities $\rho_i = |\psi_i|^2$, and total density $\rho = \rho_1 + \rho_0 + \rho_{-1}$; we obtain a set of three coupled nonlinear equations,

$$i\hbar\frac{\partial\psi_{+1}}{\partial t} = \mathcal{L}_{+1}\psi_{+1} + c_0\rho\psi_{+1} + c_2(\rho_{+1} + \rho_0 - \rho_{-1})\psi_{+1} + c_2\psi_{-1}^*\psi_0^2 \,, \tag{1.34a}$$

$$i\hbar\frac{\partial\psi_0}{\partial t} = \mathcal{L}_0\psi_0 + c_0\rho\psi_0 + c_2(\rho_{+1} + \rho_{-1})\psi_0 + 2c_2\psi_0^*\psi_{+1}\psi_{-1} \,, \tag{1.34b}$$

$$i\hbar\frac{\partial\psi_{-1}}{\partial t} = \mathcal{L}_{-1}\psi_{-1} + c_0\rho\psi_{-1} + c_2(\rho_{-1} + \rho_0 - \rho_{+1})\psi_{-1} + c_2\psi_{+1}^*\psi_0^2 \,, \tag{1.34c}$$

where, $\mathcal{L}_{\pm1,0} \equiv (-\frac{\hbar^2\nabla^2}{2m} + U_{\pm1,0})$. Here, $U_{\pm1,0}$ denotes the component-dependent external potential including trapping and Zeeman contributions.

1.3 Spin-orbit coupled Bose-Einstein condensates

Spin-orbit interaction arises from the coupling between a particle's internal and external degrees of freedom. In general, a complete physical description of a system must account for possible interactions between these degrees of freedom, since they can become dynamically linked. Before discussing synthetic SO coupling in BECs, it is useful to recall how spin-orbit interaction naturally appears in physical systems.

1.3.1 Spin-orbit interaction in atomic systems

In atomic systems such as hydrogen, spin-orbit interaction arises from the coupling between the electron's spin and its orbital motion. This interaction modifies the atomic spectrum, leading to fine-structure splitting of spectral lines. In the absence of magnetic fields, electron spin states are degenerate, but SO coupling lifts this degeneracy. The origin of this interaction can be understood semi-classically. An electron moving with velocity $\mathbf{v}$ through the electric field ($\mathbf{E}$) of the nucleus experiences, in the rest frame, an effective magnetic field ($\mathbf{B_{eff}}$) due to relativistic effects, which is given by,

$$\mathbf{B_{eff}} = -\frac{\mathbf{v}\times\mathbf{E}}{c^2} \,, \tag{1.35}$$

where c represents the velocity of light.

Since this effective magnetic field defines a preferred direction, the isotropy of space is broken, and spin states aligned parallel or antiparallel to the field acquire different energies. The interaction strength depends on the electron's orbital motion, since the

TH-4102_206121026

orbital angular momentum determines the magnitude of the effective magnetic field. As a result, the interaction produces a relativistic correction to the atomic Hamiltonian of the form [42]

$$\delta H = -\mu_s \cdot \mathbf{B_{eff}} \equiv \frac{g_s \mu_B}{\hbar e m_e c^2} \frac{1}{r} \frac{\partial U(r)}{\partial r} \mathbf{L} \cdot \mathbf{S} \,. \tag{1.36}$$

This term represents the spin-orbit contribution to the hydrogen-like atomic Hamiltonian and arises from a relativistic treatment of an electron moving in a central potential $U(r)$. Here μ_S denotes the electron spin magnetic moment, $\mathbf{L}$ and $\mathbf{S}$ denote the orbital and spin angular momentum operator, μ_B is the Bohr magneton, g_s is electron's spin g-factor, and m_e is mass of electron.

The same relativistic principle applies to electrons in solids. In crystals lacking inversion symmetry, electrons moving through the lattice experience internal electric fields generated by the ions. In the electron's rest frame, these fields transform into effective magnetic fields (similar to Eq. 1.35). This field couples to the electron's spin magnetic moment, giving rise to a spin-orbit interaction. If the electric field is uniform and directed along z, i.e., $\mathbf{E} = E_0 \hat{z}$, the interaction Hamiltonian becomes [5],

$$H_{SO} = -\mu_S . \mathbf{B_{eff}} \equiv -\frac{g_s \mu_B E_0}{2mc^2} (\mathbf{k} \times \boldsymbol{\sigma}) \cdot \hat{z} \,. \tag{1.37}$$

This expression can be written as,

$$H_{SO} = -\gamma_{SO} (\mathbf{k} \times \boldsymbol{\sigma}) \cdot \hat{z} \,, \tag{1.38}$$

where $\gamma_{SO} = \frac{g_s \mu_B E_0}{2mc^2}$, $\mathbf{k}$ is the wave vector, and $\boldsymbol{\sigma}$ is the Pauli matrices. In condensed matter systems, spin-orbit interaction appears in three representative forms: Rashba coupling, Dresselhaus coupling, and their combinations, whose interplay determines the resulting spin textures and dispersion relations.

1.3.2 Different types of spin-orbit couplings

In solid-state systems, spin-orbit interaction often manifests as an effective momentum-dependent magnetic field acting on an electron's spin. In this picture, the electron's motion through internal electric fields generates an effective field in its rest frame, which couples to spin and produces energy shifts that depend on momentum. As a result, the spin splitting of electronic states becomes tied to the direction and magnitude of the crystal momentum.

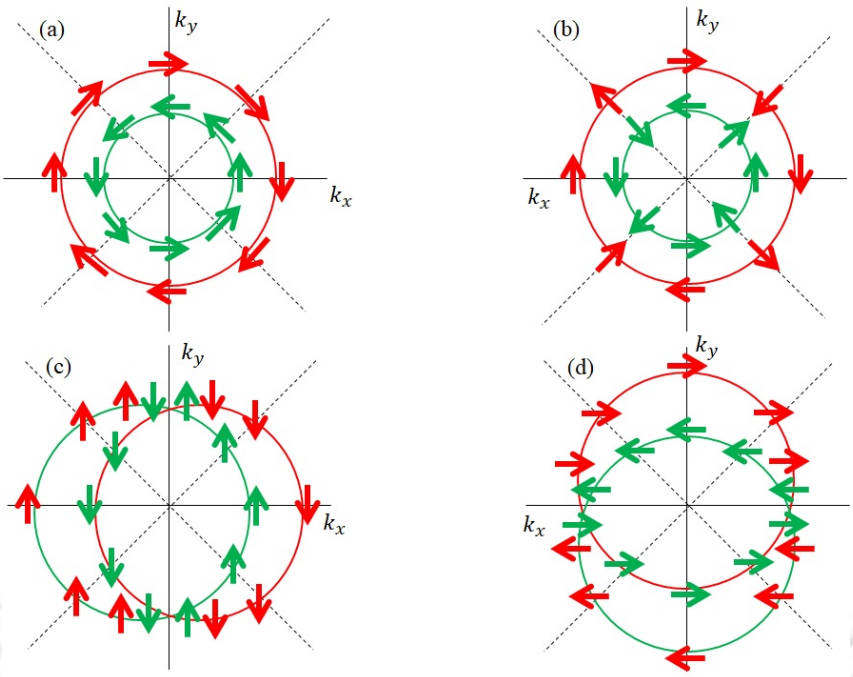


Figure 1.5: Spin textures associated with different spin-orbit coupling configurations. Panels (a) and (b) illustrate two-dimensional spin-orientations. (a) Rashba coupling, propotional to $\lambda_R \times (k_y\sigma_x - k_x\sigma_y)$ arising from structural inversion symmetry (b) Dresselhaus coupling, propotional to $\lambda_D \times (-k_y\sigma_x - k_x\sigma_y)$, originating from bulk inversion symmetry. Panels (c) and (d) depict effective one-dimensional SO couplings obtained when Rashba and Dresselhaus couplings contribute equally, producing two distinct unidirectional forms: (c) -$\lambda_{RD}k_x\sigma_y$ and (d) $\lambda_{RD}k_y\sigma_x$. The red and blue colors represent the different spins. This figure is adopted from Ref. [43]

One of the most widely studied realizations is Rashba SO coupling, which arises in systems lacking structural inversion symmetry [5]. In such environments, the interaction between the electron's momentum and spin leads to a Hamiltonian of the form

$$H_R = \lambda_R \times (k_y\sigma_x - k_x\sigma_y)\,, \tag{1.39}$$

where λ_R denotes the coupling strength and k_x, k_y are momentum components. This expression can be written compactly as

$$H_R = \Xi_R(\mathbf{k}) \cdot \boldsymbol{\sigma}\,, \tag{1.40}$$

where $\Xi_R(\mathbf{k}) = \lambda_R(-k_y, k_x, 0)$ acts as an effective momentum dependent field. Rashba coupling produces a characteristic chiral spin texture in momentum space in which the spin direction winds around the Fermi surface and depends continuously on momentum [Fig. 1.5(a)].

TH-4102_206121026

Another important form is Dresselhaus SO coupling, which originates from the bulk inversion asymmetry inherent to certain crystal lattices [6]. Its Hamiltonian is typically written as

$$H_D = \lambda_D \times (-k_y\sigma_x - k_x\sigma_y) \, . \tag{1.41}$$

In vector form, this becomes

$$H_D = \Xi_D(\mathbf{k}) \cdot \boldsymbol{\sigma} \, , \tag{1.42}$$

with $\Xi_D(\mathbf{k}) = \lambda_D(k_y, k_x, 0)$. Unlike the Rashba case, the spin orientation here is dictated by the crystal symmetry, producing a different momentum space pattern that reflects the underlying lattice structure [Fig. 1.5(b)].

When both mechanisms are present simultaneously, their combined effect can lead to qualitatively new behaviour. Linear combinations such as $H_R + H_D$ or $H_R - H_D$ generate anisotropic effective fields that constrain spin alignment along the preferred directions in momentum space. In particular regimes, this interplay yields effectively one-dimensional SO couplings, corresponding to the configurations displayed in Figs. 1.5(c,d).

The preceding discussion highlights the principal mechanisms responsible for SO coupling in electronic materials. In quantum gases, no natural analogue exists. Instead, SO coupling must be generated artificially through light-matter coupling schemes. We now describe how such synthetic spin-orbit interactions are realized in BECs.

1.3.3 Synthetic spin-orbit coupled Bose-Einstein condensates

The SO coupling is well known in condensed-matter systems, where it arises as an intrinsic relativistic interaction that links a particle's motion to its internal spin degree of freedom. In crystalline materials, this coupling originates from electric fields produced by lattice ions, which, in the rest frame of a moving electron, appear as effective magnetic fields that interact with spin. Through this mechanism, electronic energy bands can acquire momentum-dependent spin splitting, giving rise to phenomena such as spintronics [3], topological insulators [1, 44], the spin Hall effect [45, 2], and applications in quantum simulation [46, 47]. Ultracold atomic gases offer a complementary setting in which similar physics can be explored under highly controlled conditions. System parameters such as interaction strength, dimensionality, and external confinement can be tuned almost independently, allowing these systems to serve as versatile quantum simulators. However, unlike electrons in solids, neutral atoms do not nat-

TH-4102_206121026

urally experience spin-orbit interaction. Consequently, such coupling must be engineered synthetically by designing light-matter interactions that effectively link atomic momentum to internal spin states.

For the experimental realization of SO coupling in BECs, Lin *et al.* employed the dilute atomic gas of Rubidium ^{87}Rb prepared in the electronic ground state $5S_{1/2}$ [4]. The schematic diagram of the experiment is shown in Fig. 1.6. The total spin F of the atom arises from the coupling of electronic angular momentum J with nuclear spin I. Since the ground state of ^{87}Rb has orbital angular momentum $l = 0$, which leads to $J = 1/2$. For nuclear spin $I = 3/2$, hyperfine interactions split the ground state manifold into two total spin states $F = 1$ and $F = 2$. The experiment focuses on the $F = 1$ manifold, from which two hyperfine sublevels are selected to form an effective pseudospin-1/2 system [Fig. 1.6(b)].

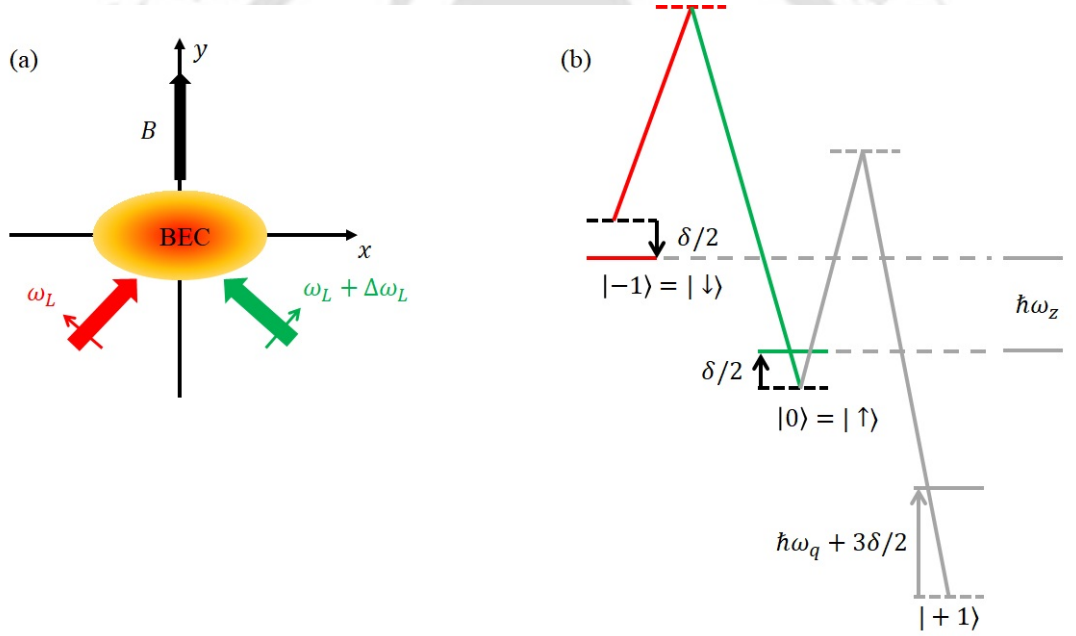


Figure 1.6: A two-photon Raman transition couples the hyperfine states $|F = 1, m_F = -1\rangle$ and $|F = 1, m_F = 0\rangle$ within the $F = 1$ ground state manifold of ^{87}Rb. The energy difference between these two states is measured by the Zeeman splitting as $\hbar\omega_Z$. The Raman lasers have frequency shift as $\Delta\omega_L = \hbar(\omega_Z + \delta)$, where δ denotes detuning from Raman resonance. The state $|F = 1, m_F = +1\rangle$ is shifted away in energy due to a large quadratic Zeeman shift ω_q, effectively decoupling it from the Raman transition. This figure is adopted from Ref. [4].

Specifically, the states $|\uparrow\rangle = |F = 1, m_F = 0\rangle$ and $|\downarrow\rangle = |F = 1, m_F = -1\rangle$ are chosen to play the roles of spin-up and spin-down components. These two internal states are coupled using a pair of Raman laser beams of wavelength $\lambda = 804.1$ nm, intersecting at an angle of 90^o [Fig. 1.6(a)]. The frequency difference between the lasers is tuned close to the Zeeman splitting between the two selected hyperfine states, producing a

TH-4102_206121026

controllable detuning δ and a Raman coupling strength Ω. The geometry of the beams transfers momentum $\pm\hbar k_L$ to the atoms, where $k_L = \sqrt{2}\pi/\lambda$, and defines the natural recoil units of momentum $\hbar k_L$ and energy $E_L = \hbar^2 k_L^2/2m$.

Including these laser-induced couplings, the single particle Hamiltonian takes the form

$$\hat{H} = \frac{\hbar^2 k^2}{2m} + \frac{\Omega}{2}\sigma_z + \frac{\delta}{2}\sigma_y + 2\alpha k_x \sigma_y \,, \tag{1.43}$$

where the quasimomentum q replaces k_x and an overall constant energy offset E_L is typically observed. The term $2\alpha q\sigma_y$ represents the effective spin-orbit interaction generated by the Raman process, with coupling strength $\alpha = E_L/k_L$, which is fixed by laser wavelength and geometry rather than by the Raman intensity Ω. Unlike condensed matter systems, where SO coupling acts within a single electronic band, this atomic realization couples the bare momentum states $|\uparrow, q + k_L\rangle$ and $|\downarrow, q - k_L\rangle$, which possess different mechanical velocities $\hbar(q \pm k_L)/m$.

In the experiment, condensates containing approximately 1.8×10^5 atoms were prepared in a crossed dipole trap with trapping frequencies $f_x = f_y = 50$ and $f_z = 140$ Hz. A bias magnetic field B_0 applied along the $\hat{y}$-direction produced a Zeeman splitting $\omega_z/2\pi = 4.81$ MHz between the two spin states. The Raman beams propagated along the directions $\hat{y} \pm \hat{x}$ and maintained a fixed frequency difference close to this splitting. The detuning parameter $\delta = \hbar(\Delta\omega_L - \omega_z)$ was controlled through the bias magnetic field. The third hyperfine state $|m_F = +1\rangle$ was effectively removed from the dynamics due to a large quadratic Zeeman shift.

In the above discussion, we described the realization of SO coupling in pseudospin-1/2 BECs. The effective Hamiltonian for such a two-level system can be written as $H = \hbar\Omega_0 + \mathbf{\Omega_1} \cdot \hat{\mathbf{S}}$, which consists of a scalar (rank-0 tensor) energy shift and a vector (rank-1 tensor) term. The first term provides a uniform energy offset, while the second term corresponds to a linear Zeeman interaction generated by an effective magnetic field proportional to $\mathbf{\Omega_1}$. In experiments realizing pseudospin-1/2 coupling, the state $|m_F = +1\rangle$ is typically removed from the dynamics through a quadratic Zeeman shift, leaving only two relevant internal states.

The situation changes fundamentally for spin-1 condensates [10]. In this case, all three Zeeman sublevels $|m_F = +1\rangle$, $|m_F = 0\rangle$, and $|m_F = -1\rangle$ must be retained, so the system can no longer be described by a simple two-component spinor. Instead, the Hamiltonian must incorporate the full spin-1 algebra, including higher rank tensor operators. In particular, a rank-2 (quadrupole) tensor term appears, allowing for ad-

TH-4102_206121026

ditional order parameters beyond ordinary magnetization. These describe nematic or polar spin configurations that have no direct analogue in spin-1/2 condensates.

Motivated by earlier results in semiconductor quantum wells [48, 49], where equal Rashba and Dresselhaus couplings generate an effective term of the form $\alpha k_x \hat{F}_z$ in the presence of a transverse Zeeman filed $\Omega_1 \hat{F}_x$, one can engineer an equivalent situation in ultracold atoms using Raman dressing. In such implementations, a pair of laser beams with wavelength λ produces a synthetic spin-orbit interaction with coupling strength $\alpha = 2\hbar k_R m$, with $E_R = \hbar^2 k_R^2/2m$ and $\hbar k_R = 2\pi\hbar/\lambda$ define the recoil energy and momentum scales.

The resulting single-particle Hamiltonian for a spin-1 condensate takes the form

$$\hat{H} = \frac{\hbar^2 k^2}{2m} + \mathbf{\Omega}_1(x) \cdot \hat{\mathbf{F}} + \mathbf{\Omega}_2 \hat{F}_{zz}^{(2)} , \tag{1.44}$$

where the momentum couples to a spatially varying effective Zeeman field $\mathbf{\Omega}_1(x)/\mathbf{\Omega}_1 = cos(2k_R x)\mathbf{e}_x - sin(2k_R x)\mathbf{e}_y$; helically precessing in the $\mathbf{e}_x - \mathbf{e}_y$ plane. The last term involves the quadrupole operator $\hat{F}_{zz}^{(2)}/\hbar = \hat{F}_z^2/\hbar^2 - 2/3$ with coupling strength $\mathbf{\Omega}_2$.

This tensor contribution leads to rich phase structure. In the limit of very small $\mathbf{\Omega}_1$, the sign of $\mathbf{\Omega}_2$ determines whether the ground state is polar ($m_F = 0$, zero magnetization, $M_z = 0$) or ferromagnetic ($m_F = \pm 1$, $|M_z| = 1$), for $\mathbf{\Omega}_2 > 0$ or < 0; separated by a first-order phase transition at $\mathbf{\Omega}_2 = 0$. For larger $\mathbf{\Omega}_1$, the system develops a spin-helix configuration that increases kinetic energy and drives a second-order transition into the ferromagnetic phase [Fig. 1.7(b)].

Experimentally, this synthetic magnetic system is realized using spin-1 ^{87}Rb condensates subjected to counter propagating Raman beams with orthogonal polarizations. Their interference generates a spatially rotating effective field with period $\lambda/2$, producing both SO and Zeeman couplings. A strong bias field along the $\hat{\mathbf{e}}_z$ introduces quadratic Zeeman shifts that separate the transition frequencies between neighboring Zeeman states, allowing the pairs $|-1\rangle \leftrightarrow |0\rangle$ and $|0\rangle \leftrightarrow |+1\rangle$ to be Raman coupled independently with equal strength $\mathbf{\Omega}_1$. By tuning the Raman frequency differences, the quadrupole coupling $\mathbf{\Omega}_2$ can be controlled, enabling exploration of the full phase diagram [Fig. 1.7(a)]. Condensates are prepared at selected parameter points, allowed to equilibrate, and their magnetization is measured from the spin-resolved momentum distributions obtained via time-of-flight imaging.

Alternative schemes have also achieved SO coupling in higher-spin condensates. For example, a tunable SO coupling in spin-1 BEC was demonstrated using a periodi-

TH-4102_206121026

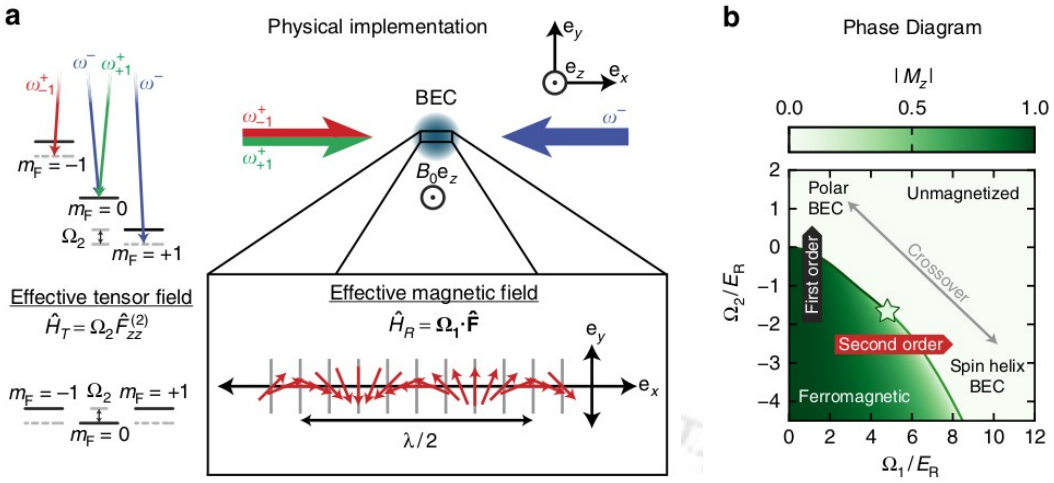


Figure 1.7: (a) Schematic and level diagram. The $|-1\rangle \leftrightarrow |0\rangle$ and $|0\rangle \leftrightarrow |+1\rangle$ transitions of the $F = 1$ ground state of ^{87}Rb were independently Raman coupled, giving experimental control of Ω_1 and Ω_2. (b) Phase diagram. The ferromagnetic order parameter is plotted against Ω_2 and Ω_1. The dashed (solid) red curve denotes the first-order (second-order) transition from the magnetized phase. This figure is taken from Ref. [10].

cally modulated gradient magnetic field, which produces spin-dependent momentum shifts and allows continuous control of the coupling strength [11]. We now turn our focus to the theoretical description required to analyze such systems. To investigate the ground-state properties, excitation spectrum, and dynamical behaviour, it is necessary to formulate the coupled GPEs appropriate for quasi-one- and two-dimensional geometries. These mean-field equations provide the foundation for the analytical and numerical studies of the upcoming sections.

1.3.4 Gross-Pitaevskii Equations for spin-orbit coupled spin-1 condensates

We now turn to the theoretical framework for analyzing BECs in the presence of SO and the Rabi coupling term. The general Hamiltonian describing spin-1 condensate and the corresponding coupled GPEs have already been introduced in Sec. 1.2, and the form of the SO interaction was discussed in Sec. 1.3. In the following, we combine these ingredients to construct the effective model for our study. For numerical simulations, it is convenient to work with dimensionless variables, so we rescale the system using standard transformations described in Ref. [50]. Rather than repeating the Hamiltonian formulation, we directly present the mean-field governing equations derived from it. The resulting coupled GPEs describe the dynamics of the spin-1 condensate with SO and Rabi couplings in reduced quasi-one- and two-dimensional geometries,

TH-4102_206121026

which serve as the basis for the analysis that follows.

In quasi-1D, the coupled GPEs are given as [50],

$$\mathrm{i}\frac{\partial\psi_{+1}}{\partial t} = \left[-\frac{1}{2}\frac{\partial^2}{\partial x^2} + V(x) + c_0(\rho_{+1}+\rho_0+\rho_{-1})\right]\psi_{+1} - \frac{k_L}{\sqrt{2}}\frac{\partial\psi_0}{\partial x} + c_2(\rho_{+1}+\rho_0-\rho_{-1})\psi_{+1} + c_2\psi_0^2\psi_{-1}^* + \frac{\Omega}{\sqrt{2}}\psi_0\,, \tag{1.45a}$$

$$\mathrm{i}\frac{\partial\psi_0}{\partial t} = \left[-\frac{1}{2}\frac{\partial^2}{\partial x^2} + V(x) + c_0(\rho_{+1}+\rho_0+\rho_{-1})\right]\psi_0 + \frac{k_L}{\sqrt{2}}\left[\frac{\partial\psi_{+1}}{\partial x} - \frac{\partial\psi_{-1}}{\partial x}\right] + c_2(\rho_{+1}+\rho_{-1})\psi_0 + 2c_2\psi_0^*\psi_{+1}\psi_{-1} + \frac{\Omega}{\sqrt{2}}(\psi_1+\psi_{-1})\,, \tag{1.45b}$$

$$\mathrm{i}\frac{\partial\psi_{-1}}{\partial t} = \left[-\frac{1}{2}\frac{\partial^2}{\partial x^2} + V(x) + c_0(\rho_{+1}+\rho_0+\rho_{-1})\right]\psi_{-1} + \frac{k_L}{\sqrt{2}}\frac{\partial\psi_0}{\partial x} + c_2(\rho_{-1}+\rho_0-\rho_{+1})\psi_{-1} + c_2\psi_0^2\psi_{+1}^* + \frac{\Omega}{\sqrt{2}}\psi_0\,. \tag{1.45c}$$

Here, ψ_{+1}, ψ_0, and ψ_{-1} are the spinor condensate wavefunctions corresponding to hyperfine sublevels $m_F = +1, 0, -1$, respectively. The quantities $\rho_j = |\psi_j|^2$ represent the density of individual spinor component, and $\rho = \Sigma_j\,\rho_j$ is the total condensate density, with $j = +1, 0, -1$. The term $V(x)$ is the trap potential. The parameters c_0 and c_2 are density-density and spin-exchange interactions, respectively, of spin-1 condensates. The parameter k_L represents the SO coupling strength, while Ω denotes the Rabi coupling strength. The energy Functional of the system is given by,

$$\begin{aligned} E = \frac{1}{2}\int dx\Big\{ &\sum_j |\partial_x\psi_j|^2 + 2V(x)\rho + c_0\rho^2 + c_2[\rho_{+1}^2+\rho_{-1}^2 \\ &+ 2(\rho_{+1}\rho_0 + \rho_{-1}\rho_0 - \rho_{+1}\rho_{-1} + \psi_{-1}^*\psi_0^2\psi_{+1}^* + \psi_{-1}\psi_0^{*2}\psi_{+1})] \\ &+\sqrt{2}\Omega[(\psi_{+1}^*+\psi_{-1}^*)\psi_0 + \psi_0^*(\psi_{+1}+\psi_{-1})] \\ &+\sqrt{2}k_L[(\psi_{-1}^*-\psi_{+1}^*)\partial_x\psi_0 + \psi_0^*(\partial_x\psi_{+1} - \partial_x\psi_{-1})]\Big\}\,. \end{aligned} \tag{1.46}$$

The Normalization and magnetization of the quasi-1D systems are given in equations below,

$$\int dx\,\rho(x) = 1\,, \tag{1.47}$$

TH-4102_206121026

$$\int dx\ [\rho_{+1}(x) - \rho_{-1}(x)] = \mathcal{M}\ . \tag{1.48}$$

In quasi-2D, the coupled GPEs are given as follows [50],

$$\mathrm{i}\frac{\partial\psi_{+1}}{\partial t} = \Big[-\frac{1}{2}\Big(\frac{\partial^2}{\partial x^2}+\frac{\partial^2}{\partial y^2}\Big) + V(x,y) + c_0(\rho_{+1}+\rho_0+\rho_{-1}) + c_2(\rho_{+1}+\rho_0-\rho_{-1})\Big]\psi_{+1}$$
$$+ c_2\psi_0^2\psi_{-1}^* - \mathrm{i}\frac{k_L}{\sqrt{2}}\Big[\nu\frac{\partial\psi_0}{\partial y} + \frac{\partial\psi_0}{\partial x}\Big] + \frac{\Omega}{\sqrt{2}}\psi_0\ , \tag{1.49a}$$

$$\mathrm{i}\frac{\partial\psi_0}{\partial t} = \Big[-\frac{1}{2}\Big(\frac{\partial^2}{\partial x^2}+\frac{\partial^2}{\partial y^2}\Big) + V(x,y) + c_0(\rho_{+1}+\rho_0+\rho_{-1}) + c_2(\rho_{+1}+\rho_{-1})\Big]\psi_0$$
$$- \mathrm{i}\frac{k_L}{\sqrt{2}}\Big[\nu\frac{\partial}{\partial y}(\psi_{+1}+\psi_{-1}) - \mathrm{i}\{\frac{\partial}{\partial x}(\psi_{+1}-\psi_{-1})\}\Big] + 2c_2\psi_0^*\psi_{+1}\psi_{-1} + \frac{\Omega}{\sqrt{2}}(\psi_1+\psi_{-1})\ , \tag{1.49b}$$

$$\mathrm{i}\frac{\partial\psi_{-1}}{\partial t} = \Big[-\frac{1}{2}\Big(\frac{\partial^2}{\partial x^2}+\frac{\partial^2}{\partial y^2}\Big) + V(x,y) + c_0(\rho_{+1}+\rho_0+\rho_{-1}) + c_2(\rho_{-1}+\rho_0-\rho_{+1})\Big]\psi_{-1}$$
$$+ c_2\psi_0^2\psi_{+1}^* - \mathrm{i}\frac{k_L}{\sqrt{2}}\Big[\nu\frac{\partial\psi_0}{\partial y} - \mathrm{i}\frac{\partial\psi_0}{\partial x}\Big] + \frac{\Omega}{\sqrt{2}}\psi_0\ , \tag{1.49c}$$

Here, ψ_j (ρ_j) is the spinor condensate wavefunctions (densities), where $j = +1, 0, -1$. The quantity $\rho = \Sigma_j\ \rho_j$ represent total density of the condensate. The term $V(x,y)$ denotes the external trap potential, c_0 is the density-density interaction strength, and c_2 is the spin-dependent interaction strength. Similar to the above case, k_L is the SO coupling strength and Ω is the Rabi coupling strength. The parameter ν governs different types of SO coupling in quasi-2D condensates. In this thesis, we consider $\nu = +1$ for Rashba-type SO-coupled BECs. The energy functional for the quasi-2D condensate is given by,

$$E = \frac{1}{2}\int dxdy\Big\{\sum_j|\nabla_{x,y}\psi_j|^2 + 2V(x,y)\rho + c_0\rho^2 + c_2[\rho_{+1}^2+\rho_{-1}^2$$
$$+ 2(\rho_{+1}\rho_0+\rho_{-1}\rho_0-\rho_{+1}\rho_{-1}) + \psi_{-1}^*\psi_0^2\psi_{+1}^* + \psi_{-1}\psi_0^{*2}\psi_{+1}]$$
$$+ 2\frac{\Omega}{\sqrt{2}}[(\psi_{+1}^*+\psi_{-1}^*)\psi_0 + \psi_0^*(\psi_{+1}+\psi_{-1})] - 2\mathrm{i}\frac{k_L}{\sqrt{2}}[\nu(\psi_{+1}^*+\psi_{-1}^*)\frac{\partial}{\partial y}\psi_0$$
$$+ \mathrm{i}(\psi_{+1}^*-\psi_{-1}^*)\frac{\partial}{\partial x}\psi_0 + \psi_0^*\{\nu\frac{\partial}{\partial y}(\psi_{+1}+\psi_{-1}) - \mathrm{i}\frac{\partial}{\partial x}(\psi_{+1}-\psi_1)\}]\Big\}\ . \tag{1.50}$$

The Normalization and magnetization of the quasi-2D system are given in equa-

TH-4102_206121026

tions below,

$$\int dxdy\ \rho(x,y) = 1\ , \tag{1.51}$$

$$\int dxdy\ [\rho_{+1}(x,y) - \rho_{-1}(x,y)] = \mathcal{M}\ . \tag{1.52}$$

After deriving the GPEs of SO coupled spin-1 BECs, we now move to the physical consequences of these governing equations. In particular, we analyze the emergent ground-state phases and collective excitation spectra. The ground state analysis reveals different phases of the condensate, while the collective excitation spectrum characterizes its stability, responses to perturbations, and dynamical properties. Together, these quantities provide a complete description of the many-body behaviour of the condensate and allow direct comparison with experimental observations.

1.4 Collective Excitation spectrum

Collective excitations are low-lying excitations that encode fundamental characteristics of BECs, such as stability, superfluid behavior, and fluctuations across different ground-state phases. In the phenomenological description of superfluids, Landau introduced the concept of elementary excitations such as phonons and rotons to characterize the dynamical response of the system. Subsequently, Bogoliubov employed field theoretical methods to derive the excitation spectrum of weakly interacting Bose gases. To develop the physical intuition, we begin by revisiting the analytical excitation spectrum of a single-component condensate and then extend the formalism to multicomponent spinor condensates with SO coupling, where the interplay between internal and motional degrees of freedom produces a significantly richer excitation spectrum.

1.4.1 Bogoliubov-de Gennes spectrum

Consider a weakly interacting BEC described by GPEs as discussed in Sec. 1.1.1,

$$i\hbar\frac{\partial\psi(\mathbf{r},t)}{\partial t} = \left[-\frac{\hbar^2}{2m}\nabla^2 + V_{trap}(\mathbf{r},t) + g|\psi(\mathbf{r},t)|^2\right]\psi(\mathbf{r},t)\ , \tag{1.53}$$

TH-4102_206121026

where the coupling constants are related by $g = NU_0$, which follows from the normalization convention adopted for the condensate wavefunction.

To study the collective excitations, the condensate wavefunction is written in terms of the ground state and a small perturbation term [27, 51],

$$\psi(\mathbf{r},t) = [\phi(\mathbf{r}) + \delta\phi(\mathbf{r},t)]e^{-i\mu t/\hbar} , \tag{1.54}$$

where, $\phi(\mathbf{r})$ is the ground state and $\delta\phi$ represents a small perturbation. For a homogenous system ($V_{trap} = 0$), the stationary solution is $\phi = \sqrt{n}$ with chemical potential $\mu = gn$.

The perturbation term is expanded in plane-wave modes,

$$\delta\phi = (u\, e^{i(\mathbf{k}\cdot\mathbf{r}-\omega t)} + v^*\, e^{-i(\mathbf{k}\cdot\mathbf{r}-\omega^* t)}) , \tag{1.55}$$

where u, and v are the Bogoliubov amplitudes. Retaining only terms linear in $\delta\phi$, the nonlinear term becomes

$$|\psi|^2\psi = |\phi|^2\phi + \phi^2\delta\phi^* + 2|\phi|^2\delta\phi . \tag{1.56}$$

Substituting Eq. (1.54) into the Eq. (1.53) and subtracting the stationary equation satisfied by ϕ eliminates zeroth order terms and yields linearized equations,

$$i\hbar\frac{\partial\delta\phi}{\partial t} = \left[-\frac{\hbar^2}{2m}\nabla^2 + 2g|\phi|^2 - \mu\right]\delta\phi + g\phi^2\delta\phi^* , \tag{1.57a}$$

$$-i\hbar\frac{\partial\delta\phi^*}{\partial t} = \left[-\frac{\hbar^2}{2m}\nabla^2 + 2g|\phi|^2 - \mu\right]\delta\phi^* + g\phi^{*2}\delta\phi . \tag{1.57b}$$

Substituting the plane-wave ansatz (given in Eq. 1.55) for the perturbation term reduces the problem to an eigenvalue equation

$$\begin{pmatrix} \epsilon_k + gn & gn \\ -gn & -(\epsilon_k + gn) \end{pmatrix}\begin{pmatrix} u \\ v \end{pmatrix} = \hbar\omega\begin{pmatrix} u \\ v \end{pmatrix} . \tag{1.58}$$

Solving the eigenvalue problem gives

$$(\hbar\omega)^2 = \epsilon_k(\epsilon_k + 2gn) \,, \tag{1.59}$$

where $\epsilon_k = \frac{\hbar^2 k^2}{2m}$. Hence, the Bogoliubov dispersion relation becomes

$$\omega_{\pm}(k) = \pm\frac{1}{\hbar}\sqrt{\epsilon_k\left(\epsilon_k + 2gn\right)} \,, \tag{1.60}$$

where, $\omega_+(k)$ branch corresponds to physical quasi-particle excitations, while the $\omega_-(k)$ branch corresponds to hole-like branch [52]. In the long-wavelength limit $k \to 0$, the spectrum becomes linear,

$$\omega \simeq ck \,, \tag{1.61}$$

where $c = \sqrt{\frac{gn}{m}}$ which describes phonon-like sound excitations propagating through the condensate.

The Bogoliubov-de Gennes (BdG) formalism outlined above for a single-component condensate can be systematically generalized to multicomponent BECs. In the spin-1 system, the order parameter is a three-component spinor, and collective excitations involve coupled fluctuations of all spin components. Linearizing the coupled GPEs around a stationary spinor ground state results in a Bogoliubov eigenvalue problem of dimension 6×6. In the presence of SO coupling, additional momentum dependent couplings between spin and motional degrees of freedom appear in linearized equations, further enriching the excitation spectrum. While the overall structure of the Bogoliubov approach remains unchanged, the resulting excitation branches reflect the interplay among density-density interaction, spin-exchange interaction, and SO coupling induced modes. In the following chapters, this framework is applied in detail to SO coupled spin-1 condensates, where the full Bogoliubov matrix is constructed and analyzed to obtain the collective excitation spectrum in quasi-one- and two-dimensional geometries.

1.4.2 Experimental measurement of collective excitations in spin-orbit coupled condensates

The collective excitation spectrum of the SO coupled BEC was experimentally measured by Khamehchi *et al.* in 2014 using Bragg spectroscopy [22]. In their work, a two-component condensate of ^{87}Rb atoms was subjected to Raman dressing, which generates an effective SO coupling between the atomic pseudospin and its center-of-

TH-4102_206121026

mass momentum. This platform allows independent control of the Raman coupling strength and detuning, thereby enabling systematic exploration of the excitation properties across different parameter regimes.

In the presence of SO coupling, the single particle dispersion acquires finite momentum minima in the momentum space. In the presence of interactions at the mean-field level, the collective excitation spectrum differs significantly from the single-particle dispersion and is described within the BdG framework. The resulting spectrum exhibits a maxon-roton mode, characterized by a local minimum at finite momentum. This roton-like feature is a direct consequence of the interplay between Raman induced SO coupling and interatomic interactions.

To probe these collective modes experimentally, Bragg spectroscopy was employed. A weak perturbing potential with well defined momentum and frequency was applied to the condensate, and the transferred population was measured as a function of Bragg frequency. This method allows direct access to the excitation energy at a given quasi-momentum and therefore provides a direct measurement of the dispersion relation. A representative Bragg spectrum is depicted in Fig. 1.8(a). The spectrum displays three distinct resonance peaks, labeled α, β, and γ. Each of these peaks corresponds to a transition to a different branch of the Bogoliubov excitation spectrum. The connection between the measured resonances and the underlying dispersion is illustrated schematically in Fig. 1.8(b). In particular, the β transition probes excitations near the finite momentum roton-like minimum in the spectrum. The position of this peak directly reflects the excitation energy at the roton momentum.

The experimentally measured excitation branches were found to be in excellent agreement with theoretical calculations based on the BdG formalism, after accounting for the trapping potential through an effective interaction parameter. These results demonstrate that the BdG framework provides an accurate and quantitative description of the collective excitations in the Raman-induced SO coupled condensate.

The experimental identification of anisotropic dispersion, roton-like minima, and detuning controlled mode softening highlights the richness of excitation spectra in systems where spin and motional degrees of freedom are coupled. This motivates extending the Bogoliubov analysis to higher spin systems. In particular, for spin-1 condensates, the presence of additional spin channels and interaction terms leads to a more intricate excitation spectrum, which will be analyzed in detail in the subsequent chapters.

TH-4102_206121026

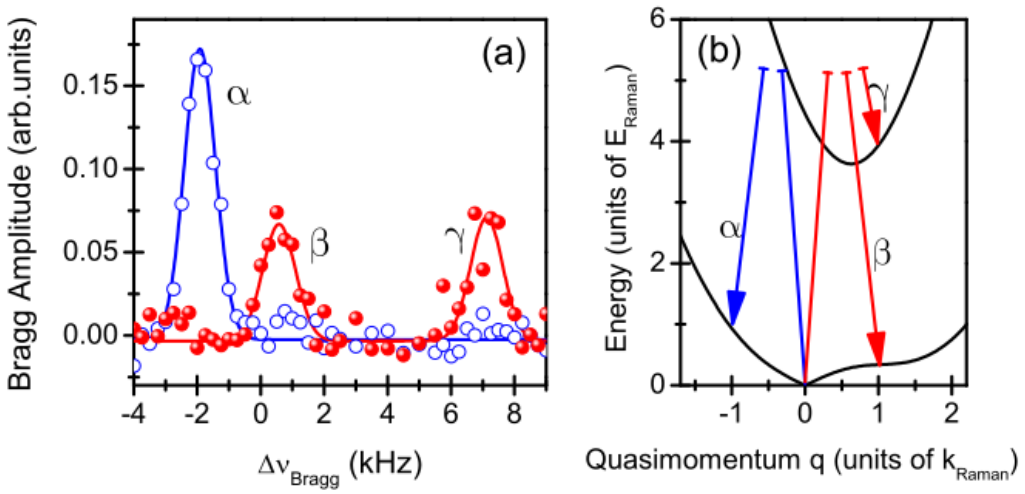


Figure 1.8: Bragg spectroscopy of a spin-orbit coupled Bose-Einstein condensate. (a) Measured Bragg response showing three resonance peaks labeled α, β, and γ. (b) Schematic representation of the corresponding transitions in the Bogoliubov excitation spectrum. The β transition probes the finite momentum roton-like minimum. The figure is take from Ref. [22].

1.5 Progress in spin-orbit coupled Bose-Einstein condensates

Ultracold atoms have been widely used to study diverse phenomena such as quantum phase transitions, superfluidity, and collective excitations, while also serving as a powerful platform for quantum simulation of complex condensed matter systems [53–56]. The tunability of interaction strength, dimensionality, and external confinement has made them particularly suitable for investigating strongly correlated quantum matter and developing new quantum technologies [57, 58]. A major milestone in ultracold atom research was the development of synthetic gauge fields, which allow neutral atoms to mimic the behaviour of charged particles in electromagnetic fields. Among these synthetic interactions, SO coupling has attracted significant attention because of its fundamental role in many condensed-matter phenomena, including topological insulators [1, 44], the quantum Hall effect [45, 59], and spintronics [3].

In electronic materials, SO coupling arises from relativistic interactions between the electron's spin and its motion in an electric field, but its strength and form are determined by the intrinsic properties of the material. In contrast, the ultracold atomic systems enable the artificial generation and precise control of SO coupling. The first experimental realization of SO coupling in BECs was achieved using the Raman laser coupling between two hyperfine states of ^{87}Rb atoms, effectively simulating equal-strength Rashba-Dresselhaus couplings [4]. This pioneering experiment demonstrated

TH-4102_206121026

that the synthetic SO coupling can fundamentally alter the single-particle dispersion and collective properties of Bose gases. Subsequent experiments extended these techniques to spin-1 BECs involving all three hyperfine states of the $F = 1$ manifold [10, 11]. More recently, experimental progress has also enabled the realization of Rashba-type SO coupling in higher-dimensional configurations [60, 61].

The introduction of SO coupling significantly enriches the physical properties of Bose gases. The modified single-particle dispersion leads to novel quantum phases that arise from the interplay between spin-dependent interactions and synthetic gauge fields. Theoretical and experimental studies have revealed a variety of exotic phenomena in SO coupled condensates, including Zitterbewegung oscillations [62], Dicke phase transition [63], supersolid and stripe phases [64–66], Faraday patterns [67], and topological spin textures [68]. One of the most striking features of SO coupled condensates is the emergence of density-modulated stripe phases, which simultaneously exhibit superfluid coherence and spatial density modulation. Such states represent the realization of supersolidity in dilute atomic gases, where crystalline order coexists with superfluid flow. Experimental observations of stripe supersolid phases have provided compelling evidence for this coexistence of broken translational symmetry and long-range coherence [69, 70].

The theoretical description of these systems is commonly based on the mean-field Gross-Pitaevskii equation, which accurately describes weakly interacting Bose gases at low temperatures. Numerical simulations based on coupled GPEs have been widely used to explore the ground-state properties, nonlinear excitations, and dynamical evolution of multicomponent condensates [71–73]. Such studies have predicted and observed various nonlinear structures, including vortices, solitons, and spin textures in SO coupled condensates. For instance, theoretical works have predicted soliton solutions in quasi-1D SO coupled condensates [74, 75]. In spin-1 condensates, more complex nonlinear excitations such as symbiotic solitons, multipeak solitons, and multiring density structures have also been reported in both quasi-one and two-dimensional geometries [76–78]. Additionally, SO coupling can induce anomalous spin-dependent velocities that lead to spin precession and spatial separation between spin components, resulting in intricate dynamical behaviour [79–81].

Another important aspect of SO coupled Bose gases is the study of collective excitations, which provide valuable information about the stability and dynamical properties of quantum fluids. The theoretical framework describing elementary excitations originates from Bogoliubov's theory of weakly interacting Bose gases [13]. Experimental observations of collective modes in trapped condensates were first reported in dilute

TH-4102_206121026

rubidium and sodium gases [16, 17]. Goldstein and Meystre extended the Hartree-Bogoliubov theory to multicomponent condensates and exhibited that the quasiparticle spectrum develops imaginary eigenfrequencies, indicating the onset of dynamical instabilities [20]. Ozawa *et al.* investigated the stability of the supercurrent in SO coupled condensates. By analyzing the Bogoliubov excitation spectrum of supercurrent states, they demonstrated that the system can exhibit both energetic and dynamical instabilities [21].

In SO coupled condensates, the interplay between interactions and SO coupling leads to nontrivial excitation spectra. Bogoliubov analyses have revealed the presence of phonon-maxon-roton structures in the excitation spectrum, where the roton minimum signals the tendency toward density modulation and stripe formation [82]. Experimental confirmation of roton-maxon excitations was later achieved using Bragg spectroscopy in Raman induced SO coupled condensates [22]. Further theoretical investigations by Chen *et al.* demonstrated collective oscillations of a harmonically confined quasi-1D SO coupled condensate. By solving the BdG spectrum in the presence of the trap, they analyzed the dipole, breathing, spin-dipole, and spin-breathing modes across the zero-momentum (ZM), plane-wave (PW), and stripe phases, demonstrating that the collective modes provide clear signatures of quantum phase transitions in SO coupled condensates [83]. The softening of roton modes near phase boundaries provides a clear dynamical signature of these phase transitions and indicates the onset of spatial ordering in the condensate [23, 24].

Closely related to these excitation properties is the study of dynamical instabilities and pattern formation in spinor condensates. Modulational instability (MI) is a fundamental mechanism describing the exponential growth of small perturbations in nonlinear systems. In multicomponent BECs, MI can lead to the formation of spatial domains, soliton trains and complex nonlinear structures [84, 85]. Numerical studies of spin-1 condensates have shown that the stability of the condensate strongly depends on the nature of spin-dependent interactions, with ferromagnetic phases often exhibiting dynamical instability while the antiferromagnetic phases remain stable under similar conditions [86, 87]. External magnetic fields and spin interactions can further induce spatial instabilities, resulting in the spontaneous formation of spin domains and periodic density patterns [88, 89]. Experimental observations have also reported spontaneous pattern formation associated with unstable excitation modes in spinor condensates [90].

The presence of SO coupling introduces additional mechanisms that significantly modify the stability landscape of Bose gases. The competition between the SO cou-

TH-4102_206121026

pling, Rabi coupling, and interatomic interactions can produce complex excitation spectra containing avoided crossings and roton-like features. Previous studies have shown that SO coupling can enhance modulational instability and promote stripe formation even in initially miscible condensates [91, 92]. At the same time, Rabi coupling tends to stabilize the condensate, suppressing its dynamical instability. Using the Bogoliubov framework, Ravisankar *et al.* systematically mapped the regimes of dynamical stability and instability in SO- and Rabi-coupled condensates. Their analysis revealed the emergence of complex excitation frequencies associated with unstable modes, and real-time Gross-Pitaevskii simulations directly demonstrated the growth of these instabilities in the dynamically unstable regime [93]. These competing effects lead to rich dynamical behavior, including the emergence of unstable avoided crossings (UACs) and spontaneous pattern formation in the condensate [90, 94, 95].

Despite substantial progress in understanding SO coupled Bose gases, most theoretical and experimental studies have primarily focused on pseudospin-1/2 condensates. Higher spin condensates, such as spin-1 condensates, possess additional degrees of freedom arising from spin-exchange interactions, allowing a richer variety of quantum phases and excited modes. Several works have investigated the phase structure of spin-1 SO coupled condensates and identified phases such as PW phase, ZM phase, and stripe-wave (SW) phase under various coupling conditions [23–25]. However, a comprehensive understanding of the relationship between these phases, their excitation spectra, and their dynamical stability remains incomplete. In particular, the interplay among spin-dependent interactions, SO coupling, and Rabi coupling can give rise to complex phenomena, including roton softening, modulational instabilities, and UACs in the excitation spectrum. These features play a crucial role in determining the stability of stripe and supersolid phases, yet their behavior across wide parameter regimes and in higher dimensions (specifically, quasi-2D) has not been fully explored. These open questions, therefore, motivate further investigation into the ground-state phases, excitation spectra, and dynamical properties of spin-1 SO-coupled BECs in quasi-one- and two-dimensional geometries.

1.6 Layout of this thesis

The layout of the following chapters is as follows.

In **Chapter 2** we present the numerical framework used throughout this thesis. The split-step Crank-Nicolson method for solving the coupled GPEs corresponding to SO

TH-4102_206121026

coupled spin-1 condensates is described in detail. Procedures for imaginary-time propagation to obtain ground states and real-time propagation to investigate dynamical evolution are outlined. The grid-convergence test is performed to assess the accuracy of the different spatial and temporal step sizes. Finally, the quench protocols used in this thesis to study the dynamics of the condensate are briefly introduced.

In **Chapter 3** we explore the different quantum phases and quench dynamics of SO coupled spin-1 BECs with ferromagnetic and antiferromagnetic interaction regimes. Using the mean-field GPEs, we have identified different ground-state phases and characterized them by spin-density vectors, miscibility, and condensate size. The dynamics of the condensate are investigated by performing sudden quenches of the SO and Rabi couplings, starting from the ground-state configurations. Time evolution reveals that quenches in different couplings influence the stability of the condensate: the Rabi coupling stabilizes it, while the SO coupling destabilizes it.

Chapter 4 analyzes the collective excitation spectrum and underlying instabilities of quasi-1D ferromagnetic spin-1 BECs in the presence of SO and Rabi couplings. Using the BdG framework, we have determined stability regimes in the SO-Rabi coupling phase plane. A key result of this chapter is the emergence of UACs between low-lying and first-excited branches, which signal the onset of dynamical instabilities. Upon perturbing the ground state via trap quenches, we have demonstrated that the dynamical instability leads to fragmentation of the condensate and formation of complex patterns.

In **Chapter 5** we investigate the collective excitation and stability analysis for SO coupled spin-1 condensates with antiferromagnetic interactions. In contrast to ferromagnetic interactions, the sign of the spin-dependent interaction qualitatively modifies the excitation spectrum and associated instability. Employing the BdG framework, we have observed the double UACs in the excitation spectrum, a feature absent in ferromagnetic interactions. We have analyzed the effect of double UACs on the growth rate of unstable modes, leading to qualitatively different dynamical behavior during real-time simulations that results in fragmentation and complex domain formation.

In **Chapter 6** we extend our study of the collective excitations and dynamical instabilities for the quasi-2D spin-1 BECs with Rashba-type SO coupling. Using the BdG framework, we have computed the excitation spectrum over a broad range of SO and Rabi coupling strengths and identified distinct stability regimes. Particular attention is given to the emergence of phonon-maxon-rotom modes in the excitation spectrum and their evolution with system parameters. We have demonstrated the emergence of unstable (double unstable) avoided crossings in ferromagnetic (antiferromagnetic) interactions. During the time evolution of the condensate, the instability-driven dynam-

TH-4102_206121026

ics lead to density fragmentation and complex pattern formation in a two-dimensional plane.

In **Chapter 7**, we have summarized the principal findings of this thesis. We have emphasized the interplay of SO coupling, Rabi coupling, and spin-dependent interactions in shaping the ground-state phases, excitation spectra, and dynamical instabilities. In this chapter, we have discussed the possible future directions, which include the extension beyond mean-field theory, the effect of disorder, and studies at finite temperature.



TH-4102_206121026

Chapter 2

Numerical method to solve the coupled mean-field equations

In this Chapter, we present the numerical framework used to solve the spin-orbit (SO) coupled Gross-Pitaevskii equations (GPEs). Owing to the nonlinear nature of GPE, a variety of numerical approaches have been developed to compute ground-state solutions and investigate the dynamical behaviour of Bose-Einstein condensates (BECs). In this thesis, we primarily employ the split-step Crank-Nicolson (CN) method for our simulations, as it provides a stable and efficient scheme for both ground state calculations and dynamical evolution. The chapter is organized as follows. We begin with the detailed formulation of SO coupled GPEs in quasi-one-dimensional (quasi-1D) geometry. The split-step CN scheme is then described systematically, emphasizing the separation of the derivative and non-derivative parts and the implementation of both imaginary- and real-time propagation. Imaginary-time propagation is employed to obtain converged ground-state solutions, while real-time propagation is used to investigate the dynamical properties of the condensate. We further discuss the extension of the method to quasi-two-dimensional (quasi-2D) SO coupled condensates. Further, we present the grid-independence test for spatial and temporal step sizes in both quasi-one and two-dimensional geometries. Finally, we discuss the quench protocols that have been employed to study the dynamics of SO coupled spin-1 BECs.

2.1 Split-step Crank-Nicolson scheme

The Crank-Nicolson method is a widely used semi-implicit time-integration scheme and is well known for its numerical stability in solving partial differential equations, in-

TH-4102_206121026

cluding the nonlinear systems such as the Gross-Pitaevskii equation. The method was established by J Crank and P Nicolson in the 20th century. One of its key advantages lies in the split-step formulation, in which derivative terms, such as kinetic energy and SO coupling terms, are treated separately from the local terms, including the external potential, nonlinear interactions, and Rabi coupling. This separation enhances both numerical stability and computational efficiency. Moreover, the time-splitting procedure provides an effective means of incorporating nonlinear terms without compromising convergence. For completeness, we first present the SO-coupled Gross-Pitaevskii equations and then describe the imaginary-time and real-time propagation methods for computing the ground-state solutions and investigating the dynamics of the condensate, respectively.

The time-dependent coupled Gross-Pitaevskii equations for quasi-1D SO coupled spin-1 condensates in the presence of a trapping potential $V(x)$ are given as [50, 77]

$$\mathrm{i}\frac{\partial\psi_{+1}}{\partial t} = \left[-\frac{1}{2}\frac{\partial^2}{\partial x^2} + V(x) + c_0(\rho_{+1}+\rho_0+\rho_{-1})\right]\psi_{+1} - \frac{k_L}{\sqrt{2}}\frac{\partial\psi_0}{\partial x} + c_2(\rho_{+1}+\rho_0-\rho_{-1})\psi_{+1} + c_2\psi_0^2\psi_{-1}^* + \frac{\Omega}{\sqrt{2}}\psi_0\,, \tag{2.1a}$$

$$\mathrm{i}\frac{\partial\psi_0}{\partial t} = \left[-\frac{1}{2}\frac{\partial^2}{\partial x^2} + V(x) + c_0(\rho_{+1}+\rho_0+\rho_{-1})\right]\psi_0 + \frac{k_L}{\sqrt{2}}\left[\frac{\partial\psi_{+1}}{\partial x} - \frac{\partial\psi_{-1}}{\partial x}\right] + c_2(\rho_{+1}+\rho_{-1})\psi_0 + 2c_2\psi_0^*\psi_{+1}\psi_{-1} + \frac{\Omega}{\sqrt{2}}(\psi_1+\psi_{-1})\,, \tag{2.1b}$$

$$\mathrm{i}\frac{\partial\psi_{-1}}{\partial t} = \left[-\frac{1}{2}\frac{\partial^2}{\partial x^2} + V(x) + c_0(\rho_{+1}+\rho_0+\rho_{-1})\right]\psi_{-1} + \frac{k_L}{\sqrt{2}}\frac{\partial\psi_0}{\partial x} + c_2(\rho_{-1}+\rho_0-\rho_{+1})\psi_{-1} + c_2\psi_0^2\psi_{+1}^* + \frac{\Omega}{\sqrt{2}}\psi_0\,. \tag{2.1c}$$

To implement the split-step CN method for the above coupled equations, the system is first separated into two operators: one containing the derivative terms and the other the non-derivative terms. The derivative operator includes the kinetic energy and the SO coupling terms. The remaining terms, including the external trapping potential, nonlinear interactions, and the Rabi coupling, constitute the non-derivative operator. For numerical implementation, the non-derivative operator is further separated into diagonal and off-diagonal parts. The diagonal part consists of terms that act independently on each condensate component, without mixing the spin states. These include the external trapping potential $V(x)$, the spin-independent interaction proportional to c_0, and the density-dependent term proportional to c_2. The off-diagonal part

TH-4102_206121026

contains terms that couple the different spin components. These arise from the Rabi coupling between the hyperfine states and from the spin-exchange interaction terms involving the products of different condensate wavefunctions, such as $c_2\psi_0^2\psi_{\pm1}^*$ and $2c_2\psi_0^*\psi_{+1}\psi_{-1}$ [50].

The numerical procedure starts with an initial trial wavefunction for the condensate components ψ_{+1}, ψ_0, and ψ_{-1}. In the present thesis, we consider a Gaussian profile as the initial guess for the stationary state, although other choices may also be employed depending on the interaction regime. The initial configuration is first propagated under the action of the non-derivative operator, allowing the effects of external potential, nonlinear interactions, and Rabi coupling to be incorporated into the wavefunction. The step produces an intermediate solution. The intermediate wavefunctions are subsequently evolved under the derivative operator. For the spatial discretization, a centered finite difference scheme with grid spacing Δx is adopted. The time evolution is then performed using the CN discretization, which treats the derivative terms semi-implicitly and improves numerical stability and accuracy [50, 72, 96, 97]. The propagation process is repeated iteratively until the condensate reaches a stationary ground-state configuration. The convergence of the calculation is verified by monitoring the behaviour of relevant physical quantities during successive iterations. In particular, the chemical potential and spatial extent of the condensate components are examined to confirm that the numerical procedure has reached a stable ground state.

For the purpose of numerical implementation, the coupled Gross-Pitaevskii equations [Eq. 2.1] are conveniently written in a compact matrix form. The time evolution of the condensate can then be expressed as

$$i\frac{\partial}{\partial t}\Psi(x,t) = H\Psi(x,t) \equiv [H_D + H_{ND}]\Psi(x,t), \tag{2.2}$$

where $\Psi(x,t)$ is the spinor wave function and written as

$$\Psi(x,t) = \begin{pmatrix} \psi_{+1}(x,t) \\ \psi_0(x,t) \\ \psi_{-1}(x,t) \end{pmatrix}, \tag{2.3}$$

and H represents the effective Hamiltonian operator of the SO coupled spin-1 condensate. To implement the split-step CN scheme, the Hamiltonian operator H is decomposed into derivative and non-derivative contributions as $H \equiv H_D + H_{ND}$, where H_D contains the kinetic energy and spin–orbit coupling and H_{ND} contains the external potential, nonlinear interactions, and Rabi coupling.

TH-4102_206121026

The non-derivative operator is further separated into diagonal and off-diagonal parts,

$$H_{ND} = H_{ND}^{d} + H_{ND}^{od}. \tag{2.4}$$

The diagonal part is given by

$$H_{ND}^{d} = \begin{pmatrix} U_{+1} & 0 & 0 \\ 0 & U_0 & 0 \\ 0 & 0 & U_{-1} \end{pmatrix}, \tag{2.5}$$

where

$$\begin{aligned} U_{+1} &= V(x) + c_0(\rho_{+1} + \rho_0 + \rho_{-1}) + c_2(\rho_{+1} + \rho_0 - \rho_{-1}), \\ U_0 &= V(x) + c_0(\rho_{+1} + \rho_0 + \rho_{-1}) + c_2(\rho_{+1} + \rho_{-1}), \\ U_{-1} &= V(x) + c_0(\rho_{+1} + \rho_0 + \rho_{-1}) + c_2(\rho_{-1} + \rho_0 - \rho_{+1}). \end{aligned} \tag{2.6}$$

The off-diagonal non-derivative operator, which represents the coupling between different spin components due to the Rabi coupling and spin-exchange interactions, can be written as

$$H_{ND}^{od} = \begin{pmatrix} 0 & c_2\psi_0\psi_{-1}^* + \frac{\Omega}{\sqrt{2}} & 0 \\ c_2\psi_0^*\psi_{-1} + \frac{\Omega}{\sqrt{2}} & 0 & c_2\psi_0^*\psi_{+1} + \frac{\Omega}{\sqrt{2}} \\ 0 & c_2\psi_0\psi_{+1}^* + \frac{\Omega}{\sqrt{2}} & 0 \end{pmatrix}. \tag{2.7}$$

The derivative operator H_D can also be decomposed into H_{Kin} and H_{SO}, given as follows

$$H_D = H_{Kin} + H_{SO}\ , \tag{2.8}$$

TH-4102_206121026

where

$$H_{Kin} = \begin{pmatrix} -\frac{1}{2}\frac{\partial^2}{\partial x^2} & 0 & 0 \\ 0 & -\frac{1}{2}\frac{\partial^2}{\partial x^2} & 0 \\ 0 & 0 & -\frac{1}{2}\frac{\partial^2}{\partial x^2} \end{pmatrix}, \tag{2.9}$$

$$H_{SO} = \begin{pmatrix} 0 & -\frac{k_L}{\sqrt{2}}\frac{\partial}{\partial x} & 0 \\ \frac{k_L}{\sqrt{2}}\frac{\partial}{\partial x} & 0 & -\frac{k_L}{\sqrt{2}}\frac{\partial}{\partial x} \\ 0 & \frac{k_L}{\sqrt{2}}\frac{\partial}{\partial x} & 0 \end{pmatrix}. \tag{2.10}$$

With this matrix representation, the coupled Gross-Pitaevskii equations can be expressed compactly as

$$i\frac{\partial \Psi}{\partial t} = \left(H_{SO} + H_{Kin} + H_{ND}^{od} + H_{ND}^{d}\right)\Psi. \tag{2.11}$$

To evolve the condensate wavefunction in time, the total time interval is divided into N_t discrete steps with time increment Δt. Beginning from the initial time t_0, the propagation is carried out using the split-step approach. In the first stage, the wavefunction is advanced by integrating the non-derivative part of the Hamiltonian, which yields an intermediate state at time $t_0 + \Delta t$. This intermediate state is then used as the input for the second stage, where the derivative terms of the Hamiltonian are treated using the CN scheme to obtain the wavefunction at the end of the time step. Having outlined the numerical framework used for the time evolution, we now describe the propagation schemes employed in this thesis. We first discuss the real-time propagation method, which is used to investigate the dynamical behaviour of the condensate. The imaginary-time propagation technique, which is employed to obtain the ground state configuration of the condensate, will be discussed subsequently [50].

2.1.1 Real-time propagation

To investigate the dynamical behaviour of the SO coupled spin-1 condensate, we employ the real-time propagation scheme. In this approach, the time-dependent coupled Gross-Pitaevskii equations are evolved in time steps of size Δt. Starting from an initial time t_0, trial wavefunctions $\psi_{+1}(x, t_0)$, $\psi_0(x, t_0)$, and $\psi_{-1}(x, t_0)$ are chosen as the initial configuration of the condensate. Within the split-step formulation, the time evolution over a single time step is carried out in two stages. First, the wavefunctions are propagated using the non-derivative part of the Hamiltonian Eq. 2.4, which yields an in-

TH-4102_206121026

termediate solution at time $t_0 + \Delta t$. The resulting intermediate wavefunctions are then used as the initial input for the derivative part of the Hamiltonian [Eq. 2.8], producing the final solutions at $t = t_0 + \Delta t$ as $\psi_{+1}(x, t_0 + \Delta t)$, $\psi_0(x, t_0 + \Delta t)$, and $\psi_{-1}(x, t_0 + \Delta t)$. By repeating this procedure sequentially, the condensate wavefunctions can be evolved up to the desired final time to obtain a converged solution.

To describe the numerical procedure more explicitly, let us assume that at time $t = n\Delta t$ the condensate is characterized by the wavefunctions ψ_{+1}^n, ψ_0^n, and ψ_{-1}^n. These wavefunctions first advance over the time interval Δt by integrating the non-derivative part of the Hamiltonian [Eq. 2.4], leading to the intermediate states $\psi_{+1}^{n+1/2}$, $\psi_0^{n+1/2}$, and $\psi_{-1}^{n+1/2}$. Since Eq. 2.4 does not contain spatial derivative terms, the evolution during this stage can be performed directly for a small time step Δt using the expressions given below [50, 72],

$$\Psi^{n+1/2} = \mathcal{O}_{nd}(H_{ND})\Psi^n, \tag{2.12}$$

where $\Psi = (\psi_{+1}, \psi_0, \psi_{-1})^T$, $\mathcal{O}_{nd}(H_{ND})$ is the time evolution operation with the matrix H_{ND} given above in Eq. 2.4. Here, the subscript 'nd' stands for the non-derivative part of the operator.

Since the matrix H_{ND} consists of diagonal and off-diagonal terms, we treat them separately. The diagonal and off-diagonal parts of the matrix are given above in Eqs. 2.5 and 2.7, respectively. We are writing both parts of the matrix before proceeding further.

$$H_{ND} = H_{ND}^d + H_{ND}^{od}\,, \tag{2.13}$$

$$H_{ND}^d = \begin{pmatrix} U_{+1} & 0 & 0 \\ 0 & U_0 & 0 \\ 0 & 0 & U_{-1} \end{pmatrix}, \tag{2.14}$$

$$H_{ND}^{od} = \begin{pmatrix} 0 & c_2\psi_0\psi_{-1}^* + \dfrac{\Omega}{\sqrt{2}} & 0 \\ c_2\psi_0^*\psi_{-1} + \dfrac{\Omega}{\sqrt{2}} & 0 & c_2\psi_0^*\psi_{+1} + \dfrac{\Omega}{\sqrt{2}} \\ 0 & c_2\psi_0\psi_{+1}^* + \dfrac{\Omega}{\sqrt{2}} & 0 \end{pmatrix}. \tag{2.15}$$

where, the elements of the diagonal matrix U_{+1}, U_0, and U_{-1} is given above in Eq. 2.6.

The diagonal term of the matrix can be treated by employing the usual time propa-

gation method, such as first-order ordinary differential equations [50, 72].

$$\mathrm{i}\frac{\partial}{\partial t}\Psi^{n+1/2} = (\mathbf{H}^{d}_{ND})\Psi^{n}, \tag{2.16}$$

$$\begin{pmatrix} \psi^{n+1/2}_{+1} \\ \psi^{n+1/2}_{0} \\ \psi^{n+1/2}_{-1} \end{pmatrix} = \begin{pmatrix} \exp(-\mathrm{i}\Delta t U_{+1}) & 0 & 0 \\ 0 & \exp(-\mathrm{i}\Delta t U_{0}) & 0 \\ 0 & 0 & \exp(-\mathrm{i}\Delta t U_{-1}) \end{pmatrix} \begin{pmatrix} \psi^{n}_{+1} \\ \psi^{n}_{0} \\ \psi^{n}_{-1} \end{pmatrix}. \tag{2.17}$$

To diagonalize the off-diagonal matrix H^{od}_{ND}, we perform the unitary transformation to obtain the diagonal matrix from the off-diagonal matrix [50]. To start with, we calculate the eigenvalue and eigenvectors of the matrix H^{od}_{ND}.

$$H^{od}_{ND} = \begin{pmatrix} 0 & c_2\psi_0\psi^*_{-1} + \dfrac{\Omega}{\sqrt{2}} & 0 \\ c_2\psi^*_0\psi_{-1} + \dfrac{\Omega}{\sqrt{2}} & 0 & c_2\psi^*_0\psi_{+1} + \dfrac{\Omega}{\sqrt{2}} \\ 0 & c_2\psi_0\psi^*_{+1} + \dfrac{\Omega}{\sqrt{2}} & 0 \end{pmatrix}. \tag{2.18}$$

Considering $A = c_2\psi^*_{-1}\psi_0 + \frac{\Omega}{\sqrt{2}}$, and $B = c_2\psi^*_0\psi_{+1} + \frac{\Omega}{\sqrt{2}}$, we can write the matrix H^{od}_{ND} as follows,

$$H^{od}_{ND} = \begin{pmatrix} 0 & A & 0 \\ A^* & 0 & B \\ 0 & B^* & 0 \end{pmatrix}. \tag{2.19}$$

The eigenvalues of matrix H^{od}_{ND} are $\lambda_1 = D = \sqrt{|A|^2 + |B|^2}$, $\lambda_2 = 0$, and $\lambda_3 = -D$, and the corresponding eigenvectors are $(v_{11}, v_{12}, v_{13})^T = (A, D, B^*)^T$, $(v_{21}, v_{22}, v_{23})^T = (B, 0, -A^*)^T$, and $(v_{31}, v_{32}, v_{33})^T = (A, -D, B^*)^T$, respectively. Using this transformation, we can write the H^{od}_{ND} in terms of $\mathbf{V}P\mathbf{V^{-1}}$, where $\mathbf{V}$ is the 3×3 matrix constructed using the eigenvectors of the matrix H^{od}_{ND}, and $\mathbf{V^{-1}}$ is simply the inverse of it. P is a diagonal matrix, which can be written as,

$$P = \begin{pmatrix} D & 0 & 0 \\ 0 & 0 & 0 \\ 0 & 0 & -D \end{pmatrix}. \tag{2.20}$$

TH-4102_206121026

Following this transformation, we can write an update in the wavefunction for the off-diagonal matrix of the non-derivative part [50, 72].

$$\mathrm{i}\frac{\partial}{\partial t}\Psi^{n+1/2} = (H_{ND}^{od})\Psi^{n}, \tag{2.21}$$

$$\mathrm{i}\frac{\partial}{\partial t}\Psi^{n+1/2} = (\mathbf{V}P\mathbf{V^{-1}})\Psi^{n}. \tag{2.22}$$

After performing the matrix operations on Ψ^n explicitly, the form of the transformed wavefunctions can be written as,

$$\begin{pmatrix}\psi_{+1}^{n+1/2}\\ \psi_{0}^{n+1/2}\\ \psi_{-1}^{n+1/2}\end{pmatrix} = \mathbf{V}\begin{pmatrix}\exp(-\mathrm{i}\Delta t D) & 0 & 0\\ 0 & 1 & 0\\ 0 & 0 & \exp(\mathrm{i}\Delta t D)\end{pmatrix}\mathbf{V^{-1}}\begin{pmatrix}\psi_{+1}^{n}\\ \psi_{0}^{n}\\ \psi_{-1}^{n}\end{pmatrix}, \tag{2.23}$$

where

$$\mathbf{V} = \begin{pmatrix}v_{11} & v_{12} & v_{13}\\ v_{21} & v_{22} & v_{23}\\ v_{31} & v_{32} & v_{33}\end{pmatrix} = \begin{pmatrix}A & B & A\\ D & 0 & -D\\ B^{*} & -A^{*} & B^{*}\end{pmatrix}, \quad \mathbf{V}^{-1} = \frac{1}{2D^{2}}\begin{pmatrix}A^{*} & D & B\\ 2B^{*} & 0 & -2A\\ A^{*} & -D & B\end{pmatrix}.$$

Consequently, the series of operations using (2.17) and (2.23) will result in propagating wavefunctions $(\psi_{+1}^{n}, \psi_{0}^{n}, \psi_{-1}^{n})$ over a time step $t_n + \Delta t$, including non-derivative terms such as non-linearity, external potential, and Rabi coupling.

Next, we implement the time propagation corresponding to the derivative operator H_D numerically by the semi-implicit CN method. Within the split-step framework, the derivative part — comprising the kinetic energy (H_{Kin}) and the SO coupling (H_{SO}) — evolves the wavefunctions from the intermediate state to the next full time step.

The discretization for the spinor wavefunction $\Psi = (\psi_{+1}, \psi_0, \psi_{-1})^T$ is given by the expression [72],

$$\frac{\Psi^{n+1} - \Psi^{n+1/2}}{-\mathrm{i}\Delta t} = \frac{1}{2}H_D\left(\Psi^{n+1} + \Psi^{n+1/2}\right). \tag{2.24}$$

The formal solution to this CN scheme is

$$\Psi^{n+1} = \mathcal{O}_{CN}(H_D)\Psi^{n+1/2} \equiv \frac{1 - \mathrm{i}\Delta t H_D/2}{1 + \mathrm{i}\Delta t H_D/2}\Psi^{n+1/2}. \tag{2.25}$$

By combining this with the previous evolution of the non-derivative part, the total update for the spinor wavefunction from time t_n to t_{n+1} can be expressed as,

$$\Psi^{n+1} = \mathcal{O}_{CN}(H_D)\mathcal{O}_{nd}(H_{ND})\Psi^n, \tag{2.26}$$

where $\mathcal{O}_{CN}$ represents the time-evolution operation for the derivative part and the suffix 'CN' indicates the Crank-Nicolson algorithm. This operation is used to propagate the intermediate solutions $\psi_{+1}^{n+1/2}$, $\psi_0^{n+1/2}$, and $\psi_{-1}^{n+1/2}$ over the time step Δt to generate the final solutions at next time step $t_{n+1} = (n+1)\Delta t$.

The time propagation of the remaining equations involving derivative operators is performed by the semi-implicit CN scheme. For the spin-1 condensate, the CN scheme is employed by mapping the evolution of each spin component onto one-dimensional spatial grid points in x. The discretization of the kinetic energy part H_{Kin} [Eq. 2.9] along the spatial grid point x is carried out as follows [98, 99],

$$\frac{\mathrm{i}(\psi_{+1,k}^{kin} - \psi_{+1,k}^{n+1/2})}{\Delta t} = \frac{-1}{4h^2}\left[(\psi_{+1,k+1}^{kin} - 2\psi_{+1,k}^{kin} + \psi_{+1,k-1}^{kin}) + (\psi_{+1,k+1}^{n+1/2} - 2\psi_{+1,k}^{n+1/2} + \psi_{+1,k-1}^{n+1/2})\right], \tag{2.27}$$

$$\frac{\mathrm{i}(\psi_{0,k}^{kin} - \psi_{0,k}^{n+1/2})}{\Delta t} = \frac{-1}{4h^2}\left[(\psi_{0,k+1}^{kin} - 2\psi_{0,k}^{kin} + \psi_{0,k-1}^{kin}) + (\psi_{0,k+1}^{n+1/2} - 2\psi_{0,k}^{n+1/2} + \psi_{0,k-1}^{n+1/2})\right], \tag{2.28}$$

$$\frac{\mathrm{i}(\psi_{-1,k}^{kin} - \psi_{-1,k}^{n+1/2})}{\Delta t} = \frac{-1}{4h^2}\left[(\psi_{-1,k+1}^{kin} - 2\psi_{-1,k}^{kin} + \psi_{-1,k-1}^{kin}) + (\psi_{-1,k+1}^{n+1/2} - 2\psi_{-1,k}^{n+1/2} + \psi_{-1,k-1}^{n+1/2})\right]. \tag{2.29}$$

Or, we can write as,

$$\psi_{+1,k}^{kin} - \psi_{+1,k}^{n+1/2} = \frac{\mathrm{i}\Delta t}{4h^2}\left[(\psi_{+1,k+1}^{kin} - 2\psi_{+1,k}^{kin} + \psi_{+1,k-1}^{kin}) + (\psi_{+1,k+1}^{n+1/2} - 2\psi_{+1,k}^{n+1/2} + \psi_{+1,k-1}^{n+1/2})\right], \tag{2.30}$$

$$\psi_{0,k}^{kin} - \psi_{0,k}^{n+1/2} = \frac{\mathrm{i}\Delta t}{4h^2}\left[(\psi_{0,k+1}^{kin} - 2\psi_{0,k}^{kin} + \psi_{0,k-1}^{kin}) + (\psi_{0,k+1}^{n+1/2} - 2\psi_{0,k}^{n+1/2} + \psi_{0,k-1}^{n+1/2})\right], \tag{2.31}$$

$$\psi_{-1,k}^{kin} - \psi_{-1,k}^{n+1/2} = \frac{\mathrm{i}\Delta t}{4h^2}\left[(\psi_{-1,k+1}^{kin} - 2\psi_{-1,k}^{kin} + \psi_{-1,k-1}^{kin}) + (\psi_{-1,k+1}^{n+1/2} - 2\psi_{-1,k}^{n+1/2} + \psi_{-1,k-1}^{n+1/2})\right]. \tag{2.32}$$

TH-4102_206121026

Here, $\psi^n_{j,k}$ represents j-th component (with $j = +1,\ 0,\ -1$) of the condensate at spatial point x_k and at time t_n. For the discretization along x, we choose $x_k = -N_x h/2 + kh$, with $k = 0, 1, 2, ..., N_x$, where N_x is total number of grid points and h is the spatial step. The above equations are essentially a set of algebraic equations for $\psi^{kin}_{j,k+1}$, $\psi^{kin}_{j,k}$, and $\psi^{kin}_{j,k-1}$ at the kinetic energy step, which are solved using homogeneous Dirichlet boundary conditions. The algebraic equations are written explicitly as [98],

$$A^-_k \psi^{kin}_{j,k-1} + A^0_k \psi^{kin}_{j,k} + A^+_k \psi^{kin}_{j,k+1} = b_{j,k}\ , \tag{2.33}$$

where the coefficients for all components $j = +1, 0, -1$ are $A^0_k = (1 + \mathrm{i}\Delta t/(2h^2))$, $A^-_k = A^+_k = -\mathrm{i}\Delta t/(4h^2)$ and the right hand side of the equations,

$$b_{j,k} = \frac{\mathrm{i}\Delta t}{4h^2}\left(\psi^{n+1/2}_{j,k+1} - 2\psi^{n+1/2}_{j,k} + \psi^{n+1/2}_{j,k-1}\right) + \psi^{n+1/2}_{j,k}\ . \tag{2.34}$$

All quantities in $b_{j,k}$ are referred to the time step $t_{n+1/2}$, which are known from the evolution using the non-derivative part [Eq. 2.12]. The unknowns are obtained using the forward recursion relation,

$$\psi^{kin}_{j,k+1} = \alpha_{j,k}\psi^{kin}_{j,k} + \beta_{j,k}\ , \tag{2.35}$$

where $\alpha_{j,k}$ and $\beta_{j,k}$ are the coefficients to be calculated. Substituting this recursion into the Eqs. 2.33 yields the solution,

$$\psi^{kin}_{j,k} = \gamma_{j,k}(A^-_k \psi^{kin}_{j,k-1} + A^+_k \beta_{j,k} - b_{j,k})\ , \tag{2.36}$$

with

$$\gamma_{j,k} = -1/(A^0_k + A^+_k \alpha_{j,k})\ , \tag{2.37}$$

$$\alpha_{j,k-1} = \gamma_{j,k} A^-_k\ , \tag{2.38}$$

$$\beta_{j,k-1} = \gamma_{j,k}(A^+_k \beta_{j,k} - b_{j,k})\ . \tag{2.39}$$

By applying the recursion relations (2.36), (2.37), and (2.39), we compute the coefficients $\alpha_{j,k}$ and $\beta_{j,k}$, where the spatial index k runs from $N_x - 2$ down to 0. The initial values are set as $\alpha_{j,N_x-1} = 0$, and $\beta_{j,N_x-1} = \psi^{kin}_{j,N_x}$, consistent with the vanishing of the wavefunction at the boundaries. Once the coefficients $\alpha_{j,k}$, $\beta_{j,k}$, and $\gamma_{j,k}$ are obtained

and stored, the intermediate "kinetic" wavefunctions are constructed using the relation Eq. 2.35.

This solution is built across the spatial domain by progressing from $k = 0$ to $N_x - 1$. We utilize the closed boundary condition where the wavefunction at the first spatial grid point is known to be $\psi^{kin}_{j,0} = 0$. By the end of this sweep, we have obtained the state of the condensate evolved under the kinetic energy operator, which we denote as $\Psi^{kin} = (\psi^{kin}_{+1}, \psi^{kin}_{0}, \psi^{kin}_{-1})^T$.

To obtain the wavefunctions at the final time step t_{n+1}, the intermediate state Ψ^{kin} is evolved under the SO coupling operator H_{SO} [Eq. 2.10]. Using the first-order approximation of the time evolution operator, the update is expressed as,

$$\Psi^{n+1} = \Psi^{kin} - \mathrm{i}\Delta t(H_{SO})\Psi^{kin} \,. \tag{2.40}$$

The accuracy of this approximation is controlled by the time step Δt, and convergence of the numerical results was verified by reducing Δt.

For the individual component, we can write,

$$\psi^{n+1}_{+1,k} = \psi^{kin}_{+1,k} + \mathrm{i}\eta \frac{\partial}{\partial x}\psi^{kin}_{0,k} \,, \tag{2.41}$$

$$\psi^{n+1}_{0,k} = \psi^{kin}_{0,k} - \mathrm{i}\eta \left(\frac{\partial}{\partial x}\psi^{kin}_{+1,k} - \frac{\partial}{\partial x}\psi^{kin}_{-1,k} \right) , \tag{2.42}$$

$$\psi^{n+1}_{-1,k} = \psi^{kin}_{-1,k} - \mathrm{i}\eta \frac{\partial}{\partial x}\psi^{kin}_{0,k} \,, \tag{2.43}$$

where, $\eta = \frac{k_L \Delta t}{\sqrt{2}}$ is the effective coupling strength. The accuracy of the SO step is highly sensitive to the discretization of the first-order spatial derivative. To maintain numerical stability and fourth-order spatial accuracy, the derivatives are computed using Richardson extrapolation,

$$\frac{\partial \psi^{kin}_{j,k}}{\partial x} \approx \frac{\psi^{kin}_{j,k-2} - 8\psi^{kin}_{j,k-1} + 8\psi^{kin}_{j,k+1} - \psi^{kin}_{j,k+2}}{12h} \,. \tag{2.44}$$

At the boundaries, the derivatives are set to zero, consistent with the boundary condition of the previous step.

For direct real-time propagation, the initial wavefunction at $t = 0$ is usually chosen as the analytically known ground state of the harmonic trap in the absence of interactions. As the system evolves in time, the interaction strength is slowly increased in an adiabatic manner until the desired nonlinear parameters are reached. In situations

TH-4102_206121026

involving more complicated potentials or when improved numerical convergence is required, it is convenient to first obtain the ground state using the imaginary-time propagation. The converged stationary wavefunction obtained from imaginary-time evolution is then used as the initial state for subsequent real-time propagation to analyze the dynamical properties of the system.

In the present thesis, we first obtain the interacting ground state of SO coupled spin-1 BECs using imaginary-time propagation. This converged state is then taken as the initial condition for real-time propagation. To investigate the dynamics of the condensate, we quench the trap strength or coupling parameters and monitor the subsequent time evolution.

2.1.2 Imaginary-time propagation

The ground-state solution of the GPEs is obtained using the imaginary-time propagation method. In this approach, the real-time variable is transformed into the imaginary time through the substitution $t \to -it$ and correspondingly $\Delta t \to -i\Delta t$. Under this transformation, the time-dependent wavefunction $\psi_j(x,t) = \psi_{j,0}(x)\exp(-iE_0t)$ changes to $\psi_{j,0}(x)\exp(-E_0t)$. As a result, higher energy components of the wavefunction decay exponentially faster than the ground-state component, allowing the system to gradually converge to the lowest energy state.

Although real-time propagation is useful for studying dynamical and non-stationary properties, it involves complex wavefunctions and is not the most efficient method for determining stationary solutions. For this reason, the ground state of the system is obtained by solving Eqs. (2.1a), (2.1b), and (2.1c) using imaginary time propagation. This procedure effectively suppresses excited states and provides a reliable route to a converged ground-state solution, particularly when the ground-state profile is not known a priori.

By switching time to imaginary-time ($t \to -it$), the dynamical equations 2.16, 2.17, 2.22, 2.23 can be modified as follows,

$$-\frac{\partial}{\partial t}\Psi^{n+1/2} = (\mathbf{H}^d_{ND})\Psi^n, \tag{2.45}$$

TH-4102_206121026

$$\begin{pmatrix} \psi_{+1}^{n+1/2} \\ \psi_{0}^{n+1/2} \\ \psi_{-1}^{n+1/2} \end{pmatrix} = \begin{pmatrix} \exp(-\Delta t U_{+1}) & 0 & 0 \\ 0 & \exp(-\Delta t U_{0}) & 0 \\ 0 & 0 & \exp(-\Delta t U_{-1}) \end{pmatrix} \begin{pmatrix} \psi_{+1}^{n} \\ \psi_{0}^{n} \\ \psi_{-1}^{n} \end{pmatrix} . \tag{2.46}$$

And,

$$-\frac{\partial}{\partial t}\Psi^{n+1/2} = (H_{ND}^{od})\Psi^{n} , \tag{2.47}$$

$$-\frac{\partial}{\partial t}\Psi^{n+1/2} = (\mathbf{V}P\mathbf{V^{-1}})\Psi^{n} , \tag{2.48}$$

$$\begin{pmatrix} \psi_{+1}^{n+1/2} \\ \psi_{0}^{n+1/2} \\ \psi_{-1}^{n+1/2} \end{pmatrix} = \mathbf{V} \begin{pmatrix} \exp(-\Delta t D) & 0 & 0 \\ 0 & 1 & 0 \\ 0 & 0 & \exp(\Delta t D) \end{pmatrix} \mathbf{V^{-1}} \begin{pmatrix} \psi_{+1}^{n} \\ \psi_{0}^{n} \\ \psi_{-1}^{n} \end{pmatrix} . \tag{2.49}$$

Similarly, equation 2.24 can be written as

$$\frac{\Psi^{n+1} - \Psi^{n+1/2}}{-\Delta t} = \frac{1}{2} H_D \left(\Psi^{n+1} + \Psi^{n+1/2} \right) , \tag{2.50}$$

where, H_D is the derivative part of the operator given in Eq. 2.8. Subsequently, the H_{kin} [Eq. 2.9] part of the derivative operator is discretized using CN scheme, and for H_{SO} [Eq. 2.10] is discretized using high order Richardson extrapolation similar to real-time propagation. The dynamics of the condensate are computed using the ground-state solution of the Gross-Pitaevskii equation.

The Normalization and magnetization of the quasi-1D systems are given in equations below,

$$\int dx \, \rho(x) = 1 , \tag{2.51}$$

$$\int dx \, [\rho_{+1}(x) - \rho_{-1}(x)] = \mathcal{M} . \tag{2.52}$$

TH-4102_206121026

2.1.3 Numerical extension to the quasi-two-dimensional condensates

The time-dependent coupled Gross-Pitaevskii equations for quasi-two-dimensional Rashba SO coupled spin-1 condensates in the presence of trapping potential $V(x,y)$ are given as [50, 100]

$$\mathrm{i}\frac{\partial\psi_{+1}}{\partial t} = \left[-\frac{1}{2}\left(\frac{\partial^2}{\partial x^2}+\frac{\partial^2}{\partial y^2}\right)+V(x,y)+c_0(\rho_{+1}+\rho_0+\rho_{-1})+c_2(\rho_{+1}+\rho_0-\rho_{-1})\right]\psi_{+1} + c_2\psi_0^2\psi_{-1}^* - \mathrm{i}\frac{k_L}{\sqrt{2}}\left[\frac{\partial\psi_0}{\partial y}+\frac{\partial\psi_0}{\partial x}\right]+\frac{\Omega}{\sqrt{2}}\psi_0\,, \tag{2.53a}$$

$$\mathrm{i}\frac{\partial\psi_0}{\partial t} = \left[-\frac{1}{2}\left(\frac{\partial^2}{\partial x^2}+\frac{\partial^2}{\partial y^2}\right)+V(x,y)+c_0(\rho_{+1}+\rho_0+\rho_{-1})+c_2(\rho_{+1}+\rho_{-1})\right]\psi_0 - \mathrm{i}\frac{k_L}{\sqrt{2}}\left[\frac{\partial}{\partial y}(\psi_{+1}+\psi_{-1})-\mathrm{i}\{\frac{\partial}{\partial x}(\psi_{+1}-\psi_{-1})\}\right]+2c_2\psi_0^*\psi_{+1}\psi_{-1}+\frac{\Omega}{\sqrt{2}}(\psi_1+\psi_{-1})\,, \tag{2.53b}$$

$$\mathrm{i}\frac{\partial\psi_{-1}}{\partial t} = \left[-\frac{1}{2}\left(\frac{\partial^2}{\partial x^2}+\frac{\partial^2}{\partial y^2}\right)+V(x,y)+c_0(\rho_{+1}+\rho_0+\rho_{-1})+c_2(\rho_{-1}+\rho_0-\rho_{+1})\right]\psi_{-1} + c_2\psi_0^2\psi_{+1}^* - \mathrm{i}\frac{k_L}{\sqrt{2}}\left[\frac{\partial\psi_0}{\partial y}-\mathrm{i}\frac{\partial\psi_0}{\partial x}\right]+\frac{\Omega}{\sqrt{2}}\psi_0\,. \tag{2.53c}$$

As in quasi-1D coupled GPEs, the quasi-two-dimensional coupled GPEs are solved numerically by decomposing the Hamiltonian into two operators: a derivative and a non-derivative operator. The derivative operator contains the kinetic energy and the SO coupling terms, whereas the non-derivative operator includes the Rabi coupling, external trapping potential, and nonlinear interaction contributions. For numerical implementation, the non-derivative operator is further separated into diagonal and off-diagonal parts. The diagonal part consists of trapping potential $V(x,y)$, the spin-independent interaction term proportional to c_0, and the density-dependent interaction term proportional to c_2. The off-diagonal part consists of Rabi coupling between the hyperfine states and the spin-exchange interaction terms.

The numerical simulation begins with an initial trial configuration for the condensate wavefunctions ψ_{+1}, ψ_0, and ψ_{-1}. In this thesis, a Gaussian profile is chosen as the initial guess for the stationary state, although other forms may also be adopted depending on the physical parameters of the system. The initial wavefunctions are first evolved under the action of the non-derivative operator, incorporating the effects of the trapping potential, nonlinear interactions, and Rabi coupling. This step produces

TH-4102_206121026

an intermediate set of wavefunctions. The intermediate states are then propagated using the derivative operator. For spatial discretization, a centered finite difference with grid spacings Δx and Δy is employed. The time evolution associated with the derivative terms is computed using the CN method, which treats these terms semi-implicitly and provides improved numerical stability and accuracy. The propagation procedure is repeated iteratively until the system converges to a stationary ground-state solution. Convergence is confirmed by monitoring the behaviour of relevant physical quantities during successive iterations, particularly the energy and spatial extent of the condensate components, to ensure that the numerical solution has reached a ground state.

To implement the numerical procedure, the coupled GPEs [Eq. 2.53] are written in a compact matrix form. The time evolution of the system can then be written as

$$i\frac{\partial}{\partial t}\Psi(x,y,t) = H\Psi(x,y,t) \equiv [H_D + H_{ND}]\Psi(x,y,t), \tag{2.54}$$

where $\Psi(x,y,t)$ is the spinor wave function and written as

$$\Psi(x,y,t) = \begin{pmatrix} \psi_{+1}(x,y,t) \\ \psi_0(x,y,t) \\ \psi_{-1}(x,y,t) \end{pmatrix}, \tag{2.55}$$

and H represents the effective Hamiltonian operator of the SO coupled condensate, which is split into derivative part (H_D) and non-derivative part (H_{ND}) to implement the CN scheme.

Let's begin with the non-derivative operator, which is further split into diagonal (H^d_{ND}) and off-diagonal (H^{od}_{ND}) terms, similar to Eqs. 2.5 and 2.7, respectively,

$$H_{ND} = H^d_{ND} + H^{od}_{ND}\,. \tag{2.56}$$

The diagonal part is given by

$$H^d_{ND} = \begin{pmatrix} U_{+1} & 0 & 0 \\ 0 & U_0 & 0 \\ 0 & 0 & U_{-1} \end{pmatrix}, \tag{2.57}$$

where

TH-4102_206121026

$$\begin{aligned} U_{+1} &= V(x,y) + c_0(\rho_{+1}+\rho_0+\rho_{-1}) + c_2(\rho_{+1}+\rho_0-\rho_{-1}), \\ U_0 &= V(x,y) + c_0(\rho_{+1}+\rho_0+\rho_{-1}) + c_2(\rho_{+1}+\rho_{-1}), \\ U_{-1} &= V(x,y) + c_0(\rho_{+1}+\rho_0+\rho_{-1}) + c_2(\rho_{-1}+\rho_0-\rho_{+1}). \end{aligned} \tag{2.58}$$

The off-diagonal part of the non-derivative operator is given as

$$H_{ND}^{od} = \begin{pmatrix} 0 & c_2\psi_0\psi_{-1}^* + \frac{\Omega}{\sqrt{2}} & 0 \\ c_2\psi_0^*\psi_{-1} + \frac{\Omega}{\sqrt{2}} & 0 & c_2\psi_0^*\psi_{+1} + \frac{\Omega}{\sqrt{2}} \\ 0 & c_2\psi_0\psi_{+1}^* + \frac{\Omega}{\sqrt{2}} & 0 \end{pmatrix}. \tag{2.59}$$

The derivative operator H_D can also be decomposed into H_{Kin} and H_{SO}, given as follows

$$H_D = H_{Kin} + H_{SO}\,, \tag{2.60}$$

where

$$H_{Kin} = \begin{pmatrix} -\frac{1}{2}(\frac{\partial^2}{\partial x^2} + \frac{\partial^2}{\partial y^2}) & 0 & 0 \\ 0 & -\frac{1}{2}(\frac{\partial^2}{\partial x^2} + \frac{\partial^2}{\partial y^2}) & 0 \\ 0 & 0 & -\frac{1}{2}(\frac{\partial^2}{\partial x^2} + \frac{\partial^2}{\partial y^2}) \end{pmatrix}, \tag{2.61}$$

$$H_{SO} = \begin{pmatrix} 0 & -\frac{ik_L}{\sqrt{2}}(\nu\frac{\partial}{\partial y} + \mathrm{i}\frac{\partial}{\partial x}) & 0 \\ -\frac{ik_L}{\sqrt{2}}(\nu\frac{\partial}{\partial y} - \mathrm{i}\frac{\partial}{\partial x}) & 0 & -\frac{ik_L}{\sqrt{2}}(\nu\frac{\partial}{\partial y} + \mathrm{i}\frac{\partial}{\partial x}) \\ 0 & -\frac{ik_L}{\sqrt{2}}(\nu\frac{\partial}{\partial y} - \mathrm{i}\frac{\partial}{\partial x}) & 0 \end{pmatrix}. \tag{2.62}$$

With this matrix representation, the coupled Gross-Pitaevskii equations can be expressed compactly as

$$i\frac{\partial\Psi}{\partial t} = \left(H_{SO} + H_{Kin} + H_{ND}^{od} + H_{ND}^{d}\right)\Psi. \tag{2.63}$$

The non-derivative part Eq. 2.56 is dealt in a similar way as we have solved it for the quasi-1D case, treating the diagonal and off-diagonal parts separately [see Eqs. 2.17, and 2.23]. For the derivative part, the spinor Gross-Pitaevskii solver in quasi-two-dimensional geometry is implemented through an *alternating direction implicit* (ADI) approach, which decomposes the two-dimensional system into successive one-dimensional updates. In this framework, the kinetic energy operator is split into two subroutines,

where the tridiagonal matrix inversion is performed along the rows and columns, respectively, maintaining the $O(N)$ efficiency of the algorithm across an $N_x \times N_y$ grid. The SO coupling, whether in the Rashba or Dresselhaus configuration, is treated as a discrete "kick" in the split-step sequence. This is achieved by calculating spatial derivatives (∂_x, ∂_y) using a high-order finite difference stencil and applying the resulting momentum-dependent coupling to three spinor components $(\psi_{+1,0,-1})$ [50].

The Normalization and magnetization of the quasi-two-dimensional system are given in equations below [50, 100],

$$\int dxdy\rho(x,y) = 1, \quad \int dxdy[\rho_{+1}(x,y) - \rho_{-1}(x,y)] = \mathcal{M} \, . \tag{2.64}$$

The present numerical implementation follows the algorithmic framework developed in Ref. [50]. The efficiency, numerical stability, and convergence properties of this solver have been discussed in detail by the authors in that work. Therefore, only the essential aspects of the numerical procedure relevant to the present study are outlined here.

2.1.4 Convergence of ground state

In the above section, we presented the CN scheme for imaginary- and real-time propagation to obtain the ground state and the dynamics of the condensate, respectively, in quasi-one and two-dimensional geometries. To validate the accuracy of the split-step CN implementation in the quasi-1D case, a systematic grid independence test is performed. As summarized in Table 2.1, the spatial grid spacing dx is refined from 0.5 to 0.04. To maintain the stability of the semi-implicit scheme, the time step dt is scaled proportionally to $(dx)^2$.

In this thesis, we report a wide range of ground-state phases, including ZM, EZM, SW, and SSW. Here, we generate the ground-state phase diagram for $k_L = 0.5$, $\Omega = 1.0$ and interaction strength $c_0 = 10$, $c_2 = -5.0$, which corresponds to ZM phase of the condensate.

The grid convergence test confirms the numerical reliability of the ground-state solutions by demonstrating a clear plateau in the physical observables. For grid values ($dx \gtrsim 0.2$), the simulation significantly overestimates the total energy and root mean square size ($\langle x \rangle$) of the condensate. As the grid is refined to $dx = 0.1$, the energy stabilizes to the third decimal place, marking the threshold where the numerical resolution captures the essential physics of the condensate. Notably, the results for $dx = 0.05$ and

TH-4102_206121026

dx	dt	Energy (E)	$\langle x \rangle$
0.5	0.125	0.340500	1.150360
0.4	0.064	0.307137	1.065104
0.2	0.008	0.294181	0.986311
0.1	0.001	0.293986	0.976607
0.05	0.00025	0.293984	0.975623
0.04	0.00016	0.293984	0.975505

Table 2.1: Grid convergence test for a quasi-one-dimensional spin-orbit coupled spin-1 Bose-Einstein condensate with $k_L = 0.5$, $\Omega = 1.0$ and interaction strengths $c_0 = 10$, $c_2 = -5.0$. The total energy (E) and root mean square size ($\langle x \rangle$) exhibit convergence up to four decimal places for $dx \lesssim 0.05$.

$dx = 0.04$ are identical up to the fourth decimal place (see Table 2.1), indicating that spatial discretization errors are effectively negligible. This convergence validates the choice $dx = 0.05$ and $dt = 0.00025$ as optimal grid spacings, providing high numerical precision while maintaining computational efficiency for subsequent simulations. In Fig. 2.1, we report the variation of the total energy and root mean square size of the condensate during the implementation of the imaginary-time propagation scheme. We observe that $t \gtrsim 20$, both energy and root mean square size attain a steady state value, indicating the preparation of a converged ZM ground-state phase, for the parameter values considered in Table 2.1.

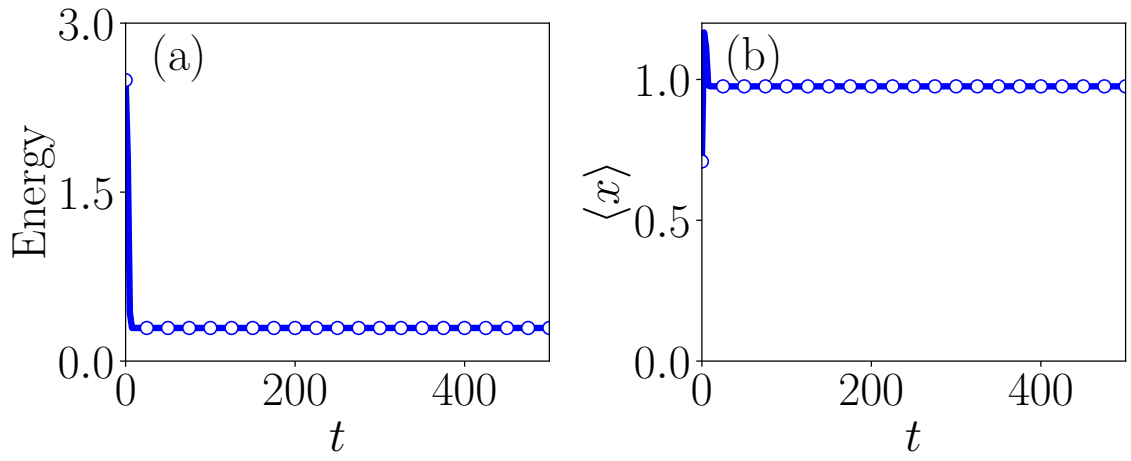


Figure 2.1: (a) Temporal evolution of the total energy and (b) temporal evolution of the root mean square size during imaginary time propagation as the system converges to the ground state. The parameters are the same as those considered in Table 2.1.

Further, in Fig. 2.2, we demonstrate the stability of the obtained ground state density profile during real-time propagation. The shape and amplitude of the condensate do not change during the time evolution, indicating the stable nature of the ground

state density profile. This further validates the accuracy of the ground-state preparation.

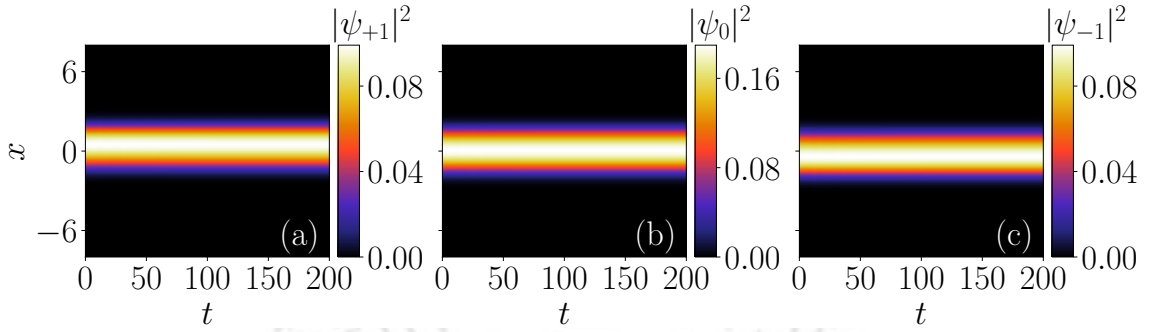


Figure 2.2: Stability of the condensate density profile during real-time propagation for (a) $|\psi_{+1}|^2$, (b) $|\psi_{+1}|^2$, and (c) $|\psi_{+1}|^2$. To obtain the ground state, we consider $k_L = 0.5$, $\Omega = 1.0$, $c_0 = 10$, and $c_2 = -5.0$. The density profile remains unchanged in both shape and amplitude during time evolution, indicating the stable nature of its ground state.

In the above part, we presented the grid-independence test for the quasi-1D case in detail. Here, we briefly discuss the corresponding analysis for the quasi-2D system. For the quasi-2D case, a similar grid-independence study is conducted to verify the numerical accuracy of the simulations. The spatial grid spacing is systematically refined while maintaining the stability condition $dt \propto (dx)^2$. The corresponding values of the total energy and root mean square size ($\langle r \rangle$) are summarized in Table 2.2. It is observed that both quantities converge with successive grid refinement, and the variations become negligible for $dx = dy \lesssim 0.1$. This confirms that the chosen grid parameters provide sufficient spatial resolution for reliable two-dimensional simulations. The results presented here correspond to interactions strengths $c_0 = 50$, $c_2 = -2.5$, and $k_L = 0.5$, $\Omega = 1.0$, which is PW phase of the condensate.

$dx(= dy)$	dt	Energy (E)	$\langle r \rangle$
0.4	0.016	1.69236	1.6925
0.2	0.004	1.69288	1.6829
0.1	0.001	1.69291	1.6806
0.1	0.0005	1.69291	1.6801
0.08	0.00032	1.69291	1.6800

Table 2.2: Grid convergence test for a quasi-two-dimensional spin-orbit coupled spin-1 Bose-Einstein condensate with $k_L = 0.5$, $\Omega = 1.0$ and interaction strengths $c_0 = 50$, $c_2 = -2.5$. The total energy (E) and root mean square size ($\langle r \rangle$) depict convergence up to four decimal places for $dx \lesssim 0.1$.

TH-4102_206121026

2.1.5 Quench dynamics of the spin-orbit coupled condensate

In this section, we report the methodology adopted to analyze the dynamics of the SO coupled spin-1 condensates. In this approach, the system is initially prepared in its ground state for a given set of parameters using imaginary-time propagation. The dynamics is then triggered by an instantaneous quench of the condensate parameters, such as SO coupling strength, Rabi coupling strength, and the trapping potential. The quench is implemented at the onset of real-time propagation by abruptly changing these parameters.

Following the quench, the system is evolved in real time using time-dependent GPEs. This sudden perturbation excites various collective modes of the condensate, enabling us to study the subsequent dynamical behaviour of the condensate under different quench conditions.

2.2 Summary

In this chapter, we have presented a numerical framework that has been used for the thesis to study the SO coupled spin-1 BECs in quasi-one and two-dimensional geometries. The imaginary-time propagation is employed to obtain the ground state of the condensate, while the real-time propagation is used to investigate the dynamics of the condensate. Both imaginary-time and real-time propagation are implemented via the split-step Crank-Nicolson method. The accuracy of the method is validated through grid convergence tests, ensuring reliable numerical results in both quasi-one- and two-dimensional cases. Furthermore, we discuss the quench protocol employed in this thesis, in which the condensate parameters are abruptly changed at the onset of real-time evolution. This approach allows us to explore the stability and nonequilibrium behaviour of the condensate under different conditions.

TH-4102_206121026

Chapter 3

Emergence of spin-mixed superstripe phases in spin-orbit coupled spin-1 condensate

In this Chapter, we present the mean-field simulation results of the ground-state phases and quench dynamics of spin-orbit coupled spin-1 Bose-Einstein condensates with ferromagnetic and antiferromagnetic interactions. For finite Rabi coupling, the system exhibits zero-momentum, elongated zero-momentum, and stripe phases, while in the zero-Rabi coupling limit, the superstripe wave phases emerge. Varying the attractive density-density (c_0) and spin-exchange (c_2) interactions induces the transition from stripe and superstripe phases to the elongated zero-momentum phase, characterized by miscibility and polarization. The condensate remains miscible in the zero-momentum phase and partially miscible for the elongated zero-momentum, stripe, and superstripe phases. Quenching in Rabi coupling stabilizes the condensate, while spin-orbit coupling quenching leads to fluctuations or the formation of complex patterns, with the stripe phase exhibiting the vanishing of the zeroth spin component over time. The work presented in the Chapter is published in Physical Review A [101].

3.1 Introduction

The introduction of different phases related to the spin-orbit (SO) coupled spin-1 Bose-Einstein condensates (BECs) have been discussed in Chapter 1. However, to make this Chapter self-contained, in this section we provide a brief overview that emphasizes the emergence of different quantum phases in SO coupled spin-1 BECs. The SO

TH-4102_206121026

coupling between a particle's spin and its orbital angular momentum has become a central concept in condensed matter physics, playing a key role in phenomena such as topological insulators [1, 44], the quantum Hall effect [45, 59], and spintronics [3]. In ultracold atomic gases, SO coupling was experimentally engineered by Lin *et al.* [4] in spin-$\frac{1}{2}$ BECs of ^{87}Rb using Raman coupling between two $F = 1$ hyperfine states, effectively realizing equal Rashba [5] and Dresselhaus [6] interactions. This achievement stimulated extensive research in SO coupled BECs, leading to the observation of various novel phenomena such as the Dicke phase transition [63], Zitterbewegung [62], Faraday patterns [67], supersolid phases [66], and elementary excitations [25]. The method was later extended to spin-1 condensates by utilizing all three $F = 1$ hyperfine states, enabling the realization of SO coupled spin-1 BECs [10, 11, 60, 102].

Theoretical studies of ultracold Bose gases largely rely on mean-field simulations based on the Gross–Pitaevskii equation (GPE), which provides an effective framework for exploring complex phases and their stability. Using this approach, several works have investigated vortex formation [103–105], soliton dynamics [106, 76, 107], and collective excitations [24]. In quasi-one-dimensional (quasi-1D) SO coupled BECs, the interplay of SO coupling and spin-dependent interactions can generate mobile vector solitons whose structure depends on the magnetic nature of the interactions: ferromagnetic interactions favor single-peak time-reversal symmetry-breaking solitons [108], while antiferromagnetic interactions support multi-peak structures such as dark–bright–dark or bright–dark–bright solitons that remain dynamically stable and exhibit quasi-elastic collisions [77].

Another important aspect of SO coupled spinor condensates is the competition between SO coupling, spin-dependent interactions, and Rabi coupling, which governs miscibility and phase separation. It has been shown that SO coupling can induce phase separation in ferromagnetic spin-1 BECs in the absence of Rabi coupling, while promoting miscibility in the antiferromagnetic case [109]. In trapped systems, harmonic confinement generally favors miscibility, although phase separation may still occur beyond a critical SO coupling strength, and Rabi coupling tends to enhance miscibility. Moreover, quench dynamics in such systems provides a powerful route to explore nonequilibrium phenomena such as quantum phase transitions, domain formation, and collective excitations [93, 110–115].

There are relatively few works that explore the intricate relationship between the spin structure and the diverse phases of complex SO coupled BECs. For a spin-1/2 condensate, Ho and Zhang [64] identified a density-modulated stripe phase with zero magnetization under a special symmetric and spin-mixed limit. Later, Yu [23] has ex-

tended this analysis to spin-1 condensates in quasi-1D geometries. Their study categorically distinguished various phases, including the plane-wave (PW), zero-momentum (ZM), and several types of stripe (STR) phases. Notably, STR1 corresponds to a spin-mixed stripe phase with density modulation and vanishing longitudinal magnetization, while STR2 and STR3 exhibit finite magnetization accompanied by spin-tensor modulations.

Along similar lines, Sun *et al.* [24] reported the existence of ZM and PW phases, as well as a stripe phase with equal spin population, characterized by uniform spin polarization and density modulation, and a magnetized stripe phase featuring oscillating spin polarization. More recently, Gangwar *et al.* [115, 116] examined the dynamical properties of quasi-1D SO coupled spin-1 BECs, focusing on excitation spectra, modulation instabilities, and avoided crossings under ferromagnetic and antiferromagnetic interactions. While these works provided rigorous instability analyses, a systematic investigation of the ground state phase structure remains lacking.

In this Chapter, we address this gap by presenting a comprehensive study of both the ground-state phases and quench dynamics of quasi-1D SO coupled spin-1 BECs, focusing on how SO and Rabi coupling affect the system. We identify phases, such as zero-momentum (ZM), elongated zero-momentum (EZM), stripe wave (SW), and superstripe wave (SSW). In antiferromagnetic interactions, the ZM, EZM, and SW phases appear with finite Rabi coupling, while the SSW phase emerges in both ferromagnetic and antiferromagnetic systems at relatively weak Rabi coupling but vanishes as Ω increases. We also explore the spin-component separation and miscibility, showing that while the ZM phase is fully miscible, other phases exhibit partial demixing, reflecting distinct spin textures and correlations.

The structure of this Chapter is as follows. In Sec. 3.2, we introduce the mean-field model to investigate ground-state phases and quench dynamics. In Sec. 3.3, we provide details of the numerical simulation methods. In Sec. 3.3.1, we discuss the emergence and characterization of ground-state phases under ferromagnetic interactions, followed by antiferromagnetic interactions in Sec. 3.3.2. In Sec. 3.3.3, we analyze the effect of interactions on the ground-state phases. In Sec. 3.3.4, we explore the quench dynamics across these phases. Finally, in Sec. 3.4, we summarize our findings.

TH-4102_206121026

3.2 Mean-Field Model

We consider a quasi-1D SO coupled spinor spin-1 BECs realized by tight confinement in the transverse direction. The GPEs govern the dynamics of the system, incorporating the effects of SO coupling and nonlinear interactions. The generalized coupled GPEs are given as follows [50, 77],

$$\begin{aligned} \mathrm{i}\frac{\partial\psi_{\pm1}}{\partial t} &= \left[-\frac{1}{2}\frac{\partial^2}{\partial x^2} + V(x) + c_0\rho\right]\psi_{\pm1} \mp \frac{k_L}{\sqrt{2}}\frac{\partial\psi_0}{\partial x} \\ &\quad + c_2(\rho_{\pm1} + \rho_0 - \rho_{\mp1})\psi_{\pm1} + c_2\psi_0^2\psi_{\mp1}^* + \frac{\Omega}{\sqrt{2}}\psi_0, \end{aligned} \tag{3.1a}$$

$$\begin{aligned} \mathrm{i}\frac{\partial\psi_0}{\partial t} &= \left[-\frac{1}{2}\frac{\partial^2}{\partial x^2} + V(x) + c_0\rho\right]\psi_0 + 2c_2\psi_0^*\psi_{+1}\psi_{-1} \\ &\quad + c_2(\rho_{+1} + \rho_{-1})\psi_0 + \frac{k_L}{\sqrt{2}}\left[\frac{\partial\psi_{+1}}{\partial x} - \frac{\partial\psi_{-1}}{\partial x}\right] + \frac{\Omega}{\sqrt{2}}(\psi_{+1} + \psi_{-1}). \end{aligned} \tag{3.1b}$$

Here, ψ_{+1}, ψ_0, and ψ_{-1} are the spinor wave functions corresponding to sublevels $m_F = +1, 0, -1$ of the hyperfine state $F = 1$. These wave functions satisfy the normalization condition

$$\int_{-\infty}^{\infty} dx \sum_{j=-1}^{1} |\psi_j(x)|^2 = 1,$$

where ρ_j denotes the density of the jth component of the condensate ($j = \pm1, 0$), and $\rho = |\psi_{+1}|^2 + |\psi_0|^2 + |\psi_{-1}|^2$ is the total density of the condensates. The coupled system of equations in (3.1a) and (3.1b) is expressed in dimensionless form, using the characteristic time, length, and energy scales as $t = \omega_x\tilde{t}$, $x = \tilde{x}/l_0$, and $\hbar\omega_x$, respectively. The condensate wave function is defined as $\psi_{\pm1,0} = \sqrt{l_0/N}\tilde{\psi}_{\pm1,0}$, where $l_0 = \sqrt{\hbar/(m\omega_x)}$ is the harmonic oscillator length for a given trap frequency ω_x along the x axis.

The trap potential is $V(x) = \lambda x^2/2$. The density-density interaction strength is $c_0 = 2Nl_0(a_0 + 2a_2)/(3l_\perp^2)$, and the spin-exchange interaction strength is $c_2 = 2Nl_0(a_2 - a_0)/(3l_\perp^2)$, where a_0 and a_2 are the s-wave scattering lengths in the total spin channels 0 and 2, respectively. By tuning $c_2 < 0$ ($c_2 > 0$), one obtains ferromagnetic (antiferromagnetic) interactions of the condensate [39, 117]. The transverse oscillator length is $l_\perp = \sqrt{\hbar/(m\omega_\perp)}$, with $\omega_\perp = \sqrt{\omega_y\omega_z}$. The SO and Rabi coupling strengths are $k_L = \tilde{k}_L/(\omega_x l_0)$ and $\Omega = \tilde{\Omega}/(\hbar\omega_x)$, respectively. In the above description, quantities with a tilde represent dimensionful parameters. In all results presented in this work, we use dimensionless parameters.

The energy Functional of the system is given by [50, 77],

$$
\begin{aligned}
E =& \frac{1}{2}\int dx\Big\{\sum_j \left|\partial_x\psi_j\right|^2 + 2V(x)\rho + c_0\rho^2 \\
&+ c_2[\rho_{+1}^2 + \rho_{-1}^2 + 2(\rho_{+1}\rho_0 + \rho_{-1}\rho_0 - \rho_{+1}\rho_{-1} \\
&+ \psi_{-1}^*\psi_0^2\psi_{+1}^* + \psi_{-1}\psi_0^{*2}\psi_{+1})] + \sqrt{2}\Omega[(\psi_{+1}^* + \psi_{-1}^*)\psi_0 \\
&+ \psi_0^*(\psi_{+1} + \psi_{-1})] + \sqrt{2}k_L[(\psi_{-1}^* - \psi_{+1}^*)\partial_x\psi_0 + \psi_0^*(\partial_x\psi_{+1} - \partial_x\psi_{-1})]\Big\}. \qquad (3.2)
\end{aligned}
$$

As the primary focus of our work is to differentiate phases based on spin-mixing and spin-demixing behavior, we start by precisely defining the key quantities: the miscibility order parameter, root mean square size, and spin-density vector (SDV) polarization of the condensate for SO coupled spin-1 BECs.

Miscibility order parameter: The miscibility order parameter (η) of the spin-1 BECs characterizes the overlap of the densities ρ_{+1}, ρ_0, and ρ_{-1}. Another overlap parameter η_{np}, which specifically represents the overlap between the densities of ρ_{+1}, and ρ_{-1} of the condensate. The overlap parameter and miscibility order parameter are given as follows [118],

$$\eta_{np} = 4\int(\sqrt{\rho_{+1}\rho_{-1}})\,dx, \qquad (3.3a)$$

$$\eta = \int(\sqrt{\rho_{+1}\rho_0} + \sqrt{\rho_{-1}\rho_0} + \sqrt{\rho_{+1}\rho_{-1}})\,dx. \qquad (3.3b)$$

Root Mean Square size: The other important entity is the root mean square size (x_{rms}) of the condensate which specifically being used to characterize the spatial extent and associated phase transformation of its ground state. The x_{rms} of the condensate is given as follows [119],

$$x_{rms} = \left(\frac{\int_{-\infty}^{\infty}(x - \langle x\rangle)^2\rho dx}{\int_{-\infty}^{\infty}\rho dx}\right)^{1/2}, \qquad (3.4)$$

with,

$$\langle x\rangle = \frac{\int_{-\infty}^{\infty} x\rho dx}{\int_{-\infty}^{\infty}\rho dx}, \qquad (3.5)$$

where ρ is the total density of the condensate.

Spin-density Vector: The spin-density vector (SDV) in spin-1 spinor BECs plays a key role in analyzing the spin textures. It is expressed as $S = \psi^\dagger \Sigma \psi$, where $\psi = [\psi_{+1}, \psi_0, \psi_{-1}]^T$ is normalized wavefunction and $\Sigma = (\Sigma_x, \Sigma_y, \Sigma_z)$ are the spin-1 Pauli matrices. The resulting SDV components are given as [39],

$$S_x = \frac{1}{\sqrt{2}} \left[(\psi_{+1}^* + \psi_{-1}^*)\psi_0 + (\psi_{+1} + \psi_{-1})\psi_0^* \right] , \tag{3.6a}$$

$$S_y = \frac{i}{\sqrt{2}} \left[(\psi_{-1}^* - \psi_{+1}^*)\psi_0 + (\psi_{+1} - \psi_{-1})\psi_0^* \right] , \tag{3.6b}$$

$$S_z = |\psi_{+1}|^2 - |\psi_{-1}|^2 . \tag{3.6c}$$

Here, we outline the experimentally realistic range of the parameters considered in our simulations. We consider the ^{87}Rb BECs with $N \sim 2 \times 10^4$ number of atoms with ferromagnetic interaction trapped under the axial trap frequency as $\omega_x = 2\pi \times 50$ Hz and the transverse trap frequencies as $\omega_y = \omega_z = 2\pi \times 500$ Hz. With these, the resultant characteristic lengths are $l_0 = 1.52\,\mu$m and $l_\perp = 0.48\,\mu$m. For the antiferromagnetic interaction, one can consider the ^{23}Na atoms with characteristic lengths as $l_0 = 2.9\mu m$, and $l_\perp = 0.9\mu m$. The spin-dependent and spin-independent interactions can be achieved by controlling the s-wave scattering lengths via Feshbach resonance [120–122]. The SO coupling strength $k_L = \{0.1 - 5\}$ can be tuned by changing the laser wavelengths in the range of $\{68.86\mu m$ - 1377.22nm$\}$. However, the dimensionless Rabi frequency interval $\Omega = [10^{-3}, 5]$ used in the simulation can be attained by tuning the Raman laser strength in the range of $2\pi\hbar \times \{0.05 - 250\}$ Hz.

The qualitative structure of the ground state can be understood from the competition among the terms appearing in Eqs. (3.1a)–(3.1b). The SO coupling favors momentum–spin locking and promotes occupation of finite–momentum components. In contrast, the Rabi coupling mixes the spin states and pulls the condensate toward a zero–momentum configuration [4]. The spin-independent interaction (c_0) controls the overall density, while the spin-dependent interaction (c_2) favors spin-polarized configurations in the ferromagnetic case and more balanced populations in the antiferromagnetic case [39]. The competition among these effects determines whether the condensate remains centered at zero momentum, shifts into a weakly modulated state (EZM), develops interference-driven stripe patterns (SW), or forms a three-component, strongly modulated SSW phase. In the following sections, we focus on the physical mechanisms, spin–momentum locking, interference, and spin-dependent interactions that determine each phase. This structure highlights the origin and evolution of the ZM, EZM, SW, and SSW phases.

3.3 Simulation results

We numerically solve the coupled GPEs (3.1a)-(3.1b) using the split-time step Crank-Nicolson scheme [50, 72]. To determine the ground state, we use imaginary-time propagation, which relaxes the system to its lowest energy state but does not conserve normalization or magnetization; hence, renormalization is applied at each time step appropriately [109]. The initial wave function is chosen as a Gaussian profile. We employ the real-time propagation method to investigate the dynamics of the condensate using the converged ground state obtained in the imaginary-time propagation method. The space and time steps used in the imaginary-time propagation method are $dx = 0.05$, $dt = 0.0002$, and in the real-time propagation method are $dx = 0.05$, $dt = 0.0001$. In the next section, we implement these and study the ground states and miscibility of the condensate in the presence of ferromagnetic interactions.

Hereafter, for brevity, we use "$\Omega \sim 0$" to denote a weak but nonvanishing Rabi coupling. Note that in the strict $\Omega = 0$ limit, the SO term can be eliminated in the single particle Hamiltonian by an appropriate gauge transformation [24, 117], thereby recovering the uniform phases of a conventional spin-1 condensates. In contrast an arbitrary small but finite Ω breaks this gauge equivalence and prevents elimination of the SO coupling.

3.3.1 Ground state phases for ferromagnetic interactions

In this section, we present the different ground state phases of quasi-1D SO coupled spin-1 ferromagnetic BECs. We analyze the ground state phases in the absence of magnetization by examining key properties such as the SDV polarization, miscibility, and the root mean square size of the condensates.

3.3.1.1 Different ground state phases

We begin our investigation with the ground state phases of the SO coupled spin-1 BECs in presence of ferromagnetic interactions with the interaction strengths $c_0 = 10$ and $c_2 = -5.0$. Fig. 3.1 illustrates the impact of SO (k_L) and Rabi (Ω) couplings on various ground state phases. In Fig. 3.1(a1), we present the ground state density profile for $\Omega \sim 0.0$, and $k_L = 0.0$. All condensate components exhibit a single density peak at the center with $\rho_{\pm 1}$ overlapping in the real space, and the component ρ_0 is doubled in the density. However, the density profiles of all three components exhibit complete spatial overlap. To characterize the detailed structure, we show the corresponding mo-

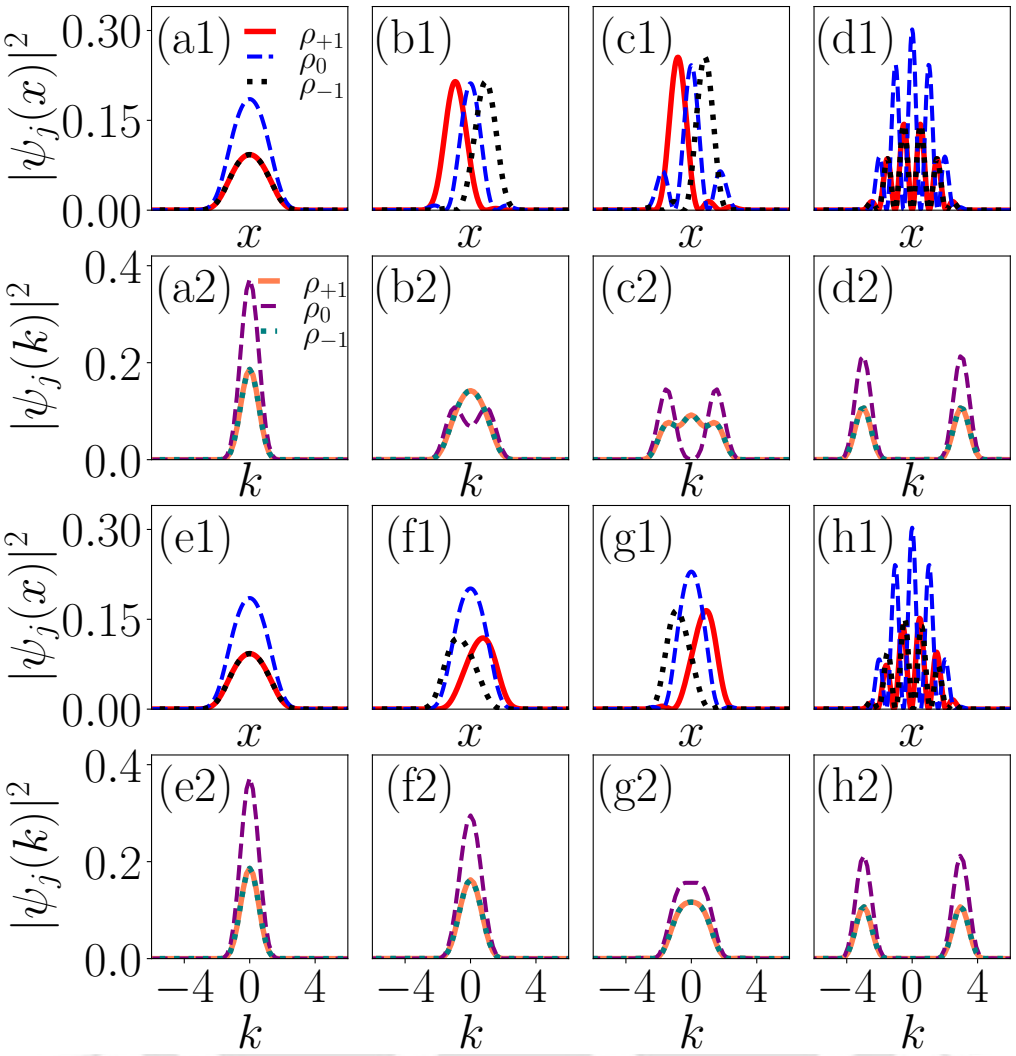


Figure 3.1: Different ground state phases of the SO coupled spin-1 BECs with ferromagnetic interaction. Real-space (top) and momentum-space (bottom) density profiles of spin components $|\psi_{+1}(x)|^2$ (solid red), $|\psi_0(x)|^2$ (dashed blue), and $|\psi_{-1}(x)|^2$ (dotted black), along with their corresponding momentum-space densities $|\psi_{+1}(k)|^2$ (solid coral), $|\psi_0(k)|^2$ (dashed purple), and $|\psi_{-1}(k)|^2$ (dotted green), under varying Rabi coupling Ω and spin-orbit coupling k_L. Interaction strengths are fixed at $c_0 = 10$ and $c_2 = -5.0$. Panels (a–d) correspond to $\Omega \sim 0$ and panels (e–h) to $\Omega = 1.0$, with $k_L = 0.0, 1.0, 1.5, 3.0$ increasing from left to right in each set. For $\Omega \sim 0$, increasing k_L induces transitions through ZM, EZM I, SW, and SSW ground state phases. At finite Ω, the SSW phase is absent.

mentum space distribution in Fig. 3.1(a2). The momentum state density distribution shows a single peak centered at $k = 0$, indicating that the condensate occupies only the zero-momentum state, which we classify as a zero-momentum (ZM) phase. Increasing the SO coupling to $k_L = 1.0$ leads to a clear spatial separation between the densities $\rho_{\pm 1}$ as seen in Fig. 3.1(b1). The densities ρ_{+1} and ρ_{-1} peak away from the trap center at $x = -0.95$ and 0.95, respectively, with a similar amplitude $\rho_{\pm 1}(max) = 0.22$, while the zeroth component density starts developing the second hump in real space

and amplitude of all the components are equal as well components are polarized. The corresponding momentum distribution [Fig. 3.1(b2)] reveals two peaks for the zeroth component of the condensate, indicating a slight deviation from the ZM phase. We classify this as an elongated zero-momentum phase of the first type (EZM I) phase due to the spatial deformation and partial separation of the spin components. For small SO coupling strength, the single–particle dispersion favors zero momentum occupation, stabilizing the ZM phase. As SO coupling increases, the dispersion develops two nearly degenerate minima at finite momentum [4, 64]. In this regime, the condensate may occupy both minima, but the spin composition of the $m_F = \pm 1$ components remains nearly identical, so interference between the counter-propagating modes is weak. As a result, density modulation remains small, leading to the EZM I phase: a finite–momentum state with only slight spatial variation.

Further, increasing k_L from 1.0 to 1.5 results in multi-peak structure in real space density profile [Fig. 3.1(c1)]. The corresponding density profile in the momentum space [Fig. 3.1(c2)] exhibits prominent peaks at finite k, especially the zeroth component, with $m_F = \pm 1$ also peaking up at finite k. These features signal the onset of the stripe-wave (SW) phase, where interference between multiple plane-wave components with finite momentum leads to spatial modulation of the condensate density. In the SW phase, the condensate occupies two counter-propagating momentum components. Although the presence of spin–orbit coupling fixes these momenta through the single-particle dispersion, the spin composition of the two branches is no longer identical once interactions are included [93]. Since each counter-propagating mode carries a slightly different mixture of the spin states, their interference produces spatial density oscillations whose contrast varies among the three components. This leads to a stripe pattern in real space, with the $m_F = \pm 1$ components showing distinguishable modulation amplitudes due to their unequal spin mixing [109]. Upon further increasing the SO coupling to $k_L = 3.0$, the condensate develops a pronounced multi-peak density profile in the real space with overlap between the ρ_{+1} and ρ_{-1}, as illustrated in Fig. 3.1(d1). The corresponding momentum density profile [Fig. 3.1(d2)] exhibits symmetric peaks at finite k, ($k = \pm k_L$) for all spin components. This structure is consistent with the characteristics of the superstripe-wave (SSW) phase, a subset of the SW phase characterized by complete overlap of $m_F = \pm 1$ components and unpolarized behaviour. In the SSW phase, all three spin components contribute non-trivially. The $m_F = \pm 1$ densities nearly overlap, while the $m_F = 0$ density fills in their maxima and minima, producing strong complementary modulation. Phase locking between these components cancels the net spin polarization, yielding $S_x = S_y = S_z = 0$ [Fig. 3.2(b4)]

while preserving pronounced density oscillations. This distinguishes the SSW phase from the SW phase.

To investigate the effect of SO coupling, we fix $\Omega = 1.0$. For $k_L = 0.0$, in real and momentum space densities [Fig. 3.1(e1,e2)] remain centered and single peaked across all components, indicating persistence of the ZM phase. For $k_L = 1.0$ as shown in Fig. 3.1(f1), due to the influence of the Rabi coupling $\Omega = k_L^2$ [c.f Fig. 3.1(b1)], the second hump in the zeroth component density disappears and densities ρ_{+1} and ρ_{-1} posses peaks away from the trap center at $x = 0.75$, and -0.75 with $\rho_{\pm1}(max) = 0.12$. The corresponding momentum density profile displays only a single peak across all components given in Fig. 3.1(f2). However, in real space $\rho_{\pm1}$ shows separation among themselves, resulting in an EZM I phase. Upon increasing $k_L = 1.0$ to 1.5, in Fig. 3.1(g1), we again obtain a single peak density across all components and $m_F = +1(-1)$ components peaks at $x = 0.9(-0.9)$ with a amplitude $\rho_{\pm1}(max) = 0.17$. In the corresponding momentum distribution in Fig. 3.1(g2), a flat-top-like distribution emerges, peaks at $k \approx 0$, and the condensate remains in the EZM I phase. Although the EZM I state develops off-center density peaks in the $m_F = \pm1$ components, its real-space profiles remain single-peaked and show no interference-driven oscillations. At $\Omega \sim 0$, the $m_F = 0$ component can acquire two weak momentum-space lobes, but these produce only negligible modulation in real space. When Ω is finite, the Rabi coupling locks the relative phase and confines the condensate to a single effective momentum branch, completely suppressing any splitting in momentum space [118]. Consequently, EZM I corresponds to an elongated zero-momentum configuration. Considering $\Omega = 1.0$ and $k_L = 3.0$ in Fig. 3.1(h1), we observe a multi-peak density profile across all components in real space, and the corresponding momentum space density profile in Fig. 3.1(h2) displays two peaks across all components. Here $m_F = \pm1$ does not superpose on each other, which indicates that the condensate is in the SW phase. Although the polarization behaviour between $m_F = \pm1$ component is not evident in the momentum space distributions, it becomes clearly discernible in the subsequent analysis of spin density vectors. Overall, we find that a finite Rabi coupling strength shifts the emergence of the SW phase to higher values of the SO coupling. The SSW phase appears only for $\Omega \sim 0$ and for large k_L. Otherwise, depending on the interplay between SO and Rabi coupling, the system predominantly exhibits the ZM, EZM I, or SW phases.

To characterize the different ground state phases, we compute the SDV polarization, which captures key features of the spin textures and their evolution. This makes it a valuable tool for distinguishing the phase transitions discussed above [118]. In

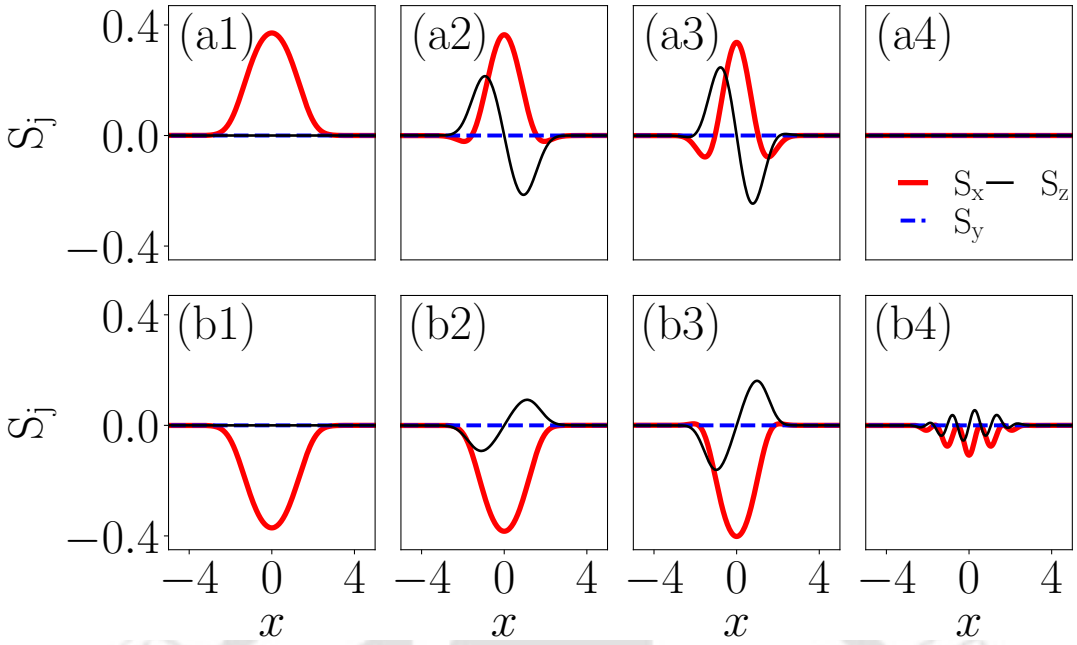


Figure 3.2: Spin-density vector (SDV) components S_x (solid red line), S_y (dashed blue line), and S_z (thin black line) shown in panels (a) and (b), corresponding to Fig. 3.1, using the same interaction and coupling parameters. The S_y component remains zero across all phases. In the ZM phase, S_x shows a single peak while S_z vanishes. The EZM I phase features a single-peak S_x accompanied by finite S_z. The SSW phase is characterized by vanishing SDV components, whereas the SW phase displays a multipeak structure in S_x and oscillations in S_z, indicating density modulation.

Fig.3.2, we present the SDV components S_x, S_y and S_z as defined in Eq. (3.6) corresponding to the different phases of Fig. 3.1. We begin with Fig. 3.2(a1), where $\Omega \sim 0$, and $k_L = 0.0$. In this case, S_x is non-zero and displays a single peak, consistent with the ZM phase of the condensate. Upon increasing the SO coupling to 1.0 [Fig. 3.2(a2)], the single peak in S_x remains, while a non-zero S_z emerges, ranging from -0.22 to 0.22. This non-zero S_z results from a distinct separation between the densities ρ_{+1} and ρ_{-1}, confirming the transition to the EZM I phase. The finite magnitude of S_z indicates that the $m_F = \pm 1$ are not superposed.

For $k_L = 1.5$ with fixed Ω shown in Fig. 3.2(a3), S_x maintains a single peak but features a peculiar negative dip over a small range of x, forming a symmetric kink-like structure. Simultaneously the amplitude of S_z increases to the range $[-0.25, 0.25]$. The kink-like feature arises in the S_x, due to appearance of the multi-peak density profiles, confirming a transition to the SW phase. At higher SO coupling $k_L = 3.0$, Fig. 3.2(a4) shows that all the SDV components vanish. Since non-zero S_z indicates a separation between the $m_F = \pm 1$ components, the condition $S_z = 0$ confirms the unpolarized configuration, confirming the unpolarized SSW phase. The vanishing S_x results from the wavefunctions ψ_{+1}, and ψ_{-1} being equal in magnitude but opposite in sign. In

Fig. 3.2(b1), we explore $\Omega = 1.0$ while varying the SO coupling. Notably, for finite Ω, spin flip effects appear in the SDV, for better understanding compare the spin densities in Figs. 3.1(c1) and (g1). For $k_L = 0.0$, S_x exhibits single peak and and $S_z = 0$, indicating a complete overlap between the densities $\rho_{\pm 1}$, characteristics of the ZM phase. Upon k_L is increased to 1.0 and then 1.5 [Figs. 3.2(b2), and (b3)], the single peak structure in S_x persists and the amplitude of S_z increases within the ranges $[-0.1, 0.1]$ and $[-0.16, 0.16]$, respectively, confirming the EZM I phase. For $k_L = 3.0$ [Fig. 3.2(b4)], S_x develops a multi-peak structure, while, S_z displays oscillation, confirming the polarized SW phase. We note that S_y is identically zero throughout. The GPE solutions can be chosen real, and Σ_y is purely imaginary, the expectation value $S_y = \psi^\dagger \Sigma_y \psi$ is negligibly small.

3.3.1.2 Effect of SO coupling and Rabi coupling on the miscibility and ground state phase transformation

Here, we examine the miscibility of the condensate and ground state phase transformation using the root mean square size of the condensate. Initially to characterize the overlap between ρ_{+1} and ρ_{-1}, we define η_{np} as given in Eq.(3.3a). We also define η, which calculates the total overlap between the densities ρ_{+1}, ρ_0, and ρ_{-1} given in Eq.(3.3b). The total overlap between the components is characterized as the miscibility of the condensate. If $\eta \approx 1$, the condensate is miscible, and if $\eta \approx 0$, it is immiscible; otherwise, it is partially miscible [118]. The miscibility parameter η quantifies how strongly the three spin components overlap in space. Across the phase diagram, it helps track how interactions and SO coupling redistribute density among components. In the ZM phase, the components largely overlap in real space, giving $\eta \approx 1$. When the system enters the SW or SSW regimes, interference induces density modulations and the local overlap decreases, leading to partially miscible states. In both SW and SSW phases, η settles at an intermediate value because the components still overlap significantly. Thus, η is a useful indicator of the onset of interference–driven structure, although it does not sharply distinguish between SW and SSW states.

In Fig. 3.3(a i), we report η_{np} upon simultaneously varying k_L and Ω. Upon varying k_L, keeping Ω at some finite value. Initially, we obtain $\eta_{np} \approx 1.0$, representing the maximum overlap between densities $\rho_{\pm 1}$ corresponding to the ZM phase reported in the first column of Fig. 3.1. For intermediate values of k_L, the value of the overlap parameter η_{np} decreases and reaches $\eta_{np} \approx 0.586$ at $\Omega = 0.5$, and $k_L = 1.50$, due to the separation between densities ρ_{+1} and ρ_{-1}, characteristic of the EZM I phase.

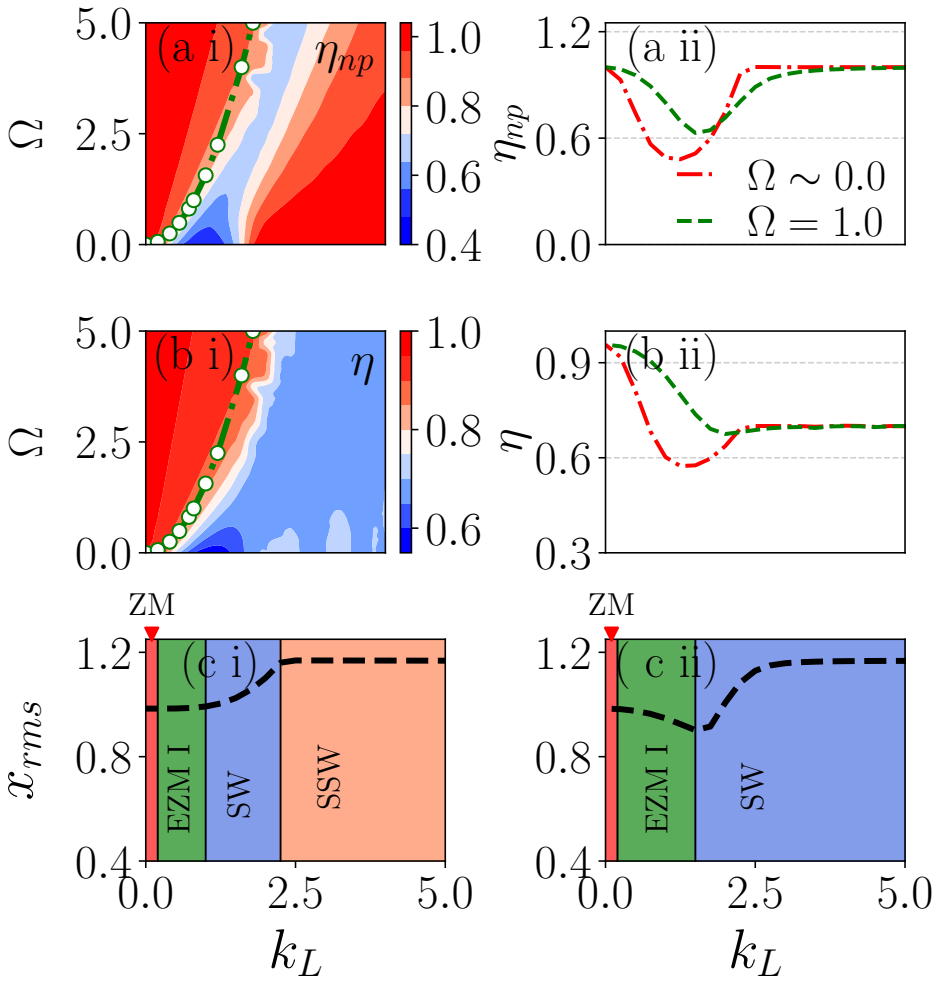


Figure 3.3: Miscibility parameters (a) η_{np} and (b) η for interaction strengths $c_0 = 10$ and $c_2 = -5.0$. The top rows of (a) and (b) show pseudo color representation of η_{np} and η as a function of k_L in the range [0,5] and Ω varies from small but finite values up to 5. The green line with white dots marks the critical relation $k_L^2 \approx \Omega$, beyond which both η_{np} and η begin to decrease. η_{np} shows decreasing trend for intermediate values of k_L and then rises again. (a ii) and (b ii) show the η_{np} and η as a function of k_L for $\Omega \sim 0.0$ (dashed-dotted red line), and 1.0 (dashed green line). Panels (c i) and (c ii) show the root mean square size ($x_{\rm rms}$) as a function of k_L for $\Omega \sim 0.0$ and $\Omega = 1.0$, respectively. Background color shading indicates distinct quantum phases: red (ZM), green (EZM I), blue (SW), and coral (SSW).

Further increasing k_L leads to a transition from the EZM I phase to the SW phase, accompanied by an increasing trend in η_{np}, which reaches approximately $\eta = 0.999$. For $\Omega \sim 0$ and $k_L > 2.5$, we observe the maximum overlap between densities ρ_{+1} and ρ_{-1} components, resulting in an unpolarized SW phase (SSW phase), which is given in Fig. 3.1(a4). For a better description of the overlap between the $m_F = \pm 1$ components of the condensate in Fig. 3.3(a ii), we report the variation of η_{np} for two different Rabi coupling strengths $\Omega \sim 0.0$ and 1.0. Considering $\Omega \sim 0.0$, at $k_L = 0.0$, we observe $\eta_{np} \approx 1.0$ which is the maximum overlap between densities ρ_{+1} and ρ_{-1} components.

TH-4102_206121026

Upon increasing the k_L, η_{np} starts decreasing, gets a minimum at $k_L \approx 1.25$. After this point, it starts to increase and gets the maximum overlap ($\eta_{np} = 1.0$) at $k_L \approx 2.5$. For $\Omega = 1.0$, η_{np} depicts the same behavior; however, the minimum shifts upward. At $k_L = 2.5$, it reaches $\eta_{np} \approx 0.889$, and for higher k_L, it approaches saturation with magnitude approximately equal to 0.999.

Next, in Fig. 3.3(b i), we report the variation of the total miscibility parameter η, which varies in the range 0.58 to 0.96. The miscibility parameter gains the maximum amplitude $\eta \approx 0.96$ in the ZM phase. As k_L increases, the strength of the miscibility parameter decreases, approaching a minimum value of $\eta \approx 0.58$ (in other phases, likely the EZM I phase, the SW phase, and the SSW phase). The lowest values of both overlap parameters are observed for $\Omega \sim 0$, and $k_L \approx 1.25$. To understand miscibility of the condensate in a better way, in Fig. 3.3(b ii), we show the variation of the miscibility parameter η with k_L for two different Rabi coupling strengths $\Omega \sim 0.0$, and 1.0. Considering $\Omega \sim 0.0$, $k_L = 0.0$, we obtain maximum overlap among the components ($\eta = 0.96$). Upon increasing k_L, the magnitude of the miscibility parameter decreases to $\eta = 0.58$ at $k_L \approx 1.30$. After this, it starts increasing and saturates at $k_L \approx 2.50$ with $\eta = 0.70$. We also calculate η for $\Omega = 1.0$, which shows similar trends with increasing k_L; however, the minimum of η shifts upward. The overlap parameter η_{np} and miscibility order parameter η begin to decrease $k_L^2 \approx \Omega$, which separates the ZM phase from other phases. However, η_{np} decreases only for the intermediate values of k_L and rises again to reach the near-maximum value. Both parameters (η_{np} and η) show a minimum amplitude at $\Omega \sim 0$ and k_L in the range [0.7, 2.0].

In Figs. 3.3(c i), and (c ii), we analyze the x_{rms} size of the condensate for Rabi coupling strengths $\Omega \sim 0$, and 1, respectively upon varying the k_L in the range [0, 5]. At first, in Fig. 3.3(c i), we consider $\Omega \sim 0.0$. For small $k_L \lesssim 0.20$, we obtain $x_{rms} = 0.984$, and the condensate is in the ZM phase. The x_{rms} remains flat up to $k_L \approx 1.0$ due to no significant change in density profile except separation between the $m_F = \pm 1$ components, which corresponds to the EZM I phase. Beyond $k_L > 1.0$, x_{rms} starts to increase due to the density modulation across all components, indicating a transition from the EZM I phase to the SW phase. The x_{rms} reaches a maximum value of 1.169 at $k_L = 2.50$ and then saturates, indicating the transition to the SSW phase with significant density modulations. Next, in Fig. 3.3(c ii), we consider $\Omega = 1.0$. For small $k_L \approx 0.20$, we obtain $x_{rms} = 0.982$, representing the ZM phase. Upon increasing k_L, the x_{rms} size starts decreasing and forms a minimum $x_{rms} = 0.902$ at $k_L = 1.50$; in this range of k_L condensate lies in the EZM I phase, where the condensate experiences an interplay between SO and Rabi couplings, where the wavefunction is compressed

under the condition $\Omega = k_L^2$ [118]. Further increase in the k_L for the SW phase, x_{rms} attains the saturation, reaching $x_{rms} = 1.164$ at $k_L = 3.50$. For $\Omega \sim 0$, at high k_L, the SSW phase dominates, while for finite Rabi coupling, the SW phase dominates. Overall, the evolution of x_{rms} reflects the size of the condensate upon the change in the quantum phases. Once the system begins to populate in counter-propagating modes (SW/SSW), the spatial profile broadens, where the interference between the opposite modes produces a modulated envelope, which further increases the spatial extent. Consequently, the rise of x_{rms} provides a clear indicator of the transition from the zero–momentum regime into density-modulated phases.

3.3.2 Ground state phases and spin texture for antiferromagnetic interactions

So far, we have explored different types of ground-state phases arising from the ferromagnetic interaction in SO coupled spin-1 BECs. In this section, we extend the analysis to different ground-state phases with antiferromagnetic interactions. Specifically, we consider the case of vanishing magnetization and characterize the phases using the SDV polarization, miscibility, and the root mean square size.

3.3.2.1 Different ground state phases

We begin our discussion by demonstrating the different ground-state phases that arise under antiferromagnetic interactions, with $c_0 = 10$ and $c_2 = 5$. Here, we vary the SO coupling row-wise and the Rabi coupling across columns.

We first consider zero SO coupling and very weak Rabi coupling ($\Omega \sim 0$). Fig. 3.4(a1) shows the condensate in the zero-momentum (ZM) polar phase, where all atoms occupy the ρ_0 component. Consequently, the densities ρ_{+1} and ρ_{-1} vanish identically. It indicates that in the absence of SO coupling and very weak Rabi coupling, the antiferromagnetic spinor BECs behaves like a scalar BEC instead of vector one. Upon increasing $k_L = 0.0 \rightarrow 0.5$ [Fig.3.4(a2)], the densities ρ_{+1} and ρ_{-1} begin to emerge with finite magnitude, while remaining fully spatially overlapping. These components peak away from the trap center at $x = \pm 1.60$, with amplitude $\rho_{\pm 1}(\text{max}) = 0.042$, and the ρ_0 is 7 times higher than $\rho_{\pm 1}$. The behavior remains spatially symmetric, indicating a redistribution of population into the $m_F = \pm 1$ components. In momentum space, the $m_F = \pm 1$ components develop peaks at finite k, whereas the ρ_0 component remains centered at $k = 0$ (not shown here). These features, symmetric off-center density peaks

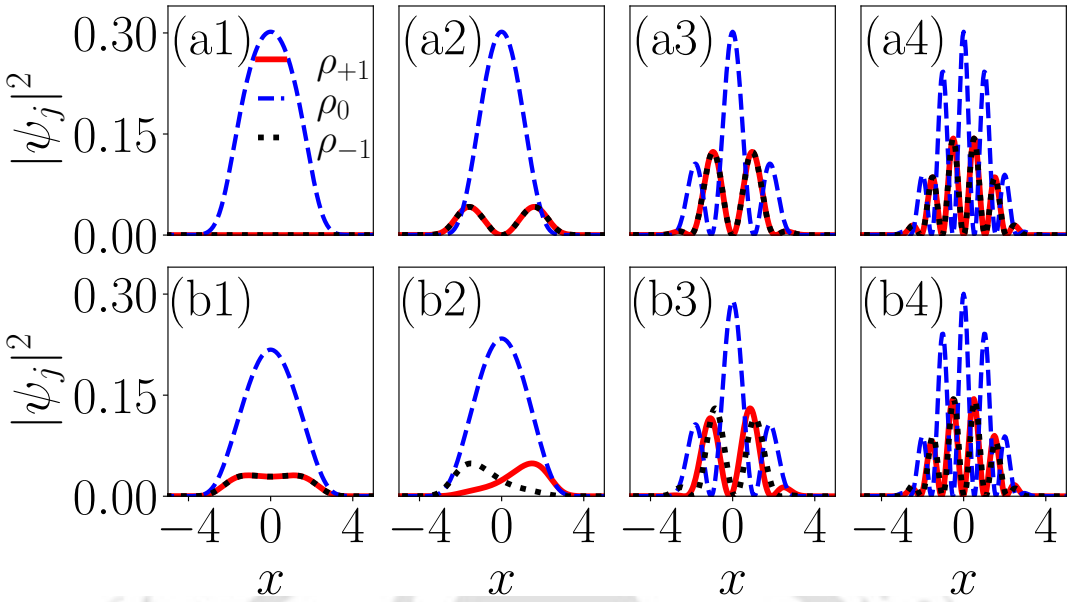


Figure 3.4: Different ground state phases of the SO coupled spin-1 BECs with antiferromagnetic interaction. Ground state density profile of the spin-component $|\psi_{+1}|^2$ (solid red line), $|\psi_0|^2$ (dashed blue line), and $|\psi_{-1}|^2$ (dotted black line) for (a1-a4) $\Omega \sim 0.0$ and (b1-b4) $\Omega = 1.0$, with interaction strengths $c_0 = 10$ and $c_2 = 5$. In each panel, k_L varies from left to right: 0.0, 0.5, 1.5, and 3.0. For $\Omega \sim 0$, the ZM phase, EZM II phase, and SSW phase are observed. For finite Ω, the SSW phase disappears, giving rise to the appearance of EZM I and SW phases.

in real space, overlapping $m_F = \pm 1$ components, and the absence of visible density modulation, are characteristic of the elongated zero-momentum phase of the second type (EZM II). Increasing $k_L = 0.5 \rightarrow 1.5$ leads to a multipeak density profile, indicative of an unpolarized SW or SSW phase, since the densities ρ_{+1} and ρ_{-1} remain fully overlapping [Fig.3.4(a3)]. Further increasing the SO coupling to $k_L = 3.0$ results in the same SSW phase, although with an increased number of stripes [Fig.3.4(a4)].

We now vary the Rabi coupling in the respective columns. Considering $\Omega = 1.0$ and $k_L = 0.0$, the condensate remains in the ZM phase, with finite and fully overlapping ρ_{+1} and ρ_{-1} densities [Fig.3.4(b1)]. The introduction of either SO or Rabi coupling induces the revival of the densities $\rho_{\pm 1}$ in $m_F = \pm 1$ manifolds under antiferromagnetic interactions. It indicates that either one of the couplings present in the system, then it behaves like a spinor/vector BECs [Figs.3.4(a2) and (b1)]. Upon increasing $k_L = 0.0 \rightarrow 0.5$ in Fig.3.4(b2), we obtain the EZM I phase with a single-peak density profile across all components. The $m_F = \pm 1$ components are centered away from the trap center at $x = \pm 1.50$, respectively, with $\rho_{\pm 1}(\text{max}) = 0.049$. The SW phase emerges as k_L is increased to 1.5 [Fig.3.4(b3)], and remains present at $k_L = 3.0$ with an enhanced number of stripes [Fig.3.4(b4)]. The polarization behavior between the $m_F = \pm 1$ components will become clearer in the subsequent discussion on spin-density vectors.

In the absence of SO coupling and very weak Rabi coupling, all atoms reside in the ψ_0 component. The introduction of SO coupling facilitates the revival of the $m_F = \pm 1$ components, enabling the formation of spin textures. As calculated in the ferromagnetic case, we also compute the momentum distribution to verify the phase identity. We observe a single peak in the momentum distribution centered at $k = 0$, corresponding to the ZM phase. In contrast, the EZM I and EZM II phases show momentum-space peaks for the $m_F = 0$ and $m_F = \pm 1$ components, respectively at $k \neq 0$, while the $\psi_{\pm 1}$ and ψ_0 components, respectively, remains centered at $k = 0$; the SW and SSW phases exhibit multi-peak momentum distributions across all components (not shown here). Similar to the ferromagnetic interactions, the SSW phase appears only for $\Omega \sim 0$. However, in contrast to the ferromagnetic case, we find that under antiferromagnetic interactions, only the ZM, EZM II, and SSW phases emerge at $\Omega \sim 0$.

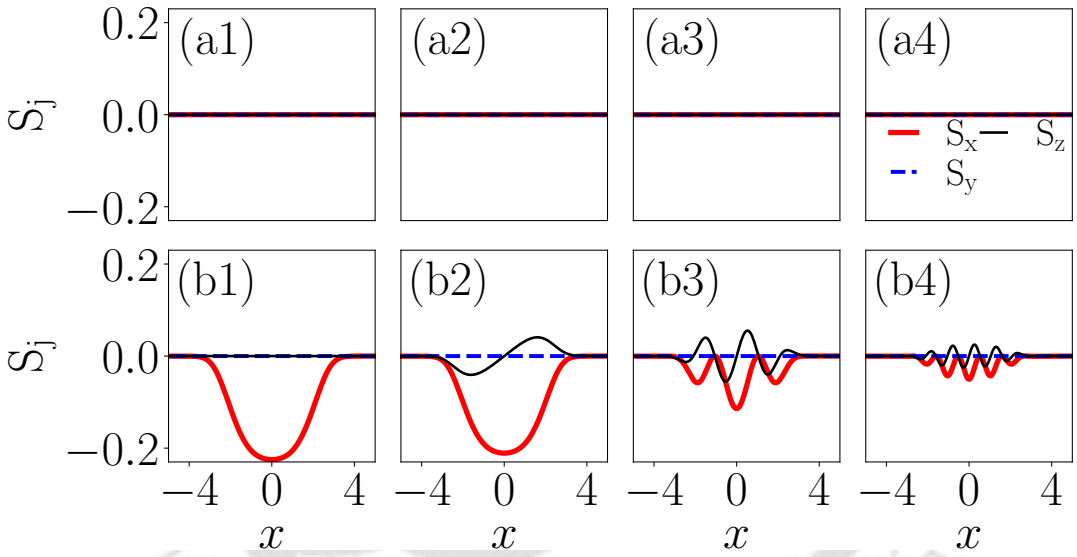


Figure 3.5: SDV component S_x, S_y, and S_z in panels (a), and (b) corresponding to the Fig. 3.4. The lines representation is the same as in Fig. 3.2. Almost zero of S_y across all phases and a single peak S_x with zero (finite) S_z, confirms the ZM (EZM I) phase for finite Ω. All SDVs remain zero in the ZM polar phase, EZM II phase, and SSW phase for $\Omega \sim 0$. Multi-peak S_x along with oscillating S_z confirms the SW phase.

In Fig. 3.5, we report the SDV polarization corresponding to the density profile shown in Fig. 3.4. Initially, in Fig. 3.5(a1), we consider $\Omega \sim 0.0$, and $k_L = 0.0$. In this case, all atoms occupy state ρ_0, and densities ρ_{+1} and ρ_{-1} vanish, which leads to S_x, S_y, and S_z to be zero and the condensate remains in the ZM polar phase since the momentum distribution shows only a single peak, peaked at zero (not shown here). Therefore, in the case of antiferromagnetic interaction, the ZM phase with $\Omega \sim 0.0$ differs from the ferromagnetic interactions, where a single peak S_x was obtained. Upon increasing

TH-4102_206121026

$k_L = 0.0 \rightarrow 0.5$ in Fig. 3.5(a2), we again find all SDVs to be zero. The momentum space density shows only a single peak centered at zero for the zeroth component, and $m_F = \pm 1$ components exhibit peaks at $k \neq 0$ (not shown here), indicating the EZM II phase. For a higher SO coupling strength $k_L = 1.5$ in Fig. 3.5(a3), we observe that all SDVs are zero with a multipeak density profile [see Fig. 3.4(a3)], confirming the presence of the unpolarized SW phase or SSW phase. This observation also holds for $k_L = 3.0$, as shown in Fig. 3.5(a4). The vanishing behavior of all phases SDVs for $\Omega \sim 0$, observed in the case of antiferromagnetic interactions, is due to the intrinsic unpolarized nature refer Eq. (3.6).

Next, in Fig. 3.5(b1), we consider $\Omega = 1.0$ and $k_L = 0.0$, in which S_x shows a single peak structure, confirming the presence of the ZM phase. Upon increasing $k_L = 0.0 \rightarrow 0.5$, we obtain a single peak S_x and non-zero S_z, which is a signature of the EZM I phase [see Fig. 3.5(b2)]. The non-zero value of S_z suggests the separation between the density of $m_F = \pm 1$ components of the condensates. Increasing $k_L = 0.5 \rightarrow 1.5$ in Fig. 3.5(b3), we obtain a multi-peak structure in S_x, and S_z, confirming the SW phase, where S_z lies between -0.055 to 0.055. For $k_L = 3.0$, we also obtain similar behavior of S_x, and S_z, leading to the SW phase; however, the magnitude of both SDVs are less than the previous case [see Fig. 3.5(b4)]. Similar to the ferromagnetic interactions, here also, spin flip occurs for finite Ω. Note that as the GPE solutions are real and Σ_y is purely imaginary, $S_y = \psi^\dagger \Sigma_y \psi$ remains identically zero. For $\Omega \sim 0$, we obtain SDVs: S_x, S_y, and S_z are zero, for all phases, which differs from the case of ferromagnetic interactions.

3.3.2.2 Effect of SO and Rabi coupling on miscibility and ground state phase transformation

Similar to ferromagnetic interactions, we report η_{np} defined in Eq.(3.3a), to characterize overlap between densities ρ_{+1}, and ρ_{-1}. In addition, we report the miscibility parameter η defined in Eq.(3.3b), which quantifies the overlap between densities ρ_{+1}, ρ_0, and ρ_{-1}.

In Fig. 3.6(a i), we show η_{np} upon varying k_L in the range $[0, 5]$, Ω from small values up to 5 and keeping $c_0 = 10.0$, and $c_2 = 5.0$. Initially, for $\Omega \sim 0$, and $k_L \sim 0$, the $\eta_{np} \sim 0$, which occurs due to the absence of densities of ρ_{+1} and ρ_{-1}, as all atoms occupy the ρ_0 state. Upon considering the finite Rabi coupling ($\Omega > 0.5$) and gradually increase k_L we find that the $\eta_{np} \approx 1.0$, which indicates a complete overlap between densities ρ_{+1}, and ρ_{-1} and condensate resides in the ZM phase. For the intermediate

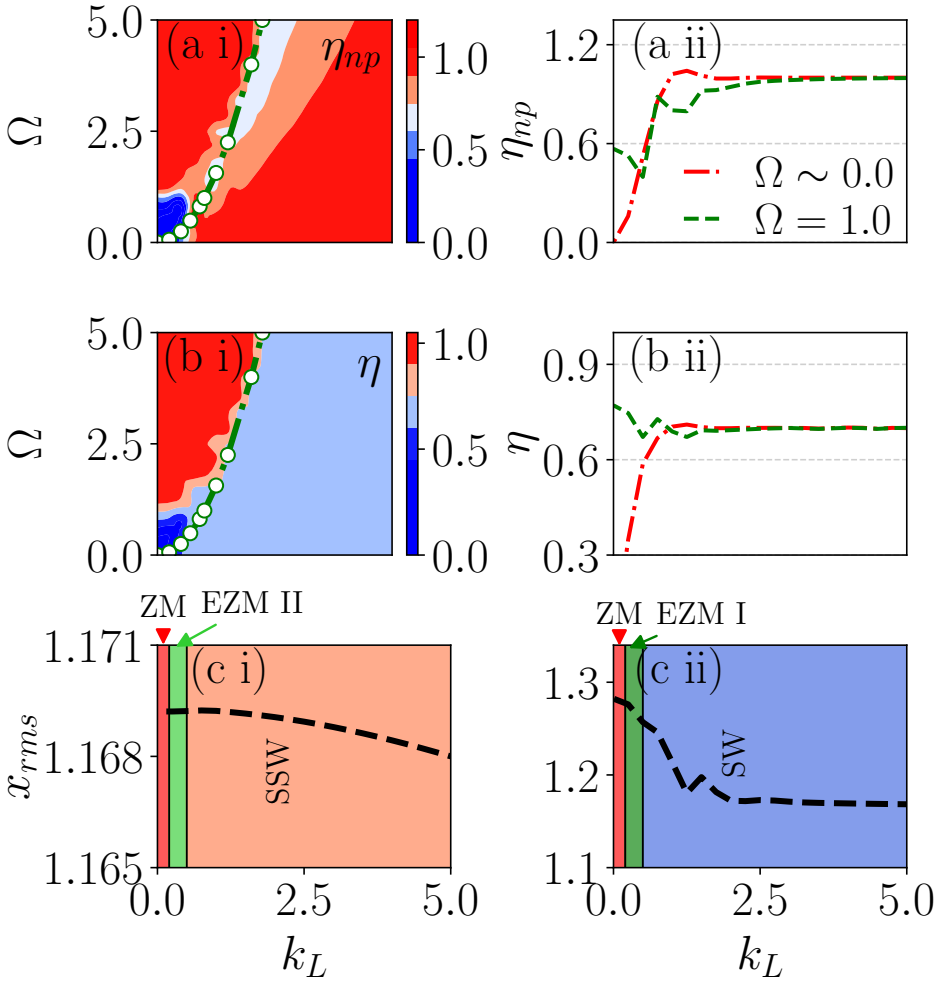


Figure 3.6: Miscibility parameters (a) η_{np} and (b) η for interaction strengths $c_0 = 10$ and $c_2 = 5.0$. (a i) and (b i) show η_{np} and η as functions of spin-orbit coupling strength k_L in the range $[0, 5]$ and Rabi coupling varies from small but finite values up to 5. The green line with white dots marks the critical relation $k_L^2 \approx \Omega$. Beyond this boundary ($k_L^2 > \Omega$), both η_{np} and η decrease. However, η_{np} exhibits a non-monotonic behavior—decreasing initially and rising again to near-maximum values. (a ii) and (b ii) display η_{np} and η as functions of k_L for fixed $\Omega \sim 0.0$ (dash-dotted red line) and $\Omega = 1.0$ (dashed green line). Panels (c i) and (c ii) show the root-mean-square condensate size $x_{\rm rms}$ versus k_L for $\Omega \sim 0.0$ and $\Omega = 1.0$, respectively. The background color represents distinct quantum phases: red (ZM), green (EZM I), limegreen (EZM II), blue (SW), and coral (SSW).

range of k_L, η_{np} decreases to 0.40 for $\Omega = 1.0$ and $k_L = 0.5$, which shows the separation between densities ρ_{+1} and ρ_{-1} a typical characteristics of the EZM I phase. Upon further increasing of k_L, η_{np} further increases and reaches as $\eta_{np} \approx 0.982$, which is the polarized SW phase. For a better description of the overlap between $m_F = \pm 1$ components of the condensate, in Fig. 3.6(a ii), we report variation in η_{np} for two different Rabi coupling strengths $\Omega \sim 0.0$, and 1.0. Initially considering $\Omega \sim 0.0$, and $k_L = 0.0$, where we observe that $\eta_{np} \approx 0$; increasing k_L leads to the higher magnitude, and satu-

TH-4102_206121026

rates further at $\eta_{np} \approx 1.0$. Upon increasing the Rabi coupling to $\Omega = 1.0$ while keeping $k_L = 0.0$, we find the revival of the densities of the ρ_{+1} and ρ_{-1} components which reflects in η_{np} showing a finite magnitude $\eta_{np} \approx 0.568$. Upon increasing k_L, the η_{np} initially decreases to $\eta_{np} \approx 0.40$ at $k_L = 0.5$ which increases upon increasing the SO coupling to $k_L = 0.75$ which yields $\eta_{np} \approx 0.885$. Further increasing k_L, another minimum occurs at $k_L = 1.25$ with $\eta \approx 0.796$. Beyond this point, it increases and saturates at $\eta_{np} \approx 0.999$.

To better characterize the different phases in Fig. 3.6(b i), we show the miscibility η upon simultaneously varying Ω, and k_L. Initially at $k_L = 0$, and $\Omega \sim 0$, $\eta \sim 0$, due to the absence of $m_F = \pm 1$ components. While considering finite $\Omega > 0.5$ and increasing k_L gradually, we find the maximum value of $\eta \approx 0.96$ in the ZM phase, which starts to decrease upon increasing k_L and attains $\eta \approx 0.70$ in the EZM I, EZM II, SW, and SSW phases. For a detailed understanding of miscibility η, in Fig. 3.6(b ii), we also show the variation of η upon varying k_L in the range [0,5] for two different $\Omega \sim 0.0$ and 1.0. For $\Omega \sim 0.0$, and $k_L = 0.0$, as all atoms occupy the state ψ_0, η appears to be zero. Upon increasing k_L, it starts to increase and reaches $\eta \approx 0.70$, which eventually gets saturated. Next, we consider $\Omega = 1.0$, and $k_L = 0.0$. Initially, upon increasing k_L, η starts from a higher magnitude $\eta \approx 0.772$, further increasing k_L, reduces its magnitude and forms a minimum at $k_L = 0.50$ with magnitude $\eta \approx 0.68$. Increasing k_L beyond this point, η reaches to $\eta \approx 0.70$ and saturates.

Similar to ferromagnetic interactions, here we also obtain η_{np} decreases beyond the $k_L^2 \approx \Omega$, in the $k_L - \Omega$ plane; however, the η_{np} show decreasing behaviour only for medium range of k_L, and rises again. For higher k_L, we obtain a value closer to the maximum of η_{np}, which arises from the increase of overlap between condensate components. The miscibility parameter η is maximum for the region $k_L^2 < \Omega$ (ZM phase), and decreases in the $k_L^2 > \Omega$ region (EZM I phase, EZM II phase, SW phase, and SSW phase). However, for small values of k_L, and Ω, we obtain minimum of η_{np}, and η in the $k_L^2 < \Omega$ region (ZM phase).

Next, in Fig. 3.6(c i) and (c ii), we report the x_{rms} size of the condensate for $\Omega \sim 0.0$ and 1.0 while varying k_L in [0, 5]. For $\Omega \sim 0.0$ and $k_L = 0.0$, we obtain $x_{\text{rms}} \approx 1.169$, and the condensate remains in the ZM phase. This value stays nearly constant up to $k_L \lesssim 0.70$, where the system occupies the EZM II phase. As k_L increases further, weak density modulation causes a slight reduction in x_{rms}, with a total change of about 4×10^{-3}, and the condensate enters the unpolarized stripe phase (SSW), as shown in Fig. 3.6(c i). For finite Rabi coupling [Fig. 3.6(c ii)], we obtain $x_{\text{rms}} \approx 1.282$ at $k_L = 0.0$, which remains flat up to $k_L \lesssim 0.20$ in the ZM phase. As k_L increases, x_{rms} again de-

creases slightly only about 1.2×10^{-2}. In this regime, the Rabi coupling transforms EZM II into EZM I and the SSW phase into the SW phase. For antiferromagnetic interactions, the onset of stripe phases shifts density toward the trap center, which reduces x_{rms}. Despite this opposite trend compared with the ferromagnetic case, the evolution of x_{rms} still reliably signals changes in the underlying momentum configuration and the emergence of density modulation.

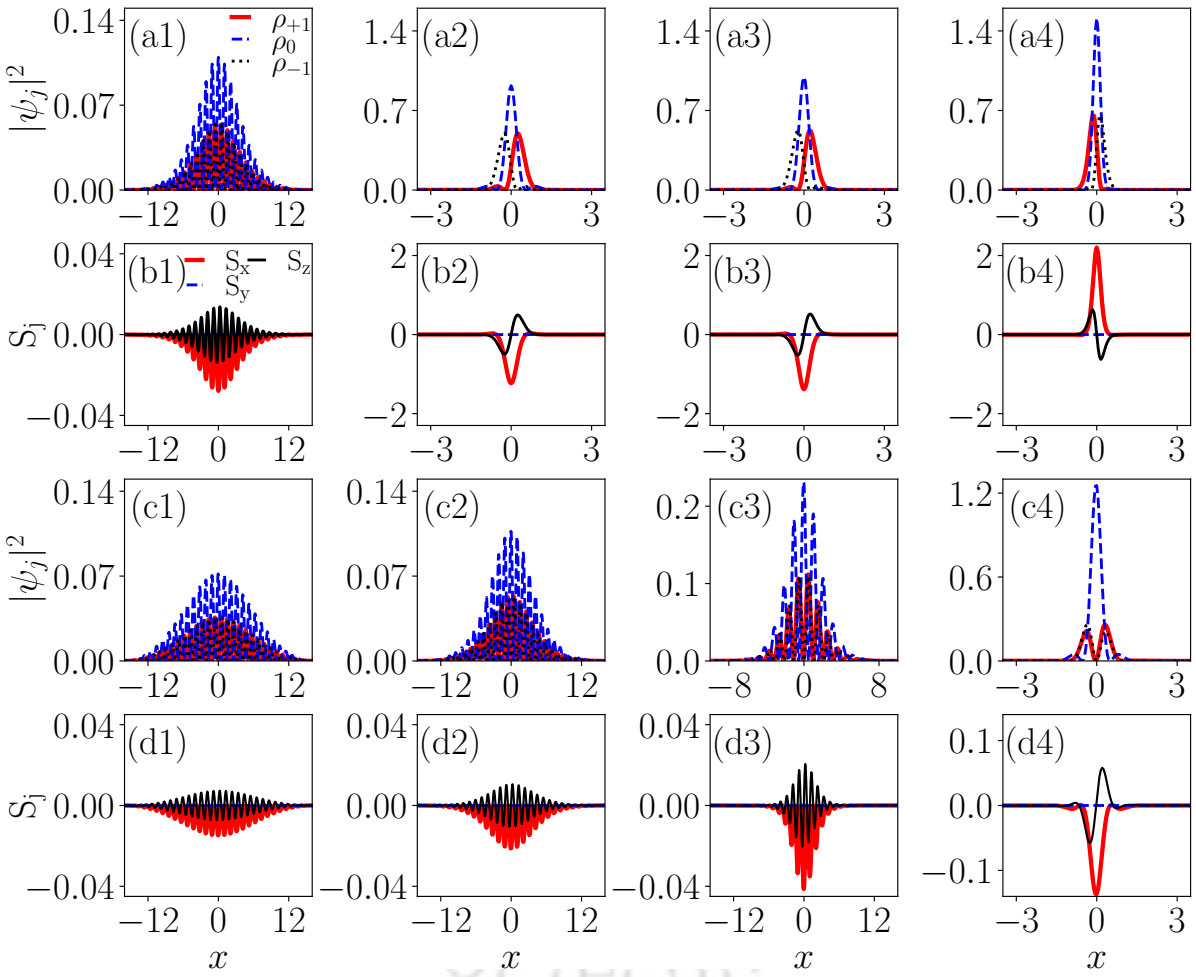


Figure 3.7: Ground state density profiles of $|\psi_{+1}|^2$ (solid red line), $|\psi_0|^2$ (dashed blue line), and $|\psi_{-1}|^2$ (dotted black line) in panels (a) and (c), and corresponding spin-density vector components S_x (solid red line), S_y (dashed blue line), and S_z (thin black line) in panels (b) and (d), for $k_L = 3.0$ and $\Omega = 1.0$. Panels (a, b) correspond to $c_2 = -5.0$, and panels (c, d) to $c_2 = 5.0$. In each case, the density-density interaction c_0 varies as -0.25, -0.50, -1.0, and -5.0 from left to right. The appearance of multipeak structures in S_x and oscillations in S_z indicates the SW phase, while a single peak in S_x with finite S_z signifies the EZM I phase. A transition from the SW to EZM I phase occurs with increasing $|c_0|$, for both $c_2 < 0$ and $c_2 > 0$. As $c_0 < 0$ in all cases, no external trapping potential is applied.

TH-4102_206121026

3.3.3 Effect of spin-independent (c_0) and spin-exchange (c_2) interactions on the ground state phases

In the above parts of the study, we have reported different ground state phases (ZM phase, EZM I phase, EZM II phase, SW phase, and SSW phase), their miscibility, and the transformation induced by varying SO and Rabi coupling strengths in ferromagnetic and antiferromagnetic condensates. Here, we fix the SO and Rabi coupling strength corresponding to (i) ZM phase, (ii) SW phase, and (iii) SSW phase, and vary the interaction parameters; density-density interaction (c_0) and spin-exchange interaction (c_2) to analyze miscibility and phase transitions. The EZM phases are excluded from the analysis, as it is a trivial extension of the ZM phase. We begin our discussion with the ZM phase.

3.3.3.1 Impact on the ZM phase

In this section, we focus on the ZM phase with $\Omega = 1.0$ in the absence of SO coupling strength ($k_L = 0$), as illustrated in Figs. 3.1(e1) and 3.4(b1). We consider two values of the spin-dependent interaction strength $c_2 = -5.0,\ 5.0$, while varying c_0 in the range [-5,5]. For attractive density-density interactions ($c_0 < 0$), the condensate naturally localizes due to self-attraction, forming a self-bound state without the need for an external trapping potential. In contrast, when $c_0 > 0$, the condensate is not naturally localized and requires an external trap for confinement [77, 108].

$$\lambda = \begin{cases} 0 & \text{for } c_0 < 0\,, \\ 1 & \text{for } c_0 \gtrsim 0\,. \end{cases} \tag{3.7}$$

Based on this, we organize the discussion into two parts: (i) without external trapping, and (ii) with a trap potential of strength ($\lambda = 1.0$). Considering the case without a trap and with $c_0 < 0$, we observe that the condensate remains in the ZM phase for both $c_2 = -5.0$ and $c_2 = 5.0$, exhibiting a single peak density profile across all components. Upon increasing the magnitude of c_0, the condensate shrinks spatially, and its amplitude increases significantly (not shown here) [77]. This behaviour is consistent regardless of whether the $c_2 < 0$ or $c_2 > 0$.

Importantly, within the ZM phase, varying c_0 and c_2 does not lead to a phase transition. However, varying c_0 can significantly affect the condensate's spatial extent and amplitude [77]. For repulsive interactions ($c_0 \gtrsim 0$), the nature of the ground state has already been discussed in Sec. 3.3.1 and 3.3.2, corresponding to $c_2 < 0$ and $c_2 > 0$ regimes, respectively.

3.3.3.2 Impact on the SW phase

In this section, we present the effect of the variation of c_0 and c_2 on the ground state (SW phase), keeping $k_L = 3.0$, and $\Omega = 1.0$. We consider $c_2 < 0$ (ferromagnetic) and $c_2 > 0$ (antiferromagnetic), and varies c_0 in the range [-5,5].

Different ground state phases: We consider $k_L = 3.0$, and $\Omega = 1.0$, which belong to the SW phase as shown in Figs. 3.1(h1) and 3.4(b4), and vary the interaction strengths c_0, and c_2. Initially, considering $c_2 = -5.0$ (ferromagnetic) and $c_0 = -0.25$ in Fig. 3.7(a1), we obtain the SW phase with 24 maxima and minima in the density profile, which extends over a large spatial region. The corresponding SDV polarization in Fig. 3.7(b1) exhibits a multi-peak structure in S_x, and S_z shows a variation of amplitude with maximum range -0.014 to 0.014, which confirms the SW phase. Next, increasing the attractive density-density interaction $c_0 = -0.50$ in Fig. 3.7(a2), we obtain a single peak structure across all components, among them the densities ρ_{+1} and ρ_{-1} peaks away from the trap center at $x = 0.20$ and $x = -0.20$, respectively, with $\rho_{\pm1}(max) = 0.52$, resulting in an elongated zero-momentum phase of first type (EZM I phase). The corresponding SDV polarization in Fig. 3.7(b2) shows a single peak structure in S_x and finite S_z, validating the EZM I phase of the condensate, which supports a phase transition from the SW phase to the EZM I phase. The SW phase transitions to the EZM I phase at $c_0(SW \rightarrow EZM\ I) = -0.50$. Further, increasing the attractive strength of c_0, we observe similar trends in the density profile, as well as in the corresponding SDVs: S_x, and S_z in Figs. 3.7(a3, b3), and (a4, b4); therefore, the condensate remains in the EZM I phase. However a spin flip occurs in SDVs (S_x, and S_z) in Figs. 3.7(b4). While comparing Figs. 3.7(a3, a4) density profiles we notice that the spins $\rho_{\pm1}$ get interchanged. In general, at $c_0 = -3.25$, the system flips for the first time and continues oscillating back and forth up to $c_0 = -4.75$. Beyond this point, the spin components remain flipped at $c_0 = -5.0$.

Next, considering $c_2 = 5.0$ (antiferromagnetic) and $c_0 = -0.25$ in Fig. 3.7(c1), we obtain a multi-peak structure in the density profile with 24 maxima and minima, which is the SW phase. Correspondingly, we obtain the multi-peak S_x and finite S_z varies with maximum range -0.021 to 0.021, which is the result of separation between densities ρ_{+1}, and ρ_{-1}, and confirms the SW phase in Fig. 3.7(d1). As the attractive strength of c_0 increases, the number of stripes in the density profile continuously decreases, as shown in Figs. 3.7(c2,c3); however, the condensate remains in the SW phase. We obtain similar features in S_x and S_z in Figs. 3.7(d2,d3) with the reduced number of maxima and min-

ima; however, the magnitude of S_x, and S_z increases, due to the increased amplitude in the SW density profiles. Finally, in Fig. 3.7(c4), we consider a higher attractive strength of $c_0 = -5.0$, where the condensate transitions from the SW wave phase to the EZM I phase. This transition takes place at $c_0(SW \rightarrow EZM\ I) = -3.75$. The corresponding SDVs show that S_x has a single peak and S_z exhibits finite magnitude, which confirms that the condensate is in the EZM I phase. We do not include the discussion of the case $c_0 \gtrsim 0$ since it is given above in Sec. 3.3.1, and Sec. 3.3.2 for $c_2 < 0.0$, and $c_2 > 0.0$, respectively. For attractive interactions $c_0 < 0$ and $c_2 < 0$, a transition from the SW phase to EZM I phases takes place at $c_0(SW \rightarrow EZM\ I) = -0.50$, and for $c_2 > 0$, it takes place at $c_0(SW \rightarrow EZM\ I) = -3.75$. It implies that while increasing attractive $c_0 < 0$ interaction, antiferromagnetic SO coupled BECs sustain the SW phase while ferromagnetic case loose the SW phase too early.

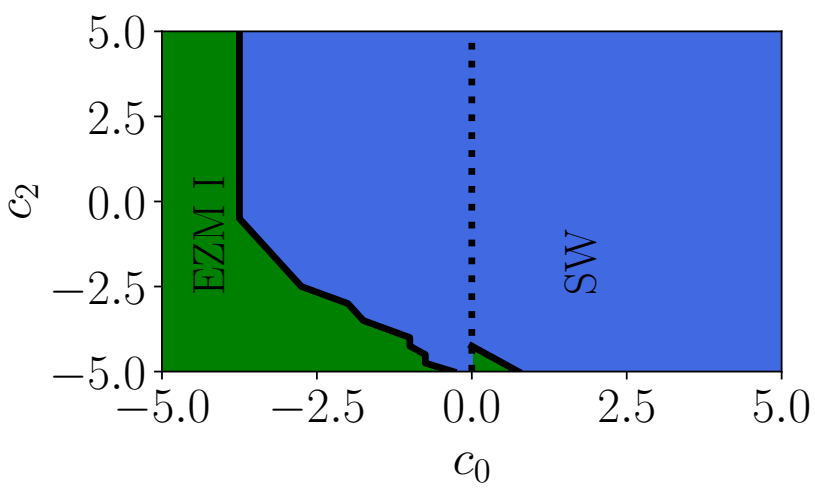


Figure 3.8: Ground state phase diagram in the c_0-c_2 plane for fixed $k_L = 3.0$ and $\Omega = 1.0$. The black dotted line separates the trapless ($c_0 < 0$) and trapped ($c_0 \gtrsim 0$) regimes. Different quantum phases are indicated by color: green denotes the EZM I phase and blue denotes the SW phase. For considered parameter (k_L, Ω) = (3.0, 1.0), the system resides in the SW phase under weak or repulsive interaction strengths, while the higher attractive strength of both c_0 and c_2 drives a transition into the EZM I phase.

In Fig. 3.8, we present the ground state phase diagram as a function of c_0 and c_2, with $k_L = 3.0$ and $\Omega = 1.0$ held fixed. The black dashed line divides the diagram into two regimes: the untrapped region ($c_0 < 0$) and the trapped region ($c_0 \gtrsim 0$), where a harmonic potential confines the condensate. We begin by analyzing the case $c_2 = -5.0$, varying c_0. For strong attractive interaction ($c_0 = -5.0$), the condensate is in the EZM I phase. As c_0 increases, weakening the attraction c_0, a EZM I phase transition to the SW phase occurs beyond $c_0 = -0.50$, which continues throughout the remaining untrapped region ($c_0 < 0$). Entering the trapped regime ($c_0 \gtrsim 0$), the

condensate briefly re-enters the EZM I phase for small repulsive values of c_0, up to $c_0 = 0.75$. Beyond this, the system transitions back to the SW phase.

With increasing c_2, the region occupied by the EZM I phase gradually shrinks in the c_0–c_2 plane. For $c_2 = -0.5$, the EZM I–SW transition shifts at $c_0 = -3.75$, remaining unchanged for larger c_2. For $c_2 = 5.0$, the condensate starts in the EZM I phase at $c_0 = -5.0$ and transitions to the SW phase at $c_0 = -3.75$, remaining in SW phase for higher c_0, including the trapped regime.

Overall, we find that upon changing the interactions can perform a phase transition, which the system holds SW phase for the coupling parameters $(k_L, \Omega) = (3.0, 1.0)$. Ultimately, the interaction $c_0 < 0$ modifies the SW phase into EZM I phase, it indicates that a phase transition is possible upon changing the c_0 interaction.

Miscibility phase diagram $c_0 - c_2$ and ground state phase transformation: In the above parts, we reported ground state density profiles such as the SW and EZM I phases, and the corresponding SDVs specifically for the $c_0 < 0$ case. Here, we report η_{np}, overlap between densities ρ_{+1}, and ρ_{-1} given in Eq.(3.3a) and also report the total miscibility parameter η, which is the overlap among the densities of ρ_{+1}, ρ_0, and ρ_{-1} given in Eq.(3.3b).

Initially, we examine the variation of η_{np} in Fig. 3.9(a i) as both c_0 and c_2 vary simultaneously within the range $[-5, 5]$, while keeping $k_L = 3.0$ and $\Omega = 1.0$ fixed. Here, we followed the previous protocol Eq. (3.7), where the dotted black line divides the phase plot into two regions: (i) the left half, corresponding to the absence of trap strength, and (ii) the right half, where the trap is present.

To clarify how interactions shape the spatial separation of spin components, in Figure 3.9(a ii) we show how the miscibility parameter η_{np} evolves with c_0 for different spin–interaction strengths. For strong attractive interactions ($c_2 = -5.0$), the system begins in a partially demixed EZM I phase. Increasing c_0 enhances density–density repulsion, driving the condensate into the strongly modulated SW phase where $\eta_{np} \approx 1$. In the trapped regime ($c_0 > 0$), confinement temporarily weakens demixing, returning the system to EZM I, before stronger repulsion again restores the SW phase. However, for moderate attraction ($c_2 = -2.5$), the condensate makes a single transition from EZM I to the SW phase, which then persists across the entire c_0 range. Here the spatial modulation remains energetically favorable even in the presence of trapping. On the other hand for repulsive spin interactions ($c_2 = 5.0$), the condensate quickly leaves the EZM I phase and enters into the SW phase as c_0 increases, with η_{np} saturating near unity. This reflects the strong tendency of repulsive spin interactions to enforce com-

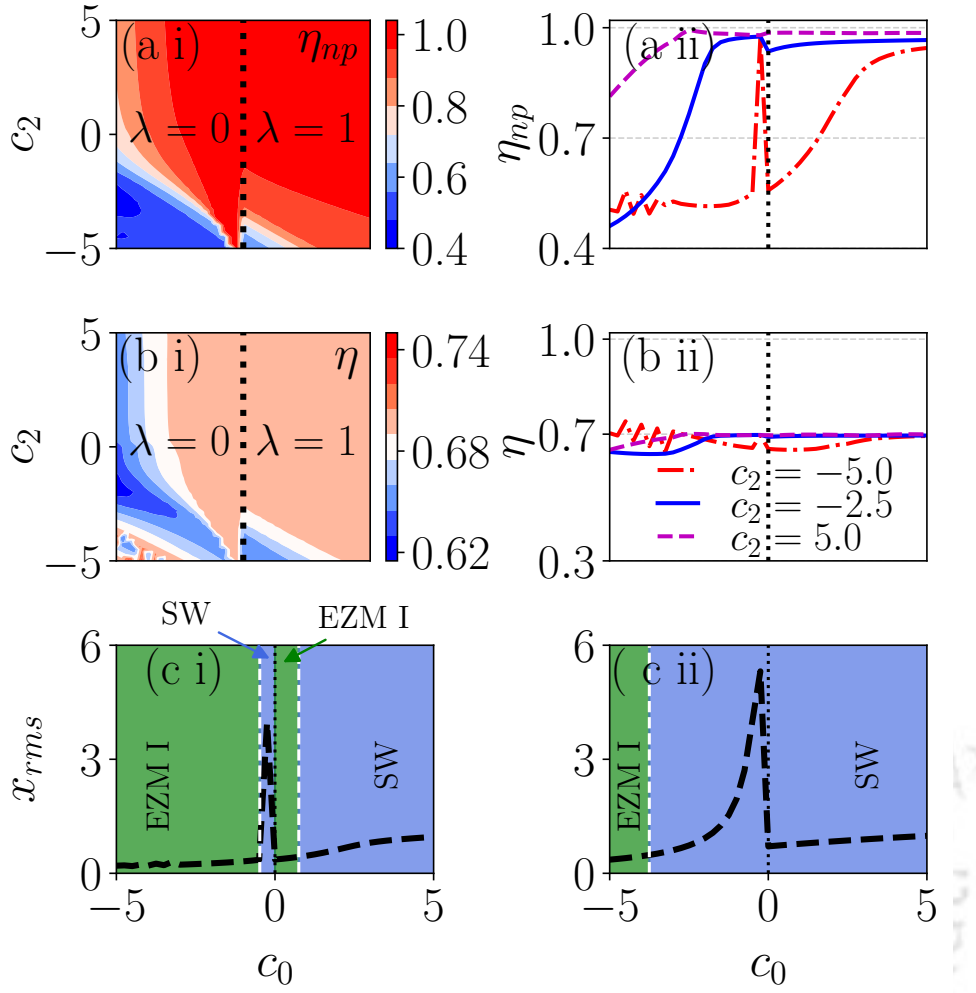


Figure 3.9: Miscibility parameters (a) η_{np} and (b) η as functions of interaction strengths c_0 and c_2, for fixed $k_L = 3.0$ and $\Omega = 1.0$. In (a i), and (b i), both c_0 and c_2 are varied within the range $[-5, 5]$. (a ii), and (b ii) show η_{np} and η as functions of c_0 for fixed values of $c_2 = -5.0$ (dash-dotted red line), -2.5 (solid blue line), and 5.0 (dashed magenta line). Panels (c i) and (c ii) depict the root-mean-square size x_{rms} of the condensate for $c_2 = -5.0$ and $c_2 = 5.0$, respectively, as c_0 is varied. The background color shading represents distinct quantum phases: green indicates the EZM I phase and blue indicates the SW phase, highlighting the phase transition of the condensate. The black dotted line indicates the boundary separating trapped regime ($c_0 \gtrsim 0$) and untrapped regime ($c_0 < 0$) condensates.

ponent separation.

Having established how the non-pairwise miscibility parameter η_{np} reflects the transition between the EZM I and SW phases, we now examine the overall miscibility of the condensate encoded in the total order parameter η. This provides a complementary, global measure of component overlap and helps clarify how interaction-driven phase changes manifest at the full spinor level. In Fig. 3.9(b i), we present the variation of η across the c_0–c_2 plane for fixed $k_L = 3.0$ and $\Omega = 1.0$. To reveal the underlying trends more clearly, Fig. 3.9(b ii) shows representative line cuts for $c_2 = -5.0$, -2.5,

and 5.0 as c_0 is scanned over $[-5, 5]$. For strong attractive spin interactions ($c_2 = -5.0$), the system begins in the EZM I phase with $\eta \simeq 0.703$ at $c_0 = -5.0$. As c_0 increases, the enhanced density–density repulsion suppresses overlap, and the condensate enters the SW phase at $c_0 \approx -0.25$, where η slightly decreases. When $c_0 \gtrsim 0$, the introduction of harmonic confinement modestly increases component overlap, leading to a gentle rise in η that saturates near $\eta \approx 0.694$ at $c_0 = 5.0$.

For moderately attractive spin interactions ($c_2 = -2.5$), the system again starts in the EZM I phase with $\eta \approx 0.643$. Increasing c_0 induces a transition into the SW phase around $c_0 \approx -2.75$, after which η shows only weak variation. Throughout the entire trapped and untrapped regime, the condensate remains in the SW phase, indicating that spatial modulation remains energetically preferred.

In the repulsive case ($c_2 = 5.0$), the condensate initially lies in the EZM I phase with $\eta \approx 0.651$ at $c_0 = -5.0$. Increasing c_0 drives a transition into the SW phase near $c_0 \approx -3.75$, followed by a gradual rise in η that saturates for $c_0 \gtrsim 0$. Here again, the SW phase persists across the entire parameter range once entered.

To further characterize these phase boundaries, we examine the root-mean-square width x_{rms} of the condensate, which provides a direct measure of spatial modulation and thus complements the miscibility analysis. Figures 3.9(c i)–(c ii) show how x_{rms} varies across the (c_0, c_2) parameter space. For strongly attractive spin interactions ($c_2 = -5.0$), the condensate is initially compact, with $x_{rms} \approx 0.201$ at $c_0 = -5.0$, consistent with the localized density profile of the EZM I phase [see Fig. 3.7(a4)]. As c_0 increases and density–density repulsion weakens the confinement, x_{rms} grows gradually but the system remains in the EZM I phase. A sharp increase occurs near $c_0 = -0.25$, where x_{rms} reaches 3.965. This dramatic broadening signals the emergence of strong spatial modulation and marks the transition into the SW phase [Fig. 3.7(a1)]. For $c_0 \gtrsim 0$, the harmonic trap compresses the condensate, reducing x_{rms} to ~ 0.363 and restoring the EZM I phase up to $c_0 \approx 0.75$. Beyond this point, x_{rms} grows again as density modulations reappear, indicating a return to the SW phase.

A similar trend is observed for repulsive spin interactions ($c_2 = 5.0$), shown in Fig. 3.9(c ii). At $c_0 = -5.0$, the condensate is again compact ($x_{rms} \approx 0.360$) and resides in the EZM I phase. The system remains in this phase until $c_0 \approx -3.75$, after which x_{rms} increases steadily, signaling the onset of the SW phase. A pronounced peak at $x_{rms} = 5.314$ near $c_0 = -0.25$ reflects the large number of density fringes characteristic of this phase. Even though x_{rms} decreases to ~ 0.701 at $c_0 = 0$ [see Fig. 3.7(c1)], the condensate remains in the SW phase, albeit with fewer modulation peaks. For $c_0 > 0$, x_{rms} grows gradually as additional density maxima and minima develop, strengthening the SW

character.

3.3.3.3 Impact on the SSW phase

In this section, we present the impact of the variation of c_0 and c_2 on the SSW ground state phase for $k_L = 3.0$, and $\Omega \sim 0$. We consider $c_2 < 0$ and $c_2 > 0$, and varies c_0 in the range [-5,5]. For $c_0 < 0$, the condensate localizes naturally, and no external trapping is required; however, for $c_0 > 0$, a trap is introduced with trap aspect ratio $\lambda = 1.0$ [77, 108].

Variation of the ground state phases: We vary the interaction strength c_0 and c_2 by considering $k_L = 3.0$ and $\Omega \sim 0$, which corresponds to the SSW phase given in Figs. 3.1(d1) and 3.4(a4). Initially, considering $c_2 = -5.0$ and $c_0 = -1.0$, in Fig. 3.10(a1) we obtain the multi-peak structure in the density profile across all components, in which the $\rho_{\pm1}$ components superpose completely, leading to unpolarized stripe wave phase (SSW phase). Increasing the attractive strength in Fig. 3.10(a2) to a higher magnitude $c_0 = -3.0$, the SSW phase transitions into the elongated zero-momentum phase of the first type (EZM I phase). This transition is characterized by the spatial separation of the ρ_{+1} and ρ_{-1} densities, resulting in a single-peak density profile for all three components. The densities ρ_{+1} and ρ_{-1} components peaks away from the trap center at $x = -0.15$ and $x = 0.15$, respectively with amplitude $\rho_{\pm1}(max) = 0.64$. This transition takes place at an earlier strength of $c_0(SSW \rightarrow EZM\ I) = -1.25$. Further, increasing the attractive strength of c_0, condensate remains in the EZM I phase; however, it shrinks spatially, and the amplitude increases given in Figs. 3.10(a3) and (a4).

Next, considering $c_2 = 5.0$ and $c_0 = -1.0$, we obtain the multi-peak structure, which is the SSW phase and is given in Fig. 3.10(b1). Furthermore, increasing the attractive strength of $c_0 = -3.0$ in Fig. 3.10(b2), we find that the condensate remains in the SSW phase, with few peaks in the density profile across all components. Upon further increasing the magnitude of c_0 in Fig. 3.10(b3), at $c_0(SSW \rightarrow EZM\ II) = -3.75$ the system makes a transition into the EZM II phase, where the densities ρ_{+1}, and ρ_{-1} overlap. This EZM II phase differs from the EZM I phase, which exhibits polarization between the $\rho_{\pm1}$ components of the condensate. Beyond this point, condensate remains in the EZM II phase as shown in the Fig. 3.10(b4). We do not discuss the case $c_0 \gtrsim 0$, as it is already elaborated extensively above in sec. 3.3.1 and in sec. 3.3.2 for $c_2 < 0$, and $c_2 > 0$, respectively. For attractive interactions with $c_0 < 0$ and $c_2 < 0$, a transition from the SSW phase to EZM I phase occurs at $c_0(SSW \rightarrow EZM\ I) = -1.25$, while for

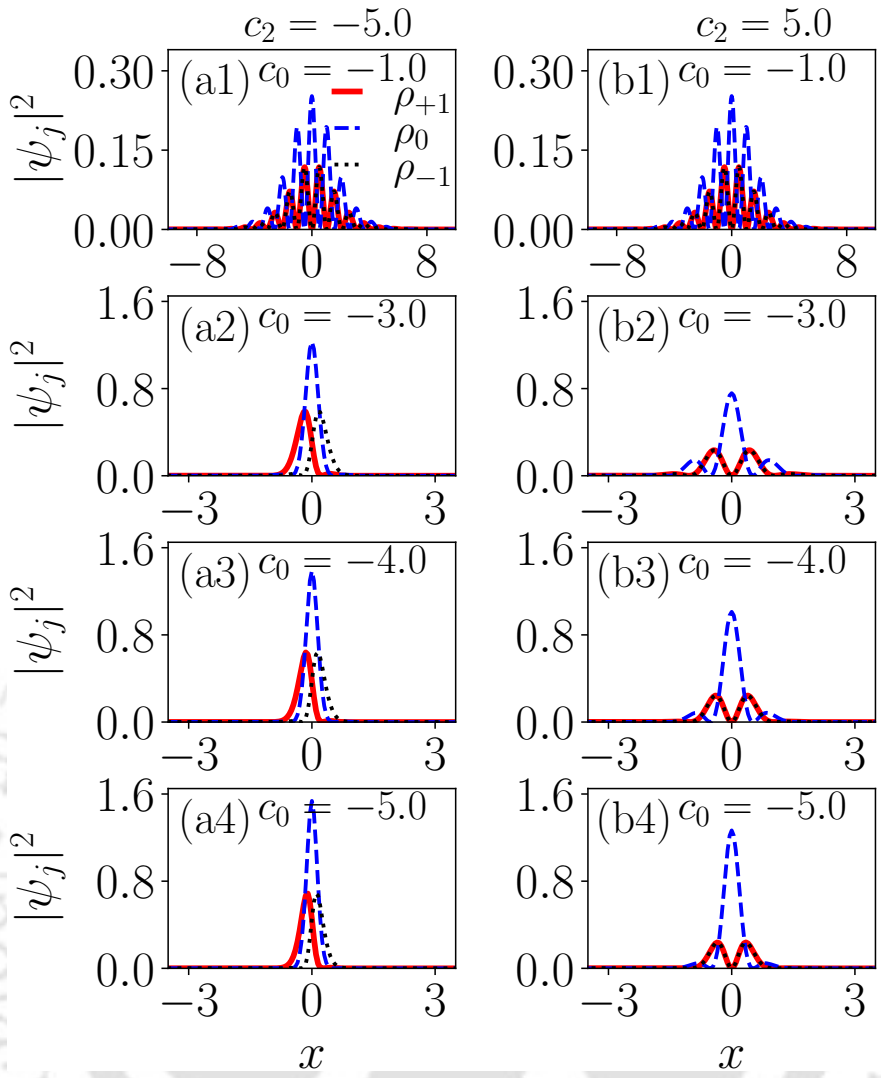


Figure 3.10: Ground state density profile $|\psi_{+1}|^2$ (solid red line), $|\psi_0|^2$ (dashed blue line), and $|\psi_{-1}|^2$ (dotted black line) upon varying c_0, keeping $k_L = 3.0$ and $\Omega \sim 0.0$ with (a) $c_2 = -5.0$, and (b) $c_2 = 5.0$. The density-density interaction strength varies as $c_0 = -1.0, -3.0, -4.0$, and -5.0 in columns from top to bottom. A phase transition takes place from the SSW phase to the EZM I phase and EZM II phase upon increasing the magnitude of c_0 for $c_2 < 0$ and $c_2 > 0$, respectively. Since $c_0 < 0$, no external trapping is required.

$c_2 > 0$, it makes a transition to EZM II phase at $c_0(SSW \rightarrow EZM\ II) = -3.75$.

In Fig. 3.11, we present the ground state phase diagram in the c_0 - c_2 plane. Using the protocol as given in the Eq. (3.7), black dashed line separates the phase diagram into two distinct regimes: (i) $\lambda = 0$ for $c_0 < 0$, where no external confinement is applied, and (ii) $\lambda = 1$ for $c_0 \gtrsim 0$, where a harmonic potential is applied to confine the condensate. Starting with $c_2 = -5.0$ we vary c_0. For strong attractive interaction $c_0 = -5.0$, the condensate remains in the EZM I phase, which persists up to $c_0 = -1.25$. Beyond this value, the condensate undergoes a phase transition into the SSW phase.

TH-4102_206121026

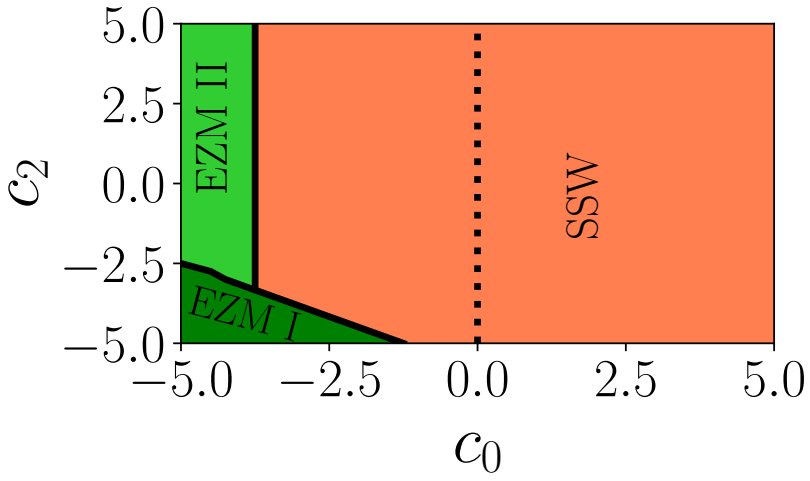


Figure 3.11: Ground state phase diagram in the c_0-c_2 plane for fixed $k_L = 3.0$, and $\Omega \sim 0$. The black dotted line separates the trapless ($c_0 < 0$) and trapped ($c_0 \gtrsim 0$) regimes. Different quantum phases are indicated by color: green denotes the EZM I phase, lime green denotes EZM II, and coral denotes the SSW phase. For considered parameter ($k_L = 3.0, \Omega \sim 0.0$), the system resides in the SSW phase under weak or repulsive interaction strengths, while the higher attractive strength of both c_0 and c_2 drives a transition into the EZM's phase.

Notably, the SSW phase extends into the trapped regime, demonstrating the robustness against the external confinement.

As c_2 increases, the region occupied by the EZM I phase in the $c_0 - c_2$ plane progressively shrinks. For $c_2 > -2.5$, a different EZM phase (EZM II phase) emerges, which persists up to $c_0 = -3.75$. The EZM II is characterized by overlapping densities ρ_{+1} and ρ_{-1}, with no observable density modulation in real space, indicating a fully mixed spin-state with suppressed stripes. Finally, for strongly repulsive spin-dependent interactions ($c_2 = 5.0$), a transition from the EZM II phase to the SSW phase occurs at $c_0 = -3.75$, beyond which the condensate remains in the SSW phase across the entire range of c_0.

Miscibility and Ground state phase transformation in the SSW phase: We report the variation of η_{np} in Fig. 3.12(a i) by simultaneously varying the c_0, and c_2 in the range [-5,5] for $k_L = 3.0$ and $\Omega \sim 0$. The black dotted line separates the phase plot into two parts: (i) the left half, in the absence of trap strength, and (ii) the right half, where the trap is present. For $c_2 = -5.0$ and $c_0 = -5.0$, we obtain the $\eta_{np} = 0.534$ which indicates a separation between the densities components ρ_{+1} and ρ_{-1} and condensate is in EZM I phase. The η_{np} shows an increasing trend upon increase in c_0, which finally attains as $\eta_{np} = 1.0$ for $c_0 = -1.0$, which also results in making the transition to the SSW phase. Note that for $c_0 \gtrsim 0$, the condensate is trapped under the harmonic potential. For

$c_0 > 0$, η_{np} remains flat and therefore condensate retains the SSW phase. However, for $c_2 = 5.0$ and $c_0 = -5.0$, we obtain $\eta_{np} = 0.824$ that indicates a separation between density component ρ_{+1}, and ρ_{-1}, and the condensate is in the EZM II phase. With increasing c_0, η_{np} keeps increasing and reaches to $\eta_{np} = 1.0$ at $c_0 = -1.0$, where the condensate transitions into the SSW phase. Similar to the previous case, for $c_0 \gtrsim 0$, a harmonic trap is introduced. Beyond this point, the η_{np} remains flat and the condensate remains in the SSW phase.

For a better description of the overlap parameters η_{np}, in Fig. 3.12(a ii), we report it by choosing three different values of $c_2 = -5.0, -2.5$, and 5.0, varying c_0 in the range [-5,5] at fixed $k_L = 3.0$, and $\Omega \sim 0$. At first, considering $c_2 = -5.0$, and $c_0 = -5.0$, we obtain $\eta_{np} = 0.534$. Increasing c_0, it remains constant up to $c_0 = -1.50$. Further, increasing c_0, η_{np} increases to a higher value at $c_0 = -1.0$ with magnitude $\eta_{np} \approx 1.0$ and saturates; however, a kink to lower amplitude appears at $c_0 = 0.0$ with magnitude $\eta_{np} = 0.885$. Next, considering $c_2 = -2.5$, we obtain $\eta_{np} = 0.787$ at $c_0 = -5.0$. Upon increasing c_0, η_{np} increases gradually and saturates at $c_0 = -1.0$ with magnitude $\eta_{np} \approx 1.0$. For $c_2 = 5.0$, η_{np} varies similar to $c_2 = -2.5$.

In Fig. 3.12(b i), we report the variation of miscibility parameter η in the c_0- c_2 plane for $k_L = 3.0$ and $\Omega \sim 0$. We begin with $c_2 < 0$ with $c_2 = -5.0$, and varying c_0. At $c_0 = -5.0$, we find $\eta = 0.728$, corresponding to the condensate residing in the EZM I phase. As c_0 increases, η decreases until $c_0 = -1.25$, reaching a minimum value of $\eta = 0.641$. Beyond this point, the η increases again and the condensate makes a transition to the SSW phase. For $c_0 \gtrsim 0$, a harmonic trap is introduced to confine the condensate, and η remains flat while the condensate stays in the SSW phase. For $c_2 > 0$ we fix $c_2 = 5.0$ and vary c_0. At $c_0 = -5.0$, indicating the condensate is in the EZM II phase. As c_0 increases η rises continuously, reaching $\eta = 0.70$ at $c_0 = -1.0$, where the condensate transitions to the SSW phase. For $c_0 \gtrsim 0$, with the harmonic trap applied, the η remains flat and the condensate retains the SSW phase. Overall in the $c_0 - c_2$ plane, the η varies between 0.60 and 0.75, indicating that the EZM I, EZM II, and SSW phases of the condensate are partially miscible.

To probe the impact of density-density interaction and spin-exchange interaction is more quantitative way, in Fig. 3.12(b ii), we show the miscibility parameter η by varying c_0 in the range [-5.0,5.0] for $c_2 = -5.0, -2.5$, and 5.0, keeping $k_L = 3.0$ and $\Omega \sim 0$. At first, considering $c_2 = -5.0$, and $c_0 = -5.0$, we obtain $\eta = 0.728$, which decreases upon increasing c_0 reaching to minimum at $c_0 = -1.25$ with magnitude $\eta = 0.641$. Upon further increasing c_0, η increases to a higher value and saturates. Next, we consider $c_2 = -2.5$, and $c_0 = -5.0$, we obtain $\eta = 0.648$. Increasing c_0,

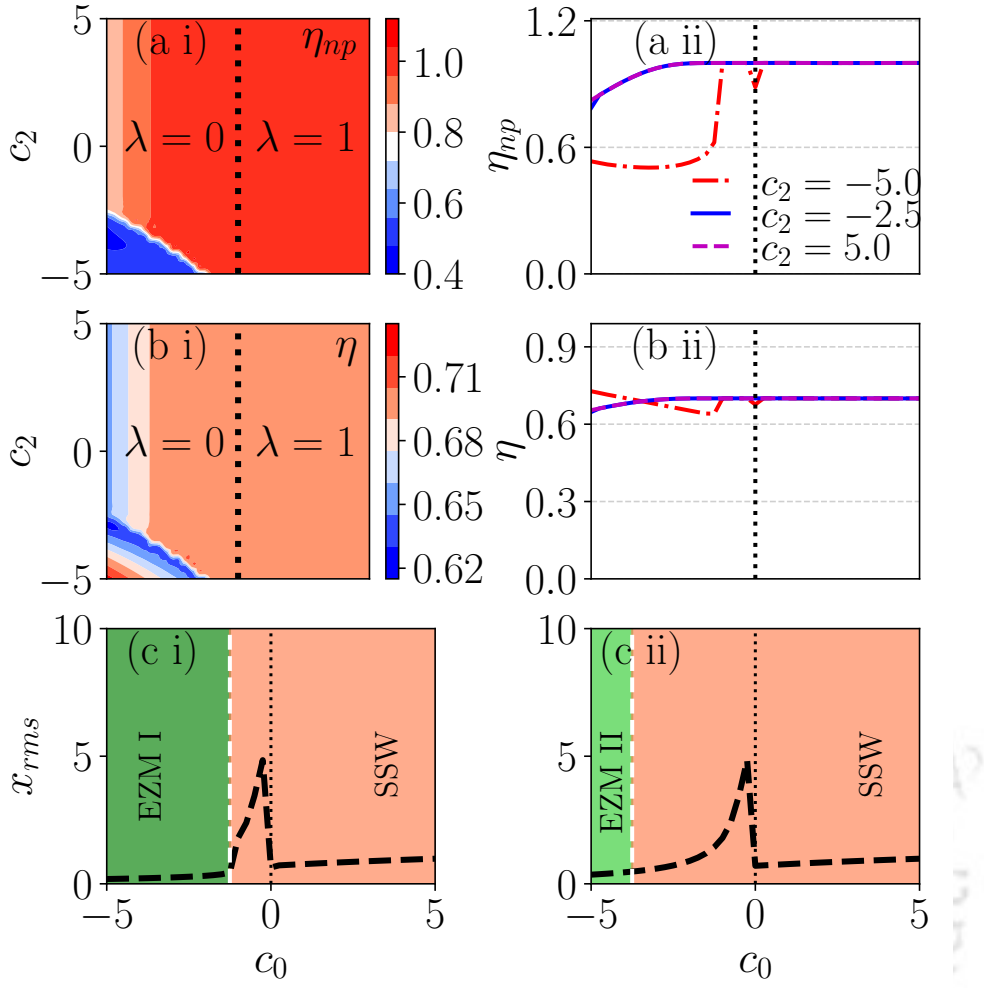


Figure 3.12: Miscibility parameters (a) η_{np}, and (b) η upon varying c_0 and keeping $k_L = 3.0$ and $\Omega \sim 0$. In (a i) and (b i), c_0 and c_2 vary within the range [-5,5]. (a ii) and (b ii) exhibit the η_{np} and η upon varying c_0 for $c_2 = -5.0$ (dashed-dotted red line), -2.5 (solid blue line), and 5.0 (dashed magenta line). In the bottom row, panels (c i) and (c ii) represent the root mean square (x_{rms}) size of the condensate for $c_2 = -5.0$ and 5.0, respectively, which indicate different phases of the condensate. The color code represents different quantum phases: green represents the EZM I phase, limegreen represents the EZM II phase, and coral represents the SSW phase. The black dotted line separates untrapped ($c_0 < 0$) and trapped ($c_0 \gtrsim 0$) regimes of the condensate.

η gradually increases to $\eta = 0.70$ at $c_0 = -2.25$, and saturates further. We obtain a similar behaviour of η throughout for $c_2 = 5.0$ as we obtained for $c_2 = -2.5$.

Finally, we present the x_{rms} of the condensate with respect to c_0, and c_2. Taking into account $c_2 = -5.0$, and $c_0 = -5.0$, in Fig. 3.12(c i), we obtain $x_{rms} \approx 0.188$ where condensate is in the EZM I phase. Upon increasing c_0, the x_{rms} increases gradually; however, the condensate remains in the EZM I phase. At $c_0(SSW \rightarrow EZM\ I) = -1.25$, the x_{rms} starts to increase and peaks with a higher magnitude of $x_{rms} = 4.847$ at $c_0 = -0.25$, which arises due to the density modulation and condensate transitions to the SSW

TH-4102_206121026

phase. For $c_0 \gtrsim 0$ (in the presence of a trap), the x_{rms} falls to $x_{rms} \approx 0.640$ and the condensate remains in the SSW phase. Beyond this point, the x_{rms} increases gradually, leading to an increase in the number of stripes, and the condensate remains in the SSW phase. However, at $c_0 = 0$, we obtain the SW phase. In Fig. 3.12(c ii), considering $c_2 = 5.0$, and $c_0 = -5.0$, we obtain $x_{rms} \approx 0.359$, corresponding to the EZM II phase. Upon increasing c_0, the x_{rms} increases gradually, and condensate transitions to SSW phase at $c_0(SSW \rightarrow EZM\ II) = -3.75$. Increasing c_0 beyond this point, the condensate is in the SSW phase. Further, increasing c_0, the x_{rms} peaks at $c_0 = -0.25$ with magnitude $x_{rms} = 4.847$. The increase in x_{rms} arises as the SSW phase consists of a large number of maxima and minima. For $c_0 = 0.0$, the x_{rms} falls to 0.706; however, the condensate remains in the SSW phase with fewer maxima and minima across all density components. Upon further increasing the c_0, the x_{rms} gradually increases with condensate remaining in the SSW phase, and the number of maxima and minima increases with increasing c_0.

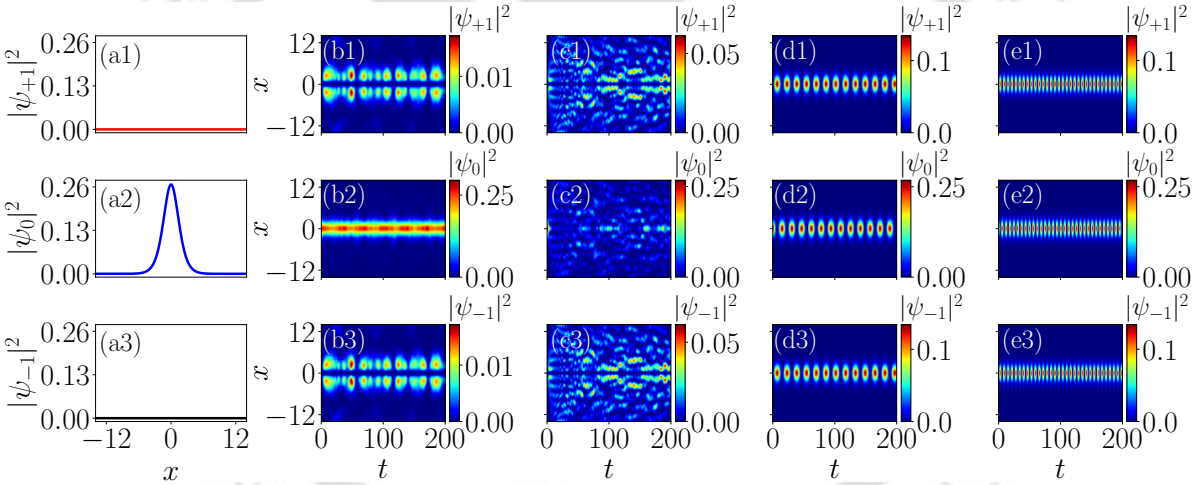


Figure 3.13: Ground state density profile (a1-a3) for $m_F = +1, 0, -1$, respectively, with $c_0 = -1.0$, and $c_2 = 5.0$, in absence of the k_L, and Ω. The condensate is in the ZM phase. Panels (b1-b3) and (c1-c3) depict the time evolution of the initially prepared density profile upon quenching the SO coupling from $k_L \sim 0 \rightarrow 0.20$ and $k_L \sim 0.0 \rightarrow 1.0$, respectively. For a small quench of the SO coupling strength, periodic high-density peaks appear along the propagation direction, whereas a complex pattern emerges for stronger quench. Panels (d1-d3) and (e1-e3) exhibit the dynamics of the condensate density upon quenching the Rabi coupling $\Omega \sim 0.0 \rightarrow 0.20$ and $\Omega \sim 0.0 \rightarrow 0.50$, respectively. In both cases, the quench of the Rabi coupling leads to the stabilization of the condensate. The SO and Rabi coupling is quenched at $t = 0$ units.

The zero-momentum (ZM) phase and the stripe wave (SW) phase discussed above can be characterized using the single-particle spectrum. To obtain the single particle dispersion, we consider $V(x) = 0$, in the absence of interaction strengths, that is, $c_0 = c_2 = 0$. Substituting $\psi_{0,\pm1} = \phi_{0,\pm1} e^{i(q_x x - \omega t)}$ into the Eqs.(3.1a)-(3.1b), we obtain the

following dispersion relations [115, 123],

$$\omega_0 = \frac{q_x^2}{2}, \tag{3.8a}$$

$$\omega_\pm = \frac{1}{2}\left(q_x^2 \pm 2\sqrt{\Omega^2 + k_L^2 q_x^2}\right). \tag{3.8b}$$

Based on this dispersion relation, the low-lying branch ω_- displays the single minimum in the $k_L^2 < \Omega$ regime, while a double minimum appears for the $k_L^2 > \Omega$ regime. The presence of a single minimum in the quasi-momentum direction leads to the zero-momentum phase (plane wave phase with zero momentum). In contrast, the appearance of the double minimum corresponds to the SW phase, characterized as the superposition of two momentum states, which leads to the density modulation in real space.

The conditions mentioned above, i.e., $k_L^2 < \Omega$ (ZM phase) and $k_L^2 > \Omega$ (SW phase), worked well in ferromagnetic interaction and antiferromagnetic interaction with repulsive density-density interaction. However, for highly attractive density-density interaction and in the presence of ferromagnetic interaction and antiferromagnetic interaction, we obtained the elongated zero-momentum phases (EZM I phase, and EZM II phase) in the $k_L^2 > \Omega$ regime given in Figs. 3.7 and 3.10. The EZM I phase in $k_L^2 > \Omega$ regime also appeared for weak repulsive density-density interaction in the presence of ferromagnetic interactions [see Fig. 3.7].

In the above sections, we reported various ground state phases: the ZM phase, EZM I phase, EZM II phase, SW phase, and the SSW phase with respect to (k_L, Ω) in the presence of ferromagnetic interaction and antiferromagnetic interaction. We also studied the effect of interaction strengths c_0 and c_2 in the ZM phase, SW phase, and the SSW phase. We extensively studied the miscibility of the condensate and ground state transformation from one phase to another with respect to coupling strengths (k_L, Ω) and interaction strengths (c_0, c_2). In the next section, we investigate the quench dynamics across these ground state phases by quenching the SO and Rabi coupling strengths, excluding the EZM phases, since these phases are trivial extensions of the ZM phase.

3.3.4 Quench dynamics of the ground state phases

After analyzing the detailed nature of the ground state phases of the spin-1 SO-coupled BECs for ferromagnetic and antiferromagnetic interactions, we now turn to their dynamics using the quenched mechanism. First, we generate the ground state profiles,

namely, the ZM phase, the SW phase, and the SSW phase of the condensate with interaction strengths $c_0 = -1.0$ and $c_2 = 5.0$ (as discussed above), in the presence of a harmonic trap with the trap strength $\lambda = 0.05$. By choosing a weak trap to minimize its influence on the system and to better reveal the underlying dynamics of the condensate following a quench, we study the quench dynamics by abruptly changing the SO (k_L) and Rabi coupling strength (Ω). The response of the condensate to a sudden change of coupling strengths depends on its underlying spin structure. In the SSW phase, the three spin components are nearly balanced, so a quench primarily excites weak breathing motion without strongly modifying the relative populations. In contrast, the SW phase exhibits unequal spin mixing; a quench shifts the balance among components and can cause the $m_F = 0$ population to decay as energy is redistributed. This distinction provides a direct physical mechanism behind the different real-time signatures observed below.

3.3.4.1 ZM phase: $k_L \sim 0.0$, and $\Omega \sim 0.0$

Initially, we generate the ground state profile given in Fig. 3.13(a) corresponding to $k_L \sim 0.0$, and $\Omega \sim 0.0$, with interactions $c_0 = -1.0$, $c_2 = 5.0$, which is a ZM phase, where all the atoms occupy the state ψ_0. A similar type of ground state profile is shown above in Fig. 3.4(a1). To start with, in Figs. 3.13(b1)-(b3), we quench the SO coupling strength $k_L \sim 0.0 \rightarrow 0.20$ for $\Omega \sim 0$ at $t = 0$, and study the quench dynamics of the ground state profile. During time evolution, periodic high-density peaks emerge along the propagation direction in the $\rho_{\pm 1}$ components of the condensate, which shows the revival of the spin components $\rho_{\pm 1}$. This behavior is symmetric in the spatial direction. Conversely, the zeroth component shows breather-like dynamics. Here, in real-time propagation, we observe all three components present [124]. Next, in Figs. 3.13(c1)-(c3), we quench $k_L \sim 0.0 \rightarrow 1.0$. We observe the appearance of the complex nonlinear wave pattern in all three components along the direction of propagation. However, $\rho_{\pm 1}$ are symmetric in spatial direction, while the zeroth component is centered at $x \approx 0$. The density profile is spatially extended, showing the spread of the condensate. The fragmentation of the density profile in spatio-temporal evaluation indicates the onset of dynamical instability [125]. Moreover, the antiferromagnetic SO coupled BECs behaves like a scalar, while the introduction of coupling strengths it modifies as vector BECs and showing different nonlinear dynamical evolution for different coupling quenches.

Now, we quench the Rabi coupling strength, keeping the SO coupling strength

TH-4102_206121026

fixed $k_L \sim 0.0$. At first, in Figs. 3.13(d1)-(d3), quenching $\Omega \sim 0.0 \rightarrow 0.20$ results in breather-like dynamics across all three components of the condensate, with the zeroth component exhibiting the highest density magnitude. Similar to SO coupling quenching, here, also, the quenching dynamics induces the revival of the $m_F = \pm 1$ components of the condensate; however, it shows stable behaviour throughout. Next, we quench $\Omega \sim 0.0 \rightarrow 0.50$ in Figs. 3.1(e1)-(e3). Here, we also obtain stable breather dynamics in all three components of the condensate; the zeroth component remains more dominant. However, the number of breathers is more than the $\Omega = 0.20$ case [114].

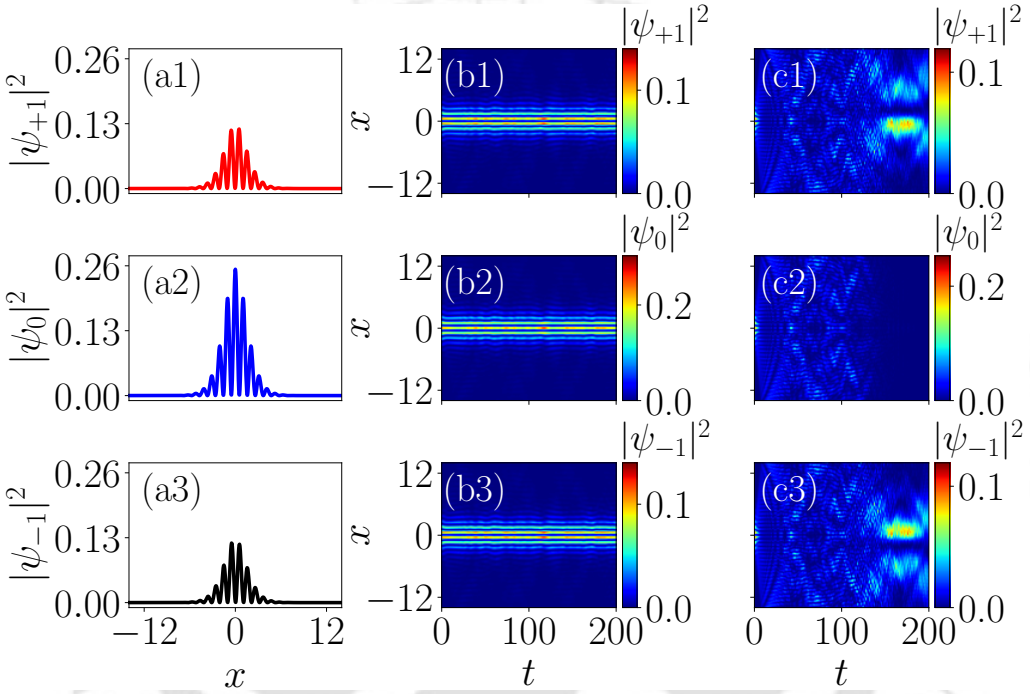


Figure 3.14: Ground state density profile (a1-a3) for $m_F = +1, 0, -1$, respectively, with $(k_L, \Omega) = (3.0, 1.0)$. The interaction strengths are $c_0 = -1.0$, and $c_2 = 5.0$. The condensate is in the SW phase. Panels (b1-b3) and (c1-c3) depict the time evolution of the initially prepared density profile in the $x - t$ plane upon quenching the SO coupling strength $k_L = 3.0 \rightarrow 3.20$ and $k_L = 3.0 \rightarrow 4.0$, respectively. The SO coupling is quenched at $t = 0$ units. For a stronger quench of the Rabi coupling strength, the condensate fragments into small domains, forming a complex pattern, and the zeroth component disappears at a later time unit.

3.3.4.2 SW phase: $k_L = 3.0$, $\Omega = 1.0$

In this section, we generate the ground state corresponding to $k_L = 3.0$, $\Omega = 1.0$, with interaction strengths $c_0 = -1.0$, and $c_2 = 5.0$, resulting the stripe wave (SW) phase given in Fig. 3.14(a). A similar type of ground state profile is shown in Fig. 3.7(b1). To initiate the quench dynamics, we first increase $k_L = 3.0 \rightarrow 3.20$ suddenly, at $t = 0$ while keeping Ω fixed and evolving the condensates in time. Due to the finite modification in

the SO coupling all three components possess same amount of fluctuations in the side-lobes, however, the centered stripes maintain their stability, as shown in Figs. 3.14(b1)-(b3). Further increase in the SO coupling $k_L = 3.0 \rightarrow 4.0$, resulting breaks the density profile initially into several small parts; further, it shows formation of complex patterns in the x-t plane. Beyond $t > 120$ units, the density profile of the zeroth component starts to disappear, and the $\rho_{\pm 1}$ get enhanced as shown in Figs. 3.14(c1)-(c3) [90, 116]. The fluctuation behaviour and formation of complex patterns during time evolution in the density profile indicate the onset of dynamical instability [115, 125]. Moreover, this quenching mechanism also confirms that the SW phase is dynamically unstable.

3.3.4.3 SSW phase: $k_L = 3.0, \Omega \sim 0.0$

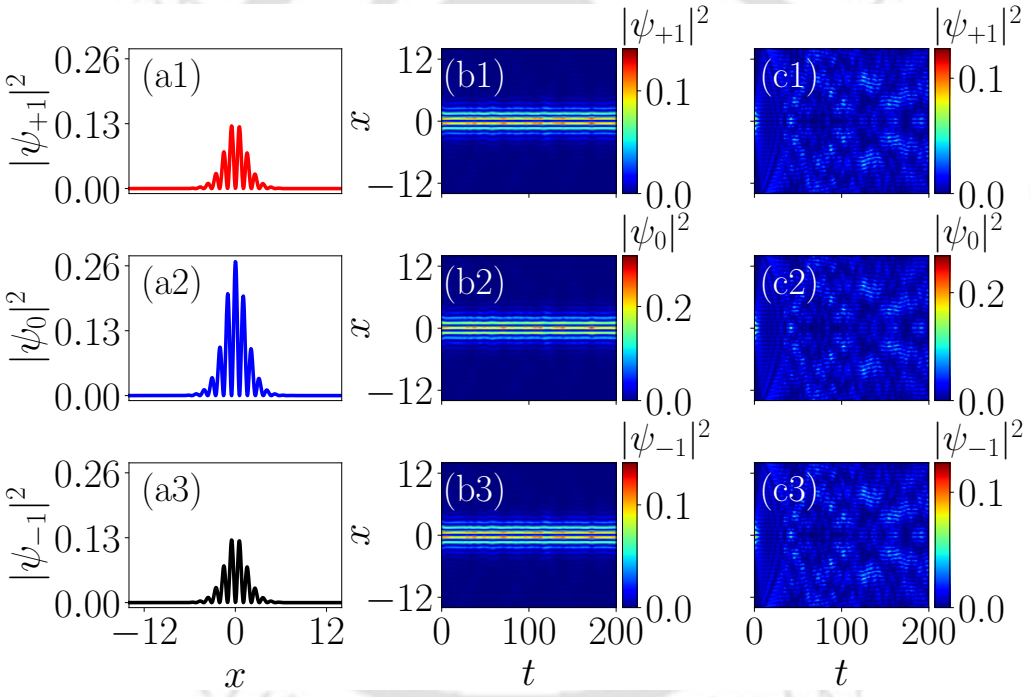


Figure 3.15: Ground state density profile (a1-a3) for $m_F = +1, 0, -1$, respectively, with $(k_L = 3.0, \Omega \sim 0.0)$. The interaction strengths are $c_0 = -1.0$, and $c_2 = 5.0$. The condensate is in the SSW phase. Panels (b1-b3) and (c1-c3) exhibit dynamics of the ground state profile in the $x - t$ plane upon quenching the SO coupling strength $k_L = 3.0 \rightarrow 3.20$ and $k_L = 3.0 \rightarrow 4.0$, respectively. The SO coupling is quenched at $t = 0$ units. The strong quench of the SO coupling strength leads to the emergence of complex patterns.

Here, we intended to investigate the quenching dynamics of the SSW phase. In this regard, we generate the ground state by considering $k_L = 3.0$, and $\Omega \sim 0$ with interaction strengths $c_0 = -1.0$, and $c_2 = 5.0$, which is an unpolarized SW phase (SSW phase) depicted in Fig. 3.15(a). Following the previous quenching protocol, firstly, at $t = 0$, we quench the SO coupling to a smaller value as $k_L = 3.0 \rightarrow 3.20$. During the time evolu-

tion, the density profiles exhibit minute fluctuations in the x–t plane, and breather-like dynamics appear across all components displayed in Figs. 3.15(b1)-(b3). While comparing previous SW phase dynamics with the SSW phase almost similar due to the phase transition condition $k_L^2 > \Omega$. Next, in Figs. 3.15(c1)-(c3) we suddenly increase the SO coupling to higher value as, $k_L = 3.0 \rightarrow 4.0$. The density profiles split into several parts and further fragments into smaller domains across all components. These fluctuations and the formation of complex patterns during time evolution indicate the dynamical instability of the SSW condensate [115, 125]. Interestingly, here the zeroth component survives throughout the dynamical evolution. The contrast between the responses of the SW and SSW phases can be understood from their spin composition. In the SSW phase, the three spin components share nearly balanced populations, so a sudden change in SO coupling mainly excites a low-lying breathing motion without strongly altering the internal spin structure. In the SW phase, however, the mixing among the components is uneven; a quench redistributes energy among the spin channels, leading to a gradual reduction of the $m_F = 0$ population. This imbalance produces noticeably different dynamical signatures in the two phases, providing a clear way to distinguish them [116].

3.4 Summary and Conclusions

In this Chapter, we have presented a systematic numerical investigation of the ground-state phases and quench dynamics of a spin-1 Bose–Einstein condensate subject to one–dimensional SO coupling, with both ferromagnetic and antiferromagnetic interactions. Our results reveal a remarkably rich phase structure arising from the interplay among density–density interactions, spin–exchange interactions, and the externally controlled Raman coupling.

For ferromagnetic interactions at $\Omega \approx 0$, we unravel four distinct phases—ZM, EZM I, SW, and SSW—with the important observation that the superstripe wave (SSW) phase disappears once Ω becomes finite. In contrast, antiferromagnetic condensates at $\Omega \approx 0$ exhibit the ZM, EZM II, and SSW phases, while, increasing Ω trigger a controlled transitions into the ZM, EZM I, and SW phases. Importantly, even when antiferromagnetic interactions naturally favor a scalar-like ZM state in the absence of couplings, the introduction of SO or Rabi coupling revives occupation in the $\psi_{\pm 1}$ components—demonstrating a controlled pathway from a single-component condensate to a fully spinor system [102].

By systematically scanning the extensive range of interaction parameters (c_0, c_2), we further identify how density and spin interactions reshape these phases. While the ZM phase remains largely insensitive to interaction variations, the SW and SSW phases exhibit strong dependence on the sign and magnitude of c_0. Strong attractive density interactions compress the condensate and eventually drive transitions into EZM-type phases, while repulsive interactions have the opposite effect. The precise transition points are summarized in Table 3.1.

Table 3.1: Phase transition points under different interaction strengths

k_L	Ω	c_2	c_0	Phase
3.0	~ 0	-5.0	-1.25	SSW-EZM I
3.0	~ 0	5.0	-3.75	SSW-EZM II
3.0	1.0	-5.0	-0.50	SW-EZM I
3.0	1.0	5.0	-3.75	SW-EZM I

The miscibility behavior further reinforces this classification—ZM remains fully miscible, whereas all other phases display partial demixing. The rms size x_{rms} acts as a complementary diagnostic: swelling of the cloud correlates with the appearance of stripe phases, whereas compression marks transitions back to extended ZM-like regimes.

Finally, our quench protocol demonstrates pronounced dynamical sensitivity to both Rabi and SO couplings. In the ZM phase, sudden coupling changes generate revivals in the $\psi_{\pm 1}$ components and breather-like oscillations. The SO quenches, in particular, produce rich dynamical behavior: small quenches generate x–t modulations, while stronger quenches nucleate complex domain structures. For sufficiently large SO quenches, the ψ_0 component can be almost entirely depleted, especially when quenching from the SW phase. These features reiterate the dynamical fragility of modulated phases under nonadiabatic driving and may provide an experimentally accessible route for creating or destabilizing stripe configurations [126].

Overall, our numerical investigations establish a unified picture of how SO coupling, Rabi coupling, and spinor interactions interact or compete to stabilize diverse ground states—ranging from structureless ZM phases to strongly modulated SW and SSW phases—and how these states respond under abrupt dynamical perturbations. The phase transitions, miscibility behavior, and dynamical pathways identified here offer viable predictions that could be tested in current Raman-dressed spin-1 experiments [60].

TH-4102_206121026

Chapter 4

Emergence of unstable avoided crossing in the collective excitations of spin-1 spin-orbit coupled Bose-Einstein condensates

After discussing the emergence of various quantum phases resulting from the interplay between spin–orbit (SO) coupling, Rabi coupling, and interatomic interactions in Chapter 3, we now extend the analysis to the study of collective excitations. In this chapter, we present analytical and numerical investigations of the collective excitation spectrum of quasi-one-dimensional SO coupled spin-1 ferromagnetic Bose–Einstein condensates, with particular emphasis on the emergence of unstable avoided crossings in the excitation spectrum. In particular, we present analytical and numerical results for the collective excitation spectrum of a quasi-one-dimensional SO coupled spin-1 ferromagnetic Bose–Einstein condensate. The collective excitation spectrum, using Bogoliubov-de-Gennes theory, reveals the existence of a diverse range of phases in the SO and Rabi coupling ($k_L - \Omega$) plane. Based on the nature of the eigenvalue of the excitation spectrum, we categorize the $k_L - \Omega$ plane into three distinct regions, namely I, II (IIa and IIb), and III. In region I, a stable mode with phonon-like excitations is observed. In region IIa, single and multi-band instabilities are noted with a gapped mode, while multi-band instability accompanied by a mode corresponding to no gap between low-lying and first excited states is realized in region IIb, which also provides evidence of unstable avoided crossing between low-lying and first excited modes, responsible for the I_o type of oscillatory non-equilibrium dynamical pattern formation. The gap

TH-4102_206121026

between low-lying and first-excited states increases upon increasing the Rabi coupling while decreases upon increase of SO coupling. Using eigenvector analysis, we confirm the presence of the spin-dipole mode in the spin-like modes in Region II. We corroborate the nature of the collective excitation through real-time dynamical evolution of the stationary state perturbed with the quench of the trap using the mean-field Gross-Pitaevskii model. This analysis suggests the presence of dynamical instability leading to the disappearance of the 0-th component of the condensate. In Region III, mainly encompassing $\Omega \sim 0$ and finite k_L, we observe phonon-like excitations in both the first excited and the low-lying state. The eigenvectors in this region reveal alternative in- and out-of-phase behaviours of the spin components. Numerical analysis reveals the presence of a super stripe phase for small Rabi coupling in this region, wherein the eigenvector indicates the presence of more complicated spin-like-density mixed modes. The work presented in the Chapter is published in Physical Review A [115].

4.1 Introduction

The collective excitations and the different quantum phases associated with spin–orbit (SO) coupled spin-1 Bose–Einstein condensates (BECs) have been discussed in Chapter 1. However, to make this chapter self-contained and to introduce the context for the emergence of unstable avoided crossings in the collective excitations of spin-1 SO coupled BECs, we briefly review the relevant works. Ultracold atoms offer a versatile but precise platform for exploring quantum matter in the presence of diverse synthetic fields [127]. The recent experimental realization of SO coupling in spinor ultracold atoms [10, 128] has sparked great interest among researchers to explore the SO coupling-related physics in large-spin systems, which is challenging to achieve in the electronic materials system of condensed matter physics. Over the last few decades, research on spinor BECs has captured the community's attention since it reveals the interesting physical phenomena such as vortices [129], turbulence state triggered by the modulational instabilities as a result of the counterflow motion between the binary component [130], quantum phase transitions [23, 131], modulational instability [132], solitons [133], magnetized vector solitons [134], and supersolidlike behaviour in quasi-two-dimensional (quasi-2D) [100].

In the field of ultracold gases, numerical simulations have become an indispensable tool for exploring numerous complex phases and the underlying detailed mechanisms that appear in those systems as low-lying excitation phases. To this end, the

mean-field model Gross-Pitaevskii equations (GPEs)-based models have been widely used to investigate various aspects of SO coupled spinor BECs, such as phase separation [109], phase separation of vector solitons [135], stability, and dynamics of solitons [77, 108, 136], spin precession and the separation between the spin component owing to the anomalous spin-dependent velocities [79–81], etc. Some studies have explored the dynamics of modulation instability [125], preparation of stripe states [137], and condensate flow past an obstacle [138] in SO coupled BECs.

One of the intriguing features of the SO coupled BECs is the presence of a modulated ground state that appears as stripe phases for high values of SO couplings [4, 118]. In recent years, there have been several studies indicating an intimate connection between the stripe phase and the supersolid behaviour of the BECs. For instance, Adhikari [100] reported supersolidlike states in quasi-2D trapped SO coupled spinor BECs. In multicomponent condensates, Goldstein *et al.* [20] have initiated the study of the Hartree-Bogoliubov theory to determine the resulting quasi-particle frequency spectrum and observed the interferences resulting from cross-coupling among the condensate leading to the reversal of the sign of two-body interaction which triggers the onset of spatial instabilities. There are some studies that suggest domain formation through the dynamical stability analysis [87].

The investigation of collective excitations, which are low-lying excitations in BECs, has played a pivotal role in comprehending the fundamental characteristics of these quantum degenerate gases. This includes aspects such as the stability of various ground state phases, superconductivity, and superfluidity [27, 139]. In 1941, Landau coined the term "excitations" to elucidate the emergence of superfluids as a combined effect of a weakly interacting mixture of phonons and rotons quasi-particles. Subsequently, Bogoliubov employed Landau's excitation spectrum tools to explicate the superfluidity in BECs [13]. Experimentally, the realization of low-lying excitations has been achieved in dilute gases of rubidium [16] and sodium [17] atoms. For trapless spinor condensates, the study of collective excitations involved considering equal Rashba and Dresselhaus couplings. This investigation revealed the presence of maxon-roton excitations [140, 82]. Utilizing Bragg spectroscopy, Khamehchi *et al.* provided experimental evidence of collective excitations by realizing roton-maxon modes in SO coupled spinor systems [22].

Following the experimental realization of the collective excitation mode for SO coupled BECs in the laboratory, a series of theoretical and numerical works have been undertaken in the recent past that reveal the more complex nature of these excitations. For instance, Chen *et al.* [83] demonstrated the collective excitation spectrum of Raman-

induced SO coupled spinor BECs confined in a quasi-one-dimensional (quasi-1D) harmonic trap. By tuning the Raman coupling strength, they projected the presence of three distinct phases: stripe (ST), plane-wave (PW), and zero-momentum (ZM). Additionally, they identified the spin dipole and breathing modes of collective excitations, indicating clear phase boundaries. Numerical confirmation of these features was obtained through quench dynamics. Few studies indicate the presence of the PW, ZM, and ST phases of the condensate as quadratic Zeeman coupling is introduced in the SO coupled spin-1 BECs [25, 141]. Ozawa *et al.* [21] numerically analyzed the dynamical and energetic instabilities of quasi-1D SO coupled BECs. Ravisankar *et al.* [93] analytically and numerically analyzed the stability of the spin-1/2 binary SO coupled BECs in quasi-2D using the collective excitation spectrum and found the presence of phonon-maxon-roton mode in the spectrum for finite SO and Rabi couplings. Katsimiga *et al.* [106] analyzed the non-linear solitary wave excitation that appear in the form of different combinations of the dark and bright solitons for the trapped spin-1 condensate in the harmonic trap. Subsequently, different sorts of vortex-bright type excitations in the two-dimensional harmonically confined spin-1 BECs were also explored [142]. Rajat *et al.* [143] theoretically and numerically analyzed the collective excitation of SO coupled spin-1 BECs in a cigar-shaped trap both at zero and finite temperature, and demonstrated the presence of density and spin excitation, which exhibits qualitatively different features at finite temperature than those at zero temperature.

So far, the studies of collective excitation in the spinor BECs are mainly restricted to the specified range of coupling parameters. However, a comprehensive picture of the instabilities arising as a result of the collective excitation has not been understood clearly. Moreover, from the dynamics point of view, it has been demonstrated that in the presence of finite detuning between the two spin states, unstable avoided crossing [95, 144] between the low-lying and first excited states appears upon perturbation. Such physical mechanism is responsible for constructing a class of I_o (oscillatory patterns) dynamically oscillatory non-equilibrium pattern formation in the quantum systems which remains to be unexplored in the SO coupled spin-1 BECs along with spin-orbit and linear Rabi coupling. In this paper, we attempt to address these issues considering the ferromagnetic SO coupled spin-1 BECs by scanning a wide range of the coupling parameters regime using analytical computation of the eigenspectrum and eigenvectors. Based on the detailed nature of the eigenspectrum, we divide $k_L - \Omega$ plane into three regimes: (i) a stable region characterized by a phonon-like mode, (ii) unstable regimes broadly divided into two parts characterized by the presence of a gap (IIa) and gapless (IIb) behaviour between the low-lying (ll) and first-excited (fe)

spectra, and also yields the evidence of unstable avoided crossing modes, and (iii) for coupling values near $\Omega \sim 0$, we find that the system exhibits a phonon-like symmetric maxon-roton mode, which is also a mode corresponding to no gap between the low-lying and first-excited spectra. In the presence of a relatively small imaginary frequency, we observe both a weak instability and the emergence of a superstripe phase. In all the regions, we corroborate the analytical observation of the eigenspectrum with the real-time dynamics of the stationary state using the GPEs.

The Chapter is organized as follows. In Sec. 4.2, we present our theoretical model for investigating the collective excitations and instabilities of SO coupled spin-1 ferromagnetic BECs. Sec. 4.3 illustrates the single-particle spectrum, followed by the analysis of the collective excitation spectrum using the Bogoliubov-de-Gennes theory in Sec. 4.4. In Sec. 4.5, we analytically and numerically report the collective excitation spectrum, identifying various stability regions. Each subsection within Sec. 4.5 provides the excitation spectrum and corresponding dynamical observations using the GPEs. Finally, Sec. 4.6 summarizes the findings.

4.2 Mean-Field Model

We consider a quasi-1D spin-1 spinor SO coupled BECs realized by tight confinement in the transverse direction [145]. The non-dimensional dynamical equations for quasi-1D SO coupled spin-1 BECs are given by [39, 76, 106, 108],

$$\mathrm{i}\frac{\partial\psi_{\pm1}}{\partial t} = \left[-\frac{1}{2}\frac{\partial^2}{\partial x^2} + V + c_0\rho\right]\psi_{\pm1} \mp \frac{k_L}{\sqrt{2}}\frac{\partial\psi_0}{\partial x} + c_2(c_2^{\pm}\psi_{\pm1} + \psi_0^2\psi_{\mp1}^*) + \frac{\Omega}{\sqrt{2}}\psi_0\,, \tag{4.1a}$$

$$\mathrm{i}\frac{\partial\psi_0}{\partial t} = \left[-\frac{1}{2}\frac{\partial^2}{\partial x^2} + V + c_0\rho\right]\psi_0 + \frac{k_L}{\sqrt{2}}\left[\frac{\partial\psi_{+1}}{\partial x} - \frac{\partial\psi_{-1}}{\partial x}\right] + c_2(c_2^0\psi_0 + 2\psi_0^*\psi_{+1}\psi_{-1}) + \frac{\Omega}{\sqrt{2}}(\psi_1 + \psi_{-1})\,, \tag{4.1b}$$

where, $c_2^{\pm} = (\rho_{\pm1} + \rho_0 - \rho_{\mp1})$, $c_2^0 = (\rho_{+1} + \rho_{-1})$, ψ_j; $j = +1, 0, -1$, are the spinor condensate wavefunctions that satisfy the normalization condition $\int_{-\infty}^{\infty}\rho dx = 1$, where $\rho_j = |\psi_j|^2$, and $\rho = |\psi_{+1}|^2 + |\psi_0|^2 + |\psi_{-1}|^2$.

The dimensionless equations (4.1a)-(4.1b) are obtained by non-dimensionalized the time, length, and energy with respect to ω^{-1}, $l_0 = \sqrt{\hbar/m\omega}$, and $\hbar\omega$ respectively, where $\omega = \omega_x$ is the trap frequency along the x-axis. The resulting condensate wavefunction

takes the form as $\psi_j = \sqrt{\frac{l_0}{N}}\tilde{\psi}_j$, and N is the total number of atoms. $V(x) = x^2/2$ is the trap potential, $c_0 = 2Nl_0(a_0 + 2a_2)/3l_\perp^2$ is the density-density interaction strength, and $c_2 = 2Nl_0(a_2 - a_0)/3l_\perp^2$, spin-exchange interaction strength with a_0 and a_2 are the s-wave scattering length in total spin channels 0 and 2, respectively . The nature of interaction strength depends on the sign of c_2. $c_2 < 0$ represents the ferromagnetic condensate, while $c_2 > 0$ denotes the anti-ferromagnetic condensate [39, 117]. Here, $l_\perp = \sqrt{\hbar/(m\omega_\perp)}$ is the harmonic oscillator length in the transverse direction with $\omega_\perp = \sqrt{\omega_y\omega_z}$. The SO and Rabi coupling strengths are given by $k_L = \tilde{k}_L/\omega_x l_0$, $\Omega = \tilde{\Omega}/(\hbar\omega_x)$, respectively. In the above description, the quantities with tilde represent dimension-full quantities.

One important quantity characterizing the spin composition of the condensate is the magnetization of spin-1 spinor condensates defined by,

$$\mathcal{M} = \int_{-\infty}^{\infty} \Big\{\rho_{+1}(x) - \rho_{-1}(x)\Big\} dx \,. \tag{4.2}$$

The energy functional corresponding to the coupled GPEs (4.1a)-(4.1b) is given by [50, 109],

$$\begin{aligned} E =& \frac{1}{2}\int_{-\infty}^{\infty} dx \Big\{ \sum_j |\partial_x\psi_j|^2 + 2V(x)\rho + c_0\rho^2 \\ &+ c_2[\rho_{+1}^2 + \rho_{-1}^2 + 2(\rho_{+1}\rho_0 + \rho_{-1}\rho_0 - \rho_{+1}\rho_{-1} \\ &+ \psi_{-1}^*\psi_0^2\psi_{+1}^* + \psi_{-1}\psi_0^{*2}\psi_{+1})] + \sqrt{2}\Omega[(\psi_{+1}^* + \psi_{-1}^*)\psi_0 \\ &+ \psi_0^*(\psi_{+1} + \psi_{-1})] + \sqrt{2}k_L[(\psi_{-1}^* - \psi_{+1}^*)\partial_x\psi_0 + \psi_0^*(\partial_x\psi_{+1} - \partial_x\psi_{-1})] \Big\} \,. \end{aligned} \tag{4.3}$$

In order to make the dimensionless set of parameters used for our simulations viable for an experiment, here, we outline the dimensionful experimental parameters. For the ferromagnetic system, we consider ^{87}Rb BECs with $N \sim 2 \times 10^4$ number of atoms. The axial trap frequency is $\omega_x = 2\pi \times 50$ Hz while the transverse trap frequencies are considered to be $\omega_y = \omega_z = 2\pi \times 500$ Hz. The spin-dependent and spin-independent interactions can be achieved by controlling the s-wave scattering lengths through Feshbach resonance; by varying the magnetic field, we can tune the s-wave scattering lengths [120–122]. We can achieve the SO coupling strengths in the range of $k_L = \{0.1 - 5\}$ by changing the laser wavelengths from $\{68.86\mu$m - 1377.22nm$\}$. Further, one can also control the Rabi coupling strength in a similar range by changing the frequency of the laser, $2\pi\hbar \times \{5 - 250\}$ Hz.

TH-4102_206121026

4.3 Single-particle spectrum

In this section, we present the single-particle spectrum [123, 134, 146] of the non-interacting spinor condensate for trapless SO and Rabi-coupled spin-1 spinor BECs. Following that, we introduce the collective excitation spectrum for the interacting systems.

For $V(x) = 0$, and $c_0 = c_2 = 0$ as we substitute $\psi_{0,\pm1} = \phi_{0,\pm1} e^{\mathrm{i}(q_x x - \omega t)}$ in the Eqs.(4.1a)-(4.1b)) we obtain

$$\mathcal{L}_{sp} \begin{pmatrix} \phi_1 \\ \phi_0 \\ \phi_{-1} \end{pmatrix} = \omega \begin{pmatrix} \phi_1 \\ \phi_0 \\ \phi_{-1} \end{pmatrix} , \tag{4.4}$$

with

$$\mathcal{L}_{sp} = \frac{1}{2} \begin{pmatrix} q_x^2 & L & 0 \\ S & q_x^2 & L \\ 0 & S & q_x^2 \end{pmatrix} , \tag{4.5}$$

where $L = -\sqrt{2}(\mathrm{i}k_L q_x - \Omega), S = \sqrt{2}(\mathrm{i}k_L q_x + \Omega)$. Upon diagonalizing the Eq.(4.4), we obtain the single-particle spectrum as

$$\omega_0 = \frac{q_x^2}{2} , \tag{4.6a}$$

$$\omega_\pm = \frac{1}{2}(q_x^2 \pm 2\sqrt{\Omega^2 + k_L^2 q_x^2}) . \tag{4.6b}$$

From Eq. 4.6(a) and Eq. 4.6(b), it is quite evident that the single-particle spectrum exhibits three branches, namely, ω_0 and $\omega_\pm$. Among them, ω_0 is independent of SO and Rabi couplings, a constant branch of the single-particle spectrum. However, the detailed nature of the other two branches $\omega_\pm$ depends on the SO and Rabi couplings, which have been designated as positive and negative branches of the spectrum, respectively, throughout the paper.

To start with, we consider both the SO (k_L) and the Rabi (Ω) coupling strengths as zero. We obtain the non-degenerate parabolic spectrum of the SO coupled spin-1 system as couplings are set to zero [see Fig. 4.1(a)]. As ω_0 of the spectrum is independent of both the SO and Rabi couplings, it does not show any change upon the variation of coupling strengths as shown in Figs. 4.1(a)- 4.1(e) with the dash-dotted green line. To understand the behaviour of the positive branch (ω_+) and negative branch (ω_-) of

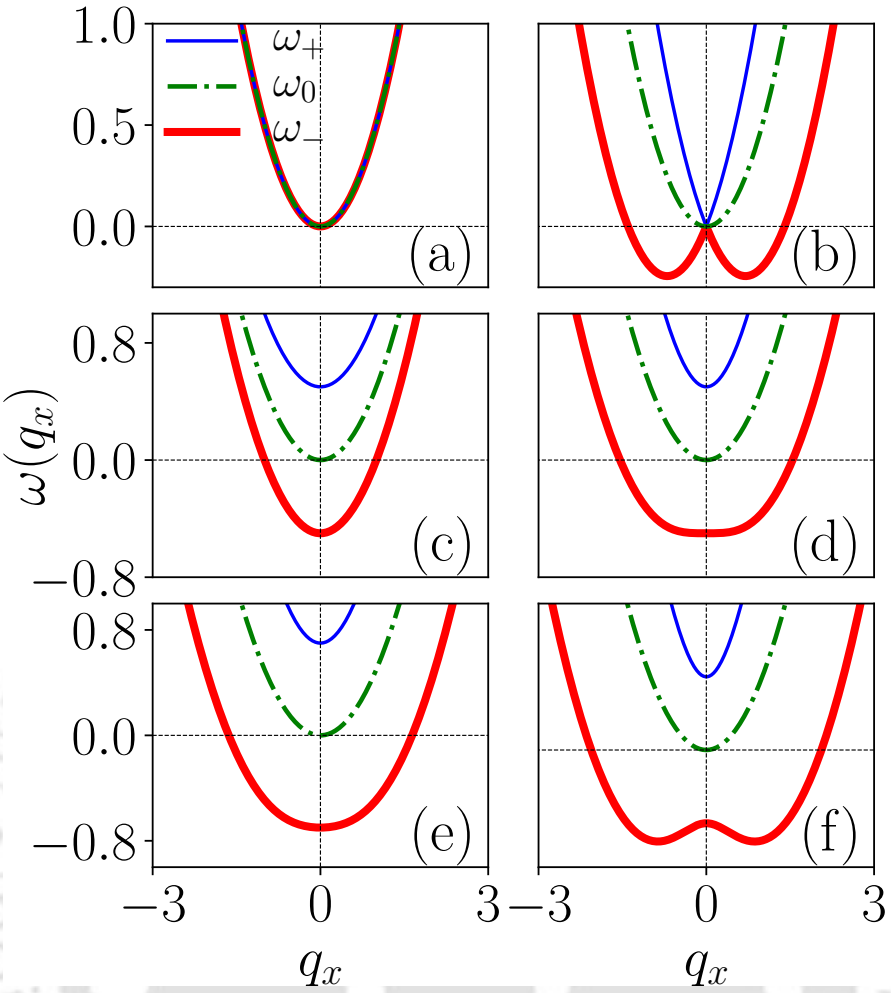


Figure 4.1: Single-particle energy spectrum in momentum space for the different set of SO and Rabi coupling strengths (k_L, Ω): (a)-(f): $(0,0)$, $(0.7,0)$, $(0,0.5)$, $(0.7,0.5)$, $(0.7,0.7)$, $(1.0,0.5)$. The thick-solid-red, dash-dotted green line and thin-solid-blue line represent the energy eigenspectrum for $\{-1,0,+1\}$ components of the spin, respectively. Varying the coupling parameters lead to the changes in the eigenspectrum of different components, where ω_-, only having the lowest minimum for $\Omega > k_L^2$, whereas $\Omega < k_L^2$, the ω_- exhibits double minima appearance of plane-wave phase, indicating the presence of stripe phase.

the single-particle spectrum, we introduce the finite value of SO coupling in the absence of Rabi coupling and vice-versa. First, we introduce a finite value to SO coupling strength, $k_L = 0.7$, in the absence of Rabi coupling strength, $\Omega = 0.0$. For this parameter, the negative branch of the spectrum gets transformed from the parabolic to double minima, which appears at $q_x = \pm k_L$ as shown in Fig. 4.1(b). Here the energy minima of $\omega_- = -0.245$ occurs at $q_x = \pm 0.7$. As Rabi coupling is increased to a finite value, $\Omega = 0.5$ while keeping $k_L = 0.0$, we find a change from double minima to a single minimum ($\Omega > k_L^2$) and also leading to opening up a gap between the $\omega_+ - \omega_0$ branches. The magnitude of the gap between the $\omega_+ - \omega_0$ branches, and $\omega_0 - \omega_-$ branches, is

TH-4102_206121026

of the order of Ω. It appears to be of 2Ω between the $\omega_+ - \omega_-$ branches as shown in Fig. 4.1(c) which exhibits a single minimum with $\omega_- = -0.5$ at $q_x = 0$. Further, we analyze the spectrum by introducing both couplings strengths,i.e., $k_L = 0.7$, $\Omega = 0.5$ for which we obtain the global minima in the spectrum, also satisfies the condition, $\Omega \approx k_L^2$. Upon increasing the Rabi coupling value from $\Omega = 0.5 \rightarrow \Omega = 0.7$, we obtain a similar kind of spectrum, but the gap between the branches increases with an increase in Rabi coupling as shown in Fig. 4.1(d) and Fig. 4.1(e), with energies $\omega_- = -0.5$, $\omega_- = -0.7$ at $q_x \approx 0.0$. On the other hand, upon increasing the SO coupling from $k_L = 0.7$ to $k_L = 1.0$, we obtain the transition of single minimum nature of ω_- into a double minimum as shown in Fig. 4.1(f). At a later stage, we will see that this feature (occurrence of double minima) in the single particle spectrum is responsible for the appearance of the stripe phase for the situation when $\Omega < k_L^2$. In Fig. 4.1(f), the lowest energy minima is $\omega_- = -0.625$ at $q_x \approx \pm 0.9$. From the observation we find that, when $\Omega > k_L^2$, the energy depends on only the Rabi coupling, while if $\Omega < k_L^2$ energy depends on SO coupling strength. Overall, we find that, upon variation of SO coupling, the positive branch exhibits a single minimum upon fixing the Rabi coupling at a finite value. However, the negative branch exhibits a transition from the single minimum to a double minimum upon varying the SO coupling, keeping the Rabi coupling fixed. This typical feature of the negative branch of the spectrum appears to indicate the change in the phases of the condensate upon varying the coupling parameters, and therefore, for later parts of our discussion, we will focus on analyzing the typical features of the ω_- branch.

In the next section, we discuss the effect of both coupling terms (SO and Rabi) on the collective excitation spectrum for the interacting SO and Rabi-coupled spin-1 BECs.

4.4 Collective Excitation spectrum: Bogoliubov-de-Gennes Analysis

In the previous section, we have discussed the single-particle spectrum of SO coupled spin-1 ferromagnetic BECs. In this section, we shall present the collective excitation spectrum of the uniform condensate using the Bogoliubov-de-Gennes (BdG) analysis. The excitation wave function in terms of perturbation term $\delta\phi_j$ and uniform ground state wave function ϕ_j can be represented as [20, 138],

$$\psi_j(x,t) = \mathrm{e}^{-\mathrm{i}\mu_j t}[\phi_j + \delta\phi_j(x,t)] \,, \tag{4.7}$$

TH-4102_206121026

where,

$$\delta\phi_j(x,t) = u_j e^{i(q_x x-\omega t)} + v_j^* e^{-i(q_x x-\omega^* t)} , \tag{4.8}$$

represents the uniform ground state wave function with $\phi_j = (1/2, -1/\sqrt{2}, 1/2)^T$. Here, μ_j denotes the chemical potential, u_j, v_j are the Bogoliubov amplitudes, with $j = +1, 0\ -1$ corresponding to the three components of spinor density of condensates. As we substitute Eq. (4.7) in the dynamical equations [Eqs. (4.1a)-(4.1b)] we obtain,

$$\mathcal{L}\begin{pmatrix} u_{+1} & v_{+1} & u_0 & v_0 & u_{-1} & v_{-1}\end{pmatrix}^T = \omega\begin{pmatrix} u_{+1} & v_{+1} & u_0 & v_0 & u_{-1} & v_{-1}\end{pmatrix}^T , \tag{4.9}$$

where T represents the transpose of the matrix and $\mathcal{L}$ is 6×6 matrix given by,

$$\mathcal{L} = \begin{pmatrix} H_+ - \mu_+ & \mathcal{L}_{12} & \mathcal{L}_{13} & \mathcal{L}_{14} & \mathcal{L}_{15} & \mathcal{L}_{16} \\ \mathcal{L}_{21} & -H_+ + \mu_+ & \mathcal{L}_{23} & \mathcal{L}_{24} & \mathcal{L}_{25} & \mathcal{L}_{26} \\ \mathcal{L}_{31} & \mathcal{L}_{32} & H_0 - \mu_0 & \mathcal{L}_{34} & \mathcal{L}_{35} & \mathcal{L}_{36} \\ \mathcal{L}_{41} & \mathcal{L}_{42} & \mathcal{L}_{43} & -H_0 + \mu_0 & \mathcal{L}_{45} & \mathcal{L}_{46} \\ \mathcal{L}_{51} & \mathcal{L}_{52} & \mathcal{L}_{53} & \mathcal{L}_{54} & H_- - \mu_- & \mathcal{L}_{56} \\ \mathcal{L}_{61} & \mathcal{L}_{62} & \mathcal{L}_{63} & \mathcal{L}_{64} & \mathcal{L}_{65} & -H_- + \mu_- \end{pmatrix} . \tag{4.10}$$

The matrix elements of $\mathcal{L}$ are given in appendix A. Bogoliubov coefficients follows the normalization condition,

$$\int \left(\sum_j \{|u_j|^2 - |v_j|^2\} \right) dx = 1 \tag{4.11}$$

The simplified form of the BdG excitation spectrum is obtained by calculating the determinant of the matrix $\mathcal{L}$ and equate it with zero, i.e., $det\ (\mathcal{L} - \omega \mathrm{I}) = 0$, where I is a 6×6 identity matrix. The characteristic equation can be written as,

$$\omega^6 + b\omega^4 + c\omega^2 + d = 0 , \tag{4.12}$$

where the coefficient of b, c, and d are given in the appendix A.

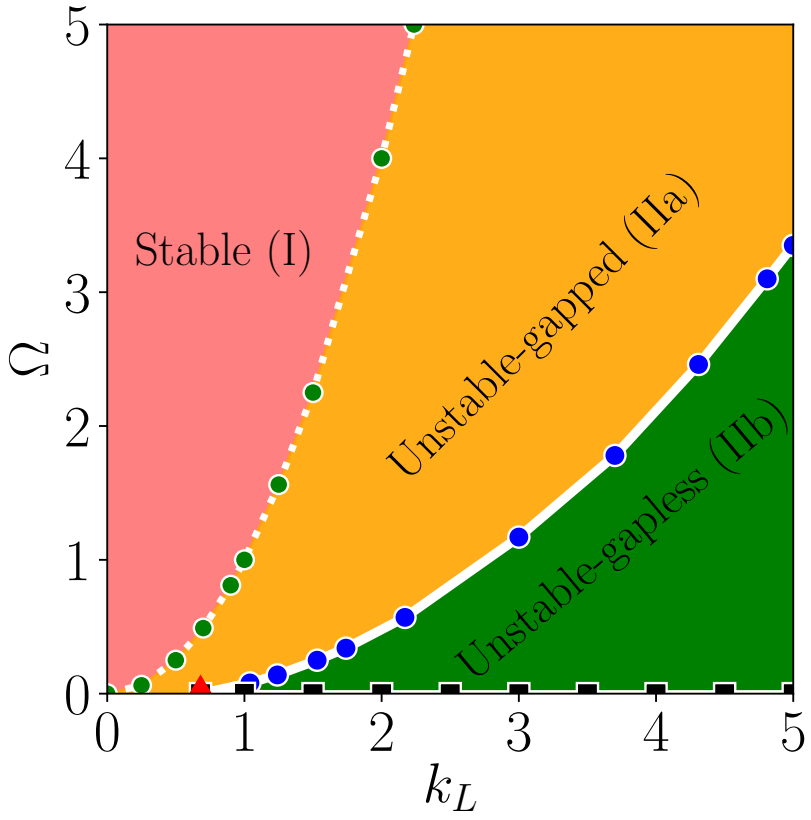


Figure 4.2: Stability phase diagram in the k_L- Ω plane for the interaction parameter $c_0 = 0.5$, $c_2 = -0.1$ which is being considered for all the simulation runs. Based on the different characteristics of the eigenspectrum and ground state, the phase diagram is divided into regions I, IIa, IIb, and III. While Region I is stable, regions IIa, IIb, and III are unstable. The dotted white line along with green dots represent the $\Omega = k_L^2$ curve that separates region I from IIa. Blue dots with a white solid line representing $\Omega \approx 0.1365k_L^2 - 0.0686$ separates the regions IIa and IIb. The horizontal line with a filled half square for $\Omega \sim 0$ denotes the region III after the cutoff, $k_L^c = 0.68$, which is a tricritical point for regions IIa-IIb-III, indicated as a red triangle.

4.5 Effect of Rabi and SO coupling on the excitation spectrum

To better understand the stability of the stationary state phases of the system, we plot the stability diagram of the system in k_L - Ω plane with interaction parameters $c_0 = 0.5$, and $c_2 = -0.1$ [147]. We obtain the stability phase plot by solving the collective excitation spectrum. The real frequencies of the BdG matrix imply the dynamically stable phase while the imaginary frequency indicates a dynamically unstable phase [20, 21, 39, 93, 148]. In Fig. 4.2, we show the stability diagram in the $k_L - \Omega$ plane. Based upon the eigenvalue, the plane is divided mainly into three regions, viz., stable region I, unstable regions II, and III. White dots with the dotted line sep-

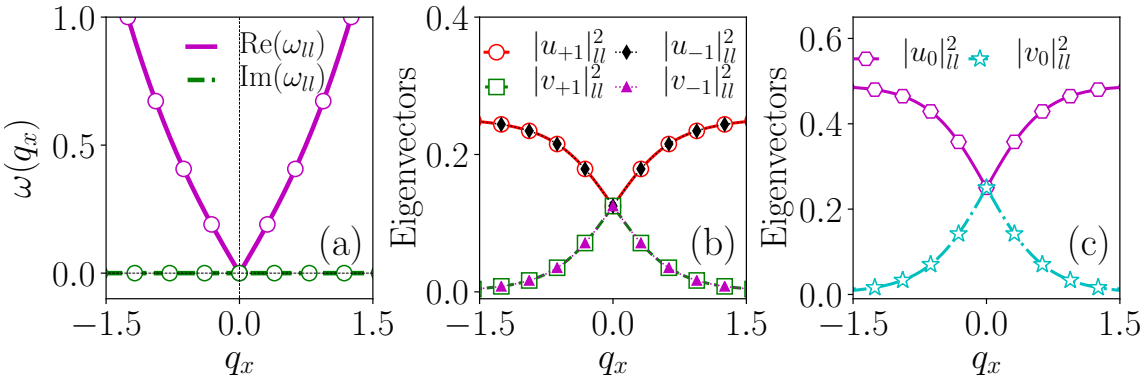


Figure 4.3: Excitation spectrum (a) and eigenvectors (b) and (c) for the coupling parameters $k_L = 0.5$, $\Omega = 2.0$. (a) solid magenta line represents $\mathrm{Re}(\omega_-)$, and dashed-dotted green line represents the $|\mathrm{Im}(\omega_-)|$, here solid and dash-dotted lines are the analytical results of BdG Eq. 4.12 and open circles are numerical results obtained by solving Eq. 4.9. In the eigenvectors, $|u_{+1}|^2$(red open circles), $|u_{-1}|^2$ (black diamonds), $|u_0|^2$ (magenta open hexagons), $|v_0|^2$ (cyan open stars), $|v_{+1}|^2$ (green open squares), and $|v_{-1}|^2$ (magenta triangles), (b-c) the eigenvectors corresponding to eigenspectrum has shown, which we obtained by solving Eq. 4.9 numerically. The first column of the figure shows the presence of phonon mode in the eigenspectrum. Also, it has no negative or complex eigenfrequency thus, it is energetically and dynamically stable.

arate the stable and unstable regions, which hold the phase transition boundary, i.e., $\Omega = k_L^2$ [93]. Further, we divide the unstable region into two separate parts: regions IIa and IIb. Blue dots with white solid line separate the regions IIa and IIb. The phase transition critical points for region-IIa to region-IIb can be obtained by a polynomial fit given by $\Omega \approx 0.1365k_L^2 - 0.0686$. In region IIa, we obtain a clear gap between the low-lying (negative branch) and first-excited (positive branch) branches of the spectrum. Also, for a fixed value of Rabi coupling strength (Ω), upon increasing the SO coupling strength (k_L), the number of instability bands changes from 1 to 2 or vice versa. In region IIb, we obtain overlap among the low-lying (ll) and first-excited (fe) branches of the eigenspectrum. Thus, the line delineates regions IIa and IIb, encompassing points where instability is present by means of multiple instability bands and gap openings between low and first excited states. Furthermore, in region IIb, we observe a spectrum characterized by multiple instability bands. In this region for a fixed value, Rabi strength (Ω), upon increasing the SO coupling strength k_L, we achieve mode corresponding to no gap between the low-lying and first-excited branches of the spectrum for some range of quasi-momentum. By increasing the Rabi coupling strength with fixed SO coupling, we can again achieve the gapped mode between the low-lying and first excited branches.

The transition from the region-IIa to IIb can be obtained after a certain critical coupling point. We obtain the gapless behaviour of eigenspectrum either increasing SO

TH-4102_206121026

coupling ($k_L > k_L^c$) for a fixed Rabi coupling ($\Omega > \Omega^c$) or decreasing Rabi coupling ($\Omega^c < \Omega$) for a fixed SO coupling ($k_L > k_L^c$), with the critical coupling parameters as $k_L^c = 0.68$, and $\Omega^c = 0.001$. This point is the origin of the line which separates regions IIa and IIb. The horizontal line at which Rabi coupling strength is approximately zero, ($\Omega \approx 0.0$), we realize the presence of phonon mode in the low-lying as well as in the first-excited branch of the spectrum, along with the presence of instability band. These features present in IIa and IIb are completely different compared to those obtained for the region I. The cutoff value of SO coupling strength to obtain this behaviour along the line is $k_L^c = 0.68$. We analyze the behaviour of the system along the horizontal line separately under Region III. Here, k_L^c is the tricritical point for regions IIa, IIb, and III, which is indicated by the red triangle in the phase plot [see Fig. 4.2]. Based on the above observations, we divide the phase plot into three different regions: regions I, IIa, IIb, and III.

As we divide the phase diagram of the $k_L - \Omega$ plane into three regions, we discuss their behaviour in each region individually. The detailed structure of the presentation in different regions is as follows. We perform collective excitation spectrum calculations to understand the stability of the system, both dynamically and energetically. As the real but negative eigenfrequencies of the BdG matrix suggests energetically unstable nature of the condensate while complex eigenfrequencies indicates dynamically unstable nature of the condensate [21, 39]. To validate these claims, we perform numerical simulations using the GPEs. We provide the eigenvalue spectrum, eigenvectors, and numerical simulation in every subsection.

Following this, we corroborate the analytical results for the excitation spectrum by numerically solving the BdG equations (4.10) from which we also obtain the eigenvectors as a function of q_x. First, we consider a $[-1000 : 1000]$ grid in real space with step size $h_x = 0.2$. Then, we use the Fourier collocation method, where we numerically compute the Fourier transform of the BdG equations and obtain a truncated reduced BdG matrix, which is subsequently diagonalized using the LAPACK package [149]. In momentum space, we consider $[-700 : 700]$ modes in the q_x direction, with a grid step size of $h_{q_x} = 0.0157$.

Further, we provide the analysis of the real-time dynamics corresponding to the collective excitation spectrum by solving coupled GPEs (Eqs. (4.1a) - (4.1b)) numerically. We use the imaginary-time propagation method to obtain the stationary state. Then, we evolve the stationary state in time using the real-time propagation method. For this purpose, we adopt the split-step Crank-Nicholson scheme outlined in Refs. [50, 72, 150]. We have considered a grid of 1280 space points with space step $dx = 0.05$,

TH-4102_206121026

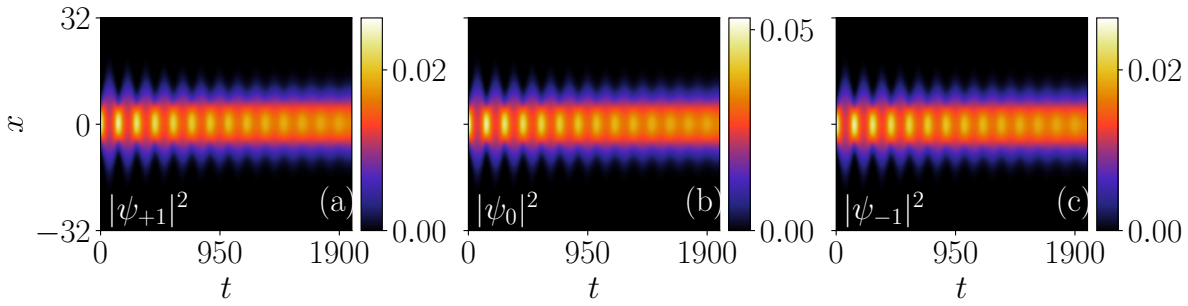


Figure 4.4: Time evolution of initially prepared stationary state density profiles illustrating dynamical stability of (a) $+1$, (b) 0, and (c) -1 components of the condensate, where the parameters are similar to Fig. 4.3. All three components $|\psi_{+1}|^2$, $|\psi_0|^2$, and $|\psi_{-1}|^2$ depict stable breather-like dynamics, which validate the dynamical stability of the condensate.

time step $dt = 0.00025$ for imaginary-time-propagation, and $dt = 0.0005$ for real-time-propagation. Initially, we obtain the stationary states according to the regions in the phase plot [see Fig. 4.2] by using imaginary-time propagation. After calculating the stationary state, we evolve it using real-time propagation by quenching the trap strength.

The Bogoliubov-de Gennes analyses are performed for homogeneous stationary condensate densities in order to identify stable and unstable modes of the excitation spectra. The corresponding real-time simulations are carried out in the presence of a weak harmonic trap. The condensate is first prepared numerically using imaginary-time propagation and subsequently evolved after externally quenching the trap strength, which leads to the post-quench dynamics of the condensate. Similar procedures are also employed in Chapters 5 and 6 of the thesis.

4.5.1 Excitation spectrum in region I

4.5.1.1 Excitation spectrum

We present the collective excitation spectrum for the stable case and corresponding eigenvectors in Fig. 4.3. Here, we consider the coupling strengths, $k_L = 0.5$ and $\Omega = 2.0$. Fig. 4.3(a) shows only the presence of $\mathrm{Re}(\omega)$ in the eigenspectrum. The above suggests the presence of phonon mode [27]. The absence of negative and imaginary eigenfrequency in the spectrum indicates that the phase is energetically and dynamically stable throughout the region-I.

We present the eigenvectors corresponding to the eigenspectrum in Fig. 4.3(b) and (c). We have three sets of eigenvectors: $|u_{+1}|^2$, $|u_{-1}|^2$, $|u_0|^2$, $|v_0|^2$, $|v_{+1}|^2$, and $|v_{-1}|^2$. The eigenvectors exhibit in-phase behaviour in all components for all wavenumber, which means that $|u_{+1}(q_x)|^2 = |u_{-1}(q_x)|^2$ and $|v_{+1}(q_x)|^2 = |v_{-1}(q_x)|^2$, indicating

TH-4102_206121026

the presence of a density-like (in-phase) excitations. [see Figs. 4.3(b) and 4.3(c)]. We demonstrate that both u and v eigenvectors are in-phase. For $q_x \approx 0$, the eigenvector components approach each other, and at $q_x = 0$, they have equal values, signifying the presence of a phonon mode, as mentioned earlier. As anticipated, the eigenspectrum and eigenvectors exhibit the same behaviour for other sets of parameters (k_L, Ω) in the same region (region I of Fig. 4.2) of the k_L-Ω plane. The critical change in the eigenspectrum is that with increasing coupling strengths, the real eigenspectrum widens similarly to how the eigenvectors also widen after the junction at $q_x = 0$.

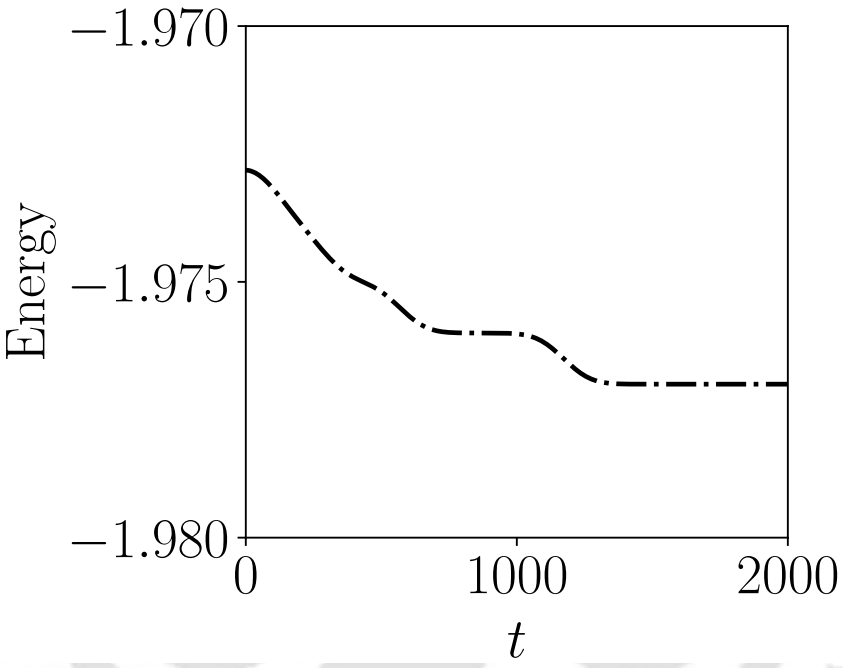


Figure 4.5: Energy variation in the time evolution for the stable region I. The parameter values considered in this figure are similar to Fig. 4.3. During time evolution, the condensate exhibits temporal variation of the energy and further shows stable behaviour.

4.5.1.2 Dynamical stability

We have considered the same coupling parameters, $(k_L, \Omega) = (0.5, 2)$, to examine the dynamical behaviour of region-I, and the interaction strengths are $c_0 = 0.5$, and $c_2 = -0.1$ by solving the GPEs (Eqs. (4.1a) - (4.1b)). Here, we obtain the plane-wave phase as a ground state of the condensate. To understand the stability of the ground state, quench the trap strength to half and further evolve the condensate. The density of the condensate shows stable breather-like motion throughout the dynamical evolution [see Fig. 4.4(a)-(c)]. In addition, the system density profile is symmetric in nature and

TH-4102_206121026

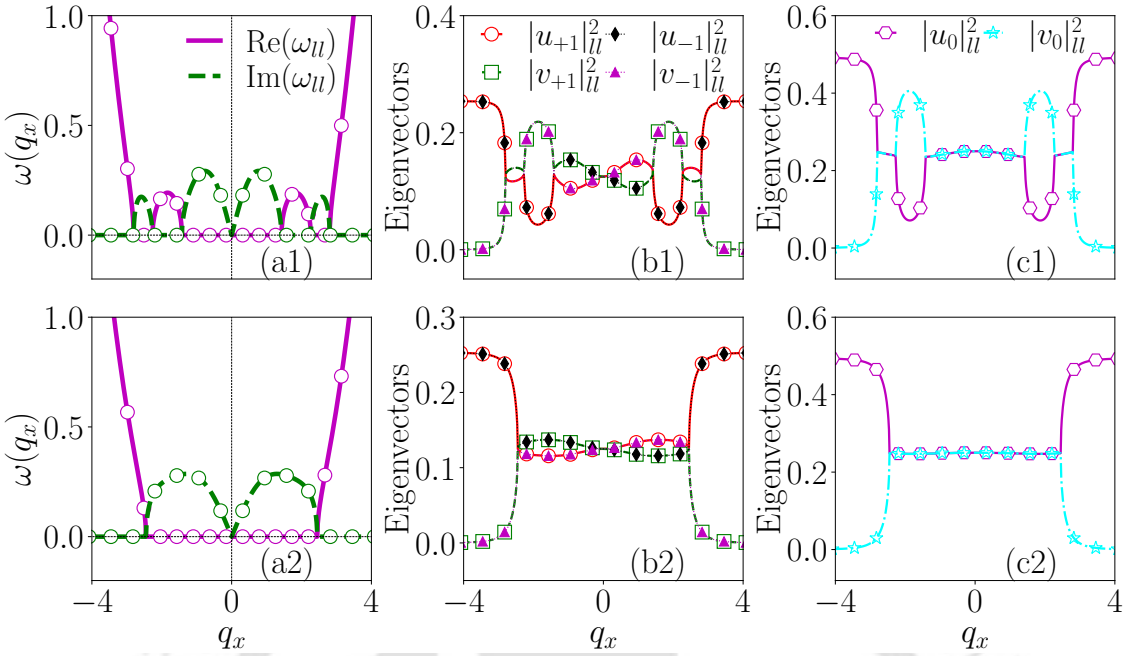


Figure 4.6: Stability excitation spectrum eigenvalues and eigenvectors: The SO and Rabi coupling strength are $(k_L, \Omega) = (2.0, 2.0)$ (top row), and $(2.35, 4.0)$ (bottom row), respectively. (a1), (a2) shows eigenenergy, (b1), (c1), and (b2), (c2) corresponding eigenvectors, figure labels are as like Fig. 4.3. The eigenenergy spectrum shows the presence of complex eigenfrequencies in terms of two (one) bands in the top (bottom) row, which indicates the system is dynamically unstable. Whereas the eigenvectors display the spin-dipole along with spin-like mode along the q_x momentum direction, also symmetric along the axis.

doesn't show any oscillations, as shown in Figs. 4.4(a)-(c). Thus, it is clear that the system is not showing polarization behaviour as we expected from the in-phase nature of eigenvectors shown in Figs. 4.3(b)-(c).

In Fig. 4.5, we plot the total energy of the condensate. In real-time evolution, we quench the trap strength to one-half its original value through the finite time step dt. Immediately after the numerical quench of the trap strength, transient nonequilibrium dynamics are generated due to finite time implementation of the quench during the time interval dt. Subsequently, the condensate exhibits the stable post-quench evolution under the post-quench Hamiltonian. Therefore, we find that the ground state of the condensate is energetically and dynamically stable, as shown in the stability phase plot Fig. 4.2 corresponding to the excitation spectrum. We also investigate the dynamical spin texture of this region, which does not change its behaviour during the dynamical evolution.

TH-4102_206121026

4.5.2 Excitation spectrum in region IIa

4.5.2.1 Excitation spectrum

To investigate region II, we divide it into two sub-parts, region IIa and IIb. In the first sub-part, we consider two points with fixed SO and Rabi coupling strengths: $(k_L, \Omega) = (2, 2)$, and $(k_L, \Omega) = (2.35, 4)$, respectively. We plot the dispersion relation of collective excitations and corresponding eigenvectors at these values of the coupling parameters in Fig. 4.6. Fig. 4.6(a1) shows the presence of the imaginary part of the eigenspectrum at larger values of quasi-momentum q_x having two imaginary bands. As we increase the value of Rabi coupling to larger extents than SO coupling strength, the double imaginary eigen-bands change into a single band [see Fig. 4.6(a2)]. It is also shown in Fig. 4.2, where the second point falls on the boundary of regions I and IIa. Therefore, we can state that the second point is approaching towards the stable regime.

The eigenvectors corresponding to the eigenenergy is presented in Figs. 4.6(b) and (c). Unlike the behaviour observed in Region I, we find complex behaviour in the eigenvector components here. The eigenvectors shows in momentum direction the transition from density-like (in-phase) excitations, where $|u_{+1}(q_x)|^2 = |u_{-1}(q_x)|^2$ and $|v_{+1}(q_x)|^2 = |v_{-1}(q_x)|^2$, to the spin-like (out-of-phase) excitations, where $|u_{+1}(q_x)|^2 = |v_{-1}(q_x)|^2$ and $|v_{+1}(q_x)|^2 = |u_{-1}(q_x)|^2$. In Fig. 4.6(a1), the eigenspectrum has double band instability; corresponding to this, dual transitions from density-like mode to the spin-like mode for ± 1 components of eigenvectors. Still, the 0-th component exists only in density-like mode. Also, there is an amplitude difference among all three components of the eigenvector; the ± 1 components have half of the amplitude value than the 0-th component [see Figs. 4.6(b1) and 4.6(c1)].

For the second point in the region [see Fig. 4.6(a2)], the eigenspectrum has only single-band instability and, corresponding to this, there is a constant transition from the density-like mode to the spin-like mode of ± 1 components of eigenvectors [see Fig. 4.6(b2)]. The amplitude of ± 1 and 0 appears the same as for the previous point. It is observed from the above discussion whenever the $\mathrm{Im}(\omega_-)$ appears, the density-like mode (where we have $\mathrm{Re}(\omega_-) = 0$) changes into the spin-like mode. From the transition point of view, when comparing these two points in this region-IIa, one can notice that the multi-band instability has mixed density-like and spin-like mode behaviour in the eigenvectors. In detail, by comparing Figs. 4.6(b1) and 4.6(b2), the second only has the density-like mode in the major portion of the momentum space. But first one has a mixed type of mode in the same range of momentum space, where imaginary eigenvalues appeared at $0 < q_x < 2$, it has spin-like mode when $2 < q_x < 3$ eigenval-

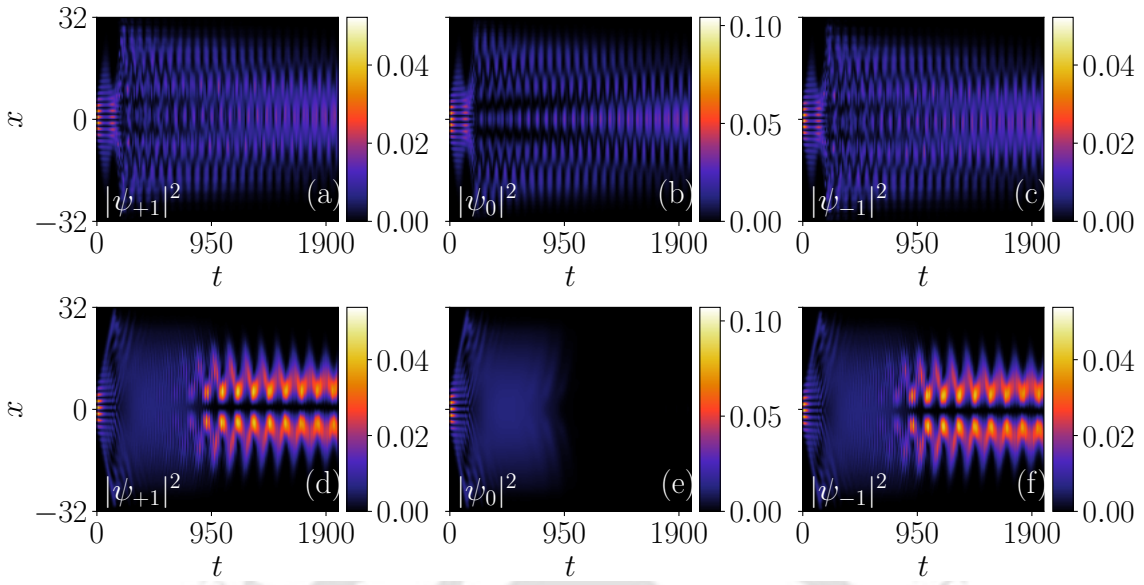


Figure 4.7: Dynamics: (a-c) and (d-f) depict temporal evolution of stationary state density profile of $|\psi_{+1}|^2$, $|\psi_0|^2$, and $|\psi_{-1}|^2$ for (k_L, Ω): top row $(2.0, 2.0)$ and bottom row $(2.35, 4.0)$, respectively. The density profile holds stripe wave behavior in both cases for $t < 150$, and $t < 180$ for the top and bottom row, respectively. Further, it gets fragmented into several small domains. This behavior signifies the change in shape and amplitude of the density profile, where the bottom row 0-th component gets diminished, whereas the ± 1 components gained the density.

ues are real, then it exhibits density-like mode, for $3 < q_x < 3.5$ again spin-like mode, $q_x > 3.5$ density-like mode (behaviour is symmetric about the momentum axis). Such complex-mixed-mode has not been explored in the spinor SO coupled system. We highlight that this study will be helpful for the experimental researcher to achieve the stable ferromagnetic spinor SO coupled BEC experimentally.

4.5.2.2 Dynamical stability

We divide region II into two subregions: IIa and IIb. We focus on the system's dynamics in region IIa, specifically at two different points within the region IIa. For each point, we analyzed the dynamic behaviour of the system separately. We discuss the dynamic behaviour of the system for each point separately. We choose $(k_L, \Omega) = (2, 2)$. We obtain the stationary state using imaginary-time propagation, which is the stripe-wave, and evolve the stationary state using real-time propagation. The dynamical evolution of the state shows the stripe wave phase holds up to $t = 150$. Furthermore, the density profile of all three components fragmented into non-periodic domains [see Figs. 4.7(a)-(c)] [125]. If the system has a nonvanishing 0-th component in the dynamical evolution, then the system tends to be less subjected to instability. Conversely, if the

TH-4102_206121026

0-th component vanishes, the system becomes more prone to instability [151]. In this case, the appearance of the 0-th component in the dynamical evolution confirms that the chosen coupling point has a lower risk of instability. We plot the total energy of the condensate in Fig. 4.8(a). The condensate energy initially has a value of -2.471 and subsequently exhibits transient variation following the numerical quench of the trap strength. The energy becomes positive near $t = 205$ units and later approaches stable behaviour around $t \sim 365$ time units. The observed transient energy variation originates from the finite-time numerical implementation of the quench during the interval dt. For this point, as shown in Fig. 4.6(a1), the BdG excitation spectrum has complex eigenfrequencies, and the eigenvector shows the out-of-phase behaviour for the certain range of quasi-momentum. The above indicates that the system is dynamically unstable and generates non-linear wave patterns, which matches well with numerical simulation results.

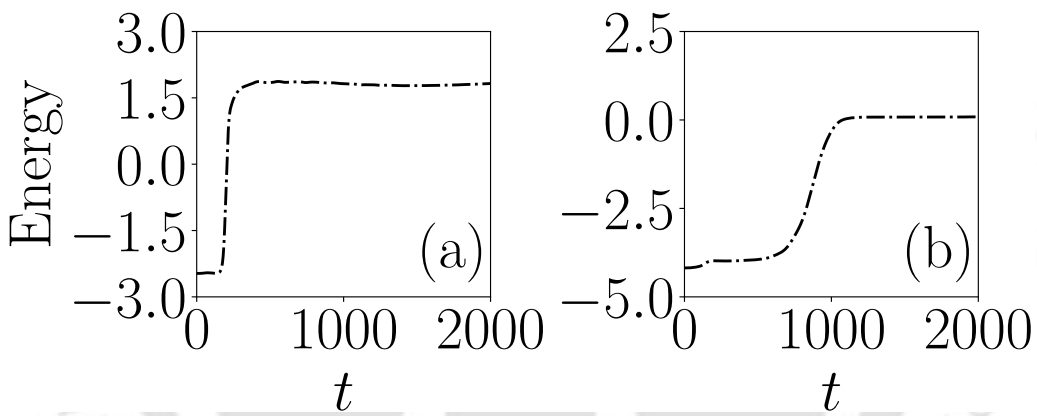


Figure 4.8: (a) and (b) represent the total energy of the condensate for the density evolution in Fig. 4.7. In both cases, the energy of the condensate increases at the beginning of dynamical evolution, but finally shows well-settled stable behavior; such a sudden change happened due to the external perturbation.

We choose another point in the region IIa at which we consider the value of SO coupling strength $k_L = 2.35$ and $\Omega = 4.0$. We achieve the stationary state, which is stripe-wave-phase. The excitation spectrum has complex eigenfrequencies, as shown in Fig. 4.6(a2). The presence of complex eigenfrequencies indicates that the system is dynamically unstable. To verify this claim numerically, we evolve the stationary state of the system using the real-time-propagation method as illustrated in Figs. 4.7(d)-(f). The stripe wave behaviour of the condensate holds its shape for a while. Then, it gets fragmented into several small domains [125]. In addition, we observe that with time, the zeroth component of density starts diminishing, and finally, it disappears [see Fig. 4.7(e)]. Other components of the condensate density ($|\psi_{\pm 1}|^2$) boosted the magnitude after the zeroth component of the density disappears [see Figs. 4.7(d), and (f)].

As one considers the quadratic Zeeman effect, then such kind of dynamical disappearance does not take place [151]. However, in this work, we see such sort of dynamical instability in the excitation of spin-1 BECs in the presence of SO coupling alone. So far we find that the density pattern of the system changes its shape and amplitude accompanied with disappearance of the 0-th component, which is a signature of dynamical instability. Further, we show the total energy of the condensate in Fig. 4.8(b). It starts from -4.182 and changes its sign from negative to positive at $t = 1080$, which is higher for this point, where the 0-th component vanishes, and then the particles are shared by the spin-up and down components, there, the energy gets settled. Such kind of 0-th component vanishing behaviour is not observed for the previous case due to the appearance of spin and density-mixed modes. The transient energy variation arises from the finite-time numerical quench process. After the transient evolution, the energy approaches a nearly constant value $E \sim 0.08$ at $t = 1195$ units. Upon investigating the dynamical spin texture of this region, we notice that the initial pattern does not maintain its shape as time progresses and changes its spin texture during the dynamical evolution [not shown here]. We note that the apparent increase in the total energy observed in Fig. 4.8 occurs during the early time evolution following the quench. We emphasize that this behavior is associated with the transient nonequilibrium dynamics induced by the sudden change in the trapping potential, during which the system evolves from an initial stationary state of the pre-quench Hamiltonian to the dynamics governed by the post-quench Hamiltonian. In this short transient regime, the condensate undergoes rapid internal readjustment, leading to strong redistribution among kinetic, interaction, spin–orbit, and Rabi energy contributions. We further note that the total energy is evaluated using the post-quench Hamiltonian and is conserved within numerical accuracy once the transient stage is completed. The norm of the condensate is strictly conserved throughout the entire time evolution for all parameter sets considered. To ensure the robustness of this behavior, we have performed convergence tests with reduced time step dt and we find that the qualitative features remain unchanged, while the onset of the transient redistribution shifts slightly at later time. This confirms that the observed behavior is not a numerical artifact but a manifestation of the intrinsic nonequilibrium dynamics of the system following the quench.

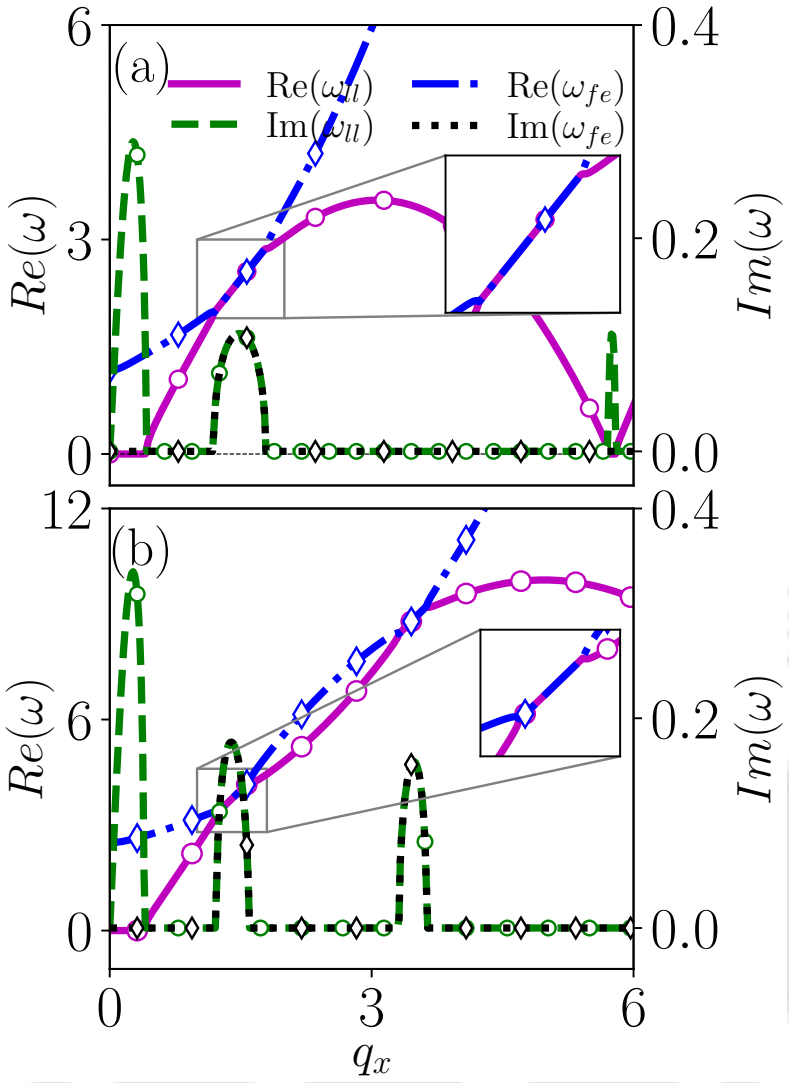


Figure 4.9: Excitation spectrum (a), and (b) for the coupling strengths, $(k_L, \Omega) = (3.1, 1.17)$ and $(5.0, 2.5)$ depict the low-lying and first-excited branches of the spectrum. The solid magenta line represents the $\mathrm{Re}(\omega_-)$ and the dashed green line represents the $|\mathrm{Im}(\omega_-)|$ which is low-lying branch of the spectrum, while the blue dash-dotted line represents $\mathrm{Re}(\omega_+)$ and black dotted line represents $|\mathrm{Im}(\omega_+)|$ corresponding to the first-excited branch of the spectrum, which obtained from Eq. 4.12. The eigenspectrum in (a, b) shows multiple instability bands as we obtained in 4.6(a1), however, (a) and (b) show one and two mode corresponding to no gap exists between the lower branch and first excited branch. Insets are for the better visualization of no gap mode between the lower and first excited state branch, the secondary y-axis scale is for representing the imaginary eigenfrequencies magnitudes.

4.5.3 Excitation spectrum in region IIb

4.5.3.1 Excitation spectrum:

In this subpart of region II, we choose two different points at which we consider the coupling strengths as $k_L = 3.1$, $\Omega = 1.17$, and $k_L = 5.0$, $\Omega = 2.5$, respectively. The collective excitation spectrum of the condensate for these sets of parameters is given in

TH-4102_206121026

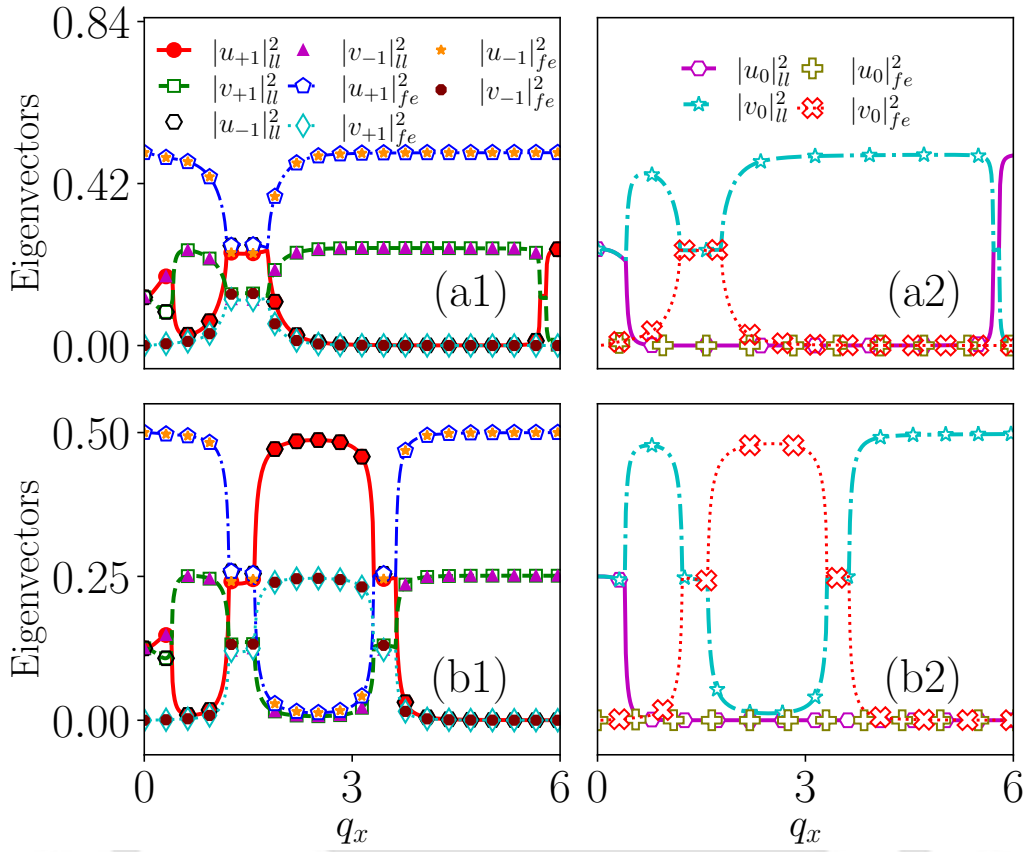


Figure 4.10: The eigenvectors top and bottom rows corresponding to Fig. 4.9(a), and Fig. 4.9(b), respectively. The eigenvectors represents as $|u_{+1}|^2_{ll}$ (red dot), $|u_{-1}|^2_{ll}$ (black hexagons), $|u_0|^2_{ll}$ (magenta hexagons), $|v_0|^2_{ll}$ (cyan open stars), $|v_{+1}|^2_{ll}$ (green open squares), and $|v_{-1}|^2_{ll}$ (magenta triangles). Whereas, $|u_{+1}|^2_{fe}$ (blue open pentagon), $|u_{-1}|^2_{fe}$ (orange stars), $|u_0|^2_{fe}$ (olive open plus), $|v_0|^2_{fe}$ (red open x with the dotted line), $|v_{+1}|^2_{fe}$ (cyan open diamond), and $|v_{-1}|^2_{fe}$ (maroon dots). We depict the $+q_x$, however, the eigenfrequencies and eigenvectors are symmetric about the axis. Here we found that the eigenvectors show the spin-like mode when the complex-frequency exhibits, the density-like mode when it is only real.

Fig. 4.9. We obtain complex eigen frequencies for both points [see Figs. 4.9(a)- 4.9(b)]. Still, the number of instability bands along the quasimomentum direction and its amplitude differ for both points. In Fig. 4.9(a), the number of low-lying instability bands is three, and the positions and amplitudes are $\{q_x, \omega\} = \{0.27, 0.29\}$, $\{1.48, 0.11\}$, and $\{5.75, 0.11\}$, respectively. Further, we show the first excited (ω_{fe}) and low-lying (ω_{ll}) branches of the eigenspectrum, which overlap with each other, where we also find that the complex eigenfrequency is not similar to the eigenspectrum of the previous case region-IIa. This results in modes corresponding to no gap between the first- and low-lying excited spectrum. However, we find three complex eigenfrequencies in which the overlapping point shows complex eigenfrequencies for both spectra. The phenomenon

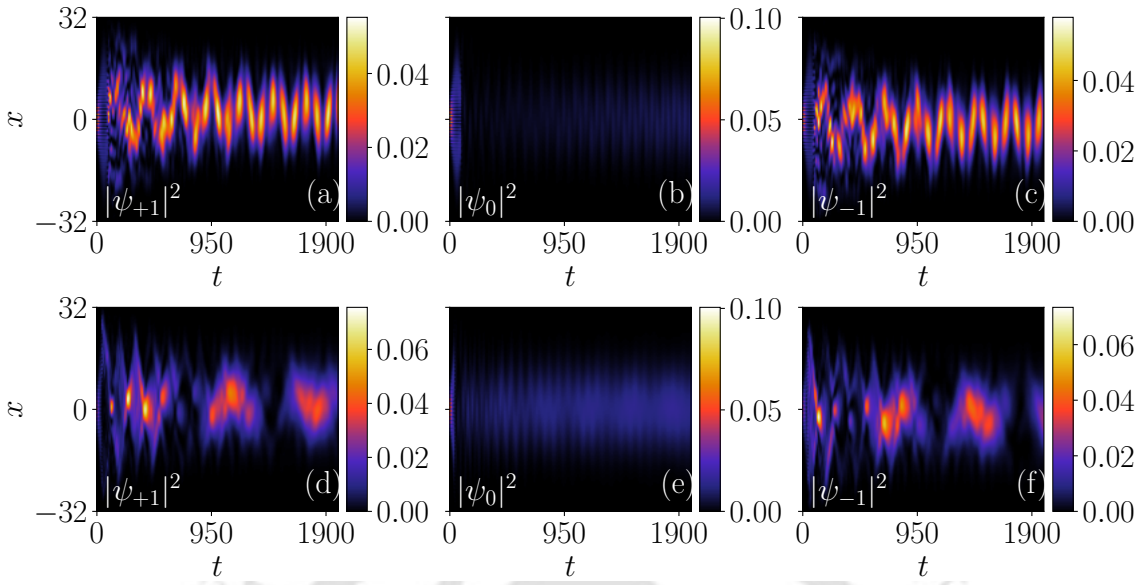


Figure 4.11: Dynamics: (a)-(c) and (d)-(f) represent the dynamics of the condensate density profile of $|\psi_{+1}|^2$, $|\psi_0|^2$, and $|\psi_{-1}|^2$ components for (k_L, Ω) top row $(3.1, 1.17)$, and bottom row $(5.0, 2.5)$. The density profile holds stripe wave behavior in both cases for $t < 100$ and $t < 50$ units for the top and bottom row, respectively. Top row: $t > 100$, it shows non-periodic oscillation and non-uniform density in space-time, whereas the 0-th component gets disappeared. Bottom row: $t > 50$, it further gets fragmented into several small domains. This behaviour signifies the change in shape and amplitude of the density profile, along with the disappearance of the 0-th component, which confirms the dynamical instability.

that has been observed in the spinor BECs is related to the *unstable avoided crossing* between spin and charge modes by considering $\theta = \pi$, the phase difference between the perturbed wave fields, which also provides the class I_o oscillatory patterns as a result of the dynamical instability [95, 144]. However, in this work, we have realized the same phenomenon only for the symmetric case $\theta = 0$, even though we consider only SO and Rabi couplings without Raman detuning. Due to the I_o dynamical instability, we find out-of-equilibrium dynamics in the density patterns, and it is the route to the nonlinear patterns formation, which we shall discuss later in this subsection. In Fig. 4.9(b), the number of instability bands is four, and the positions and amplitudes are $\{q_x, \omega\} = \{0.27, 0.33\}$, $\{1.39, 0.18\}$, $\{3.48, 0.16\}$, and $\{9.45, 0.11\}$ (not shown in figure), respectively. The appearance of instability bands for both points is symmetric about the momentum (q_x) axis. In addition to this, we show the first excited state in the same plot. Here, the first excited and low-lying branches overlap twice, where we observed that double-unstable avoided crossing in SO-coupled spinor ferromagnetic BECs. For this case, the first excited spectrum also has two complex eigenfrequencies, while the unstable-crossing avoided points.

The eigenvector corresponding to the eigenspectrum is shown in the subsequent

columns of Fig. 4.10. For the choice of parameters $(k_L, \Omega) = (3.1, 1.17)$, we observed no overlap between the low-lying and the first excited spectrum eigenvectors. However, the gap between them closes, and the overlap happens for certain values of quasimomentum q_x. The interval $q_x = (-0.4, 0.4)$, where the low-lying spectrum exhibits imaginary eigenvalues, for this case, the eigenvectors correspond to the spin-like mode, as we see from the out-of-phase behaviour between the low-lying eigenvectors. Further, when $q_x > \pm 0.4$ up to the gapless point, we notice that the low-lying eigenvectors display density-like (in-phase) mode. However, the first-excited state only have a density-like mode up to this gapless point. Nevertheless, in the region of the spectra where the low-lying and the first excited branches overlap, we see that the eigenvectors of both the low-lying and first-excited states are out-of-phase among them. When the mode corresponding to no gap between the low-lying branch and first excited state branch transforms as gapped mode, all the eigenvectors are in phase [see Fig. 4.10(a1)], where the 0-th component shows only density-like mode [see Fig. 4.10(a2)].

For the second point of this region, all eigenvector components have the same amplitude value. Choosing the coupling parameters $(k_L, \Omega) = (5, 2.5)$ reveals a substantial difference. With these parameters, we observed double overlaps between the low-lying and the first-excited spectrum, closing the gap between them. These overlaps occur for certain values of quasi-momentum q_x. The first two eigenvectors exhibit behaviour similar to that observed at the previous point.

As the mode corresponding to the no gap between the low-lying and first excited state branch transforms into a gapped mode, all the eigenvectors become in phase. We also observe similar feature for the next no gap mode and further momentum directions. Additionally, we find that when the real eigenvalues fall to zero and then rise, the eigenvectors are flipped but remain in phase as shown in Fig. 4.10(a1). The obvious change in the spectrum from the gapped to the mode corresponding to the no gap between the low-lying branch and first excited state branch of the eigenvectors demonstrates the transition from a constant density-like mode to a hybridized density-spin-like mode [152] [see Figs. 4.10(b1, b2)].

4.5.3.2 Dynamical stability

We consider the points $(k_L, \Omega) = (3.1, 1.17)$, with interaction parameters, $c_0 = 0.5$ and $c_2 = -0.1$. The collective excitation spectrum corresponding to this point is shown in Fig. 4.9(a), which has complex eigenfrequencies in terms of multiple bands. The presence of complex eigenfrequencies makes the system dynamically unstable. To verify

that the system is dynamically unstable, we perform numerical simulation. We obtain the stationary state, which is the stripe-wave phase. We evolve the stationary state by quenching the trap, and during dynamical evolution, the density profile holds stripe wave behaviour initially. After a while, the ± 1 components are fragmented into small domains and show non-periodic oscillation in space-time evolution, shown in the density profiles in Figs. 4.11(a) and 4.11(c)]. On the other hand, the zeroth component of density starts diminishing as time progresses [see Fig. 4.11(b)]. Thus, we state that the density pattern of the condensate changes its shape and amplitude during dynamical evolution, which confirms the dynamical instability as the 0-th component disappears due to the instability of the system [151].

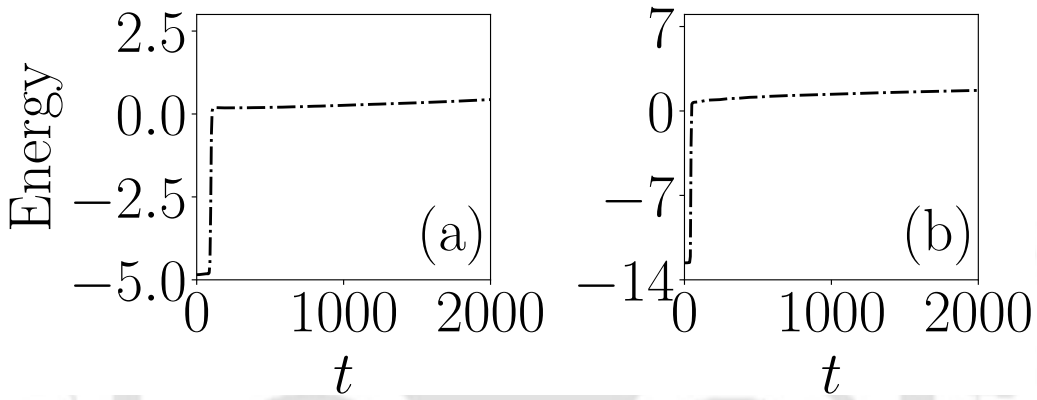


Figure 4.12: (a) and (b) depict the total energy of the condensate for the dynamical evolution for the Fig. 4.11. Following the quenching of trap strength, the condensate exhibits temporal variation in the energy during the evolution, followed by a steady behaviour at later times.

We investigate the second point by choosing $(k_L, \Omega) = (5, 2.5)$. For this, we obtain the stationary state as the stripe wave and evolve the condensate density numerically. The dynamical evolution of this phase shows the stripe wave phase holds for a while. Further, the density profile of all three components fragmented into non-periodic domains [see Figs. 4.11(d)-(f)] [125]. Also, the density of the zeroth component starts diminishing, explicitly showing that the system holds dynamical instability. We also observe that the density pattern of the system changes its shape and amplitude during dynamical evolution.

We plot the total energy of the condensate in the Fig. 4.12. The energy of the condensate starts with the values (a) $E_0 = -4.845$, (b) $E_0 = -12.593$. Following the numerical quench of the trapping parameter during the real-time evolution, the condensate energy exhibits pronounced transient variation and changes sign from negative to positive before approaching comparatively stable behaviour at later times. We observed that the second point is more energetic than the first point as well as in the stationary

state and excited state, i.e., (a) $E_{ex} \approx 0.432$, (b) $E_{ex} \approx 1.708$. The pronounced transient variation in the condensate energy corresponds to the nonequilibrium post-quench dynamics arising during the short time-dependent quench interval and the subsequent instability-driven density redistribution. Further, we investigated the dynamical spin texture, where the initial pattern is not observed, and at the final time, they changed their spin-textures in the dynamical evolution [not shown here].

4.5.4 Excitation spectrum in region-III

4.5.4.1 Excitation spectrum

In region-III, we choose points along the horizontal axis to understand the system's behaviour in the absence of Rabi coupling strength ($\Omega = 0$), and we consider the SO coupling strength as $k_L = 5.0$. The collective excitation spectrum for this is demonstrated in Fig. 4.13(a, b), where differently from the previous cases, in region III we observe the presence of roton-maxon-like modes. As demonstrated in previous studies [22, 25, 153] when $\Omega \to 0$ there is the appearance of roton-maxon modes and the subsequent softening of the roton mode when Ω approaches to zero. The softening of the roton mode favors the appearance of superstripe structures. The low-lying excitation has complex eigenfrequencies alongside the phonon and symmetric roton-like mode, indicating that the system is dynamically unstable due to the presence of the imaginary eigenfrequencies. Further, the first-excited state also shows similar behaviour, i.e., the presence of the phonon mode along with the complex eigenfrequencies but no symmetric roton-like structure. Although, the unstable avoided-crossing is noticed at $q_x \approx 4.8499$, between the first- and low-lying states. After that point, the real eigenfrequency decreases and reaches zero, where it exhibits the imaginary eigenfrequency. Beyond this point, the real frequency gains the growth. Based on this observation, one has to understand such behaviour using the eigenvectors. Additionally, the complex eigenfrequency presents multiple instability bands along the quasimomentum axis. The positions of the low-lying excitation spectrum instability bands are $q_x = 0.06, 4.91, 9.97$, and the corresponding complex eigenfrequencies are $\omega_- = 0.1037, 0.1404, 0.0993$, respectively. The first excited state has two instability bands, and its position and complex eigenfrequency are the same as those of the low-lying state. Notably, the instability bands are symmetric about the x-axis.

Fig. 4.14 represents the eigenvector components, in this region, the low-lying excitation eigenvectors exhibits in-phase mode between $|u_{+1}|^2_{ll}$ and $|u_{-1}|^2_{ll}$ as well as between $|v_{+1}|^2_{ll}$ and $|v_{-1}|^2_{ll}$. This feature continues up to the point of real eigenvalues, when

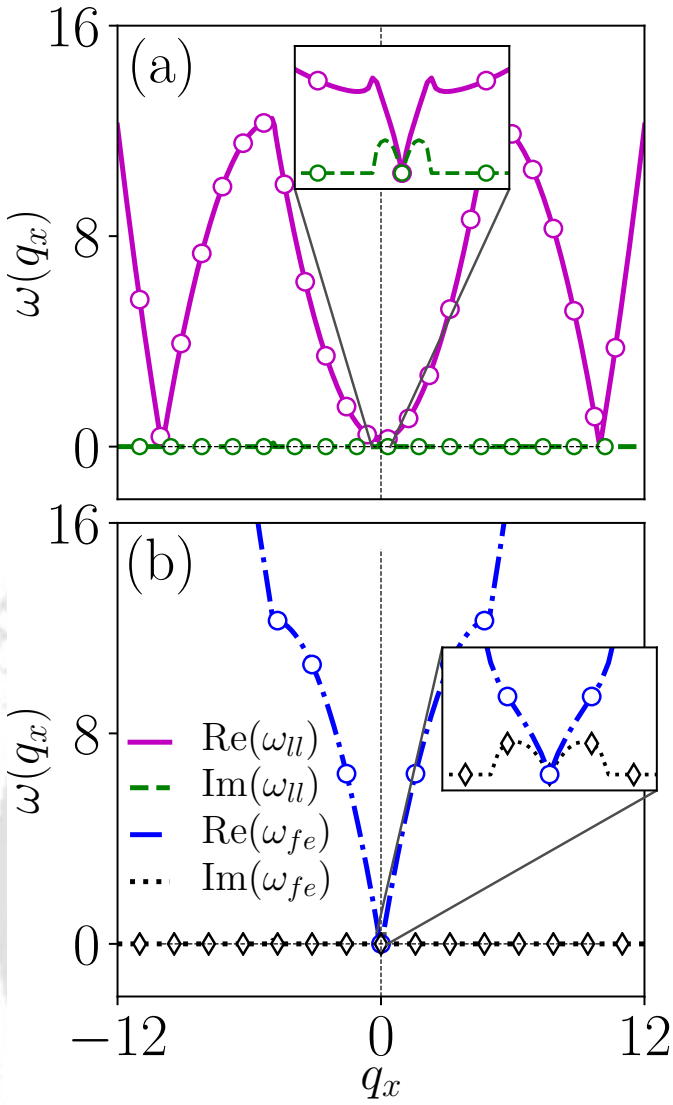


Figure 4.13: Excitation spectrum (a) low-lying and (b) first-excited branches, for the coupling strengths $k_L = 5.0$, $\Omega = 0.0$. The label representation is similar to the Fig. 4.9. Insets are maximized for the visualization of the complex frequency mode. Whereas the mode corresponding to the no gap between the low-lying and first excited state branch also appeared along with the symmetric roton mode.

the imaginary eigenvalues exhibit out-of-phase between them ($|u_{+1}|^2_{ll} - |u_{-1}|^2_{ll} \neq 0$). Although at $q_x = 0$, the eigenvalues become zero $\omega = 0$, a phonon-mode is observed, which is explicitly shown in the form of sharp spike-like-eigenvectors appeared in $|u_{+1}|^2_{ll}$ and $|v_{+1}|^2_{ll}$. However, in this complex eigenvalues regime, we have both phonon-mode as well as complicated spin-like mode. In addition to this, the 0-th component eigenvectors show a mixed-mode behaviour, and as a result of this, we observed different dynamical phases from the stationary state. Also, the first excited state exhibits $\omega = 0$ for $q_x = 0$, where all the eigenvectors met at a single point as before.

TH-4102_206121026

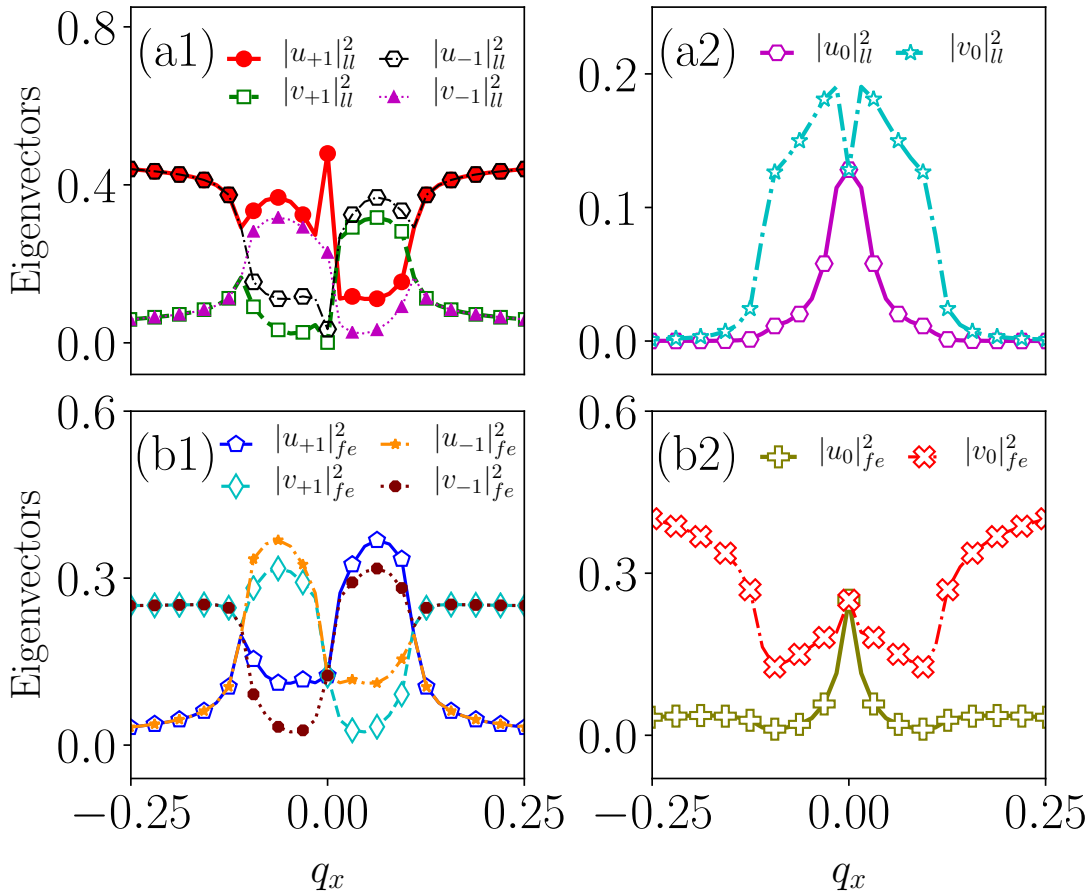


Figure 4.14: Eigenvectors top and bottom rows are corresponding to the Fig. 4.13(a) and, Fig. 4.13(b) respectively. The label representation is similar to the Fig. 4.10. In this region, both low-lying and the first excited state assume the value $\omega = 0$ for $q_x = 0$ with eigenvectors are in-phase with the low-lying and first-excited states, which indicates the existence of the phonon mode for these branches.

The first-excited state behaves like a spin-like mode with an asymmetric nature, indicating the existence of the superstripe phase. Further, the density mode appears while the real eigenfrequency is present, also evident from the 0-th component eigenvector behaviour.

4.5.4.2 Dynamical stability

We consider a case with SO coupling strength $k_L = 5.0$ and zero Rabi coupling strength $\Omega = 0.0$. The corresponding BdG excitation spectrum in Figs. 4.13(a) and (b) reveal the presence of phonon-gapless complex eigenfrequencies indicating the dynamical unstable nature of the condensate. To investigate this numerically, we obtained the stationary state of the condensate, which falls within the unpolarized stripe-wave phase. We then evolved this state in time using a real-time propagation method. The density pro-

TH-4102_206121026

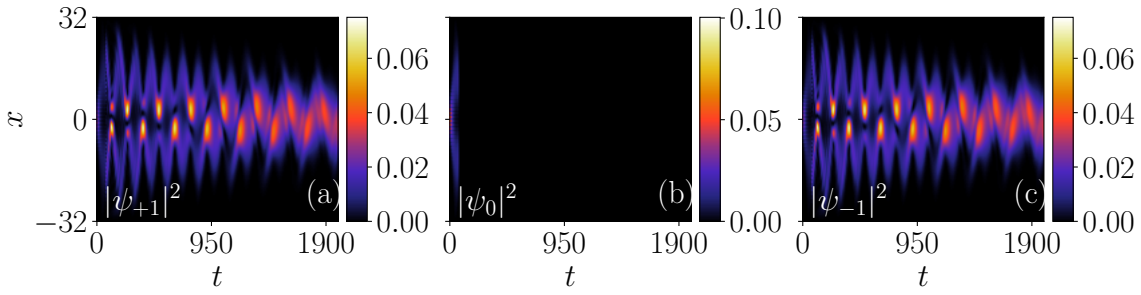


Figure 4.15: Dynamics: (a)-(c) represent the time evolution of super-stripe phase density profiles of $|\psi_{+1}|^2$, $|\psi_0|^2$, and $|\psi_{-1}|^2$ components of the condensate. The coupling strengths are $k_L = 5.0$, $\Omega = 0.0$ with interaction parameters $c_0 = 0.5$ and $c_2 = -0.1$. During dynamics, the unpolarized super-stripe wave holds its behavior for $t < 30$. Further, it breaks into two domains and oscillated either sides of the condensates of ± 1 components, and the 0-th component disappears, where ± 1 components densities are obtaining the gain, which shows the change in the density profile confirms the dynamical instability.

file initially maintains its unpolarized stripe-wave behaviour however subsequently breaks into two parts at $t = 85$. Following this, the density of ± 1 components oscillates around the trap centre, exhibiting accumulated breather behaviour for a period. Ultimately, the fragmented oscillating waves merge and form several small domains [see Figs. 4.15(a) and (c)] [125], while the zeroth component of the density disappears [see Fig. 4.15(b)]. This behaviour signifies that the dynamical instability also changes its shape and size [151]. We examined the energy during its dynamic evolution, which eventually stabilizes, indicating energetic stability. This finding is consistent with the analysis of the excitation spectrum, suggesting that the numerical simulation accurately reflects the theoretical predictions.

4.5.5 Effect of coupling strength on the Band gap

So far, we have discussed the nature of collective excitations, eigenvectors and further the dynamical behaviour of the condensate in different regions of the $k_L - \Omega$ plane, next we consider the effect of SO and Rabi coupling strengths on the band gap Δ_g between the positive and negative branches of the spectrum, where we define the band gap as Δ_g. In Fig. 4.16(a1), we show the band gap variation upon varying the Rabi coupling strength (Ω) for a fixed k_L. In what follows we discuss it for two distinct SO coupling strengths, for instance, $k_L = 1.14$ and 3.10. The gap closes at a certain value of Ω for these SO couplings. For $k_L = 1.14$, $\Delta_g = 0$ for $\Omega = 0.107$ and similarly for $k_L = 3.10$, it closes at $\Omega = 1.218$ for the quasi-momentum values $q = 0.521$, 1.486, respectively. Starting from the point $\Delta_g = 0$, upon increasing the Ω, we observe that the gap becomes non-zero even for a relatively small increment in the Rabi coupling

strength, and the magnitude of the band gap increases with an increase in Ω. Also, we provide the logarithmic scale plot corresponding to Fig. 4.16(a1) wherein we show the fitting curve $\Delta_g = a\Omega^b$ with the maroon and orange dotted line for $k_L = 1.14$ and $k_L = 3.10$, respectively. The coefficient for the fitting function is $a = 0.981$, $b = 0.997$ and $a = 1.083$, $b = 1.026$ for the SO coupling strength $k_L = 1.14$ and $k_L = 3.10$, respectively. Here, we wish to highlight that the band gap gets increased upon increasing Ω for fixed k_L. For higher k_L, the gap attains sudden maximum even for the lesser Ω while comparing small k_L, evident from the red dashed line crosses the green dashed-dotted line in Fig. 4.16(a1). Moreover, for higher k_L the gap closes at higher Ω, compare starting points in Fig. 4.16(a1).

Further, we discuss the variation of band gap upon varying the SO coupling for fixed Rabi coupling strength. We choose two different values of Rabi coupling strength $\Omega = 1.3, 3.1$. Since Rabi coupling strength is responsible for opening the gap among the branches of the collective excitation spectrum (as discussed above). As result of this the band gap Δ_g value is higher for a lesser value of k_L at fixed Ω [see Fig. 4.16(b1)]. Upon increasing k_L, the Δ_g starts decreasing, and further, it reaches zero at the certain quasi-momentum value $q_x = 1.5325, 2.3381$ with $k_L = 3.20, 4.86$ for the Rabi coupling strengths $\Omega = 1.3, 3.1$, respectively. We find that the band gap Δ_g decreases upon increasing the k_L at fixed Ω. In Fig. 4.16(b2), we show the fitting function $\Delta_g = c\Omega^d$ with the maroon and orange dotted line for $\Omega = 1.3$ and $\omega = 3.1$, respectively. The coefficient of fitting function is $c = 126.30, d = -4.96$ and $c = 46.44, d = -2.22$ for the SO coupling strength $\Omega = 1.3$ and $k_L = 3.1$, respectively.

4.6 Summary and Conclusions

In this Chapter, we have investigated the collective excitation spectrum of SO coupled spin-1 ferromagnetic BECs with Rabi coupling in quasi-one dimension using Bogoliubov-de Gennes theory and numerical simulation. Firstly we have analyzed the single-particle spectrum for different sets of SO and Rabi coupling strengths. Upon increasing the strength of coupling parameters, we noticed separation among different negative (ω_-) and positive (ω_+) branches of the eigenspectrum, with ω_- having the lowest minima. However for $\Omega < k_L^2$, the negative branch of the spectrum shows double minima indicating the presence of a stripe phases.

Based upon collective excitation calculation, we have obtained the phase diagram in the $k_L - \Omega$ plane which have been broadly divided into three regions: stable phase

TH-4102_206121026

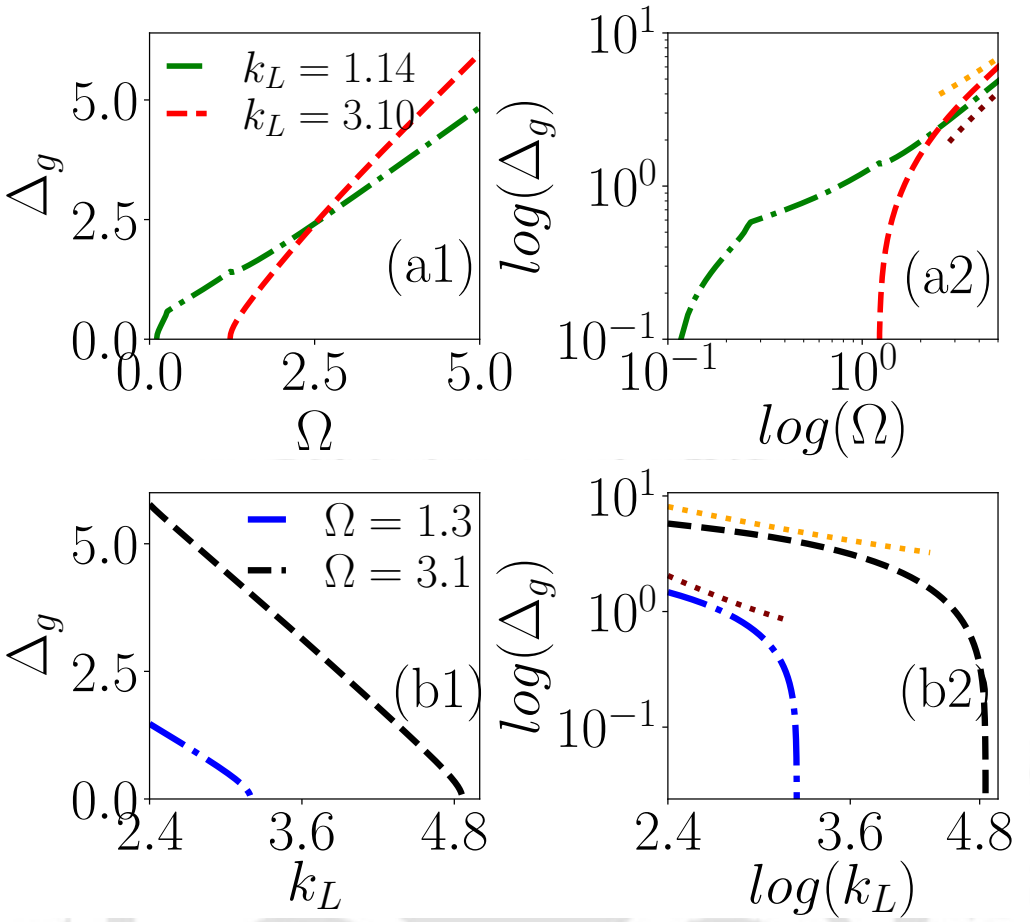


Figure 4.16: Variation of band gap Δ_g between negative and positive branches of the spectrum. (a1) For the fixed value SO coupling strength upon variation of Rabi coupling strength, vice versa in (b1). In (a1), the dash-dotted green and the dashed red lines represent gap calculation for $k_L = 1.14$ and $k_L = 3.10$, respectively. In (b1), the dash-dotted blue and the dashed black lines represent gap calculation for $\Omega = 1.3$ and $\Omega = 3.1$, respectively. The interaction parameter strength are $c_0 = 0.5$, and $c_2 = -0.1$. (a2) and (b2) are the logarithmic scale plots corresponding to (a1) and (b1), respectively. Further, in (a2) and (b2) the maroon (orange) dotted lines represent the fitting curve $\Delta_g = a\Omega^b$ with the parameters $a = 0.9811, b = 0.9974$, ($a = 1.0825, b = 1.0258$), and $a = 126.2992, b = -4.9568$, ($a = 46.4438, b = -2.2146$), respectively.

(region I) and unstable (region II, III). We have divided the unstable region II into two subparts according the nature of eigenspectrum, which is based upon the appearance of the the gapped and gapless (unstable-avoided crossing) mode. In region I, the excitation spectrum exhibits solely real positive eigenvalues with the presence of a phonon mode. The eigenvectors corresponding to these eigenvalues substantiate the existence of the phonon mode by exhibiting the density like mode in the wavenumber space. The absence of the negative and complex eigenfrequencies in the spectrum confirms dynamically and energetically stable condensate in this region.

As the coupling strengths increase, we find a transition from Region I to the unsta-

TH-4102_206121026

ble region II, attributed to the relation $\Omega < k_L^2$. In this region, complex eigenfrequencies emerge throughout the spectrum, accompanied by a gapped mode and a mode corresponding to the no gap between the low-lying (ω_-) and first-excited (ω_+) branches. Based on the presence of a gapped mode and a mode corresponding to the no gap between the low-lying branch and first excited state branch, region II is divided into two subregions, IIa and IIb, respectively. The eigenspectrum in region IIa exhibits gapped behaviour across the entire region. Notably, the presence of complex eigenfrequencies is reflected in the corresponding eigenvectors, indicating a transition from spin-mode to density-mode nature of the eigenvectors as the eigenfrequency shifts from complex to real. This phenomenon is evident in the ± 1 components of the eigenspectrum, while the zeroth component exclusively displays a density-like mode. The combined analysis of eigenvectors and dynamic behaviour reveals a mixed-spin-density mode.

Region IIb is separated from Region IIa by a line, the latter of which exhibits a multi-instability band across its entirety. Upon increasing the SO coupling for a point along the separation line, we observe gapless behaviour in the eigenspectrum for a particular range of quasi-momentum among the low-lying and first-excited branches of the spectrum. Similarly, decreasing the Rabi coupling strength for any point on the separation line will also yield gapless behaviour. Similar to the previous region, we also identify the mixed-spin-density eigenvector mode in this region. For the gapless region, the eigenvector of the low-lying and first-excited branches exhibits a spin-like mode for all its components. We also characterize the mode corresponding to the no gap between the low-lying branch and first-excited-state branch as an unstable avoided crossing between the low-lying and first-excited spectrum. This instability manifests as the emergence of complex eigenfrequencies when the two branches come into contact. The corresponding dynamical evolution also exhibits an unstable stripe state, which we have examined numerically. We observed that the 0-th component is non-zero in region IIa but disappears in region IIb. This suggests that a non-zero 0-th component tends to be less susceptible to dynamical instability, while a vanishing 0-th component tends to be higher than the previous one.

In addition to these two regions, we have identified the region III which corresponds to the $\Omega = 0$ line. In this region, both the low-lying and the first excited states assume the value $\omega = 0$ for $q_x = 0$ with eigenvectors in phase with the low-lying state. This indicates the existence of a phonon mode. The low-lying and first-excited spectra also exhibit gapless, unstable-avoided crossing behaviour between them. Further analysis of the eigenvectors reveals not only the phonon character but also the presence of a spin-like mode in both states. Numerical simulations for this case reveal the

TH-4102_206121026

presence of superstripe stationary state, and their respective dynamics exhibit unstable dynamical-nonlinear patterns. Our observations suggest that this work would be a valuable resource for experimental researchers seeking to achieve stable and unstable SO coupled spinor ferromagnetic BECs. Here, we have provided a comprehensive numerical simulation of regions with diverse dynamical behaviours.

TH-4102_206121026

Chapter 5

Double unstable avoided crossings and complex domain patterns formation in spin-orbit coupled spin-1 condensates

After presenting the different quantum phases in Chapter 3 and analyzing the collective excitations of these phases for ferromagnetic interactions in Chapter 4, this chapter focuses on the impact of spin–orbit and Rabi couplings on the dynamical stability of spin-orbit-coupled spin-1 Bose–Einstein condensates, considering both ferromagnetic and antiferromagnetic interactions. In particular we determine the collective excitation spectrum through Bogoliubov-de-Gennes theory and characterize the corresponding dynamical stability regime via modulational instability. For antiferromagnetic interactions, the eigenspectrum reveals the presence of both stable and unstable avoided crossings (UAC), with the first-excited branch undergoing a double unstable avoided crossing. In contrast, with ferromagnetic interactions, only a single UAC, which occurs between the low-lying and first-excited branches, is observed. Furthermore, the eigenvectors demonstrate the transition from density-like to spin-like behaviour, as the collective excitation shows the transition from stable to unstable mode for both the ferromagnetic and antiferromagnetic interactions. In the multi-band instability state, eigenvectors display spin-density mixed mode, while they show spin-flip nature in the avoided crossing regime. Our analysis suggests that spin-orbit coupling enhances the instability gain, while Rabi coupling plays the opposite role. Finally, we corroborate our analytical findings of stable and unstable regimes through numerical simulations of the dynamical evolution of the condensates by introducing the perturbations upon quenching the trap strength. The dynamical phases show the formation of complex

TH-4102_206121026

domains with antiferromagnetic interaction, which may be attributed to the double unstable avoided crossings in such a system. The work presented in the Chapter is published in Physical Review A [116].

5.1 Introduction

The collective excitations and the different quantum phases associated with spin–orbit (SO) coupled spin-1 Bose–Einstein condensates (BECs) have been discussed in detail in Chapter 1. However, to make this chapter self-contained and to introduce the context of different sort of instabilities and patterns formation in spin-1 SO coupled BECs, we briefly review the relevant works. The experimental realization of spin-orbit (SO) coupled Bose-Einstein condensates (BECs) in the laboratory has opened up a wide range of phenomena to explore in ultracold atomic physics. Initially achieved in experiments using two of the three hyperfine components of the $F = 1$ states of ^{87}Rb [4], and later extended to spin-1 BECs [10, 11], these systems have become a rich ground for exploring exotic quantum phenomena, such as superfluidity [148], supersolidity [65], metastable supersolid [154], modulation instability [92, 91, 132], vortices [105, 155], solitons [74, 75], etc.

Numerical simulations have played a crucial role in revealing many fascinating properties of SO coupled BECs, primarily through the use of the mean-field Gross-Pitaevskii equation (GPE) [36, 37, 50, 72, 73, 156, 157]. Liu *et al.* reported exact soliton solutions and manifold mixing dynamics in quasi-one-dimensional (quasi-1D) SO coupled spin-1 BECs [158]. Numerical studies along similar lines suggest the emergence of more complex phases, such as multiring structures, stripes, and superlattice solitons, in quasi-two-dimensional (quasi-2D) SO coupled spin-1 BECs [78]. In addition to these phases, the formation of symbiotic spinor solitons has been reported in quasi-1D and quasi-2D spin-1 ferromagnetic BECs [76]. For antiferromagnetic SO coupled spin-1 BECs, the formation of stable multi-peak vector solitons in quasi-1D systems has been reported [77]. Recently, He *et al.*, through linear stability analysis, demonstrated the existence of stationary and moving bright solitons in quasi-1D SO coupled spin-1 BECs under the influence of a Zeeman field [141]. There have been some works that report the coexistence of spin-precession as well the separation between the spin-component because of anomalous spin-dependent velocities arising solely due to the SO coupling, which also result in the appearance of complex dynamics in the condensate [79–81].

Collective excitations, which are low-lying excitations of the quantum gas, are key

in determining the stability properties of ground-state phases and the behaviour of fluctuations and superfluidity of the BECs. Landau developed a framework for studying elementary excitations in superfluid helium, while for weakly interacting Bose gases, Bogoliubov derived the theory of elementary excitations [13]. Numerous theoretical works have reported the collective excitations in single-component BECs [159–162]. Goldstein *et al.* [20] extended the Hartree-Bogoliubov theory for multi-component BECs and derived the quasi-particle frequency spectrum. They further demonstrated that interferences arising from cross-coupling between condensate components resulted in a reversal of the sign of the effective two-body interaction and the onset of spatial instabilities. The stability of supercurrents in BECs with one-dimensional SO coupling has also been studied, showing that supercurrents in the plane-wave phase exhibit dynamical instability. Additionally, extensive energetic instability analysis of supercurrent states has been reported [21]. Several laboratory experiments have reported collective excitations, including phonon-like excitations in a dilute gas of ^{87}Rb [16], and collective excitations of sodium atoms in a magnetic trap [17]. Khamehchi *et al.* [22] used Bragg spectroscopy to measure the collective excitations in SO coupled BECs, revealing the presence of phonon-maxon-roton modes, as predicted using the Bogoliubov-de Gennes (BdG) theory. In a recent study, Ravisankar *et al.* [93] investigated the influence of SO coupling and Rabi coupling strengths on the dynamical instability of quasi-2D binary BECs using Bogoliubov theory. Their analysis revealed the presence of phonon, roton, and maxon modes, demonstrating that increasing the SO coupling enhances instability, whereas stronger Rabi coupling stabilizes the system.

Modulation instability (MI) is a measure of instability in BECs, which becomes one of the key criteria for determining the stability of the condensate. In recent years, numerous studies have been carried out to examine the stability of the spinor condensate using MI. For instance, Tsubota *et al.* [84, 85] demonstrated that MI in two-component BECs leads to the formation of multiple domains and regions dominated by the solitary waves. Robins et al. [86] and Zhang et al. [87] performed numerical MI analyses on the ferromagnetic and antiferromagnetic phases of spin-1 BECs, revealing that the ferromagnetic phase is unstable, while the antiferromagnetic phase is stable. Some works show the stability analysis of these phases in the presence of the external field. For instance, Matuszewski *et al.* showed that a homogeneous magnetic field induces spatial MI in antiferromagnetic spin-1 BECs, resulting in the formation of spin domains in sodium condensates confined in optical traps [88]. In a subsequent study, they found that the metastable phases of an antiferromagnetic spin-1 condensate, in a simple model with pure contact interactions, could exhibit a roton-like minimum in the

excitation spectrum. The presence of an external magnetic field gives rise to the instability of the roton modes, which can lead to the spontaneous emergence of regular periodic patterns [89]. Similarly, Kronjäger *et al.* reported spontaneous pattern formation in antiferromagnetic spinor BECs and identified several linearly unstable modes using a mean-field approach [90]. In other direction, Pu *et al.* reported that magnetic-field-induced dynamical instabilities in spin-1 BECs are accompanied by I_o type instabilities in the presence of nonzero magnetic field [94]. Systems with such embedded instabilities spontaneously develop a spatial pattern on time evolution from the uniform initial state.

On the other hand, studies on instabilities in SO coupled BECs remain relatively limited. Bhuvaneswari *et al.* [92] theoretically investigated the MI in quasi-2D SO coupled BECs with Rabi coupling, assuming equal densities for both pseudo-spin components. They found that unstable modulations arise from initially miscible condensates, depending on the combination of signs of intra- and intercomponent interaction strengths. The SO coupling enhances instability regardless of the interaction type; however, in the case of attractive interactions, SO coupling further amplifies the MI. In quasi-1D systems, Bhat *et al.* [91] demonstrated that two-component SO coupled BECs with equal component densities exhibit MI, leading to the formation of a striped phase as the ground state. Additionally, *Li et al.* [132] studied MI in quasi-1D SO coupled BECs with Raman coupling, showing that instability occurs for repulsive density-density and spin-exchange interactions even in the absence of SO coupling and Raman coupling.

Identifying unstable phases and their underlying mechanisms in complex spin-1 BECs remains a significant challenge. For instance, a recent study by Gangwar *et al.* reported the occurrence of unstable avoided crossings (UACs) in the context of ferromagnetic interactions in spin-1 SO coupled BECs [115]. However, a comprehensive understanding of the interplay among interaction strength, SO coupling, and Rabi coupling, the key factors in the emergence of complex phases, remains elusive. In this paper, we present a detailed analysis of modulational instabilities in SO coupled spin-1 BECs, exploring how interaction types (antiferromagnetic and ferromagnetic) and coupling parameters influence the eigenspectrum and resulting dynamics. For antiferromagnetic interactions, the eigenspectrum exhibits both stable and UACs between the low-lying and first-excited branches, as well as between the first-excited and second-excited branches. Notably, the first-excited branch under antiferromagnetic interactions displays a double UAC, a phenomenon previously reported for spin-1 BECs in the presence of a magnetic field [90, 94]. In this study, however, we explicitly demon-

TH-4102_206121026

strate that this double unstable avoided crossing is induced by SO coupling. For ferromagnetic interactions, we find that a single UAC occurs between the low-lying and first-excited branches, with a double UAC appearing only when the Rabi coupling strength is negative. The UAC is associated with the I_o-type instability, which drives pattern formation in the density profile of the condensate [95]. To complement our analytical findings, we conduct numerical simulations for both antiferromagnetic and ferromagnetic interactions. These simulations provide deeper insight into the dynamics and pattern formation arising from modulational instability.

The structure of our paper is as follows. In section 5.2, we present the mean-field model to explore MI of SO coupled spin-1 BECs with Rabi-coupling. Following this, we provide a detailed theoretical formalism using BdG to calculate the collective excitation spectrum in Sec. 5.3. In Sec. 5.3.1, we present the collective excitation spectrum for ferromagnetic interactions, followed by an analysis for antiferromagnetic interactions in Sec. 5.3.2. In Sec. 5.4, we present the effect of interaction strengths on MI. In Sec. 5.5, we demonstrate the variation of the Band gaps between the low-lying and first excited states and between the first and second excited states for ferromagnetic and antiferromagnetic interaction. In Sec. 5.6, we present numerical simulations using the GPEs, which complement the dynamical instability regions obtained from the BdG analysis. Finally, in Sec. 5.7, we summarize our findings.

5.2 Mean-field model

We consider a quasi-one dimensional SO coupled spin-1 BECs with tight confinement in the transverse direction [145], which can be described using three sets of coupled GPEs, given as [39, 76, 106, 108],

$$\begin{aligned} \mathrm{i}\frac{\partial\psi_{\pm1}}{\partial t} =& \left[-\frac{1}{2}\frac{\partial^2}{\partial x^2} + V(x) + c_0\rho\right]\psi_{\pm1} \mp \frac{k_L}{\sqrt{2}}\frac{\partial\psi_0}{\partial x} + c_2\left(\rho_{\pm1} + \rho_0 - \rho_{\mp1}\right)\psi_{\pm1} \\ &+ c_2\psi_0^2\psi_{\mp1}^* + \frac{\Omega}{\sqrt{2}}\psi_0, \end{aligned} \tag{5.1a}$$

$$\begin{aligned} \mathrm{i}\frac{\partial\psi_0}{\partial t} =& \left[-\frac{1}{2}\frac{\partial^2}{\partial x^2} + V(x) + c_0\rho\right]\psi_0 + \frac{k_L}{\sqrt{2}}\left[\frac{\partial\psi_{+1}}{\partial x} - \frac{\partial\psi_{-1}}{\partial x}\right] + c_2(\rho_{+1} + \rho_{-1})\psi_0 \\ &+ 2c_2\psi_0^*\psi_{+1}\psi_{-1} + \frac{\Omega}{\sqrt{2}}(\psi_1 + \psi_{-1})\,. \end{aligned} \tag{5.1b}$$

Here, ψ_{+1}, ψ_0, and ψ_{-1} are the spinor wavefunctions that satisfy the normaliza-

tion condition $\int_{-\infty}^{\infty} dx\ \rho = 1$ with $\rho = \sum_{j=-1}^{1} \rho_j$, total atomic density of the condensate, and $\rho_j = |\psi_j(x)|^2$ represents the density of j-th component of the condensate with j = $\pm 1, 0$. The Eqs. (5.1a) and (5.1b) are non-dimensionalized, using time, length, and energy $t = \omega_x \tilde{t}$, $x = \tilde{x}/l_0$, and $\hbar\omega_x$, respectively. The resulting condensate wavefunction is $\psi_{\pm 1,0} = \sqrt{\frac{l_0}{N}}\tilde{\psi}_{\pm 1,0}$, where, $l_0 = \sqrt{\hbar/m\omega_x}$, is the oscillator length for the trap frequency ω_x along the x-axis. The trap strength is given by $V(x) = x^2/2$, density-density interaction strength $c_0 = 2Nl_0(a_0 + 2a_2)/3l_\perp^2$, spin-exchange interaction strength $c_2 = 2Nl_0(a_2 - a_0)/3l_\perp^2$, where a_0 and a_2 are the s-wave scattering lengths in total spin channels 0 and 2, respectively. Upon tuning $c_2 < 0$ ($c_2 > 0$), one can have the ferromagnetic (antiferromagnetic) interaction of the condensates [39, 117]. Here, $l_\perp = \sqrt{\hbar/(m\omega_\perp)}$ is the oscillator length in transverse direction with $\omega_\perp = \sqrt{\omega_y\omega_z}$. The SO and Rabi coupling strengths are given by $k_L = \tilde{k_L}/\omega_x l_0$, $\Omega = \tilde{\Omega}/(\hbar\omega_x)$, respectively. In the above description, the quantities with the tilde represent dimensionful quantities. In this entire work, we consider all parameters to be dimensionless. The energy functional corresponding to the coupled GPEs (5.1a)-(5.1b) is given by [50],

$$
\begin{aligned}
E =& \frac{1}{2}\int dx \Big\{ \sum_j |\partial_x \psi_j|^2 + 2V(x)\rho + c_0\rho^2 \\
&+ c_2[\rho_{+1}^2 + \rho_{-1}^2 + 2(\rho_{+1}\rho_0 + \rho_{-1}\rho_0 - \rho_{+1}\rho_{-1} \\
&+ \psi_{-1}^*\psi_0^2\psi_{+1}^* + \psi_{-1}\psi_0^{*2}\psi_{+1})] + \sqrt{2}\Omega[(\psi_{+1}^* + \psi_{-1}^*)\psi_0 \\
&+ \psi_0^*(\psi_{+1} + \psi_{-1})] + \sqrt{2}k_L[(\psi_{-1}^* - \psi_{+1}^*)\partial_x\psi_0 + \psi_0^*(\partial_x\psi_{+1} - \partial_x\psi_{-1})] \Big\}. \qquad (5.2)
\end{aligned}
$$

Here, we outline the experimentally viable range for the parameters that we have considered for our simulations. For the ferromagnetic interaction, we consider ^{87}Rb BECs with $N \sim 2 \times 10^4$ number of atoms. The axial trap frequency as $\omega_x = 2\pi \times 50$ Hz and the transverse trap frequencies as $\omega_y = \omega_z = 2\pi \times 500$ Hz. The resultant characteristic lengths would be $l_0 = 1.52\mu m$, and $l_\perp = 0.48\mu m$. For the antiferromagnetic interaction, we consider the BECs of ^{23}Na atoms. The resultant characteristic lengths for ^{23}Na BECs are $l_0 = 2.9\mu m$, and $l_\perp = 0.9\mu m$. The spin-dependent and spin-independent interactions can be achieved by controlling the s-wave scattering lengths through Feshbach resonance [120–122]. However, the SO coupling strength $k_L = \{0.1 - 5\}$ can be tuned by changing the laser wavelengths in the range of $\{68.86\mu$m - 1377.22nm$\}$. However, the dimensionless Rabi frequency interval $\Omega = [0, 5]$ used in the simulation can be attained by tuning the Raman laser strength in the range of $2\pi\hbar \times \{5 - 250\}$ Hz.

5.3 Collective Excitation spectrum

In this section, we present the collective excitation spectrum of SO coupled spin-1 BECs using the Bogoliubov-de-Gennes (BdG) analysis. We consider the uniform ground state wavefunction (ϕ_j) is perturbed by the wavefunction $\delta\phi_j$ for which the excited state wavefunction is given by [94, 138],

$$\psi_j(x,t) = e^{-i\mu_j t}[\phi_j + \delta\phi_j(x,t)] \,, \tag{5.3}$$

where,

$$\delta\phi_j(x,t) = u_j e^{i(q_x x - \omega t)} + v_j^* e^{-i(q_x x - \omega^* t)} \,, \tag{5.4}$$

and the uniform ground state wavefunction is considered as $\phi_j = (1/2, -1/\sqrt{2}, 1/2)^T$, μ_j denotes the chemical potential, and u_j, v_j are the Bogoliubov amplitudes corresponding to the three spin-components. As we substitute Eq. (5.3) in the dynamical Eqs. (5.1a)-(5.1b), we obtain

$$(\mathcal{L} - \omega \mathrm{I}) \begin{pmatrix} u_{+1} & v_{+1} & u_0 & v_0 & u_{-1} & v_{-1} \end{pmatrix}^T = 0, \tag{5.5}$$

where T represents the transpose of the matrix, I is a 6×6 identity matrix and $\mathcal{L}$ is 6×6 matrix given by,

$$\mathcal{L} = \begin{pmatrix} H_+ - \mu_+ & \mathcal{L}_{12} & \mathcal{L}_{13} & \mathcal{L}_{14} & \mathcal{L}_{15} & \mathcal{L}_{16} \\ \mathcal{L}_{21} & -H_+ + \mu_+ & \mathcal{L}_{23} & \mathcal{L}_{24} & \mathcal{L}_{25} & \mathcal{L}_{26} \\ \mathcal{L}_{31} & \mathcal{L}_{32} & H_0 - \mu_0 & \mathcal{L}_{34} & \mathcal{L}_{35} & \mathcal{L}_{36} \\ \mathcal{L}_{41} & \mathcal{L}_{42} & \mathcal{L}_{43} & -H_0 + \mu_0 & \mathcal{L}_{45} & \mathcal{L}_{46} \\ \mathcal{L}_{51} & \mathcal{L}_{52} & \mathcal{L}_{53} & \mathcal{L}_{54} & H_- - \mu_- & \mathcal{L}_{56} \\ \mathcal{L}_{61} & \mathcal{L}_{62} & \mathcal{L}_{63} & \mathcal{L}_{64} & \mathcal{L}_{65} & -H_- + \mu_- \end{pmatrix} . \tag{5.6}$$

The matrix elements of $\mathcal{L}$ have been provided in the Appendix. A. Bogoliubov coefficients follow the normalization condition,

$$\int \left(\sum_j \{ |u_j|^2 - |v_j|^2 \} \right) dx = 1 \,. \tag{5.7}$$

We compute the determinant of the matrix $\mathcal{L}$ and equate it to zero $det(\mathcal{L} - \mathrm{I}\omega) = 0$,

which yields the characteristic equation given as,

$$\omega^6 + b\omega^4 + c\omega^2 + d = 0\,, \tag{5.8}$$

where the coefficients b, c, and d are supplied in the Appendix. A.

By numerically solving the BdG equations (5.6), we complement the reliability of the analytical results for the excitation spectrum and obtain the eigenvectors as a function of q_x. For the numerical calculation, we have considered the real space $[-1000 : 1000]$ grid with a step size of $h_x = 0.2$. We employ the Fourier collocation method, which utilizes the LAPACK package [149] to diagonalize the truncated BdG matrix we acquire by numerically computing the Fourier transform of the BdG equations. In momentum space q_x, we consider $[-700 : 700]$ modes, with a grid step size of $h_{q_x} = 0.0157$.

In our recent work, we conducted a detailed analysis of the collective excitation spectrum for ferromagnetic interactions in SO coupled spin-1 BECs. We reported the presence of unstable avoided crossings between the low-lying and first excited states of the eigenspectrum [115]. In this paper, we extend this analysis to antiferromagnetic interactions, where we observe evidence of double avoided crossings. In the following section, first, we discuss the effects of SO coupling and Rabi coupling on the eigenspectrum for ferromagnetic interactions and subsequently, we extend the analysis to antiferromagnetic interactions.

5.3.1 Collective excitation spectrum of ferromagnetic SO coupled BECs ($c_0 > 0, c_2 < 0$)

In this section, we present the collective spectrum analysis for SO coupled BECs with ferromagnetic interaction, characterized by $c_0 = 5.0$ and $c_2 = -2.0$. The negative (ω_-), positive (ω_+), and zeroth (ω_0) branches are designated as the low-lying (ω_{ll}), first-excited (ω_{fe}), and second-excited (ω_{se}) branches of the eigenspectrum, respectively. It has been shown that the eigenspectrum of SO coupled BECs exhibits intriguing features, including I_o-type instabilities [94, 95]. Generally, these I_o-type instabilities arise from unstable avoided crossings (UACs) between the branches.

We begin our analysis by first calculating the eigenvalues of the BdG matrix, as given in Eq. 5.6. In Fig. 5.1, we present the eigenspectrum corresponding to regime I ($k_L^2 < \Omega$) (top panel) and regime II ($k_L^2 > \Omega$) (bottom panel) of the condensate. In regime I ($k_L^2 < \Omega$), we observe only real eigenfrequencies, accompanied by a gap

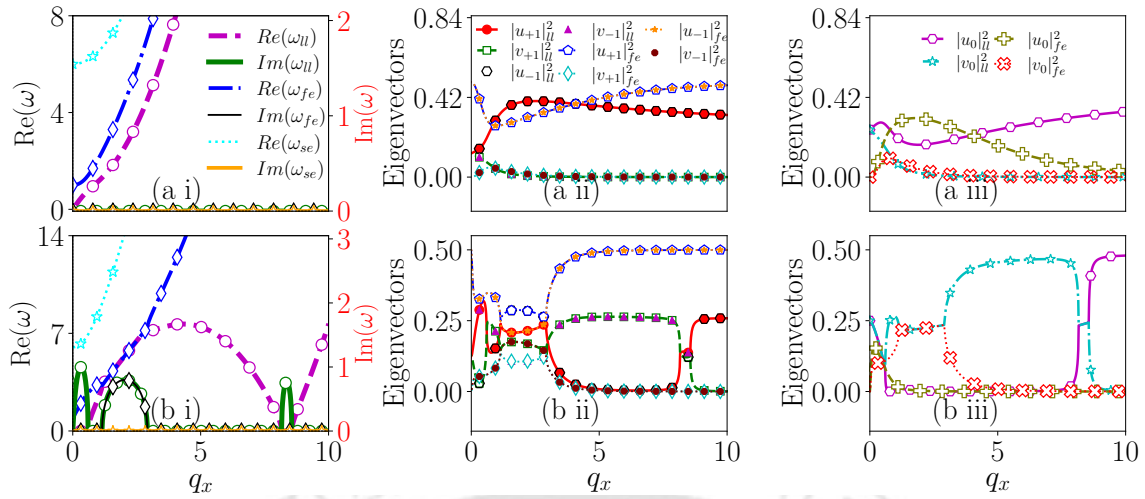


Figure 5.1: Eigenvalue and corresponding eigenvectors for (a) (k_L, Ω) = (0.5, 1.0) showing real eigenfrequencies and (b) (k_L, Ω) =(4.5, 1.0) showing the multiband instability for ferromagnetic interaction $c_0 = 5, c_2 = -2.0$. The dashed magenta line represents $\mathrm{Re}(\omega_{ll})$, the thick green line represents $|\mathrm{Im}(\omega_{ll})|$, dash-dotted blue line represents $\mathrm{Re}(\omega_{fe})$, the solid black line represents $|\mathrm{Im}(\omega_{fe})|$, dotted cyan line represents $\mathrm{Re}(\omega_{se})$, and the solid orange line represents $|\mathrm{Im}(\omega_{se})|$, here solid and dash-dotted lines are the analytical results of BdG Eq. 5.8 and open circles are numerical results obtained by solving Eq. 5.5. Eigenvectors of low-lying branch are $|u_{+1}|^2_{ll}$ (red dot), $|u_{-1}|^2_{ll}$ (black hexagons), $|u_0|^2_{ll}$ (magenta hexagons), $|v_0|^2_{ll}$ (cyan open stars), $|v_{+1}|^2_{ll}$ (green open squares), and $|v_{-1}|^2_{ll}$ (magenta triangles). For the first-excited branch, $|u_{+1}|^2_{fe}$ (blue open pentagon), $|u_{-1}|^2_{fe}$ (orange stars), $|u_0|^2_{fe}$ (olive open plus), $|v_0|^2_{fe}$ (red open x with the dotted line), $|v_{+1}|^2_{fe}$ (cyan open diamond), and $|v_{-1}|^2_{fe}$ (maroon dots). (a i) exhibits only real eigenfrequencies, and (b i) depicts multi-band instability, which is symmetric in the quasi-momentum direction. Corresponding eigenvectors depict density-like mode and spin-like mode, respectively. The UAC among branches results in I_o type instability band in the eigenspectrum. The vertical scale on the right represents the magnitude of imaginary eigenfrequencies.

between all branches. The low-lying branch exhibits a phonon mode, as shown in Fig. 5.1(a i). The eigenspectrum is symmetric about the quasi-momentum direction. To further explore the detailed nature of the excitations, we plot the eigenvectors corresponding to the eigenspectrum in Fig. 5.1(a i) in Figs. 5.1(a ii) and 5.1(a iii). Here, we display three sets of eigenvector components, namely, $|u_{+1}|^2$, $|v_{+1}|^2$, $|u_0|^2$, $|v_0|^2$, $|u_{-1}|^2$, and $|v_{-1}|^2$, for a specific branch of the eigenspectrum. We find that all eigenvector components exhibit a density-like mode consistent with the real eigenfrequencies observed, aligning with previous studies on spin-1/2 SO coupled BECs [93, 152]. Additionally, these eigenvectors satisfy the following relations for the low-lying and first-excited branches:

$$\begin{aligned} |u_{+1}|^2_{ll} - |u_{-1}|^2_{ll} = 0, \quad |v_{+1}|^2_{ll} - |v_{-1}|^2_{ll} = 0, \\ |u_{+1}|^2_{fe} - |u_{-1}|^2_{fe} = 0, \quad |v_{+1}|^2_{fe} - |v_{-1}|^2_{fe} = 0. \end{aligned} \tag{5.9}$$

Apart from this, we find that the eigenvector components of the low-lying branch appear to approach the same value at $q_x \approx 0$, a typical feature of the phonon mode in the eigenspectrum [see Figs. 5.1(a ii, a iii)]. In Fig. 5.1(b i), we present the eigenfrequency for regime II ($k_L^2 > \Omega$) of the condensate, which clearly reveals the presence of imaginary eigenfrequencies in the low-lying and first-excited branches of the eigenspectrum, whereas the second-excited branch exhibits only real eigenfrequencies. The low-lying branch displays three instability bands at wave number and corresponding eigenfrequency pairs given by $\{q_x, \omega\} = \{0.33, 0.999\}$, $\{2.04, 0.799\}$, and $\{8.37, 0.773\}$, while the first-excited branch exhibits a single instability band at $q_x = 2.04$ with an eigenfrequency of $\omega = 0.799$. This single-band instability in the first-excited branch arises due to an UAC between the low-lying and first-excited branches of the eigenspectrum, occurring within the quasi-momentum range $1.14 \lesssim q_x \lesssim 2.94$. This interaction is primarily responsible for the I_o-type dynamical instability [94, 95, 115]. The presence of imaginary eigenfrequencies indicates dynamical instability in the condensate phase. Similar to regime I, in regime II, we also observe that the eigenspectrum is symmetric about the quasi-momentum direction; however, it distinctly exhibits multi-band instability. This multi-band nature manifests in the eigenvectors as a spin-like mode, satisfying a specific relationship between the low-lying and first-excited branches of the excitation spectrum.

$$\begin{aligned} &|u_{+1}|^2_{ll} - |u_{-1}|^2_{ll} \neq 0, |v_{+1}|^2_{ll} - |v_{-1}|^2_{ll} \neq 0, \\ &|u_{+1}|^2_{fe} - |u_{-1}|^2_{fe} \neq 0, |v_{+1}|^2_{fe} - |v_{-1}|^2_{fe} \neq 0. \end{aligned} \tag{5.10}$$

The eigenvectors of the low-lying branch display an interesting feature of the transition from spin-like mode to density-like mode which indicates the presence of transition from $\mathrm{Im}(\omega) \to \mathrm{Re}(\omega)$ and then density-like mode to spin-like mode informs that $\mathrm{Re}(\omega) \to \mathrm{Im}(\omega)$ and in the weak wavelength limit only $\mathrm{Re}(\omega)$ is present and $\mathrm{Im}(\omega)$ is absent. This particular feature suggests the presence of spin-density-spin mixed mode of the eigenvector in the three instability bands regions of the eigenspectrum. The first-excited branch of the eigenspectrum has a single instability band that occurs due to the UAC between the low-lying and first-excited branches, which lies in the quasimomentum range $1.14 \lesssim q_x \lesssim 2.94$. Closer to the q_x of UAC, the eigenvectors of the low-lying and first-excited branches display out-of-phase behaviour among the branches [see Fig. 5.1(b ii)]. However, the zeroth component of eigenvectors exhibits density-like mode only [see Fig. 5.1(b iii)].

After analyzing the collective excitation spectrum, we wish to understand the ap-

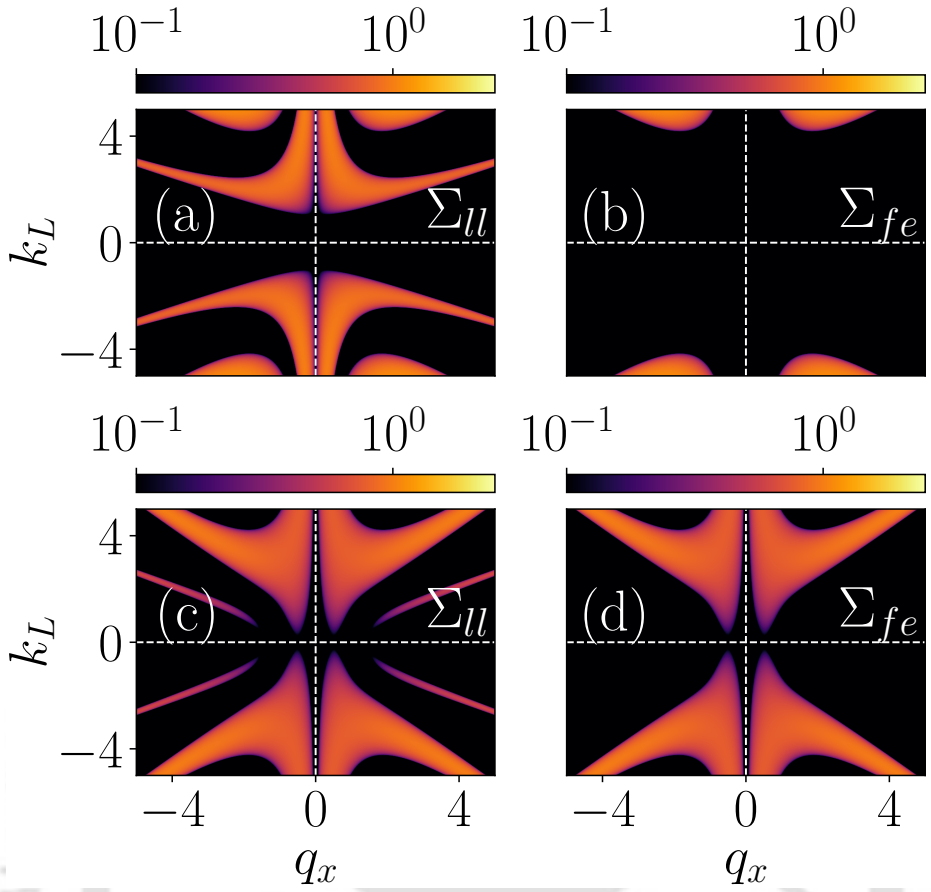


Figure 5.2: Pseudo color plot of modulational instability gain for the ferromagnetic phase ($c_0 = 5$, $c_2 = -2$) in $k_L - q_x$ plane for (a, b) $\Omega = 1$ and (c, d) $\Omega = -1$. Left column panel corresponds to $\Sigma_{ll} \equiv |\mathrm{Im}(\omega_{ll})|$ and right column panel corresponds to $\Sigma_{fe} \equiv |\mathrm{Im}(\omega_{fe})|$. In (a), multi-band instability gain appears at $k_L = 1$, and in (b) a single-band instability appears at $k_L \approx 4.0$. In (c) and (d) double and single band instabilities appear at $k_L > 0.25$, respectively. The second-excited branch of the eigenspectrum shows the absence of instability gain for both sets of parameters. The instability gain is symmetric about k_L and q_x.

pearance of MI in the phase plots. Specifically, we focus on the $k_L - q_x$ plane for the ferromagnetic SO coupled BECs. In Figs. 5.2(a, b), we present the pseudo color representation of the modulational instability (MI) gain, defined as imaginary part of the modulus of eigenfrequency, for a Rabi coupling strength $\Omega = 1$ and with ferromagnetic interaction strengths $c_0 = 5.0, c_2 = -2.0$. We observe that instability bands start emerging in the range where $k_L^2 > \Omega$, first appearing in the low-lying branch (Σ_{ll}) as a single band. However for $k_L > 3$ two instability band emerge and for $k_L > 4$ three bands are observed[see fig. 5.2(a)]. For the first-excited branch (Σ_{fe}), instability emerges only at higher values of the SO coupling ($k_L \gtrsim 4.0$). This can be attributed to the emergence of a UAC between the ω_{ll} and ω_{fe} branches within the quasi-momentum range $0.95 < q_x < 3.64$. Initially, this forms a single instability band, which expands as the

TH-4102_206121026

SO coupling strength increases. In Figs. 5.2(c) and 5.2(d), we present the MI gain for the low-lying and first-excited modes, respectively, at $\Omega = -1$, with all other parameters held constant as those used for $\Omega = 1$. Here, we observe a markedly different trend compared to those results obtained with a positive Rabi frequency. In a spin-1 condensate, negative Rabi coupling increases the system's energy, manifesting as a higher number of instability bands [114]. For negative Rabi strength, we notice that the instability appears at a lower SO coupling value ($k_L > 0.25$) compared to positive Rabi strength [see Figs. 5.2(c) and 5.2(d)]. The instability manifests as double bands in the low-lying branch and a single band in the first-excited branch, both of which intensify with increasing SO coupling strength. The instability gain is symmetric about the quasi-momentum q_x and the SO coupling strength k_L. Notably, the second-excited branch exhibits no instability gain in the ferromagnetic BECs, even in the presence of SO coupling (k_L).

After getting a clear understanding of how Rabi coupling affects the MI gain in the $k_L - q_x$ plane, we now shift our focus on exploring the same in the $\Omega - q_x$ plane by fixing the SO coupling strength as $k_L = 1$. We analyze the impact of Rabi coupling on the MI gain for the ferromagnetic interaction strengths $c_0 = 5.0$, $c_2 = -2.0$. To systematically investigate the impact of Rabi coupling strength on the eigenspectrum, we begin our analysis by choosing $k_L = 1.0$. We find that the low-lying branch of the eigenspectrum exhibits finite instability gain for $\Omega < 1$ [see figure 5.3(a)], but, for $\Omega > 1$, the modes become stable. Upon examining the other two branches, namely, the first-excited branch and the second-excited branch, we observe that instability gain becomes finite only for $\Omega < 0$ as illustrated in Fig. 5.3(b), and Fig. 5.3(c), respectively. Interestingly, the low-lying and first-excited branches of the eigenspectrum display multiple instability bands for $\Omega < 0$, whereas the second-excited branch exhibits only a single instability band starting at $\Omega \lesssim -1.66$. Upon considering relatively stronger SO coupling strength ($k_L = 4.0$), multi-band instabilities appear in both the low-lying and the first-excited branches [see Figs. 5.3(d)-(f)]. The second-excited branch, however, still only shows a single instability band, similar to the case with $k_L = 1$. Comparing the instability features across the range of Rabi frequencies from $-\Omega$ to $+\Omega$, we observe a transition from multi-band instability to a single instability band in the low-lying branch, accompanied by the existence of a primary band in the first-excited branch for $\Omega > 0$. The primary instability band in the low-lying branch appears at $k_L^2 = \Omega$. In the second-excited branch, a single instability band is present for $\Omega \lesssim -1.44$. Furthermore, the instability gains (Σ_{ll}, Σ_{fe}, Σ_{se}) in all three branches increase as the Rabi coupling strength decreases, and they exhibit symmetry about q_x.

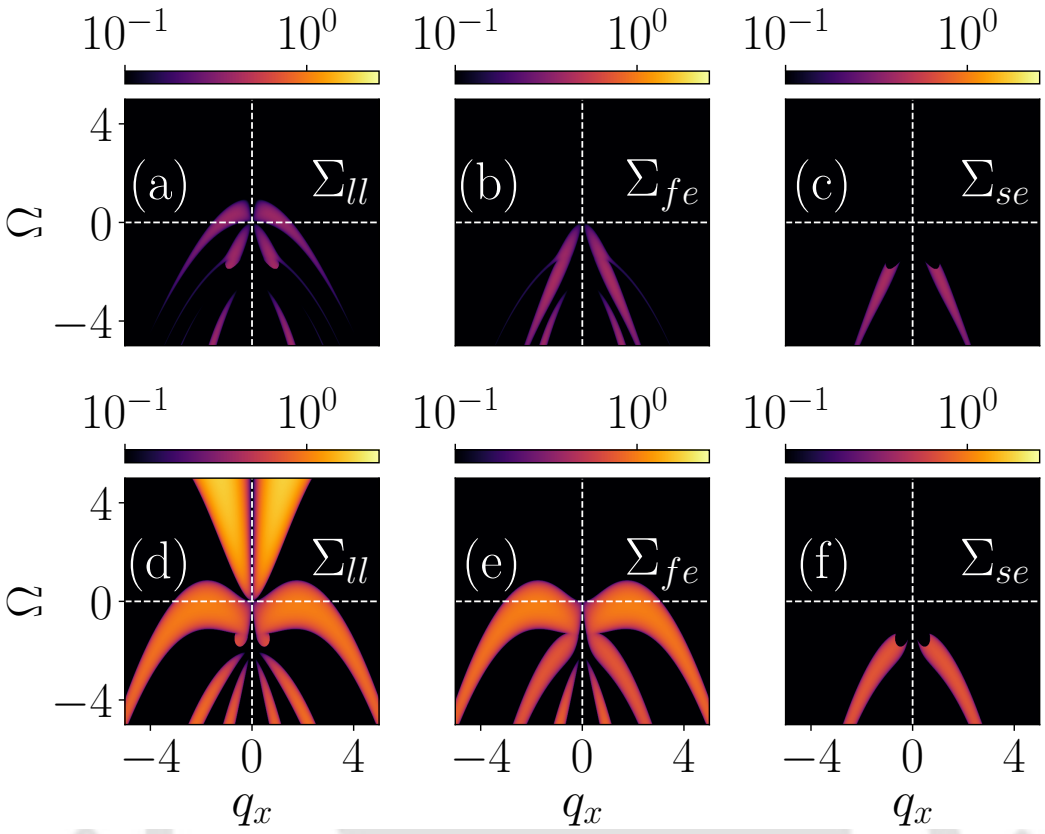


Figure 5.3: Pseudo color plot of the Modulational instability gain in $\Omega - q_x$ phase plane for ferromagnetic interactions ($c_0 = 5.0$, and $c_2 = -2.0$) with (a-c) for $k_L = 1$, and (d-f) for $k_L = 4.0$. (a,d) represents $\Sigma_{ll} \equiv |\mathrm{Im}(\omega_{ll})|$, (b,e) represents $\Sigma_{fe} \equiv |\mathrm{Im}(\omega_{fe})|$ and (c,f) for $\Sigma_{se} \equiv |\mathrm{Im}(\omega_{se})|$ low-lying, first-excited, and second-excited branches of the excitation spectrum. In (a), the primary band appears for $\Omega > 0$ following the relation $k_L^2 = \Omega$, while in (b) and (c), it appears only for $\Omega < 0$, with a cutoff in (c), $\Omega \approx -1.66$. Similar to the top row, the primary instability band in (d) appears for $\Omega > 0$. In (d) and (e), the secondary and primary bands appear for $\Omega > 0$ different than the top row. In (f), single band instability appears for $\Omega < 0$, following a cutoff value $\Omega \approx -1.44$. The instability gain appears is not symmetric about Ω and increases upon decreasing the Ω. However, it shows symmetric behaviour about q_x.

Overall, we find that SO coupled BECs with ferromagnetic interaction exhibit a single UAC between ω_{ll} and ω_{fe}, as previously reported [115]. This UAC emerges at critical values of coupling strength, following the relation $\Omega \approx 0.1278 k_L^2 - 1.1358$, with its origin at $(k_L, \Omega) = (2.94, 0.01)$. Interestingly, in MI analysis [86, 132], we observe that for $\Omega < 0$, the first excited branch (ω_{fe}) exhibits a second UAC with the second excited branch (ω_{se}), accompanied by the emergence of more number of multi-band instabilities compared to cases where $\Omega > 0$.

After analyzing the collective excitation for ferromagnetic interaction, we now present the corresponding analysis for the antiferromagnetic interaction in the next section.

TH-4102_206121026

5.3.2 Collective excitation spectrum of antiferromagnetic SO coupled BECs ($c_0 > 0, c_2 > 0$)

In this section, we present the collective excitation spectrum for antiferromagnetic interaction SO coupled BECs by considering $c_0 = c_2 = 5.0$. In regime I, with $k_L = 0.5$ and $\Omega = 1.0$, the eigenspectrum exhibits only real eigenfrequencies. However, avoided crossings occur between the $\omega_{ll} - \omega_{fe}$ branches at $q_x \sim 2.70$ and the $\omega_{fe} - \omega_{se}$ branches at $q_x \sim 1.87$ [see Fig. 5.4(a)]. As the imaginary part of the eigenspectrum is zero ($\mathrm{Im}(\omega_j) = 0$), the condensate remains dynamically stable. The involvement of the first-excited branch in both of these stable avoided crossings results in a double stable avoided crossing near $q_x \sim 1.87$ and $q_x \sim 2.70$, as depicted in Fig. 5.4(a). Furthermore, the minimum of the low-lying excitation spectrum occurs at $q_x = 4.06$, corresponding to the phonon energy minimum. This minimum corresponds to the rotonic minimum and is responsible for the emergence of the plane-wave phase in spin-1 antiferromagnetic SO coupled BECs [23, 82]. Such features are not observed in ferromagnetic SO coupled BECs.

In Fig. 5.4(b), we show the eigenspectrum corresponding to the regime II where we have considered $k_L = 4.5$ and $\Omega = 1.0$. The other parameters are the same as those in panel (a). In this regime, we notice the appearance of multi-band imaginary eigenfrequency both in the ω_{ll} and ω_{fe} branches. There are three instability bands present in the low-lying branch whose location and corresponding amplitude are given as $\{q_x, \omega\} = \{1.63, 3.037\}, \{4.81, 2.149\}, \{9.06, 1.585\}$. However, the other two instability bands appear in the first excited branch with position and amplitudes $\{q_x, \omega\} = \{1.46, 0.802\}, \{4.81, 2.149\}$. Additionally, we notice the presence of a single-band instability in the ω_{se} branch with $\{q_x, \omega\} = \{1.46, 0.802\}$ which arises solely due to crossing between $\omega_{se} - \omega_{fe}$. The presence of imaginary eigenfrequency leads to dynamical instability in regime II, as also obtained in [20, 21, 93]. The ω_{fe} branch experiences a double UAC, arising from avoided crossings with the other two branches. The first UAC between $\omega_{ll} - \omega_{fe}$ appears in the quasimomentum range $4.01 \lesssim q_x \lesssim 5.49$, while, the second UAC appears between $\omega_{fe} - \omega_{se}$ in the quasi-momentum range $1.14 \lesssim q_x \lesssim 1.78$ [see figure 5.4(b)]. Such an instability is responsible for a I_o type of dynamical instability [94, 95], which will be discussed in the later part of the paper.

Next, we analyze the corresponding eigenvectors of the regime I and II for the antiferromagnetic SO coupled BECs. In Fig. 5.5, we demonstrate the nature of eigenvectors corresponding to Fig. 5.4. First, we report for regime I the respective eigenspectrum is presented in Fig. 5.4(a). As all the eigenfrequencies ω_{ll}, ω_{fe} and ω_{se} are real, the

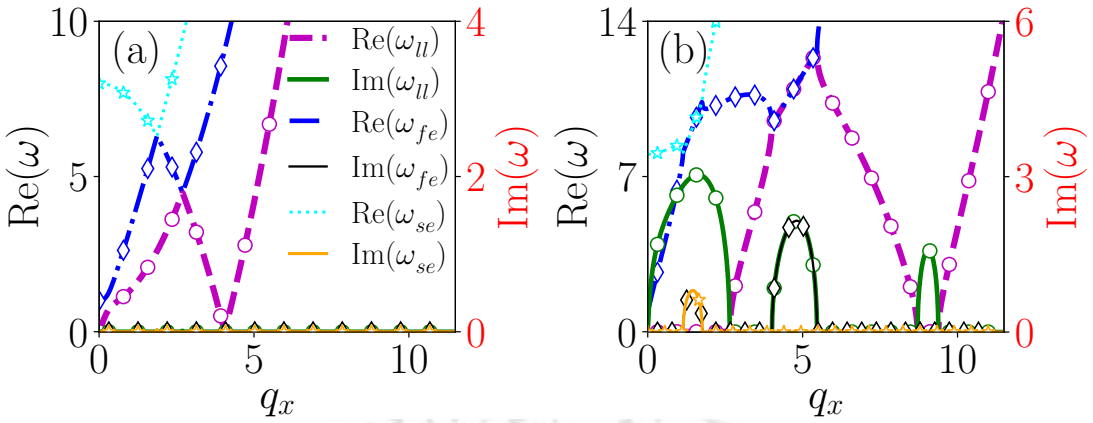


Figure 5.4: Eigenspectrum with antiferromagnetic interaction ($c_0 = 5.0$, $c_2 = 5.0$) for (a) $(k_L, \Omega) = (0.5, 1.0)$, and (b) $(k_L, \Omega) = (4.5, 1.0)$. The lines and symbols representation is same as in Fig. 5.1(a i) and (b i). In panel (a), a stable avoided crossing appears between first-excited (ω_{fe}) and second-excited (ω_{se}) as well as low-lying (ω_{ll}) and ω_{fe} branches. As SO coupling is increased in panel (b) multi-band instability emerges in the eigenspectrum accompanied by the appearance of UAC between ω_{fe}- ω_{se} and ω_{ll}- ω_{fe} branches. The first-excited branch exhibits the double UAC. The right vertical axis represents the imaginary eigenfrequencies.

corresponding eigenvector components display in-phase (density-like) behaviour in quasi-momentum direction (q_x), which holds the criterion given in Eq. 5.9 (also holds for the eigenvectors of the second-excited branch). A flip in the eigenvector components occurs at the point of first stable avoided crossing around $q_x \sim 2.70$ between the $\omega_{ll} - \omega_{fe}$ branches [see Figs. 5.5(a i)] similar as reported in the Ref. [152]. As the second stable avoided crossing is observed between $\omega_{fe} - \omega_{se}$, the eigenvector components for corresponding branches also show the flipping tendency at the point of crossing at $q_x \sim 1.87$ [see Figs. 5.5(a iii)]. The zeroth component of eigenvectors of low-lying, first- and second-excited branches of the eigenspectrum show density-like mode, which is given in Figs. 5.5(a ii), and (a iv). Overall, we observe that at the point of stable avoided crossing between the branches, the flip in eigenvectors of both branches occurs simultaneously at $q_x \approx 2.70$ and ≈ 1.87. Moreover, further flip in the eigenvectors of the low-lying branch takes place at $q_x \approx 4.06$, when the eigenvalue spectrum approaches zero, where $\mathrm{Re}(\omega) = \mathrm{Im}(\omega) = 0$.

We present the nature of eigenvectors for high k_L corresponding to the eigenspectrum shown in Fig. 5.4(b). We observe that due to the presence of complex eigenfrequency ($\mathrm{Im}(\omega_j) \neq 0$), the eigenvector components show the spin-like (out-of-phase) behaviour characterized by the Eq. 5.10 (the same applied for the eigenvectors of the second-excited branch). As the low-lying and first-excited branches have multi-band instability in the eigenspectrum, the eigenvectors exhibit a transition from spin-like to density-like mode resulting in a mixed mode. At the first UAC between $\omega_{ll} - \omega_{fe}$

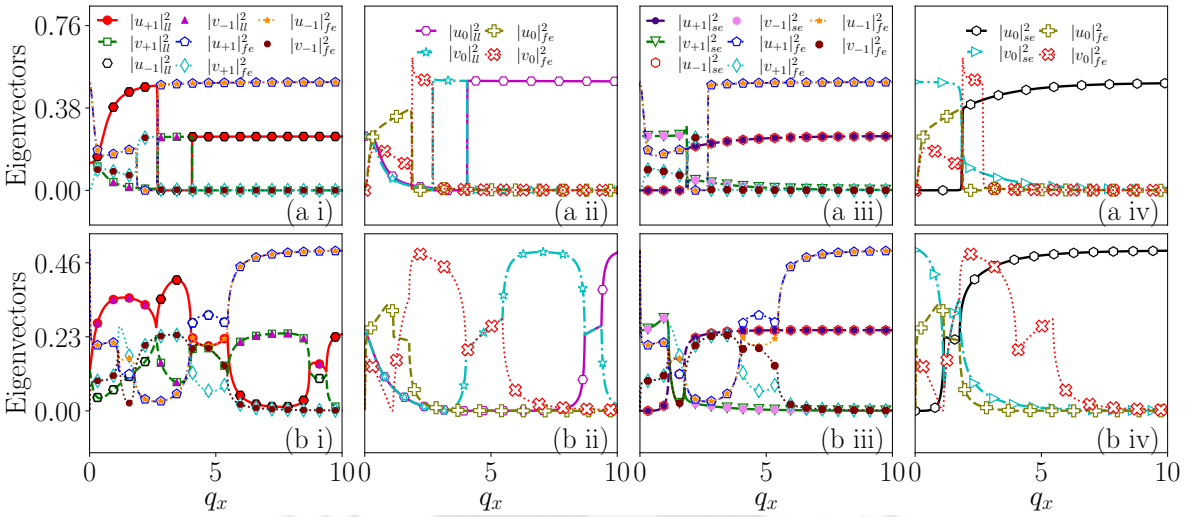


Figure 5.5: Eigenvectors corresponding to Figs. 5.4(a) and (b), in (a) and (b), respectively. (a i, a ii), and (b i, b ii) represents eigenvectors of the low-lying and first-excited branch, while (a iii, a iv) and (b iii, biv) for the second-excited and first-excited branch of the eigenspectrum. The eigenvectors of the low-lying branch are given as $|u_{+1}|^2_{ll}$ (red dot), $|u_{-1}|^2_{ll}$ (black hexagons), $|u_0|^2_{ll}$ (magenta hexagons), $|v_0|^2_{ll}$ (cyan open stars), $|v_{+1}|^2_{ll}$ (green open squares), and $|v_{-1}|^2_{ll}$ (magenta triangles). For the first-excited branch, $|u_{+1}|^2_{fe}$ (blue open pentagon), $|u_{-1}|^2_{fe}$ (orange stars), $|u_0|^2_{fe}$ (olive open plus), $|v_0|^2_{fe}$ (red open x with the dotted line), $|v_{+1}|^2_{fe}$ (cyan open diamond), and $|v_{-1}|^2_{fe}$ (maroon dots). The eigenvectors of the second-excited branch are given as $|u_{+1}|^2_{se}$ (indigo dot), $|u_{-1}|^2_{se}$ (red hexagons), $|u_0|^2_{se}$ (black hexagons), $|v_0|^2_{se}$ (cyan triangle left), $|v_{+1}|^2_{se}$ (green open triangle down), and $|v_{-1}|^2_{se}$ (violet dots). (a i - a iv) depict in-phase behaviour (density-like mode) with the occurrence of flip at the point of stable avoided crossing between $\omega_{ll} - \omega_{fe}$, and $\omega_{se} - \omega_{fe}$. (b i, b iii) exhibit the out-of-phase behaviour (spin-like mode). At the point of UAC, eigenvectors are out-of-phase among the branches. However, (b ii, b iv) only depict density-like mode.

branches occur in the quasi-momentum range $4.01 \lesssim q_x \lesssim 5.49$ in the eigenspectrum [see Fig. 5.4(b)], the corresponding eigenvectors exhibit complicated out-of-phase behaviour among these branches as illustrated in Fig. 5.5(b i). As we look at the eigenvector in the second UAC region ($1.14 \lesssim q_x \lesssim 1.78$), we find that they exhibit similar out-of-phase features [see Fig. 5.5(b iii)]. Interestingly, the zeroth component of eigenvectors for the low-lying, first- and second-excited branches exhibit density-like mode independently [see Fig. 5.5(b ii), and (b iv)] [115].

In the preceding section, we derived the multi-band imaginary eigenfrequencies for the low-lying and first-excited branches, as well as the single-band imaginary eigenfrequency for the second-excited branch of the spectrum. The instability gains in these eigenspectra are characterized as $\Sigma_{ll,fe,se} = \left|\mathrm{Im}(\omega_{ll,fe,se})\right|$.

After analyzing the presence of instability in the collective excitation spectrum of antiferromagnetic SO coupled BECs, we aim to investigate the nature of this instability through instability gains using phase plots, varying the parameters k_L and Ω. We

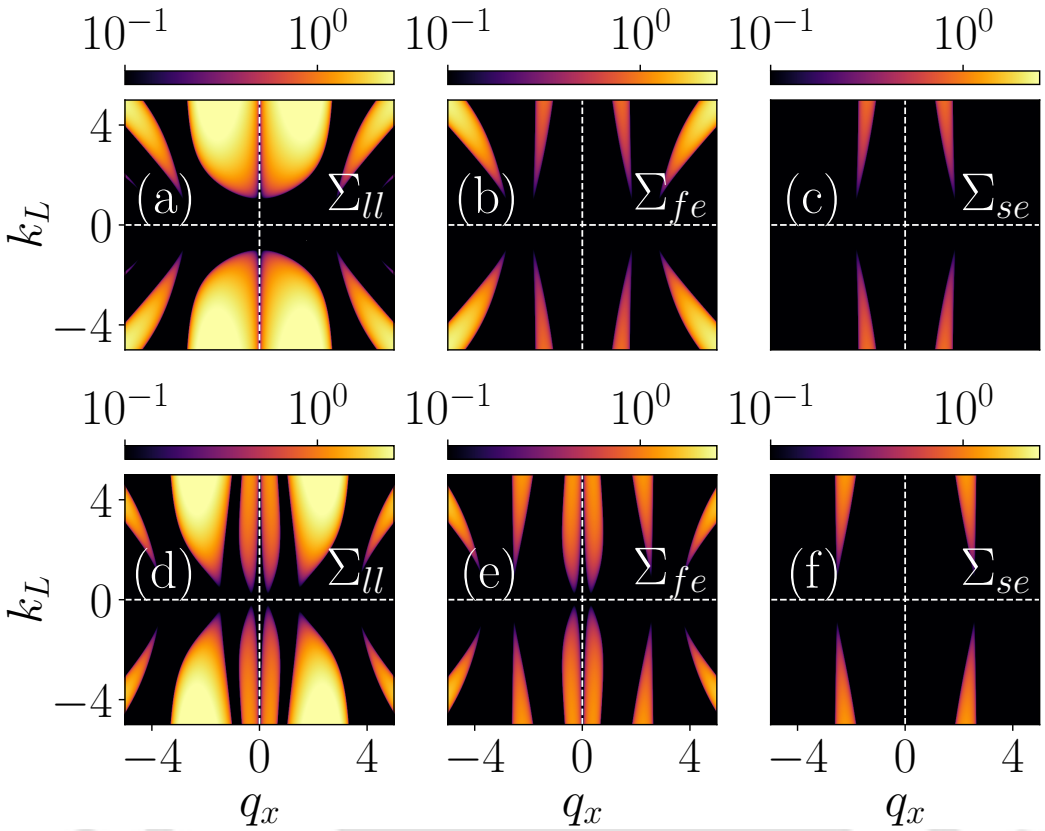


Figure 5.6: MI gain in the $k_L - q_x$ phase plane for (a-c) $\Omega = 1$ and (d-f) $\Omega = -1$. The interaction strengths are $c_0 = c_2 = 5.0$. In the panel, the pseudo color represents similar denotations as Fig. 5.3. In the top row, we obtain the instability bands at $k_L = 1.0$, following the critical relation $k_L^2 = \Omega$, while in the bottom row, it appears for $k_L > 0.25$. Symmetry arguments are similar to Fig.5.2.

begin by examining the role of k_L (SO coupling strength) on the instability gain of antiferromagnetic condensates with interaction strengths $c_0 = c_2 = 5.0$. In Figs. 5.6(a)-(c), the Rabi coupling strength is fixed at $\Omega = 1$. Instability emerges when $k_L > 1$. In the low-lying branch (Σ_{ll}), we observe the emergence of double-band instability along the quasi-momentum direction. The growth of the primary instability increases with increasing SO coupling strength. Additionally, the bandwidth of the secondary instability widens, exhibiting a horn-like shape. The first- and second-excited branches also display instability gains (Σ_{fe} and Σ_{se}), characterized by double- and single-band structures, respectively. For the instability gain of the first excited state (Σ_{fe}), two humps appear: the primary instability band remains constant, while the secondary instability band expands with increasing SO coupling strength. The instability gain of the second-excited branch (Σ_{se}) and its bandwidth also exhibit an increasing trend as k_L increases. Interestingly, for a negative Rabi coupling ($\Omega = -1$), we observe a distinctly different trend compared to the positive Rabi coupling case. In a spin-1 system, negative Rabi

TH-4102_206121026

coupling injects additional energy into the system [114], resulting in a higher number of instability bands. Consequently, instability arises earlier (at $k_L > 0.25$) compared to the positive Rabi coupling case [see Figs. 5.6(d)-(f)]. Here, triple instability bands appear in the low-lying and first-excited branches. The first band remains constant, while the bandwidth and instability gain of the second band varies with k_L, and the third band grows gradually with increasing SO coupling strength, consistent with the previous case. For both $\Omega = 1$ and $\Omega = -1$, the instability bandwidth of all branches remains symmetric about the quasi-momentum q_x and the SO coupling strength k_L.

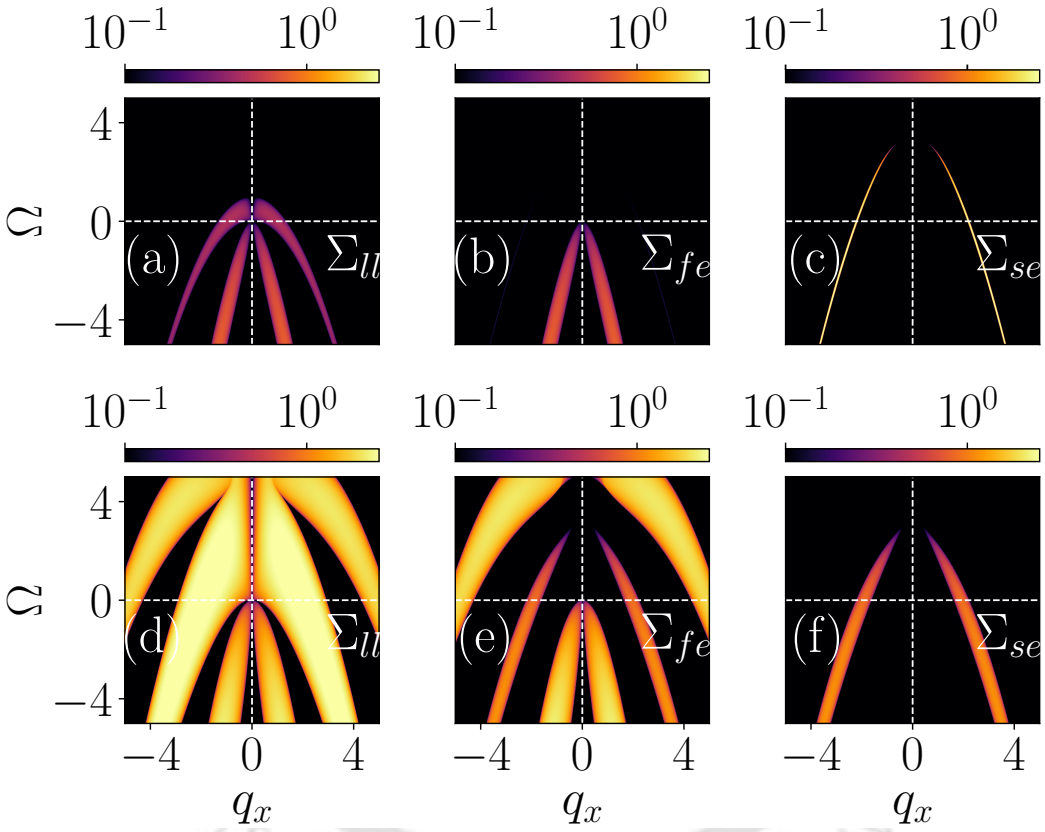


Figure 5.7: MI gain in $\Omega - q_x$ phase diagram for (a-c) $k_L = 1$, and (d-f) $k_L = 4.0$. Here, the density-density interaction, $c_0 = 5.0$, and spin-dependent interaction $c_2 = 5.0$. The pseudo-color bar in the figure is similar to Fig. 5.3. Multi-band instability appears for the low-lying and first-excited branches of the spectrum, while the second-excited branch shows single-band instability. The instability gain appears is not symmetric about Ω and increases upon decreasing the Ω. However, it shows symmetric behaviour about q_x.

Next, we investigate the effect of Rabi coupling strength on the instability gain, denoted as $\Sigma_{ll,fe,se}$, in SO coupled spin-1 BECs with antiferromagnetic interactions, where $c_0 = c_2 = 5$. In Figs. 5.7(a)–(c), we fix the SO coupling strength at $k_L = 1$ and vary the Rabi coupling strength, Ω. This reveals double instability bands in the low-lying branch of the eigenspectrum, whereas the first-excited and second-excited branches

exhibit only single-band instability. In the low-lying branch, the primary instability band emerges at $\Omega = 1.0$, increases in magnitude for $\Omega < 1.0$, and disappears, becoming stable for $\Omega > 1.0$. Additionally, a secondary instability band appears for $\Omega < 0$. In the first-excited branch, instability gain is observed for $\Omega < 0$, inheriting an UAC between the low-lying and first-excited branches. In the second-excited branch, a single instability band emerges, growing for $\Omega \lesssim 3.15$; at $\Omega < 0$, a second UAC appears. Thus, when $\Omega < 0$, the antiferromagnetic system exhibits double UACs and double instability gain bands [see Fig. 5.7(c)]. Note that as the amplitude of the instability gain for this branch is one order smaller than those compared to the other two branches, we multiply a factor of 20 to bring it to the same scale as the other two branches.

For a relatively strong SO coupling strength of $k_L = 4.0$, we observe multi-band instability in the low-lying and first-excited branches of the eigenspectrum, while the second-excited branch displays single-band instability for $\Omega < 3.0$. Due to the significantly higher SO coupling strength, the instability gain exhibits both a larger amplitude and higher coverage in the phase plane [see Figs. 5.7(d)–(f)]. Comparing the two cases, we find that for weak SO coupling ($k_L = 1$), the maximum unstable phase occurs only for negative Ω (i.e., $-\Omega$), with stability observed for positive Ω (i.e., $+\Omega$). In contrast, for strong SO coupling ($k_L = 4.0$), the entire considered range of Ω is unstable.

In Figs. 5.7, the instability gain along the quasi-momentum direction (q_x) increases as the Rabi coupling strength decreases, displaying symmetric behaviour about q_x. Furthermore, we confirm that in regime II of the antiferromagnetic interaction, double UACs are present for both positive and negative Ω ($\pm\Omega$), whereas, in the ferromagnetic interaction, double UACs occur only for negative Ω ($-\Omega$). Thus, both systems exhibit double UACs, with their appearance dependent on the Rabi coupling strength.

Further, we study the behaviour of the system at fixed interaction strengths c_0, c_2, and quasi-momentum q_x, upon simultaneous varying the SO coupling (k_L) and Rabi coupling (Ω) strengths [see Figs. 5.8(a), (b)]. We demonstrate instability gain of the low-lying branch of the eigenspectrum corresponding to two different sets of interaction strengths at $q_x = 1$. In Figs. 5.8(a), we consider interaction strengths corresponding to antiferromagnetic interaction, and in figure 5.8(b), corresponding to ferromagnetic interaction. We obtain multi-band instability for both cases, which is not symmetric about Ω. The instability gain is symmetric about k_L and increases upon increasing the SO coupling strength. Here, we conclude that the regime I, ($\Omega > k_L^2$) is dynamically stable while the regime II ($\Omega < k_L^2$) is dynamically unstable and exhibit multi-instability bands. Moreover, with respect to the negative Rabi couplings, both spinor BECs exhibit double UAC. Additionally, we observe that the instability gain of

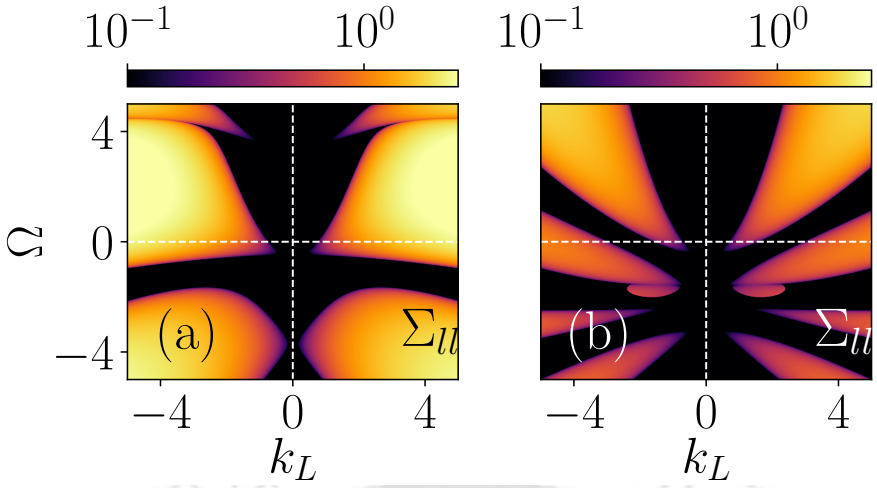


Figure 5.8: Pseudo color representation of the MI gain for $\Sigma_{ll} \equiv |\mathrm{Im}(\omega_{ll})|$ in $k_L - \Omega$ phase plane for (a) $(c_0, c_2) = (5, 5)$ and (b) $(c_0, c_2) = (5, -2)$ at quasi-momentum $q_x = 1$. Multi-band instability appears in each case, which increases upon increasing the k_L. The instability bands show symmetric behaviour about k_L, however, it is not symmetric with the variation in Ω.

the ferromagnetic condensate is reduced by approximately half for antiferromagnetic condensate, indicating that the latter is dynamically more unstable and sensitive to perturbations.

5.4 Impact of density-density interaction and spin-exchange interaction on the MI

So far we have analyzed the effect of k_L and Ω on the collective excitation spectrum for the ferromagnetic $(c_0, c_2) = (5.0, -2.0)$ and antiferromagnetic $(c_0, c_2) = (5.0, 5.0)$ interaction phases of the SO coupled spin-1 condensate. For ferromagnetic interactions, the instabilities mainly appear in the low-lying and first-excited branches of the eigenspectrum. However, for antiferromagnetic interactions, they appear in the low-lying, first- and second-excited branches. Next, to make our analysis more general, we scan a wide range of interactions $((c_2, c_0) \in [-10, 10])$ for low SO coupling $(k_L^2 < \Omega)$ and high SO coupling $(k_L^2 > \Omega)$ regimes.

First, we consider the effect of density-density interaction term c_0 by choosing c_2 positive or negative. At first, we choose $c_2 = -2.0$ along with two different sets of coupling strengths (k_L, Ω). For $(k_L^2 < \Omega)$, we find that the instability gain is zero as long as the total interaction strength remains repulsive, i.e., $c_0 + c_2 > 0$. However, single-band instability appears in the low-lying branch of the eigenspectrum when the total

TH-4102_206121026

interaction strength is attractive, i.e., $c_0 + c_2 < 0$. For $c_2 = -2.0$ and $c_0 > 2.0$, the instability gain is absent. The instability appears where the interaction follows the relation $c_0 + c_2 < 0$. The instability gain appears to increase upon further decreasing the c_0 [see figure 5.9(a)]. However, there is a lack of instability in the first- and second-excited branches (not shown here). Now, we consider regime II that holds $k_L^2 > \Omega$, and we obtain multi-band instability that appears in the low-lying and first-excited branches of the spectrum. The instability gain of the spectrum increases upon decreasing the c_0 [see Figs. 5.9(b), and (c)]. On the other hand, instability gain is absent in the second-excited branch of the eigenspectrum. We found that regime I has instability only for the attractive system and no UAC, but regime II is stable only for $c_0 + c_2 \approx 0$, otherwise exhibits UAC, also no appearance of double UAC. For both sets of coupling strengths, the instability gain of the spectrum is symmetric about q_x and not symmetric about c_0.

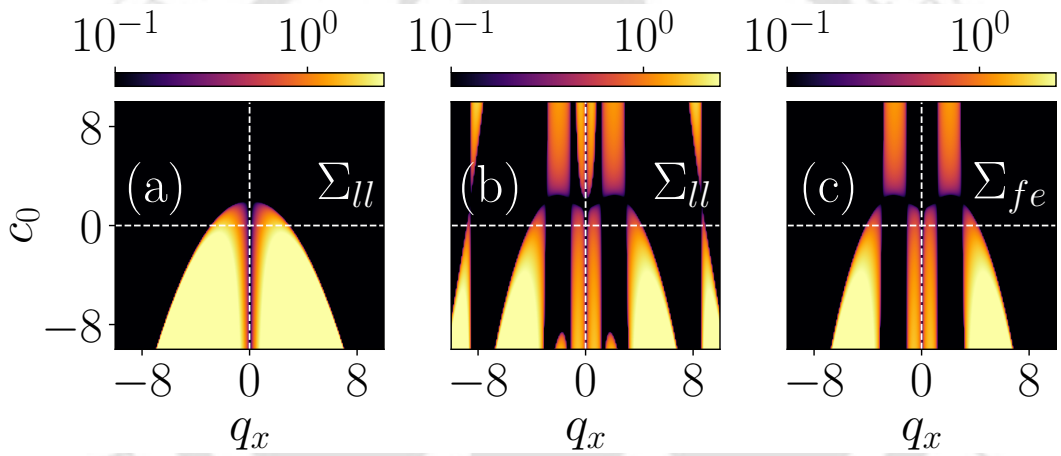


Figure 5.9: (a) Pseudo color representation of MI gain for low-lying mode $\Sigma_{ll} \equiv |\mathrm{Im}(\omega_{ll})|$ in $c_0 - q_x$ phase plane with $(k_L, \Omega) = (0.5, 1.0)$. (b) and (c) represent the pseudo color representation of MI gain for low-lying mode $\Sigma_{ll} \equiv |\mathrm{Im}(\omega_{ll})|$ and first excited mode $\Sigma_{fe} \equiv |\mathrm{Im}(\omega_{fe})|$ respectively in the $c_0 - q_x$ phase plane for $(k_L, \Omega) = (4.5, 1.0)$. The spin-exchange interaction is $c_2 = -2.0$. In (a), the instability gain appears only in the low-lying branch, while in (b, c), it appears in a low-lying and first-excited branch of the excitation spectrum. In the panel, the instability gain increases upon decreasing the c_0, showing symmetric behaviour about q_x. However, it is not symmetric about c_0.

In the above part, we analyzed the effect of c_0 in the presence of $c_2 = -2.0$. Further, to analyze the impact of positive interaction, we consider $c_2 = 5.0$. Here also we consider the low-k_L regime, regime I ($k_L^2 < \Omega$) and high k_L regime, regime II ($k_L^2 > \Omega$). For regime I, we consider c_0 in the range [-5:5], and obtain only real eigenfrequencies in the eigenspectrum. Therefore, the instability gain remains absent and is responsible for the dynamical stable phases (not shown here). Further, we choose regime II, which exhibits multi-band instability that appears in low-lying and first-excited branches of the eigenspectrum [see Figs. 5.10(a) and (b)], while the second-excited branch shows

TH-4102_206121026

single band instability [see figure 5.10(c)]. The regime II is stable only for the attractive c_0 interactions results as $c_0 + c_2 \approx 0$. The instability gain increases upon increasing c_0, showing symmetric behaviour about q_x, while not symmetric about c_0.

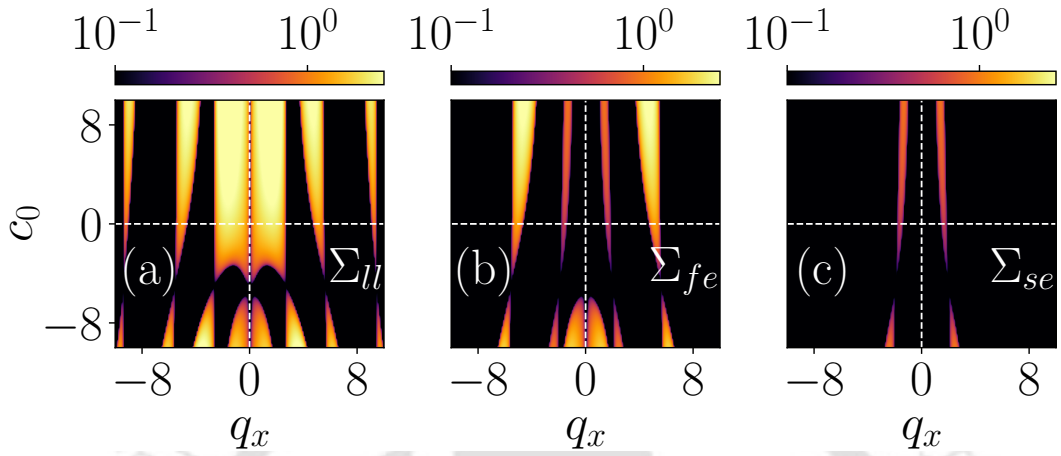


Figure 5.10: MI of antiferromagnetic interaction ($c_2 = 5.0$) in $c_0 - q_x$ phase for (a-c) $k_L = 4.5, \Omega = 1.0$. The pseudo color bar is similar to Fig. 5.3. Multi-band instability in low-lying and first-excited branches and single-band instability in the second-excited branch of eigenspectrum increases upon increasing the c_0 and symmetry arguments are similar to figure 5.9.

After exploring the density-density interaction parameter regime, we now shift our focus to analyzing the impact of the spin-exchange interaction strength, c_2, on the instability while keeping the density-density interaction strength fixed at $c_0 = 5.0$. In regime I, we consider c_2 in the range [-5:5], and the eigenspectrum yields only real eigenfrequencies, indicating an absence of instability (not shown here). In contrast, for regime II, we observe the emergence of multi-band instability in both the low-lying and first-excited branches of the eigenspectrum. The low-lying branch remains unstable across the considered range of c_2 (except where $c_0 + c_2 \approx 0$), while the first-excited branch exhibits instability accompanied by the first UAC. Conversely, the second-excited branch displays single-band instability when the effective interaction is antiferromagnetic, coinciding with the appearance of a second UAC in the system, but only for $c_2 > 2$ [see Figs. 5.11(a)-(c)]. The instability gain increases upon increasing the c_2, showing symmetric behaviour about q_x, preserving asymmetric behaviour about c_2.

In Fig.5.12(a), we show the instability gain of the eigenspectrum upon simultaneously varying density-density interaction strength (c_0) and spin-exchange interaction strength (c_2) for (k_L, Ω) =(0.5, 1.0). We find that the instability only occurs for the low-lying branch of the eigenspectrum for attractive interaction when $c_0 + c_2 < 0$. However for the repulsive case ($c_0 + c_2 > 0$) system appears to be stable one. In Fig.5.12(b), we

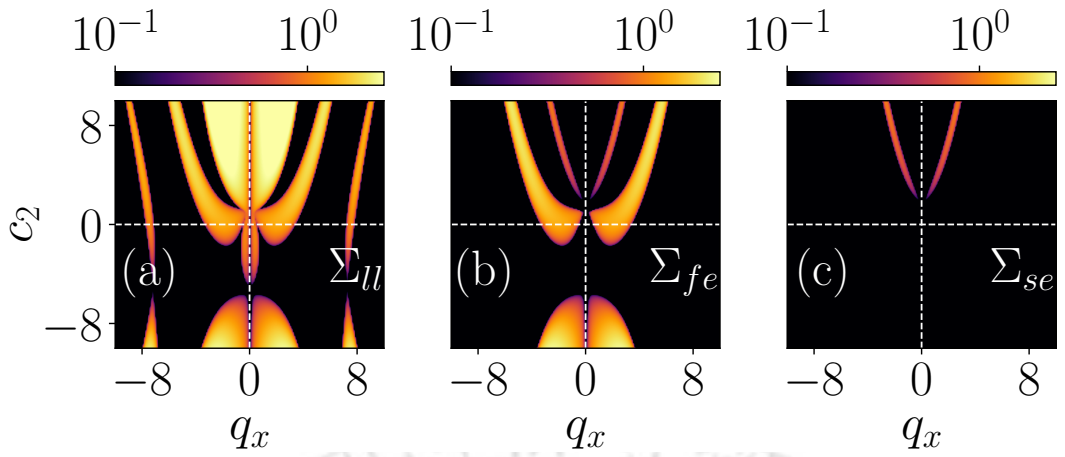


Figure 5.11: MI in $c_2 - q_x$ phase plane for (a-c) $k_L = 4.0, \Omega = 1.0$, with $c_0 = 5.0$. The pseudo color bar is similar to Fig. 5.3. The instability gain of the spectrum increases upon increasing c_2, showing the symmetric behaviour about q_x. However, it is not symmetric about c_2.

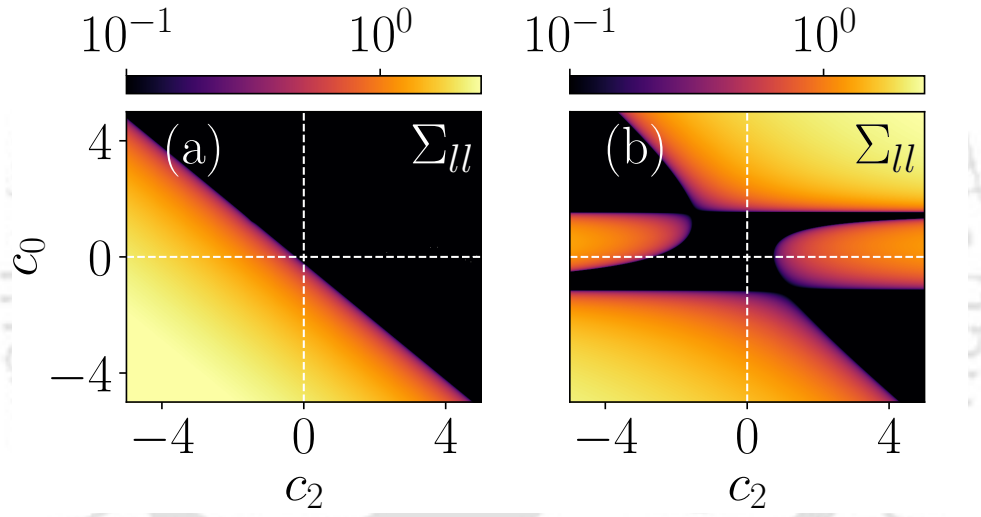


Figure 5.12: The pseudo color representation of MI gain of lowest eigen mode $\Sigma_{ll} \equiv |\mathrm{Im}(\omega_{ll})|$ in $c_0 - c_2$ phase plane for (a) (k_L, Ω) =(0.5, 1.0) and (b) (k_L, Ω) =(4.0, 1.0). The quasi-momentum strength is fixed at $q_x = 1$. In (a) the instability gain appears only in the low-lying branch when the total interaction strength is attractive $c_0 + c_2 < 0$, while in (b) the spectrum exhibits multi-band instability. The instability gain in the eigenspectrum is neither symmetric about c_0 nor about c_2.

show the instability gain corresponding to the low-lying eigenspectrum for $k_L = 4.0$ and $\Omega = 1.0$). For this case, we find the presence of a wider instability region in the entire range of interaction strengths, including both attractive and repulsive, as well as for the mixed case. Interestingly, we find that, for the mixed case of interactions, the system gets stabilized. Overall, we find that for the repulsive case, regime II shows instability, however, for regime I, the repulsive interaction shows a stable nature. The instability gain of the eigenspectrum is neither symmetric about c_0 nor symmetric about c_2.

TH-4102_206121026

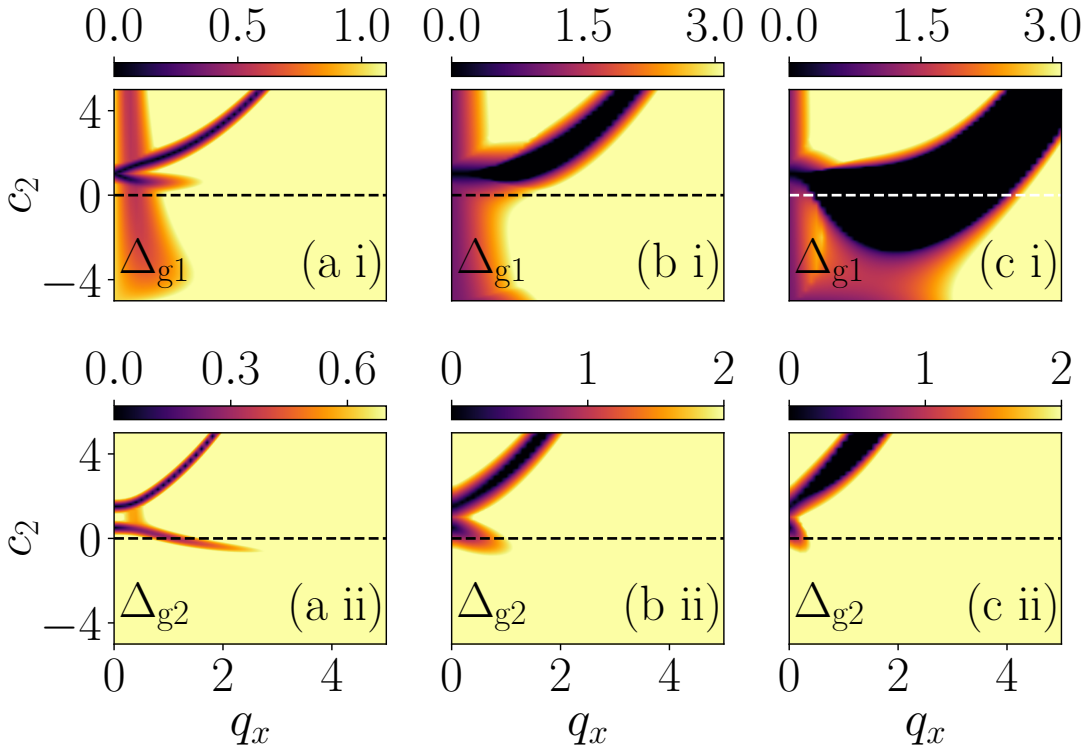


Figure 5.13: Pseudo color representation of the change in band gap $\Delta_{g1} = \mathrm{Re}(\omega_{fe}) - \mathrm{Re}(\omega_{ll})$ and $\Delta_{g2} = \mathrm{Re}(\omega_{se}) - \mathrm{Re}(\omega_{fe})$ for different k_L in $c_2 - q_x$ plane by keeping $\Omega = 1.0$, and $c_0 = 5.0$. (a i, a ii) for $k_L = 0.5$, (b i, b ii) for $k_L = 2.0$ and (c i, c ii) for $k_L = 4.5$. For (a i, b i), the band gap Δ_{g1} closes for positive $c_2 > 0$ (antiferromagnetic interaction). However, in (c i), it closes for both antiferromagnetic ($c_2 > 0$) and ferromagnetic ($c_2 < 0$) interactions. In (a ii - c ii), the band gap Δ_{g2} closes for antiferromagnetic interactions only ($c_2 > 0$).

5.5 Characterization of double unavoided crossings using the band gap Δ_{g1}, and Δ_{g2} of the eigen-spectrum

After gaining a comprehensive understanding of the instability of ferromagnetic and antiferromagnetic interactions, we now characterize the band gap between the eigen-branches. The band gaps in the eigenspectrum are defined as the difference between the first-excited and low-lying states, expressed as $\Delta_{g1} = \mathrm{Re}(\omega_{fe}) - \mathrm{Re}(\omega_{ll})$, and the difference between the second-excited and first-excited states, denoted as $\Delta_{g2} = \mathrm{Re}(\omega_{se}) - \mathrm{Re}(\omega_{fe})$. A value of $\Delta_{g1} \sim 0$ indicates the presence of a gapless mode between ω_{ll} and ω_{fe}, while $\Delta_{g2} \sim 0$ signifies a gapless mode between ω_{fe} and ω_{se}.

In this study, we fix the density-density interaction at $c_0 = 5$ and the Rabi coupling at $\Omega = 1$, while varying the SO coupling strength as $k_L = 0.5$ (regime I), 2.0, and 4.5

TH-4102_206121026

(regime II), as shown in Figs. 5.13(a–c), respectively. Figures 5.13(a i) and 5.13(a ii) demonstrate that, when simultaneously varying the spin-exchange interaction c_2 and quasi-momentum q_x with a fixed $c_0 = 5$, no bandgap exists ($\Delta_{g1} = \Delta_{g2} = 0$) only for $c_2 > 0$ (antiferromagnetic interactions). This gapless state persists as c_2 increases, indicating no gap between $\omega_{fe} - \omega_{ll}$ and $\omega_{se} - \omega_{fe}$. Conversely, for $c_2 < 0$ (ferromagnetic interactions), only gapped modes are observed between all branches.

Similarly, upon increasing the SO coupling strength to $k_L = 2.0$, the bandgaps close only for $c_2 > 0$, with the gapless region expanding in the $c_2 - q_x$ plane and maintaining its gapless nature as c_2 increases [see Figs. 5.13(b i) and 5.13(b ii)]. Next, we consider a relatively large SO coupling strength of $k_L = 4.5$. In this case, the first UAC appears with $\Delta_{g1} = 0$ between the low-lying and first-excited branches only for $-2 < c_2 < 0$ (ferromagnetic case), consistent with findings in SO coupled spin-1 ferromagnetic BECs [115]. This first UAC persists even in the $c_2 > 0$ regime [see Fig. 5.13(c i)]. However, a second UAC emerges for $c_2 > 0$ [see Fig. 5.13(c ii)]. Thus, a relatively strong SO coupling exhibits two gapless UACs when $c_2 > 0$, whereas a single gapless UAC occurs for $-2 < c_2 < 0$.

In conclusion, in regime II, ferromagnetic SO coupled BECs exhibit a single UAC, while antiferromagnetic interactions result in double UACs between the branches. In contrast, regime I remains stable, displaying two gapless stable avoided crossings for $c_2 > 0$ and only gapped modes for $c_2 < 0$.

5.6 Numerical Simulation

In this section, we present the numerical simulation results to understand the nature of the dynamical stability of the condensate. We obtain the stationary state of the condensate using the imaginary-time-propagation (ITP) method and then evolve it using the real-time-propagation method (RTP) by quenching the trap strength. We use the split-step-Crank-Nicolson scheme to implement both ITP and RTP methods [50, 72]. We consider space grid $[-32, 32]$ with the space step $dx = 0.05$ in both ITP and RTP. The considered time step is $dt = 0.00025$ and $dt = 0.0005$ for ITP and RTP, respectively. Here, we choose two quantum phases in the two different SO coupled BECs, namely, ferromagnetic and antiferromagnetic BECs.

5.6.1 Dynamics of ferromagnetic SO coupled BECs

In this section we present the dynamics of the ground state for the two regimes of the ferromagnetic SO coupled BECs.

For Regime I ($k_L = 0.5$, $\Omega = 1.0$), we generate the PW phase of the ferromagnetic interaction ground-state phase using the parameters $c_0 = 5.0$, $c_2 = -2.0$, $k_L = 0.5$, and $\Omega = 1.0$ under a harmonic trap with strength $\lambda = 0.10$. After obtaining the ground state, we apply an instantaneous quench in the trap strength, triggering the dynamics of the condensate, which are computed using real-time propagation. In Figs. 5.14(a i–a iii), we present the dynamical evolution of the density profiles for the three components of the condensate, revealing breathing oscillations. This characteristic response of the condensate to perturbation confirms the real eigenfrequency for these parameters, as illustrated in Fig. 5.1(a).

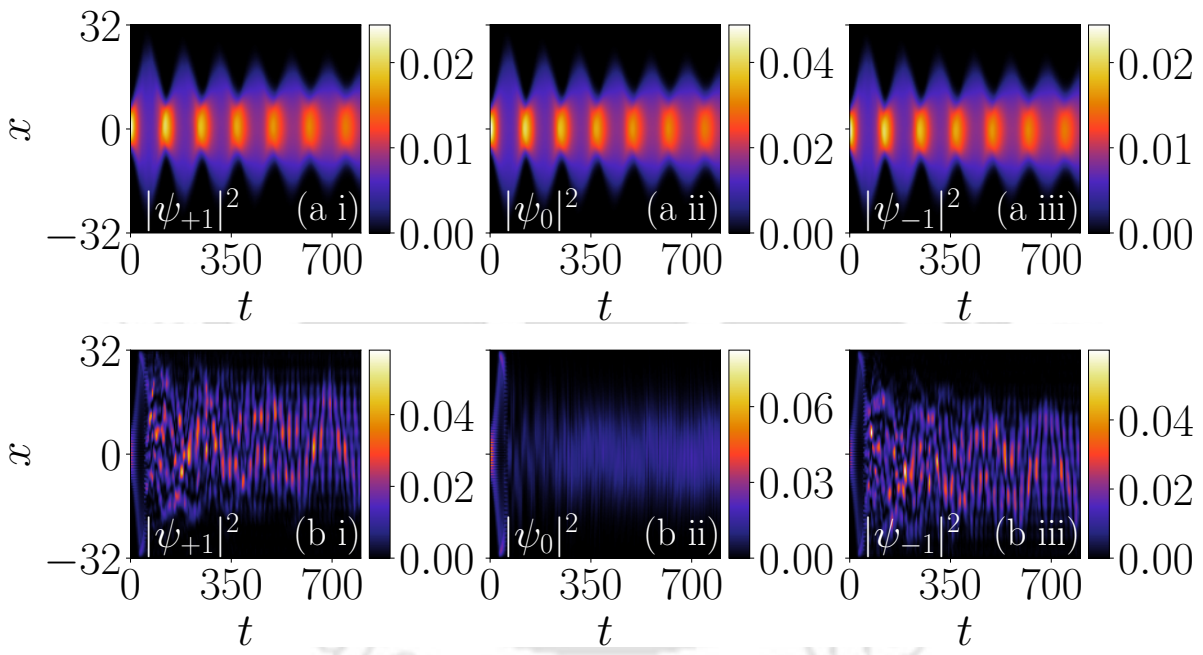


Figure 5.14: Time evolution of the condensate in $x - t$ plane for $|\psi_{+1}|^2$, $|\psi_0|^2$, $|\psi_{-1}|^2$ components of the condensate for (top row) (k_L, Ω) = (0.5, 1.0), and (bottom row) (k_L, Ω) = (4.5, 1.0), upon quenching the trap strength to one-third of its initial value. The interaction strengths are $c_0 = 5.0$ and $c_2 = -2.0$. In the top row, the density profile shows stable behaviour throughout, showing the dynamical stability of the condensate. In the bottom row, the density profile holds its SW nature for a while; at a later time, $|\psi_{\pm 1}|^2$ fragments in small domains and show decay in amplitude while the zeroth component diminishes at first, further gains the amplitude.

For regime II ($k_L = 4.5, \Omega = 1.0$), we obtain the stationary state with the interaction strength $c_0 = 5.0$, $c_2 = -2.0$, and considering SO and Rabi couplings strength as $k_L = 4.5$ and $\Omega = 1.0$, respectively, which is a stripe wave (SW) phase. Further, in

TH-4102_206121026

time evolution, perturbing the trap strength of the density profile of the condensate changes its shape and amplitude. Here, we discuss it in the $x-t$ plane. The density profile evolves as the SW in the beginning, but $t > 0$, densities $|\psi_{\pm1}|^2$ fragments into several small domains, while the zeroth component density diminishes up to $t \approx 400$, and afterwards $|\psi_0|^2$ has very week growth, further $t > 400$, all the components exhibit an immiscible like nonlinear wave patterns. Moreover, we find that in the absence of magnetization ($m = 0$), the condensates remain polarized in the $\pm x$ directions, which is not observed in regime I [see Figs. 5.14(b i - b iii)] [115, 125], due to the appearance of instability as shown in Fig. 5.1(b). Overall, we find that the numerical simulation confirms the dynamical instability of the condensate, which is in line with the collective excitation spectrum calculation.

5.6.2 Dynamics of anti-ferromagnetic SO coupled BECs

First, we consider the dynamics of the Regime I ($k_L = 0.5, \Omega = 1.0$) also yields the PW phase of the antiferromagnetic interaction of the SO coupled BECs. Initially, we generate the ground state with equal interaction strengths $c_0 = 5.0$, $c_2 = 5.0$, keeping the Rabi coupling and SO coupling as $\Omega = 1.0$ and $k_L = 0.5$, respectively. We then generate the dynamics of the condensate by quenching the trap strength. The dynamical evolution of the condensate is obtained by using the RTP of the GPE. In Figs. 5.15(a i - a iii) we show the densities of the three component, $|\psi_{+1}|^2$, $|\psi_0|^2$, and $|\psi_{-1}|^2$, respectively. During temporal evolution, the density shows stable breather oscillation. This particular feature of the condensate complements the real nature of the collective excitation spectrum corresponding to this regime as presented in Fig. 5.4(a). This constant behaviour of the density profile during dynamical evolution and stable energy complements the dynamically and energetically stable nature of the condensate.

In Figs. 5.15(b i - b iii) we show the dynamical evolution of the density component for the regime (ii) ($k_L = 4.5, \Omega = 1.0$) attained after the quench of potential strength for the stationary state prepared with interaction strengths $c_0 = 5.0$, $c_2 = 5.0$. We find that the density profile, which has a stripe wave nature for all the components at $t = 0$, starts getting fragmented into several small domains upon evolution. While ±1 components get polarized [see Figs. 5.15(b i),(b iii)], the zeroth component density starts diminishing [see Fig. 5.15(b ii)] [88, 90, 151]. This particular dynamical feature of the condensate complements the presence of the double UAC, which is present with both low-lying and second-excited branches, resulting in I_o type of instabilities and thus making the condensate dynamically unstable. It is worth noting that a similar

domain formation has been realized in the presence of a weak Zeeman coupling [90].

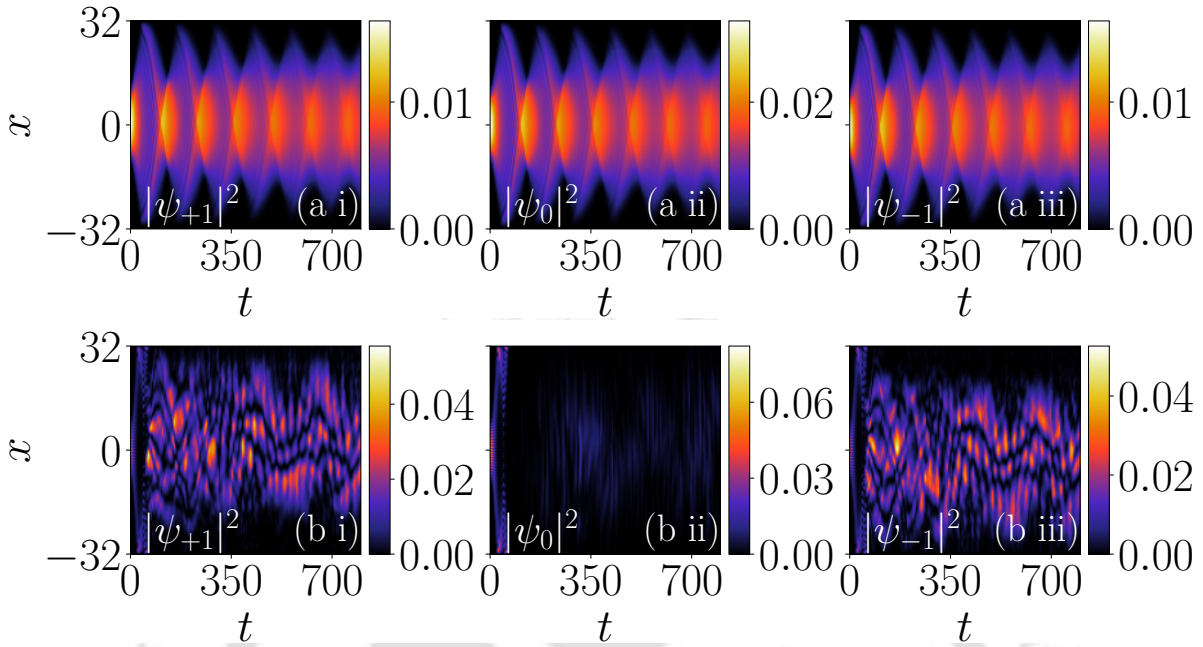


Figure 5.15: Dynamical evolution of the condensate in $x-t$ plane for $|\psi_{+1}|^2$, $|\psi_0|^2$, $|\psi_{-1}|^2$ components of the condensate for (top row) $k_L = 0.5, \Omega = 1.0$ and (bottom row) $k_L = 4.5, \Omega = 1.0$, by quenching the trap strength to one-third of its initial value. The interaction strengths are $c_0 = 5.0$, and $c_2 = 5.0$. In the PW phase, the density of the condensate shows stable breather-like dynamics. The SW phase holds its shape in the beginning, further $|\psi_{\pm 1}|^2$ components fragments in several small domains, and zeroth components start diminishing, confirming the dynamical instability of the condensate.

5.7 Summary and Conclusions

In this Chapter we have explored the stability of various phases in spin-orbit coupled spin-1 BECs with ferromagnetic and antiferromagnetic interactions. The Bogoliubov-de Gennes theory was employed to compute the eigenspectrum of the condensate.

For ferromagnetic interactions in the low SO coupling regime ($k_L^2 < \Omega$), the eigenspectrum exhibits real eigenfrequencies with a gap between the branches, showing phonon modes in the low-lying branch. The eigenvectors corresponding to the low-lying branch components approach the same value at $q_x \approx 0$, confirming the presence of phonon modes. In the high SO coupling regime ($k_L^2 > \Omega$), we observe multi-band imaginary eigenfrequencies in the low-lying branch. For ferromagnetic interactions, we find the emergence of an UAC between the low-lying and first-excited branches, indicating the presence of I_o-type instability in each branch. The eigenvectors in this regime exhibit spin-density-like mixed modes arising from the multi-band eigenfre-

TH-4102_206121026

quencies in quasi-momentum space. At the wave number regime where UAC occurs, the eigenvector shows out-of-phase behaviour for all the components of the condensate.

For antiferromagnetic interactions with low SO coupling, we observe stable avoided crossings between the low-lying and first-excited branches, as well as between the first- and second-excited branches. At these stable avoided crossings, the eigenvectors of all components display flipping characteristics. In the high SO coupling regime ($\Omega < k_L^2$), we identify multi-band imaginary eigenfrequencies in the low-lying and first-excited branches, accompanied by single-band instability in the second-excited branch. Evidence of I_o-type instability is observed in the excitation spectrum, primarily originating from the first UAC between the low-lying and first-excited branches and the second UAC between the first- and second-excited branches. Notably, for antiferromagnetic interactions, the first-excited branch exhibits a double UAC, a feature not present in the ferromagnetic case. The eigenvectors for antiferromagnetic interactions reveal spin-density-like mixed modes in the low-lying and first-excited branches, while the second-excited branch transitions from density to spin modes due to single-band instability. The presence of UAC and double UAC induces out-of-phase behaviour in the respective components.

Further investigation into instability in momentum space reveals that while the instability region is symmetric in the SO coupling range, it shows an asymmetric character in the Rabi coupling plane. For fixed values of Rabi coupling (positive or negative), both ferromagnetic and antiferromagnetic SO coupled BECs are destabilized only for high SO coupling ($k_L^2 > \Omega$). In the case of weak SO coupling in antiferromagnetic BECs, instability and UAC are observed within the range $\Omega < 3$, while the system remains stable otherwise. In contrast, the ferromagnetic condensate remains stable in this regime. Both systems exhibit double UAC when $\Omega \lesssim 0$. For larger SO coupling, antiferromagnetic interactions show UAC for $\Omega \gtrsim 6$, with double UAC appearing for $\Omega \lesssim 3$. The ferromagnetic condensate, however, remains unstable throughout the entire Rabi coupling range, with UAC observed for $\Omega \lesssim 1$ and double UAC for $\Omega \lesssim -2$. In the $k_L - \Omega$ phase plane, both systems exhibit stability only in regime I; instability prevails in all other regimes, driven by the SO coupling strength and multi-band instability. Finally, we have investigated the variation of the band gaps between low-lying excitation branches in the interaction parameter space, noting that antiferromagnetic SO coupled BECs consistently showed double UAC, while ferromagnetic interactions displayed single UAC in the eigenspectrum.

We have complemented the dynamical stability of the condensate obtained using

TH-4102_206121026

the BdG analysis through the mean-field GPEs for both the low (regime I) and high (regime II) SO coupling regimes. For low SO coupling, we have reported the stable breather pattern of the condensate with ferromagnetic and antiferromagnetic interactions, which very well complement the dynamically stable nature of the condensate as shown using the BdG analysis. At high SO coupling, for which the stationary state is of striped wave phase nature exhibits dynamically fragmented condensate upon evolution for both the interactions. This fragmentation is more pronounced with in the antiferromagnetic interaction which may be attributed to the presence of instabilities across all branches. In antiferromagnetic SO coupled BECs, the fragmentation is accompanied with the complex domain formation in which the amplitude of the component remains unchanged, however shape of the condensate fluctuates. In contrast, for ferromagnetic SO coupled BECs shows decay in the density profile, evidenced by the reduced amplitude and immiscibility of the condensates.

TH-4102_206121026

Chapter 6

Supersolid phases and collective excitations in two-dimensional Rashba spin-orbit coupled spin-1 condensates

After presenting the different quantum phases and collective excitations of spin-orbit (SO) coupled spin-1 BECs in Chapter 3, Chapter 4, and Chapter 5, in this Chapter we extend the analysis for quasi-two-dimensional spin-1 BECs. In particular, we present the collective excitation spectrum and dynamics of a quasi-two-dimensional spin-1 Bose-Einstein condensate with Rashba-type SO coupling. Employing Bogoliubov-de-Gennes analysis, we analytically compute the excitation spectra across a wide range of interaction strengths and coupling parameters. By systematically varying the SO and Rabi couplings, we uncover distinct dynamical signatures of quantum phase transitions, including mode softening, the appearance of roton-like minima, and miscibility-driven instabilities in both ferromagnetic and antiferromagnetic interaction regimes. In the antiferromagnetic case, these instabilities lead to a dynamically unstable supersolid phase characterized by the coexistence of density modulation and global phase coherence. To corroborate the analytical predictions, we numerically solve the coupled Gross-Pitaevskii equations and analyze the dynamical stability of the condensate. Our results provide experimentally accessible signatures for spinor condensates with tunable spin-orbit coupling and demonstrate the rich interplay between spin-dependent interactions and synthetic couplings in nonequilibrium quantum fluids.

TH-4102_206121026

6.1 Introduction

Ultracold gases provide a highly versatile and controllable platform for exploring many-body physics in the laboratory [53–56], serving as a guiding framework for frontier quantum technologies [57, 58]. The realization of Bose–Einstein condensates (BECs) enabled the study of macroscopic quantum coherence in dilute gases [14, 15, 163], which was later extended to spinor condensates in which atoms retain internal spin degrees of freedom [31]. This internal spin structure has enabled the engineering of synthetic gauge fields, most notably spin–orbit (SO) coupling, which has been experimentally realized in quasi-one-dimensional condensates via Raman-induced equal Rashba–Dresselhaus coupling [4, 10, 11] and in quasi-two-dimensional systems with Rashba-type coupling [60, 61]. The incorporation of synthetic SO coupling into ultracold atomic gases has opened new avenues for engineering novel quasiparticle spectra and emergent quantum phases, including roton-like minima [164], supersolid and stripe phases [64, 65, 69], topological textures [68], and Zitterbewegung oscillations [62]. Most recently, a robust supersolid stripe phase in SO coupled BECs was observed experimentally, where both superfluid and crystalline excitation modes were directly measured, confirming the compelling evidence for the coexistence of long-range phase coherence and spontaneous density modulation [70].

Numerical simulations of the mean-field Gross–Pitaevskii equations (GPEs) have played a central role in understanding SO coupled BECs, enabling detailed exploration of ground-state phases, spin textures, collective excitations, and nonequilibrium dynamics [71]. In quasi-one-dimensional (quasi-1D) spin-1 BECs, SO coupling has been shown to induce rich physics, including stripe phases [25], mode softening, and characteristic roton-like features in the excitation spectrum [165]. In particular, the Bogoliubov analyses of Raman-induced SO-coupled spin-1 condensates revealed roton–maxon structures in the plane-wave and zero-momentum phases, where the softening of roton modes signals instabilities toward stripe and supersolid-like order [23, 24]. Our previous works further demonstrated that in quasi-1D spin-1 condensates, SO coupling gives rise to dynamical instabilities manifested as unstable or double-unstable avoided crossings in ferromagnetic and antiferromagnetic phases, providing clear dynamical signatures of phase transitions [115, 116, 101]. Related studies also uncovered mode softening and double-roton structures across phase boundaries in quasi-1D systems at finite temperature [165].

In quasi-two-dimensional (quasi-2D) spin-1 systems, the interplay between SO coupling and interatomic interactions facilitates spontaneous density modulation and the

emergence of supersolid-like phases [100, 166]. Adhikari et al. demonstrated the formation of stable self-bound supersolid solitons in Rashba SO coupled spin-1 condensates, characterized by stripe and superlattice density order [78, 167]. This framework was later extended to nonmagnetic spin-1 and spin-2 condensates, where quasi-degenerate stripe and superlattice solitons remain stable over a wide range of SO coupling strengths [166].

Collective excitations provide a powerful and effective probe of complex quantum phases, such as stripe and supersolid states. Their spectra encode essential information about dynamical stability, symmetry breaking, and quantum phase transitions, with the softening of roton modes serving as a hallmark of emerging density order [13, 16, 17]. In SO coupled BECs, the interplay between Raman or Rashba coupling and interactions fundamentally reshapes the Bogoliubov spectrum, giving rise to anisotropic phonon modes, tunable roton minima, and interaction-driven instabilities [82, 93, 168–170].

Extensive theoretical studies have demonstrated that SO coupling can induce single or multiple roton structures, suppress long-wavelength phonon modes, and trigger dynamical instabilities in two-dimensional condensates and quantum droplets [21, 171, 172]. Moreover, SO coupling strongly modifies hydrodynamic responses and critical velocities, underscoring its profound impact on superfluid behavior [173, 174]. Recent work on quasi-two-dimensional binary spin-1/2 condensates has further revealed that while Rabi coupling tends to stabilize the system, SO coupling generates intricate instability landscapes near phase boundaries, offering access to unconventional quantum phase transitions [93, 169, 170].

Despite these advances, a comprehensive understanding of collective excitations in spin-1 SO-coupled condensates remains notably incomplete. In particular, homogeneous two-dimensional systems with Rashba SO coupling, where, the competition between spin-dependent interactions, higher-spin degrees of freedom, and synthetic gauge fields is most pronounced, have received comparatively little attention [24, 61]. As a result, the excitation spectra and dynamical stability of superstripe and supersolid phases in spin-1 condensates, especially across both ferromagnetic and antiferromagnetic interaction regimes, are not well explored. Clarifying how these complex phases manifest in the collective modes is essential for identifying experimentally accessible signatures and for distinguishing stable supersolids from dynamically unstable stripe states [100, 167].

In this Chapter, we address this gap by performing a systematic Bogoliubov analysis of a uniform quasi-two-dimensional spin-1 Bose–Einstein condensate with Rashba

SO and Rabi couplings. We compute the collective excitation spectra across a wide range of interaction parameters, encompassing both ferromagnetic and antiferromagnetic regimes. Our analysis reveals distinct mode softening, roton minima, and miscibility-driven instabilities that serve as clear dynamical signatures of quantum phase transitions. Notably, we demonstrate that supersolid phases in this system are generically dynamically unstable, while superstripe phases exhibit characteristic excitation features. Our results may be useful to observe these supersolid and superstripe behavior through collective excitation measurements experimentally in SO coupled spinor condensates.

The Chapter is structured as follows. In Sec. 6.2, we introduce the mean-field model and describe the numerical framework used to investigate collective excitations. The single-particle spectrum is analyzed in Sec. 6.3, laying the groundwork for the derivation of the collective excitation spectrum in Sec. 6.4. In Sec. 6.5, we present the stability phase diagram for ferromagnetic interactions, followed by the stability analysis with Rabi coupling (Sec. 6.5.1) and without Rabi coupling (Sec. 6.5.2). The stability analysis for antiferromagnetic interactions is given in Sec. 6.6. Finally, in Sec. 6.7, we offer the summary and conclusions of our findings. A detailed derivation of the Bogoliubov-de Gennes (BdG) matrix is provided in Appendix B.

6.2 Mean-Field Model

We consider a harmonically trapped quasi-two-dimensional (quasi-2D) spin-1 condensate with SO coupling realized via the tight confinement along the z-direction ($\omega_z \gg \omega$), where ω_z and ω are the angular trap frequencies in the z-direction and in the $x-y$ plane, respectively. Within this framework, the dimensionless coupled Gross–Pitaevskii equations (GPEs) governing the dynamics of the SO-coupled spin-1 condensate are given by [39, 50, 100, 175],

$$\begin{aligned} \mathrm{i}\frac{\partial}{\partial t}\psi_{\pm1}(\vec{r}) &= \left[-\frac{1}{2}\nabla^2 + V(\vec{r}) + c_0\rho + c_2\rho_2^{\pm}\right]\psi_{\pm1}(\vec{r}) + c_2\psi_0^2(\vec{r})\psi_{\mp1}^*(\vec{r}) \\ &\quad + \frac{\Omega}{\sqrt{2}}\psi_0(\vec{r}) - \mathrm{i}\frac{k_L}{\sqrt{2}}\left[\left(\frac{\partial}{\partial y} \pm \mathrm{i}\frac{\partial}{\partial x}\right)\psi_0(\vec{r})\right], \qquad (6.1a) \\ \mathrm{i}\frac{\partial}{\partial t}\psi_0(\vec{r}) &= \left[-\frac{1}{2}\nabla^2 + V(\vec{r}) + c_0\rho + c_2\rho_2^{0}\right]\psi_0(\vec{r}) + 2c_2\psi_{+1}(\vec{r})\psi_{-1}(\vec{r})\psi_0^*(\vec{r}) \\ &\quad + \frac{\Omega}{\sqrt{2}}(\psi_+(\vec{r})) - \mathrm{i}\frac{k_L}{\sqrt{2}}\left[\frac{\partial}{\partial y}\psi_+(\vec{r}) - \mathrm{i}\frac{\partial}{\partial x}\psi_-(\vec{r})\right], \qquad (6.1b) \end{aligned}$$

where $\vec{r} = \{x, y\}$, ψ_j; $j = +1, 0, -1$, are the spinor condensate wavefunctions corresponding to sublevels $m_F = +1, 0, -1$ of the hyperfine state $F = 1$ that satisfy the normalization condition $\int_{-\infty}^{\infty} \rho \, dxdy = 1$, where $\rho_j = |\psi_j|^2$, and $\rho = |\psi_{+1}|^2 + |\psi_0|^2 + |\psi_{-1}|^2$. Also, $\psi_\pm = \psi_{+1} \pm \psi_{-1}$, $\rho_2^\pm = (\rho_{\pm1} + \rho_0 - \rho_{\mp1})$, $\rho_2^0 = (\rho_{+1} + \rho_{-1})$. The equations (6.1a), and (6.1b) are non-dimensionalized using time, lengths, and energy $t = \omega\tilde{t}$, $x = \tilde{x}/l_0$, $y = \tilde{y}/l_0$, and $\hbar\omega$, respectively. The resulting condensate wavefunction is $\psi_{\pm1,0} = \frac{l_0}{\sqrt{N}}\tilde{\psi}_{\pm1,0}$, where, $l_0 = \sqrt{\hbar/m\omega}$, is the oscillator length for the trap frequency ω in the x-y plane. The trap strength is given by $V(x, y) = (x^2 + y^2)/2$, density-density interaction strength $c_0 = 2N\sqrt{2\pi\kappa}(a_0 + 2a_2)/3l_0$, and spin-exchange interaction strength $c_2 = 2N\sqrt{2\pi\kappa}(a_2 - a_0)/3l_0$, where $\kappa = \omega_z/\omega$, a_0 and a_2 are the s-wave scattering lengths in total spin channels 0 and 2, respectively. Upon tuning $c_2 < 0$ ($c_2 > 0$), one can have the FM (AFM) interaction of the condensates [39]. The SO and Rabi coupling strengths are given by $k_L = \tilde{k}_L/\omega l_0$, $\Omega = \tilde{\Omega}/(\hbar\omega)$, respectively. In the above description, the quantities with the tilde represent dimensionful quantities. In this entire work, we consider all parameters to be dimensionless.

The energy functional corresponding to the coupled GPEs (6.1a)-(6.1b) is given by [50, 100],

$$
\begin{aligned}
E = & \frac{1}{2}\int dxdy \Big\{ \sum_j (|\partial_x\psi_j|^2 + |\partial_y\psi_j|^2) + 2V(x,y)\rho + c_0\rho^2 \\
& + c_2[\rho_{+1}^2 + \rho_{-1}^2 + 2(\rho_{+1}\rho_0 + \rho_{-1}\rho_0 - \rho_{+1}\rho_{-1} + \psi_{-1}^*\psi_0^2\psi_{+1}^* + \psi_{-1}\psi_0^{*2}\psi_{+1})] \\
& + \sqrt{2}\Omega[\psi_+^*\psi_0 + \psi_0^*\psi_+] - \sqrt{2}ik_L[\psi_+^*\partial_y\psi_0 + i\psi_-^*\partial_x\psi_0 - i\psi_0^*\partial_x\psi_- + \psi_0^*\partial_y\psi_+] \Big\} .
\end{aligned}
\tag{6.2}
$$

Here, we outline the experimentally feasible parameter ranges relevant to our simulations. For the ferromagnetic interaction, we consider ^{87}Rb BECs with $N \sim 3 \times 10^5$ atoms confined in a harmonic trap with the frequencies $(\omega, \omega_z) = 2\pi\times$ (20Hz, 600Hz). The corresponding characteristic lengths would be $l_0 = 2.4\mu$m, and $l_z = 0.44\mu$m. For the antiferromagnetic interaction, we consider the BECs of ^{23}Na atoms, for which the characteristic lengths are $l_0 = 4.7\mu$m, and $l_z = 0.85\mu$m [100, 176]. The spin-dependent and spin-independent interactions can be achieved by controlling the s-wave scattering lengths through Feshbach resonance [120–122]. The SO coupling strength $k_L = \{0.1 - 5\}$ can be tuned by changing the laser wavelengths in the range of $\{151.19\mu$m - 3023.89nm$\}$. However, the dimensionless Rabi frequency interval $\Omega = [0, 11]$ used in the simulation can be attained by tuning the Raman laser strength in the range of

TH-4102_206121026

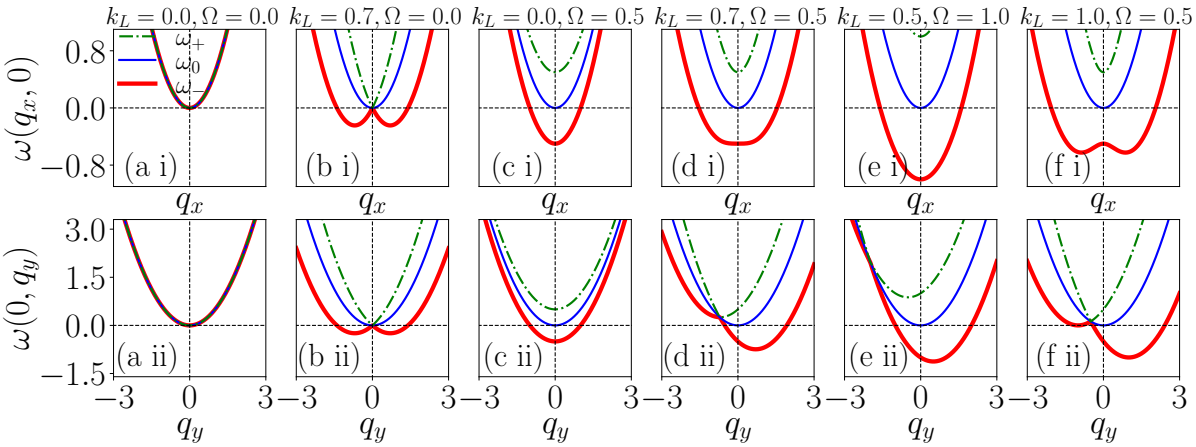


Figure 6.1: Single-particle energy spectrum top row along q_x direction and bottom row along q_y direction for the different set of SO and Rabi coupling strengths (k_L, Ω): (a)-(f): $(0,0)$, $(0.7,0)$, $(0,0.5)$, $(0.7,0.5)$, $(0.5,1.0)$, $(1.0,0.5)$. The thick solid red, thin solid blue line, and dash-dotted green line represent the energy eigenspectrum for $\{-1,0,+1\}$ components of the spin, respectively. Along q_x direction, the double minimum appears in the eigenvalue dispersion, following the relation $k_L^2 > \Omega$, indicating the emergence of finite momentum minima, whereas for $k_L^2 < \Omega$ the spectrum retains a single minimum at zero momentum. Along the q_y direction, the combined presence of SO and Rabi couplings produces an anisotropic dispersion with shifted minima due to symmetry breaking.

$2\pi\hbar \times \{5 - 220\}$ Hz.

6.3 Single-particle spectrum

In this section, we present the single-particle spectrum of the non-interacting spinor condensate for trapless SO and Rabi-coupled spin-1 spinor BECs. Following that, we introduce the collective excitation spectrum for the interacting systems.

For $V(x,y) = 0$, and $c_0 = c_2 = 0$ and substituting plane wave solution, $\psi_{0,\pm1} = \phi_{0,\pm1} e^{\mathrm{i}(q_x x + q_y y - \omega t)}$ in the Eqs.(6.1a)-(6.1b) we obtain,

$$\mathcal{L}_{sp} \begin{pmatrix} \phi_1 \\ \phi_0 \\ \phi_{-1} \end{pmatrix} = \omega \begin{pmatrix} \phi_1 \\ \phi_0 \\ \phi_{-1} \end{pmatrix}, \tag{6.3}$$

with

$$\mathcal{L}_{sp} = \begin{pmatrix} \frac{Q^2}{2} & \mathcal{L}_{12} & 0 \\ \mathcal{L}_{21} & \frac{Q^2}{2} & \mathcal{L}_{23} \\ 0 & \mathcal{L}_{32} & \frac{Q^2}{2} \end{pmatrix}, \tag{6.4}$$

where, $Q^2 = q_x^2 + q_y^2$, $\mathcal{L}_{12} = \frac{\Omega}{\sqrt{2}} + \frac{k_L}{\sqrt{2}}(iq_x + q_y)$, $\mathcal{L}_{21} = \frac{\Omega}{\sqrt{2}} - \frac{k_L}{\sqrt{2}}(iq_x - q_y)$, $\mathcal{L}_{23} = \frac{\Omega}{\sqrt{2}} + \frac{k_L}{\sqrt{2}}(iq_x + q_y)$, and $\mathcal{L}_{32} = \frac{\Omega}{\sqrt{2}} - \frac{k_L}{\sqrt{2}}(iq_x - q_y)$. Upon diagonalizing the Eq.(6.3), we obtain the single-particle dispersion as,

$$\omega_0(q_x, q_y) = \frac{Q^2}{2}\,, \tag{6.5a}$$

$$\omega_\pm(q_x, q_y) = \frac{1}{2}\left(Q^2 \pm 2\sqrt{k_L^2 Q^2 + 2q_y k_L \Omega + \Omega^2}\right). \tag{6.5b}$$

The structure of the single-particle spectrum in general provides direct insight into how SO and Rabi couplings modify the underlying energy landscape and thereby control the ground-state momentum of the system. In particular, the appearance or disappearance of degenerate minima in the lower branch determines whether the system favors a zero-momentum or finite-momentum state which directly dictate different ground state phases of the condensate [93, 153, 101]. In the single particle spectrum, we obtain three distinct branches, namely, ω_+, ω_0, and ω_-. Among these, the ω_0 branch remains independent of the SO and Rabi couplings, whereas the ω_+ and ω_- exhibit explicit dependence on the SO and Rabi couplings. To simplify the analysis, we first consider the case $q_y = 0.0$ and examine the spectrum as a function of q_x. We then reverse the scenario by fixing $q_x = 0.0$ and exploring the variation with respect to q_y.

In q_x direction. The top row of Fig.6.1 shows the single-particle dispersion along the q_x direction for $q_y = 0$. In the absence of the SO and Rabi couplings ($k_L = \Omega = 0$) the spectrum consists of a non-degenerate parabolic dispersion band [see Fig.6.1(a i)], in line with the expression in Eq. 6.5. Introducing SO coupling alone ($k_L = 0.7$) qualitatively alters the dispersion: the lower branch ω_- develops two degenerate minima at finite momenta $q_x = \pm 0.7$ as shown in the Fig. 6.1(b i), signaling the tendency toward finite-momentum states induced by SO coupling. In contrast, when only the Rabi coupling is present ($k_L = 0$, $\Omega = 0.5$), the degeneracy is lifted and a gap opens between the branches [Fig. 6.1(c i)]. The energy separation between ω_0 and $\omega_\pm$ is Ω, while the gap between ω_+ and ω_- equals 2Ω, reflecting coherent spin mixing due to the Rabi term. As a result, the lower branch exhibits a single minimum at zero momentum.

When both SO couplings are present ($k_L = 0.7$, $\Omega = 0.5$), the competition between momentum-dependent SO effects and spin mixing leads to a partial flattening of the minimum of the ω_- branch [see Fig. 6.1(d i)]. Increasing the Rabi coupling further ($\Omega = 1.0$) and decreasing the SO coupling ($k_L = 0.5$) suppresses this flattening and restores a single minimum [see Fig. 6.1(e i)]. However, for stronger SO coupling ($k_L =$

1.0) at fixed $\Omega = 0.5$, the lower branch again develops a clear double minimum despite the presence of a finite gap as illustrated in Fig. 6.1(f i). The emergence of a double minimum signals towards a transition from the zero-momentum (ZM) phase to the degenerate finite momentum minima phase, governed by the condition $k_L^2 > \Omega$.

In q_y direction. We now turn to the dispersion along the q_y direction by fixing $q_x = 0$, as shown in the bottom row of Fig. 6.1. Here we find the modification in the momentum dependence of the spectrum which leads to qualitatively distinct behavior compared to the q_x direction. In the absence of both couplings, or when only one of them is present, the dispersions in panels Fig. 6.1(a ii–c ii) closely resemble their counterparts along the q_x direction [Fig. 6.1(a i–c i)]. In particular, finite SO coupling in the absence of Rabi coupling produces a symmetric double minimum in the lower branch ω_-, reflecting degenerate finite-momentum states.

A qualitatively new feature emerges when both the SO and Rabi couplings are finite. For $k_L = 0.7$ and $\Omega = 0.5$ [Fig. 6.1(d ii)], the lower branch develops an asymmetric double-minimum structure. The global minimum occurs at $q_y = +0.7$ with energy $\omega_- = -0.745$, while the secondary minimum lies at positive energy, where the condensate may not exist, resulting in a finite momentum plane-wave phase. Increasing the Rabi coupling to $\Omega = 1.0$ and reducing SO coupling ($k_L = 0.5$) further increases the depth of the global minimum to $\omega_- = -1.138$ [Fig. 6.1(e ii)] accompanied with the disappearance of other minima. In both cases, the two minima are energetically inequivalent, indicating a lifting of the degeneracy between opposite momenta suggesting that the Rabi coupling influences momentum selection by lifting degeneracy between competing minima [93].

For stronger SO coupling, $k_L = 1.0$ with $\Omega = 0.5$ [Fig. 6.1(f ii)], the asymmetric double-minimum structure persists. One minimum appears at zero energy ($\omega_- = 0$ at $q_y = -1.0$), while the other remains at negative energy ($\omega_- = -1.0$ at $q_y = 1.0$), demonstrating a pronounced imbalance between positive and negative momenta. Overall, we find that while symmetric double minima arise solely from SO coupling and correspond to degenerate finite-momentum states, the simultaneous presence of SO and Rabi couplings breaks this symmetry and selects a preferred momentum direction. This underlined asymmetry originates because of presence of the linear $k_L \Omega q_y$ term in the dispersion, which explicitly breaks the $q_y \to -q_y$ symmetry and produces an anisotropic energy landscape which aided effect appear in the section of momentum and finally altering the ground-state phases [24, 93].

TH-4102_206121026

6.4 Collective Excitation spectrum

In the previous section, we analyzed the single-particle spectrum of SO coupled spin-1 BECs, which determines the underlying band structure and ground-state momentum configurations. However, the stability and dynamical response of the condensate are governed by collective excitations, which crucially depend on interatomic interactions. Within this approach, the condensate wave function is expressed as a small fluctuation about the uniform mean-field ground state. The excitation wave function for the jth spin component can be written as [93, 138],

$$\psi_j(x,y,t) = \mathrm{e}^{-\mathrm{i}\mu_j t}[\phi_j + \delta\phi_j(x,t)] \tag{6.6}$$

where, where ϕ_j denotes the uniform ground-state wave function, μ_j is the chemical potential, and $\delta\phi_j$ represents a small time-dependent perturbation.

The fluctuation term is expanded in plane-wave modes as

$$\delta\phi_j(x,y,t) = u_j \mathrm{e}^{\mathrm{i}(q_x x + q_y y - \omega t)} + v_j^* \mathrm{e}^{-\mathrm{i}(q_x x + q_y y - \omega^* t)} \tag{6.7}$$

where, u_j, v_j are the Bogoliubov amplitudes and (q_x, q_y) denotes the excitation momentum. The ground state of the spinor is taken as $\phi_j = (1/2, -1/\sqrt{2}, 1/2)^T$ corresponding to the uniform density. Here, μ_j denotes the chemical potential. The index $j = +1, 0, -1$ labels the three spin components of the spin-1 condensate. Substituting Eq. (6.6) into the coupled Gross–Pitaevskii equations [Eqs. (6.1a)–(6.1b)] and retaining terms up to linear order in the fluctuations, we obtain the BdG equations governing the collective excitation spectrum as given by

$$(\mathcal{L} - \omega \mathrm{I}) \begin{pmatrix} u_{+1} & v_{+1} & u_0 & v_0 & u_{-1} & v_{-1} \end{pmatrix}^T = 0\,, \tag{6.8}$$

where T represents the transpose of the matrix and $\mathcal{L}$ is 6×6 matrix given by,

$$\mathcal{L} = \begin{pmatrix} H_+ - \mu_+ & \mathcal{L}_{12} & \mathcal{L}_{13} & \mathcal{L}_{14} & \mathcal{L}_{15} & \mathcal{L}_{16} \\ \mathcal{L}_{21} & -H_+ + \mu_+ & \mathcal{L}_{23} & \mathcal{L}_{24} & \mathcal{L}_{25} & \mathcal{L}_{26} \\ \mathcal{L}_{31} & \mathcal{L}_{32} & H_0 - \mu_0 & \mathcal{L}_{34} & \mathcal{L}_{35} & \mathcal{L}_{36} \\ \mathcal{L}_{41} & \mathcal{L}_{42} & \mathcal{L}_{43} & -H_0 + \mu_0 & \mathcal{L}_{45} & \mathcal{L}_{46} \\ \mathcal{L}_{51} & \mathcal{L}_{52} & \mathcal{L}_{53} & \mathcal{L}_{54} & H_- - \mu_- & \mathcal{L}_{56} \\ \mathcal{L}_{61} & \mathcal{L}_{62} & \mathcal{L}_{63} & \mathcal{L}_{64} & \mathcal{L}_{65} & -H_- + \mu_- \end{pmatrix}. \tag{6.9}$$

The matrix elements of $\mathcal{L}$ are given in appendix B. Bogoliubov coefficients follow the normalization condition,

$$\int \left(\sum_j \{|u_j|^2 - |v_j|^2\} \right) dxdy = 1 \, . \tag{6.10}$$

The simplified form of the BdG excitation spectrum is obtained by calculating the determinant of the matrix $\mathcal{L}$ and equating it with zero, i.e., $det\ (\mathcal{L} - \omega \mathrm{I}) = 0$, where I is a 6×6 identity matrix. The characteristic equation can be written as,

$$\omega^6 + b\omega^5 + c\omega^4 + d\omega^3 + e\omega^2 + f\omega + g = 0 \, , \tag{6.11}$$

where the coefficients b, c, d, e, f, and g are given in the appendix B.

6.5 Stability phases based on collective excitation for Ferromagnetic interactions

The dynamical and energetic stability of the condensate is determined from the associated eigenfrequencies. The condensate is both dynamically and energetically stable when all eigenfrequencies are real and positive. The appearance of complex eigenfrequencies signals dynamical instability, while purely real but negative eigenfrequencies indicate energetic instability [20, 21, 93]. Fig. 6.2 presents the stability phase diagram in the $k_L - \Omega$ plane in presence of ferromagnetic interactions with interaction strengths $c_0 = 50.0$ and $c_2 = -2.5$ along q_x at $q_y = 0.0$.

Based on the eigenspectrum, in Fig. 6.2, we divide the $k_L - \Omega$ phase plane into three different regions: region I, region II (further divided into the regions IIa and IIb), and region III. The white dashed-dotted line with green dots follows the criterion $k_L^2 \approx \Omega$ and separates region I and region II. Region I exhibits only real, positive eigenfrequencies and is both dynamically and energetically stable; region II contains a complex eigenspectrum and is dynamically unstable. Further, the solid white line with blue dots separates region II into two parts: IIa and IIb, which holds the relation $\Omega = -1.6329 + 0.13k_L^2$ with origin point ($k_L = 3.54$, $\Omega \sim 0$). We obtain the gapped mode between the branches in IIa, and the gapless mode between the branches in region IIb. The case with vanishing Rabi coupling ($\Omega \sim 0.0$) is treated separately as region III. This region is dynamically unstable, supporting both single-band instabilities with a gapped mode and multi-band instabilities with gapless modes. For larger

TH-4102_206121026

SO coupling ($k_L \gtrsim 4.1$), region III also exhibits phonon modes together with instability bands in the low-lying and first-excited branches, which will be discussed in more detail at the later part of the manuscript.

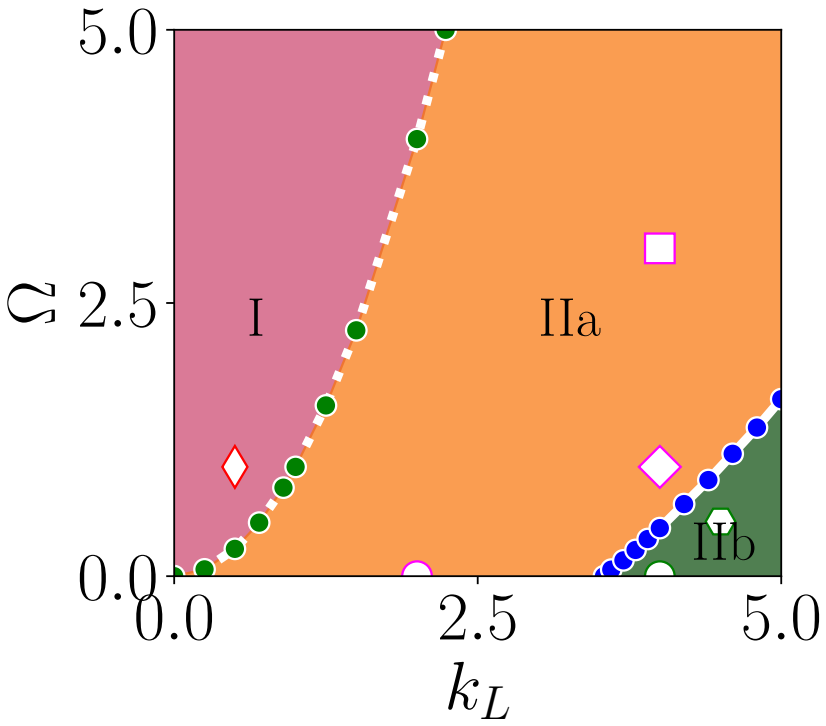


Figure 6.2: Stability phase diagram in the k_L–Ω plane for ferromagnetic interactions ($c_0 = 50.0$ and $c_2 = -2.5$) for full range of q_x with $q_y = 0$. The dash–dotted white line with green dots ($k_L^2 \simeq \Omega$) separates stable (I) and unstable (II) regions. Within region II, the solid white line with blue dots ($\Omega = -1.6329 + 0.13k_L^2$) distinguishes gapped (IIa) and gapless (IIb) spectra. The case $\Omega \sim 0$ lies in the unstable regime. The markers in different regions represent the coupling parameter points for which detailed collective excitation analysis is reported in the paper.

To analyze these features in more quantitative way, we also calculate the excitation spectrum analytically and employ numerical solution of the BdG equation [Eq. 6.9]. In addition, we also compute the corresponding eigenvectors for the eigenvalue spectrum along the quasi-momentum direction q_x at $q_y = 0$, and along the q_y direction at $q_x = 0$. First, we consider a real space grid $[-300 : 300][-300 : 300]$ with step size $h_x = h_y = 0.05$. We then apply the Fourier collocation method, where we numerically compute the Fourier transform of the BdG equations and obtain a truncated reduced BdG matrix, which is subsequently diagonalized using the LAPACK package [149]. In momentum space, we consider $[-50 : 50][-50 : 50]$ modes in the q_x, q_y directions, with a grid step size of $h_{q_x} = h_{q_y} = 0.21$. Following this, we present the time evolution of the condensate associated with the collective excitation spectrum of

TH-4102_206121026

the coupled Gross-Pitaevskii equations (GPEs) (Eqs.(6.1a)-(6.1b)). The stationary state is obtained using the imaginary-time propagation method and subsequently evolved using the real-time propagation method. For this purpose, we employ the split-step Crank-Nicholson scheme described in Refs. [50, 72, 150]. We have considered a grid of $N_x = N_y = 256$ space points with space step $dx = dy = 0.1$, time step $dt = 0.001$ for imaginary-time-propagation, and $dt = 0.00025$ for real-time-propagation. Initially, we obtain the stationary states according to the regions in the phase plot [Fig. 6.2] by using imaginary-time propagation. After calculating the stationary phase, we evolve it using real-time propagation by quenching the trap strength.

Since the $k_L - \Omega$ phase plane is divided into three distinct regions: regions I, II (subdivided into IIa and IIb), and III, in the following subsections, we analyze the condensate behaviour by separating it into two cases: (A) in the presence of Rabi coupling (regions I and II), and (B) in the absence of Rabi coupling (region III). For each case, we report the collective excitations and numerical simulations using the mean-field GPEs.

6.5.1 Effect of finite SO and Rabi coupling on collective excitation spectrum

In the previous section, we presented the stability phase diagram, which is divided into two distinct regimes for finite Rabi coupling: I and II (subdivided into IIa and IIb), while in the absence of Rabi coupling, there is a single region, III. In what follows, we present the detailed analysis of the eigenspectrum and eigenvectors in these regions.

6.5.1.1 Region I

We begin by considering the coupling parameters $(k_L, \Omega) = (0.5, 1.0)$, which lie within region I of the stability phase diagram and are shown with a diamond marker in Fig. 6.2. For this choice of coupling strengths, we analyze both the collective excitation spectrum and the corresponding numerical simulations.

Collective excitation spectrum: Figure 6.3 displays the collective excitation spectra for the regime when $k_L^2 < \Omega$, i.e., for $(k_L, \Omega) = (0.5, 1.0)$ with interaction strengths $c_0 = 50$ and $c_2 = -2.5$, plotted along the quasi-momentum directions q_x (top row) and q_y (bottom row). In the top row, Fig. 6.3(a i) shows that the low-lying branch of the spectrum consists solely of real and positive eigenfrequencies and supports a phonon mode. For a selected branch of the eigenspectrum, we examine the eigenvector com-

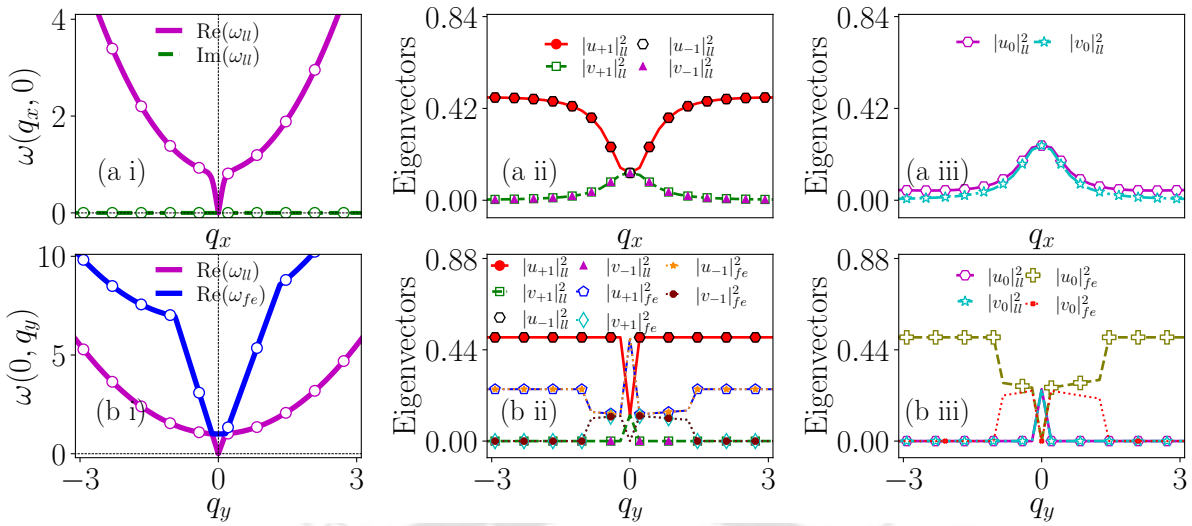


Figure 6.3: Eigenvalue spectrum and eigenvectors along the quasi-momentum directions q_x and q_y for $k_L = 0.5$, $\Omega = 1.0$, $c_0 = 50$, and $c_2 = -2.5$. Top row: low-lying branch. (a i) Eigenvalue spectrum, with $\mathrm{Re}(\omega_{ll})$ (solid magenta) and $|\mathrm{Im}(\omega_{ll})|$ (dashed dotted green). (a ii, a iii)Corresponding eigenvector components $|u_m|^2_{ll}$ and $|v_m|^2_{ll}$ for $m = 0, \pm 1$. Bottom row: first excited branch. (b i) Eigenvalue spectrum with $\mathrm{Re}(\omega_{fe})$ (solid blue). (b ii, b iii) Corresponding eigenvector components $|u_m|^2_{fe}$ and $|u_m|^2_{fe}$. All eigenvalues are real and positive, and the low-lying branch exhibits a phonon mode, indicating both dynamical and energetic stability.

ponents $|u_{\pm1}|^2$, $|v_{\pm1}|^2$, $|u_0|^2$, and $|v_0|^2$. As shown in Fig. 6.3(a ii), the eigenvectors exhibit in-phase behavior, characteristic of a density-like mode, satisfying the condition [93, 116],

$$|u_{+1}|^2_{ll} - |u_{-1}|^2_{ll} = 0, \quad |v_{+1}|^2_{ll} - |v_{-1}|^2_{ll} = 0. \tag{6.12}$$

The zeroth component, shown in Fig. 6.3(a iii), also exhibits independent in-phase behavior. Moreover, in the long-wavelength limit $q_x \approx 0$, all eigenvector components converge to the same value, confirming the phonon character of the low-lying excitation.

In the bottom row, Fig. 6.3(b i) likewise displays only real and positive eigenfrequencies in both the low-lying (denoted by the subscript ll) and first-excited (denoted by the subscript fe) branches of the eigenspectrum. While the low-lying branch again hosts the phonon mode, the first-excited branch exhibits a pronounced asymmetry in momentum space. The corresponding eigenvector components shown in Fig. 6.3(b ii)

display in-phase (density-like) behavior in both branches, satisfying,

$$|u_{+1}|^2_{ll} - |u_{-1}|^2_{ll} = 0, \quad |v_{+1}|^2_{ll} - |v_{-1}|^2_{ll} = 0,$$
$$|u_{+1}|^2_{fe} - |u_{-1}|^2_{fe} = 0, \quad |v_{+1}|^2_{fe} - |v_{-1}|^2_{fe} = 0. \tag{6.13}$$

The zeroth component shown in Fig. 6.3(b iii) exhibits a density-like mode for both excitation branches, consistent with previous studies on spin-1/2 SO coupled BECs [93]. For the low-lying branch, all eigenvector components converge to the same value at $q_y \approx 0$, confirming the phonon character of this mode. In the first-excited branch, the eigenvector components $|u_{+1}|^2_{fe}$ and $|u_{-1}|^2_{fe}$ remain finite, while $|v_{+1}|^2_{fe}$ and $|v_{-1}|^2_{fe}$ vanish for $q_y < -1.08$ and $q_y > 1.48$. As q_y approaches -1.08, the particle-like components $|u_{\pm1}|^2_{fe}$ begin to decrease, accompanied by the emergence of finite hole-like contributions $|v_{\pm1}|^2_{fe}$. At $q_y \approx -0.21$, all four components attain comparable magnitudes, indicating strong particle–hole mixing [71, 177]. Upon further approaching $q_y \approx 0$, the particle-like components reach their maximum values, while the hole-like components again diminish. For $q_y > 0$, a similar evolution is observed; however, due to the inherent asymmetry of the excitation spectrum, the recovery of finite $|u_{\pm1}|^2_{fe}$ and vanishing $|v_{\pm1}|^2_{fe}$ occurs only near $q_y \approx 1.48$. Analogous behavior is also present in the zeroth component of the eigenvectors; notably, at $q_y \approx 0$, both $|u_0|^2_{fe}$ and $|v_0|^2_{fe}$ vanish. The Bogoliubov spectra and eigenvector analysis therefore indicate that although the excitation branches remain dynamically stable, the first-excited branch undergoes momentum-dependent quasiparticle hybridization. Following this, we perform numerical simulations of the coupled Gross–Pitaevskii equations, starting from the mean-field ground states and initiate the dynamics of the condensate by quenching the trap strength.

Numerical Simulation: We first obtain the ground state of the condensate for coupling parameters $(k_L, \Omega) = (0.5, 1.0)$ and interaction strengths $c_0 = 50$, $c_2 = -2.5$ in presence of the harmonic trap with strength $\lambda = 1.0$. This state exhibits a circularly asymmetric density profile [Figs. 6.4(a i - a iii)] [100]. To probe the time evolution of the condensate, we abruptly quench the trap strength from $\lambda = 1.0$ to $\lambda = 0.5$. Due to the sudden change in the system, in the beginning, the condensate shape modified at $t = 200$ units, as given in Figs. 6.4(b i-b iii). At later times, the density profile begins to recover, and by $t = 500$ units [Fig. 6.4(c i-c iii)] the original shape is largely restored. When $t > 500$ units [Figs. 6.4(d i–d iii)], the condensate fully returns to its initial configuration. This revival indicates that the state is dynamically stable, consistent with

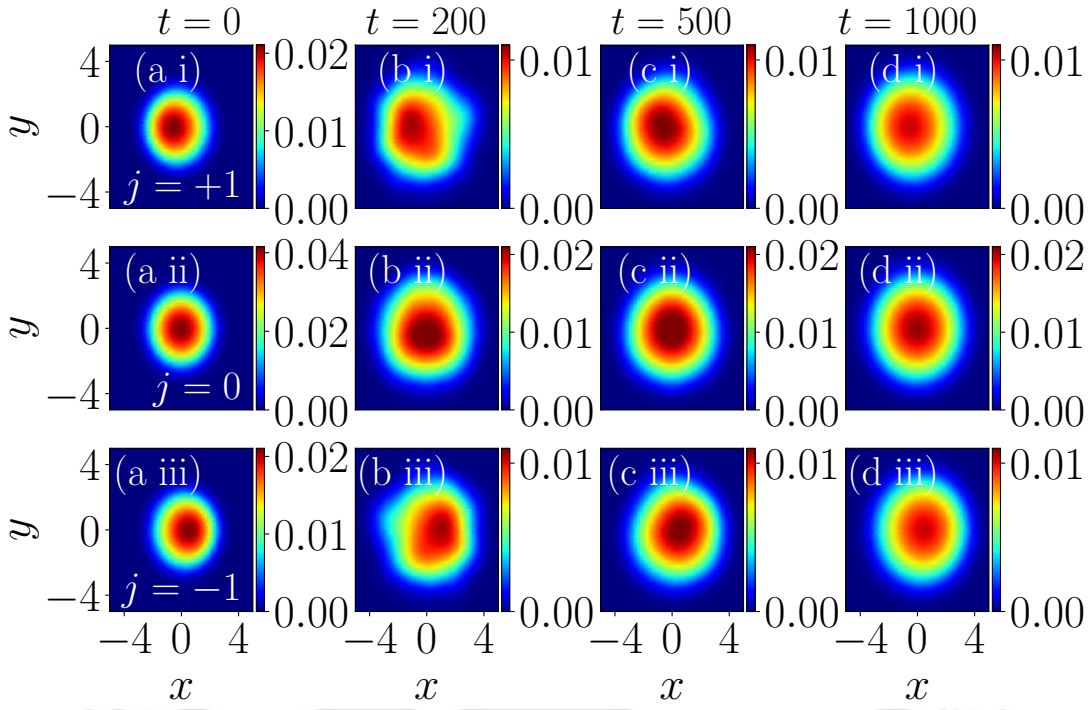


Figure 6.4: Pseudocolor density plots showing the time evolution of the condensate following a quench of the harmonic trap strength from $\lambda = 1$ to $\lambda = 0.5$. Panel (a) shows the ground-state density profile, while panels (b-d) correspond to the evolution at $t = 200$, 500, and 1000, respectively, for coupling parameters $(k_L, \Omega) = (0.5, 1.0)$ and interaction strengths $c_0 = 50$, $c_2 = -2.5$. Columns (i-iii) represent the $j = +1, 0, -1$ components of the spinor condensate. The persistence of the density profiles over long times demonstrates the dynamical stability of the condensate under the trap quench.

the excitation spectrum containing only real eigenfrequencies.

We report the total energy of the condensate in region I for $(k_L, \Omega) = (0.5, 1.0)$ with interaction strengths $c_0 = 50$, $c_2 = -2.5$. The energy starts with a magnitude $E \approx 0.64$ at $t = 0$, which starts to decrease and reaches $E \approx 0.29$ at $t = 370$. Beyond this point, the density of the condensate saturates, showing stable behaviour (not shown here).

6.5.1.2 Region IIa

In region IIa of the stability phase diagram [Fig. 6.2(a)], we consider the regimes as $k_L^2 > \Omega$ for which we present here the analysis for two different points. The first point $(k_L, \Omega) = (4.0, 1.0)$ is marked with a big diamond, and the second point $(4.0, 3.0)$ is marked with a square shape. Corresponding to these points, we present the collective excitation spectrum and numerical simulation results separately.

Collective excitation spectrum: In Figure 6.5, we present the collective excitation spectrum for the coupling parameters $(k_L, \Omega) = (4.0, 1.0)$ with interaction strengths

TH-4102_206121026

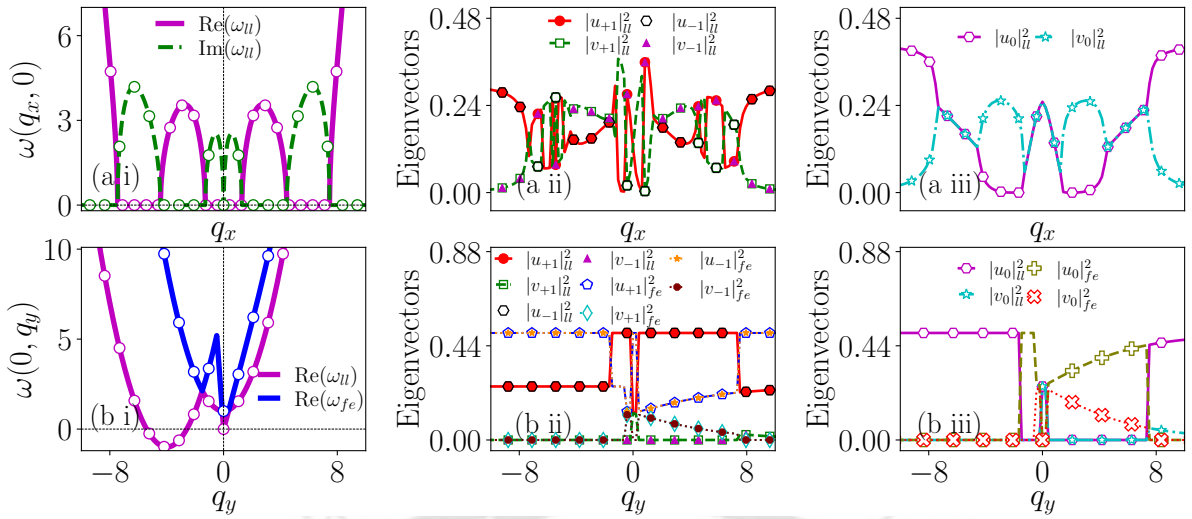


Figure 6.5: Eigenvalue spectra [(a i), (b i)] and corresponding eigenvectors [(a ii, a iii) and (b ii, b iii)] for $k_L = 4.0$ and $\Omega = 1.0$ with interaction strengths $c_0 = 50.0$ and $c_2 = -2.5$, shown along the quasi-momentum directions q_x and q_y, respectively. Line styles and symbols follow the conventions of Fig. 6.3. A multiband instability develops along the q_x direction, leading to spin–density–spin mixed modes in the eigenvector components, while the low-lying branch exhibits negative-energy excitations along the q_y direction.

$c_0 = 50.0$ and $c_2 = -2.5$. The top and bottom panels display the excitation spectrum along quasi-momentum directions q_x and q_y, respectively. In Fig. 6.5(a i), we obtain the multi-band imaginary eigenfrequencies extended over the finite range of quasi-momentum, the first band exhibits in the range of $q_x \in [0, 1.30]$ with amplitude $\omega = 2.55$ and the second band available in the range of $q_x \in [4.41, 7.57]$ with amplitude $\omega = 4.24$. The presence of instability bands is symmetric about the quasimomentum direction. The presence of the imaginary eigenfrequency results in the out-of-phase behaviour (spin-like mode) in eigenvector components [Fig. 6.5(a ii)], which holds the criterion [93, 116],

$$|u_{+1}|^2_{ll} - |u_{-1}|^2_{ll} \neq 0, \quad |v_{+1}|^2_{ll} - |v_{-1}|^2_{ll} \neq 0. \tag{6.14}$$

The eigenvector components exhibit the density-like mode in the presence of real eigenfrequencies as discussed in the previous section. Here, in this part, due to the transition of $\mathrm{Re}(\omega) \to \mathrm{Im}(\omega)$, density-like mode changes to a spin-like mode, and the presence of multiband instabilities leads to density-spin-density or spin-density-spin mixed mode [115]. The zeroth component of eigenvectors depicts in-phase behaviour (density-like mode) independently [Fig. 6.5(a iii)].

In the bottom row, Fig. 6.5(b i) depicts that the low-lying and first-excited branches

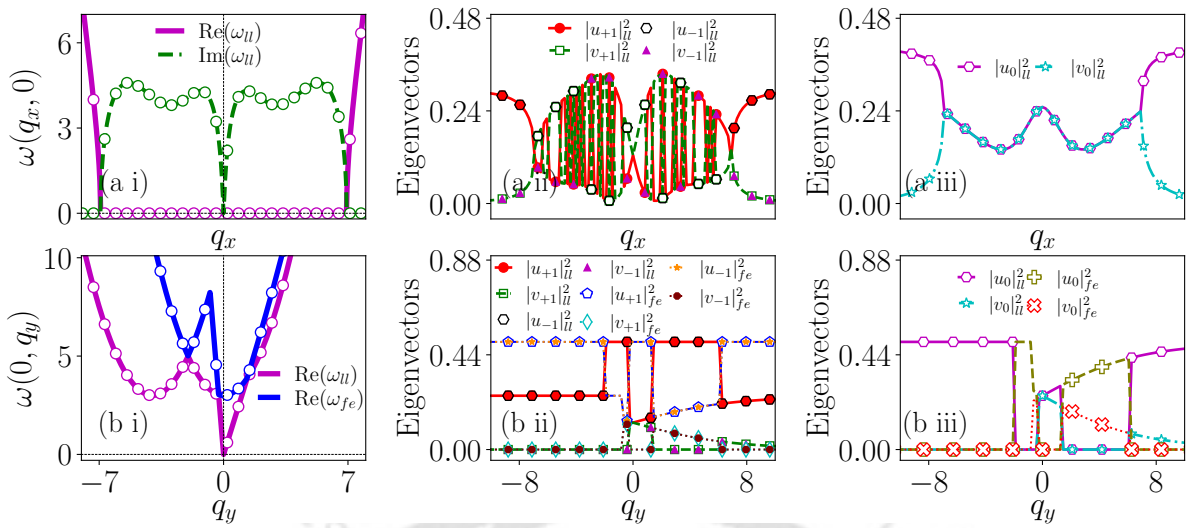


Figure 6.6: Eigenvalue spectra [(a i), (b i)] and corresponding eigenvectors [(a ii, a iii) and (b ii, b iii)] for $k_L = 4.0$ and $\Omega = 3.0$ with interaction strengths $c_0 = 50.0$ and $c_2 = -2.5$, shown along the quasi-momentum directions q_x and q_y, respectively. Line styles and symbols follow the conventions of Fig. 6.3. A single-band instability appears in the low-lying branch along the q_x direction, while a roton-maxon-like feature develops in the low-lying branch along the q_y direction.

of the eigenspectrum contain only real eigenfrequencies, with the low-lying branch developing the negative excitation spectrum. The presence of negative excitation makes the condensate energetically unstable [21]. The stable avoided crossings emerge at $q_y = -1.50, -0.11$, and 0.43. Owing to the real eigenfrequencies, the eigenvector components in Fig. 6.5(b ii) exhibit the density-like mode, which follows the criterion given in Eq. 6.13. At the point of avoided crossings $q_y = -1.50, -0.11$ and 0.43, the eigenvector components undergo a flip [152]. The zeroth component of eigenvectors exhibits the density-like mode independently [Fig. 6.5(b iii)].

In Fig. 6.6, we examine the second point in region IIa, where the coupling parameters are $(k_L, \Omega) = (4.0, 3.0)$ and the interaction strengths are $c_0 = 50.0$ and $c_2 = -2.5$. In Fig. 6.6(a i), we observe the presence of an imaginary eigenfrequency in the low-lying branch of the eigenspectrum for a certain range of quasi-momentum direction $q_x \in [0, 7.0]$ with maximum amplitude 4.62, and it is symmetric about the q_x. Due to the presence of imaginary eigenfrequencies, the eigenvector components exhibit the spin-like mode in the quasi-momentum range $q_x \in [0, 7.0]$, as shown in Fig. 6.6(a ii), which satisfies the criterion given in Eq. 6.14. It is symmetric due to the presence of the symmetric instability band in the eigenspectrum, and density-like mode transitions to spin-like mode when the complex eigenfrequency is present. The zeroth component of the eigenvector exhibits density-like mode independently [Fig. 6.6(a iii)].

In Fig. 6.6(b i), the low-lying and first-excited branches of the eigenspectrum yield

only real, positive eigenfrequencies. Within the low-lying branch, the excitation spectrum exhibits a local minimum at $q_y = -4.14$, resembling a roton-like feature. This branch thus contains the characteristic maxon-roton modes. Notably, the structure of the spectrum suggests an asymmetric roton-like feature within the low-lying branch. Avoided crossing between the low-lying and first-excited branch of the eigenspectrum emerges at $q_y = -2.08, -0.30$, and 1.39, respectively. Owing to the real eigenfrequencies, in Fig. 6.6(b ii), the eigenvector components display the density-like mode, consistent with the criterion given in Eq. 6.13. At the point of avoided crossings $q_y = -2.08, -0.30$, and 1.39, a flip emerges in the eigenvector components. The zeroth component of the eigenvector exhibits the density-like mode independently, and also undergoes a flip at the avoided crossing points [Fig. 6.6(b iii)].

Further, we extend the analysis to characterize the variation of maxon and roton modes by fixing $k_L = 4.0$, $c_0 = 50$, $c_2 = -2.5$, and varying the Rabi coupling strength. In Fig. 6.7(a), red right open triangles represent the maxon and green open diamonds represent the roton minimum. For $k_L = 4.0$, the roton minimum is sustained at $\Omega = 1.50$, with $\omega_-(0, q_y) = 0.000013$. A further decrease in Rabi coupling leads the excitation branch to negative energy modes. Upon increasing Rabi coupling, the maxon and roton minima approach each other and coincide at $\Omega = 10.95$, where both their magnitudes and positions are equal, and the roton minimum no longer exists beyond this point. Fig. 6.7(b), open blue hexagons indicate the roton depth, defined as the difference between the maxon and roton minima. The roton depth decays with increasing Rabi coupling and goes to zero at $\Omega = 10.95$. Fig. 6.7(c) exhibits the positions of maxon (red open pentagons) and roton minimum (green open hexagons). As the Rabi coupling increases, the position of the maxon mode increases, and the roton minimum remains at the same position throughout. At $\Omega = 10.95$, the maxon mode reaches a similar position as the roton minimum merges with it. Since the maxon and roton modes occur at the negative q_y, we plot them using $-q_y$.

In Fig. 6.7(d), the $k_L - \Omega$ phase plane (along q_y direction at $q_x = 0.0$) is divided into three distinct regions: the gray (blue) region contains only real, positive eigenfrequencies without (with) roton modes, separated by a white dashed line with blue dots, however both are energetically stable. The red region contains negative eigenfrequencies and is energetically unstable. The blue and red region is separated by a solid white line with red dots. Maxon-roton modes occur only in the blue region. Additionally, comparing this with the phase plot Fig. 6.2, it is evident that the blue region is a subset of region IIa. The case discussed above with $k_L = 4.0$ lies in the blue region and requires a relatively large Rabi coupling, $\Omega = 10.95$, for the maxon and roton to

TH-4102_206121026

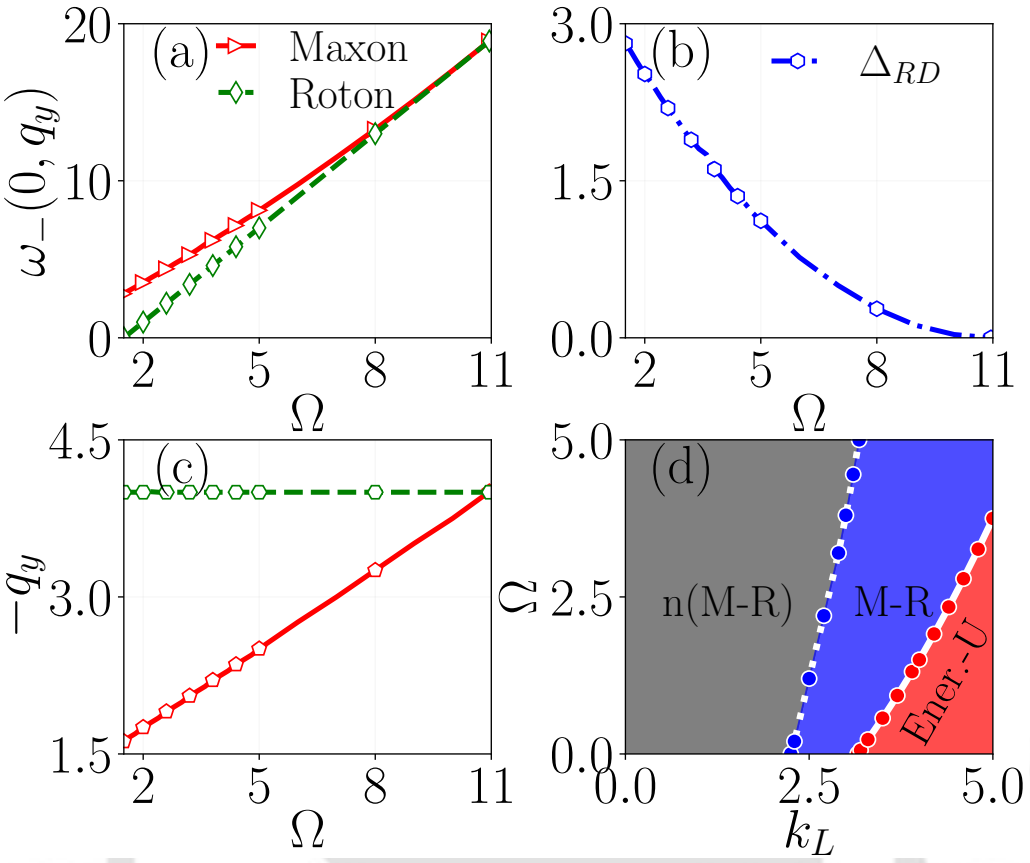


Figure 6.7: Variation of roton-maxon modes for ferromagnetic interaction ($c_0 = 50$, $c_2 = -2.5$). Panels (a-c) show the results obtained for $k_L = 4.0$ as the Rabi coupling is varied. Panel (a) displays the evolution of the maxon (red open right triangles) and roton (green open diamonds) modes, while panel (b) shows the corresponding decay of the roton depth Δ_{RD} (blue open hexagons). Panel (c) illustrates quasi-momentum positions of the maxon (red open pentagon) and roton (green open hexagons) modes along the q_y direction. Panel (d) presents the phase diagram in the $k_L - \Omega$ plane at $q_x = 0.0$, with gray, blue, and red regions indicating the absence of maxon–roton modes n(M–R), the presence of maxon–roton modes (M–R), and energetic instability (Ener.-U), respectively, along the q_y direction.

merge. These observations are consistent with previous experimental and theoretical works [22, 24, 153, 178, 179].

As mentioned earlier, the considered first point lies in the red region of this phase, which is energetically unstable, and the second point lies in the blue region, energetically stable; however, both points are dynamically unstable due to the presence of imaginary eigenfrequencies.

Numerical Simulation: Similar to the collective excitation discussed in the previous part, we consider two different points to perform the numerical simulation in region IIa. We generate the stationary state for coupling parameters $(k_L, \Omega) = (4.0, 1.0)$, and $(4.0, 3.0)$ with interaction strengths $c_0 = 50$, and $c_2 = -2.5$, and study its dynamics by

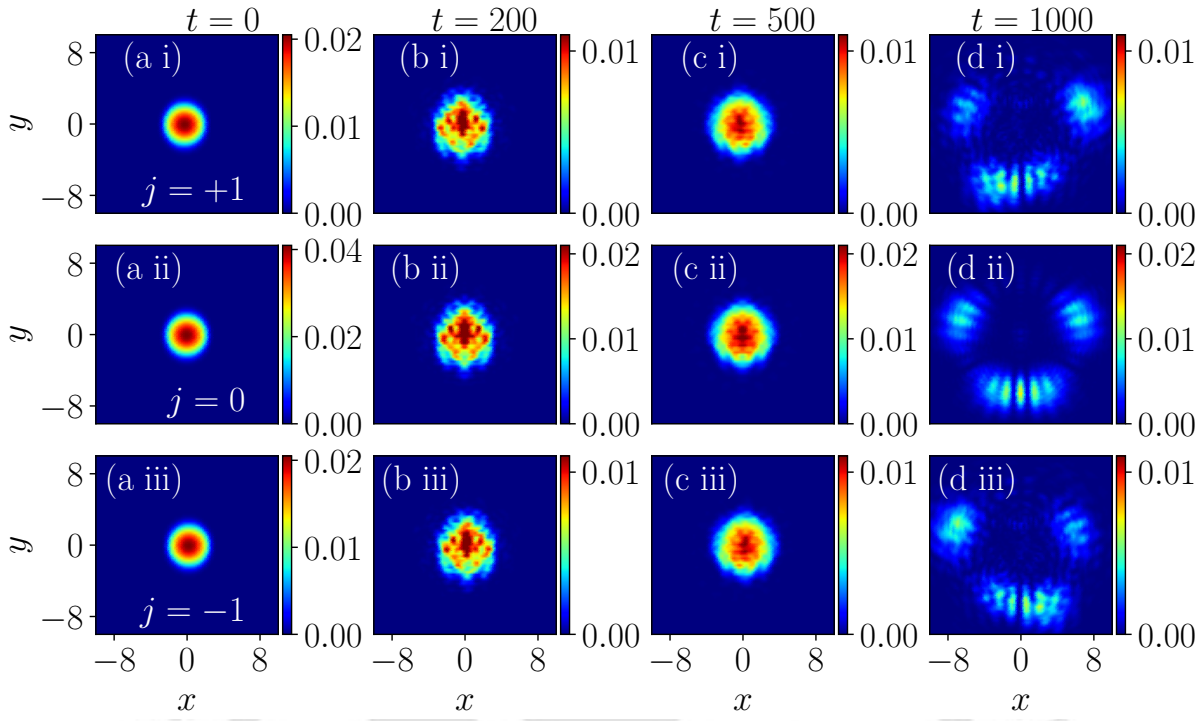


Figure 6.8: Pseudocolor density plots showing the time evolution of the condensate following a quench of the harmonic trap strength from $\lambda = 1$ to $\lambda = 0.5$. (a) Stationary state density profile. (b-d) snapshots during time evolution at t = 200, 500, 1000, respectively, for coupling parameters (k_L, Ω) = (4.0, 1.0), with interaction strengths $c_0 = 50$, $c_2 = -2.5$. Each column represents the spinor components, with $j = +1$ (top) , 0 (middle), and -1 (bottom).

sudden quenching of trap strength to half of its initial strength.

We first consider the point $(k_L, \Omega) = (4.0, 1.0)$ and generate the stationary state of the condensate, which is a circularly asymmetric state [Fig. 6.8(a i-a iii)] [100]. During time evolution, in Fig. 6.8(b i-b iii), initially the shape of the condensate changes due to a sudden quench of trap strength (as observed in the previous case). At $t = 500$ units [Fig. 6.8(c i-c iii)], the condensate continues to deform, and at later times $t = 1000$ units, it fragments, forming a ring shape profile [Fig. 6.8(d i-d iii)]. The fragmentation of the density profile occurs at the onset of dynamical instability, triggered by the emergence of imaginary frequencies in the excitation spectrum [125, 84, 180].

For the second point in region IIa with coupling parameters $(k_L, \Omega) = (4.0, 3.0)$. We again obtain a circularly asymmetric state. During dynamics, we quench the trap to half of its original strength. During the time evolution, the shape deformation begins to appear at $t = 200$ units and continues to grow. At $t = 500$, it deforms further, and at a later time $t = 1000$, the fragmentation of density components leaves only lobes of density in ring shape; owing to the presence of the imaginary eigenfrequency in the collective excitation spectrum, similar to the previous case (not shown here).

We calculate the total energy during the time evolution of the condensate for the parameter sets discussed above. For the coupling parameters $(k_L, \Omega) = (4.0, 1.0)$, the condensate energy begins at $E = -7.30$ at $t = 0$. Following the quench in the trap strength, the system relaxes toward a lower-energy configuration, attaining $E = -7.59$ at $t = 300$ units, and remains flat up to $t = 412$ units. Beyond this point, energy starts to increase and reaches $E = 16.11$ at $t = 1000$ units (not shown here). For the second point in the region, $(k_L, \Omega) = (4.0, 3.0)$, the condensate has energy $E = -9.29$ at $t = 0$. During the time evolution, the energy decreases to $E = -9.60$ by $t = 276.5$ units and remains flat up to $t = 475.25$. Beyond this point, it starts to increase and reaches $E = 7.93$ at $t = 1000$ units. The energetic instability of the condensate is characterized by the presence of negative-energy modes in the BdG spectrum. Although energy distribution and decay of the initial state may be observed during dynamics, such behavior is not unique to energetic instability and can also arise from dynamical instabilities associated with complex excitation frequencies. The observed temporal modulation of the total energy in both cases reflects the dynamical instability of the condensate following the quench [93].

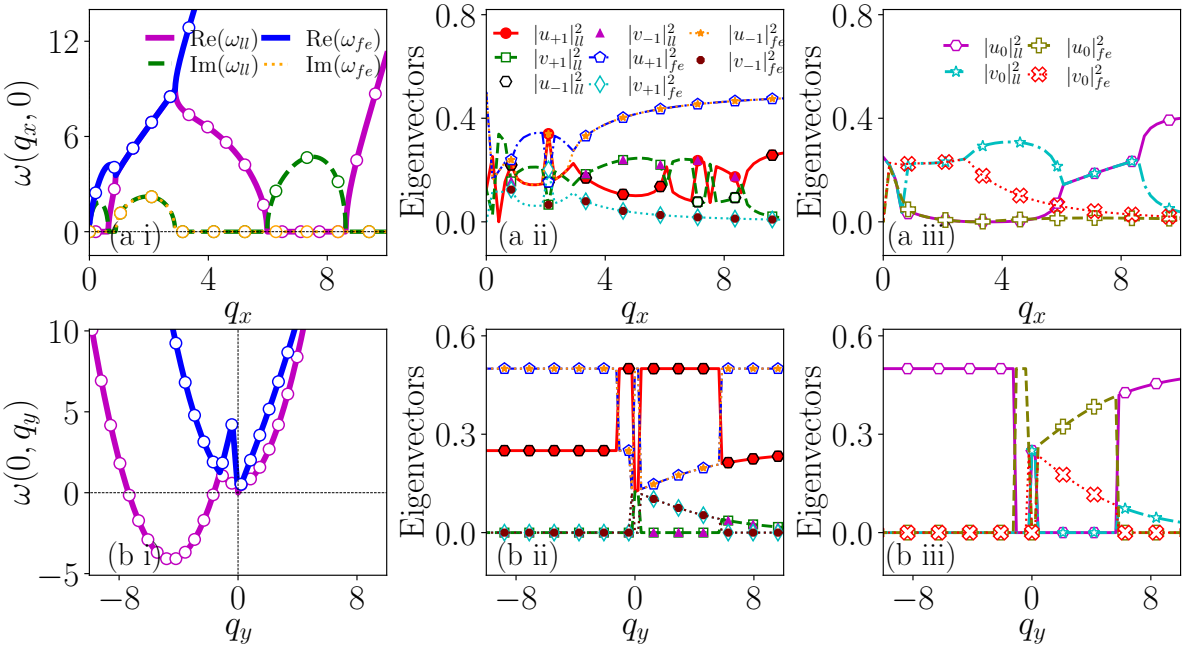


Figure 6.9: Eigenspectra and corresponding eigenvectors for the spinor condensate are shown, with the top (bottom) row corresponding to quasi-momentum along q_x (q_y) for $(k_L, \Omega) = (4.5, 0.5)$, and interaction strengths $c_0 = 50.0$, $c_2 = -2.5$. Panels (a i) and (b i) display the eigenspectra, with Re(ω) shown as solid lines and $|\mathrm{Im}(\omega)|$ as dashed or dotted lines. The eigenvector components for the low-lying and first-excited branches are shown in panels (a ii, a iii) and (b ii, b iii), respectively. Multi-band instability appears in the low-lying branch, single-band instability in the first-excited branch arises from avoided crossings along q_x, and negative eigenfrequencies are observed along q_y.

TH-4102_206121026

6.5.1.3 Region IIb

In the stability region IIb, we consider the point with coupling parameters (k_L, Ω) = (4.5, 0.5), marked by the hexagon. The collective excitation spectrum and numerical simulation results for this case are presented in the following section.

Collective excitation spectrum: In Fig. 6.9, we present the collective excitation spectrum for the coupling parameters $(k_L, \Omega) = (4.5, 0.5)$, with interaction strengths $c_0 = 50.0$ and $c_2 = -2.5$. The spectrum is shown along the quasi-momentum directions q_x (top row) and q_y (bottom row). In Fig. 6.9(a i), the low-lying branch of the eigenspectrum exhibits three bands of imaginary eigenfrequencies. The first band extends over $q_x \in [0, 0.61]$ with an amplitude of 1.90, the second over $q_x \in [0.87, 2.87]$ with an amplitude of 2.20, and the third over $q_x \in [5.98, 8.65]$ with an amplitude of 4.83. In contrast, the first excited branch displays only a single band of imaginary eigenfrequency. This arises from an avoided crossing between the low-lying and first excited branches of the eigenspectrum. The band extends over $q_x \in [0.87, 2.87]$ with an amplitude of 2.20, coinciding with the second band of the low-lying branch. Since this avoided crossing produces imaginary eigenfrequencies, it corresponds to an unstable avoided crossing [95, 115]. Owing to the presence of the imaginary eigenfrequencies, the eigenvector components in the low-lying branch and in the first-excited branch in Fig. 6.9(a ii) exhibit the out-of-phase behaviour (spin-like mode) following the criterion,

$$\begin{aligned} &|u_{+1}|^2_{ll} - |u_{-1}|^2_{ll} \neq 0, \quad |v_{+1}|^2_{ll} - |v_{-1}|^2_{ll} \neq 0, \\ &|u_{+1}|^2_{fe} - |u_{-1}|^2_{fe} \neq 0, \quad |v_{+1}|^2_{fe} - |v_{-1}|^2_{fe} \neq 0. \end{aligned} \tag{6.15}$$

At the point of unstable avoided crossing, the eigenvector components of the low-lying and first excited branches are out of phase with each other for $q_x \in [0.87, 2.87]$, due to multiband instability, resulting in spin-density-spin mixed modes in the eigenvector components, whereas, the zeroth component eigenvectors exhibits the usual density-like mode [Fig. 6.9(a iii)].

In the bottom row along q_y direction, Fig. 6.9(b i) shows only real eigenfrequencies in both the low-lying and first-excited branches of the eigenspectrum. An avoided crossing occurs between these branches at $q_y = -1.22$. We also observe a negative eigenfrequency in the low-lying branch. The real eigenfrequencies lead the eigenvector components in Fig. 6.9(b ii) to display in-phase behavior (density-like mode), as

defined in Eq. 6.13. At the avoided crossing, the eigenvector components flip [152]. The zeroth component independently displays in-phase behavior [Fig. 6.9(b iii)]. The presence of imaginary and negative eigenfrequencies causes dynamic and energetic instability throughout [21].

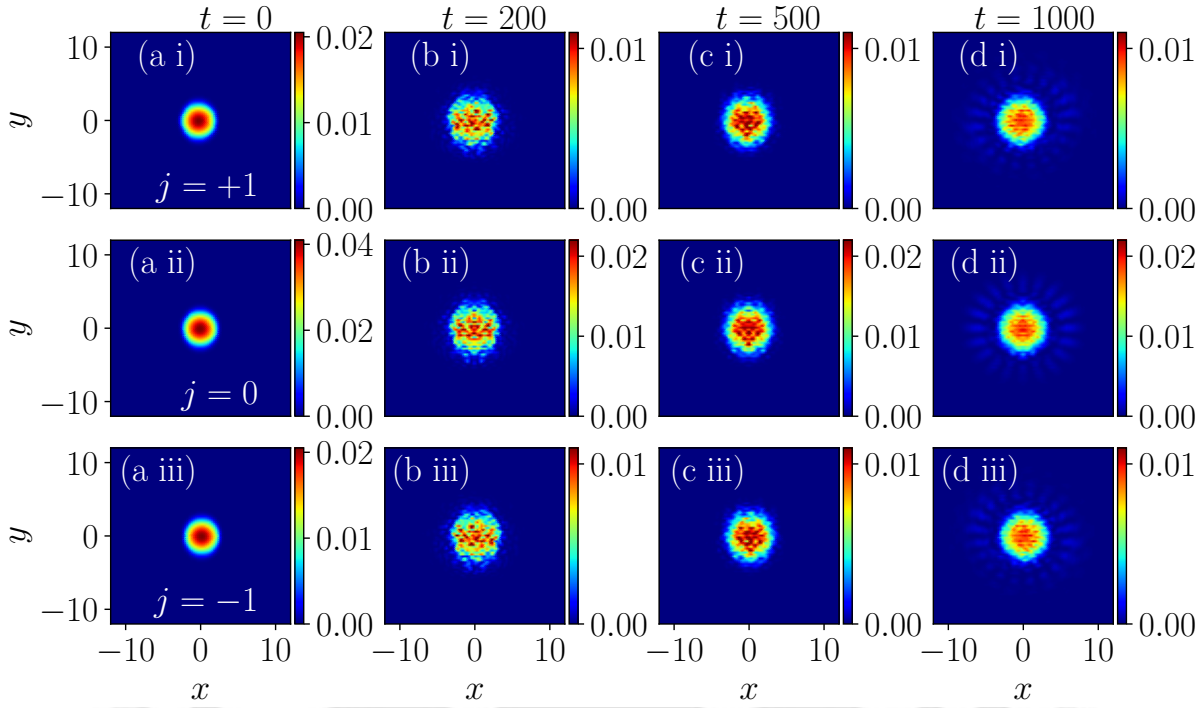


Figure 6.10: Pseudocolor plots in panel represent (a) stationary state density and (b-d) density profile during time evolution at times $t = 200, 500, 100$, respectively, for coupling parameters $(k_L, \Omega) = (4.5, 0.5)$ with interaction strengths $c_0 = 50$, $c_2 = -2.5$. Each column (i–iii) corresponds to the density of the spinor components $|\psi_{+1}|^2$, $|\psi_0|^2$, and $|\psi_{-1}|^2$, respectively. During the time evolution, the trap strength is suddenly reduced to half of its original value.

Numerical Simulation: In this part of the study, we present numerical simulations in region IIb with coupling parameters $k_L = 4.5$ and $\Omega = 0.5$, and interaction strengths $c_0 = 50$ and $c_2 = -2.5$. The initial stationary state obtained is circularly asymmetric [Fig. 6.10(a i-a iii)] [100]. To study the condensate dynamics, the trap strength is suddenly reduced to half its original value. As shown in Fig. 6.10(b i-b iii), the condensate deforms and changes shape at $t = 200$ units. By $t = 500$ units, the shape of condensate densities keep deforming [Fig. 6.10(c i-c iii)]. At a later time, $t = 1000$ units, the amplitude of the density profile decreases, and a ring shape geometry emerges on the top of all components [Fig. 6.10(d i-d iii)], confirming dynamical instability nature of the condensate in this region [125, 84, 180].

Additionally, we also report the variation in the condensate energy during dynam-

ics, it starts from $E = -8.93$ at $t = 0$ and decreases during the evolution, and attains the value $E = -9.20$ at $t = 325$, remains flat up to $t = 760.25$ units. Beyond this point, it starts to increase and reaches $E = -6.55$ at $t = 1000$ units [not shown here].

6.5.2 Collective excitation spectrum in absence of Rabi coupling (Ω): Region III

In the previous section, we discussed the collective excitation spectrum with both SO and Rabi couplings, covering regions I, IIa, and IIb of the stability phase diagram [Fig. 6.2]. Now, we focus on the case without Rabi coupling ($\Omega \sim 0$). We refer to this regime as region III of the stability phase diagram and present both the collective excitation spectrum and the corresponding numerical simulation results.

In region III of the stability phase diagram [Fig. 6.2], we examine two representative points with coupling parameters $(k_L, \Omega) = (2.0, 0.0)$ and $(4.0, 0.0)$ in which we have $k_L^2 > \Omega$, but we consider $\Omega \sim 0$. To investigate the behavior of the condensate in this regime, we analyze the collective excitation spectrum together with numerical simulations.

Collective excitation spectrum: In Fig. 6.11, we present the eigenvalue spectrum for coupling parameters $(k_L, \Omega) = (2.0, 0.0)$ and interaction strengths $c_0 = 50.0$, $c_2 = -2.5$. The top row presents the eigenspectrum along the quasi-momentum direction q_x, while the bottom row corresponds to the q_y direction of quasi-momentum. In Fig. 6.11(a i), we obtain the imaginary eigenfrequency in the spectrum for a finite range of quasi-momentum direction $q_x \in [0, 3.55]$ with band amplitude of about 1.56. The presence of the imaginary eigenfrequency is symmetric about q_x. The corresponding eigenvectors in Fig. 6.11(a ii) display the spin-like mode in a certain quasi-momentum range $q_x \in [0, \pm 3.55]$, consistent with the criterion in Eq. 6.14, owing to the presence of the imaginary eigenfrequencies. A kink-like feature emerges in the $|u_{+1}|^2_{ll}$ and $|v_{+1}|^2_{ll}$ at $q_x \approx 0$, which was absent in the presence of the Rabi coupling strength. The zeroth component of the eigenvectors exhibits the density-like mode independently [Fig. 6.11(a iii)]. In the bottom row, in Fig. 6.11(b i), we obtain only real, positive eigenfrequencies in the eigenspectrum in the low-lying and first-excited branch. A stable avoided crossing occurs between the low-lying branch and first-excited branch at $q_y = -2.5$. Owing to the real eigenfrequencies, in Fig. 6.11(b ii), the eigenvector exhibits the density-like mode, which holds the criterion Eq. 6.13. At avoided crossing, the eigenvector undergoes a flip at $q_y = -2.5$ [152]. A similar kink-like structure appears in $|u_{+1}|^2_{ll}$ and $|v_{+1}|^2_{ll}$ at $q_x \approx 0$. The zeroth component of the eigenvectors depicts

the density-like mode independently [Fig. 6.11(b iii)].

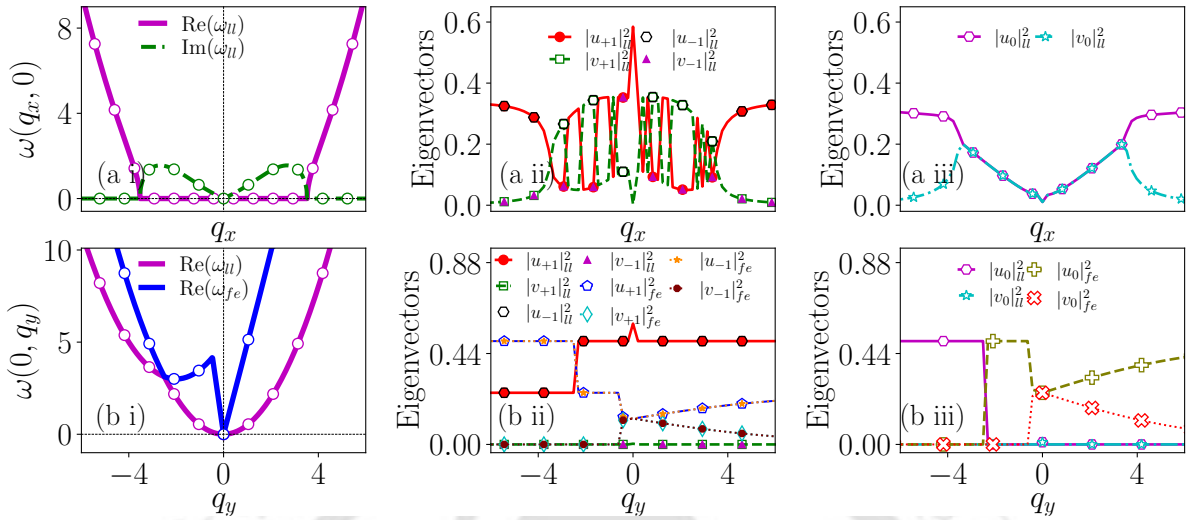


Figure 6.11: Collective excitation spectrum (a i) and (b i) with the corresponding eigenvectors (a ii, a iii) and (b ii, b iii) for $k_L = 2.0$, $\Omega \sim 0.0$, using interaction strengths $c_0 = 50.0$ and $c_2 = -2.5$ along with quasi-momentum directions q_x and q_y, respectively. The line styles and symbols in the top and bottom rows follow the same convention as in Fig. 6.3.

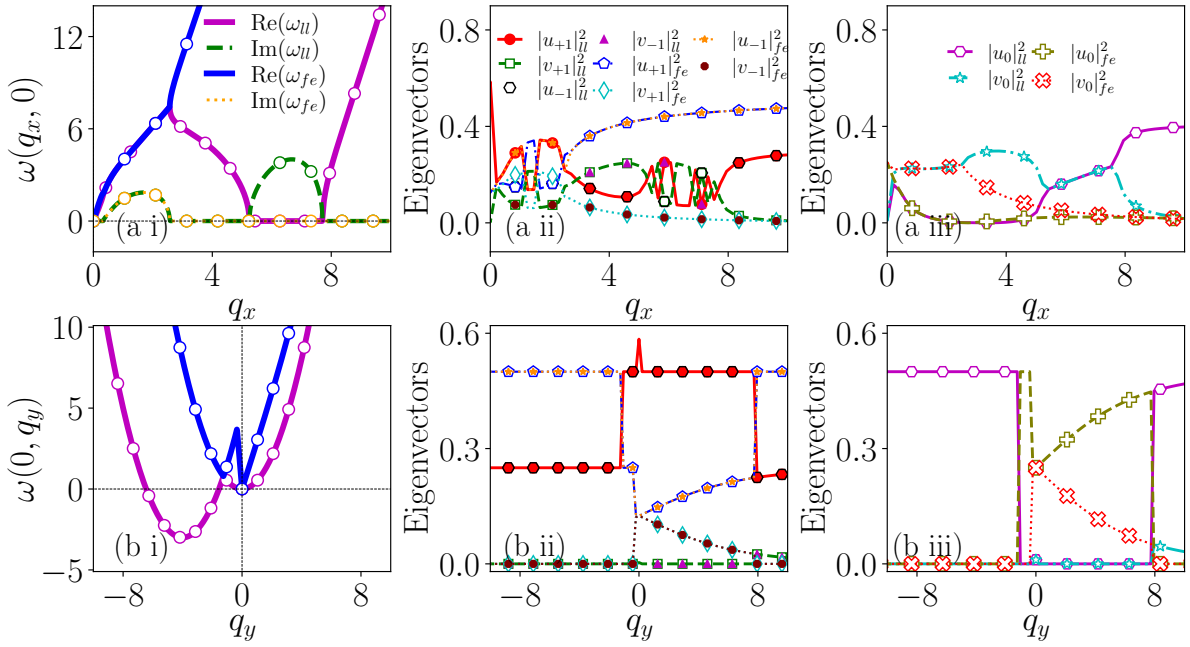


Figure 6.12: (a i, b i) Eigenvalue spectrum and (a ii, a iii, b ii, b iii) corresponding eigenvectors for $k_L = 4.0$ in the static limit ($\Omega = 0$), with interaction strengths $c_0 = 50.0$ and $c_2 = -2.5$. The spectra and eigenvectors are plotted as functions of the quasi-momenta q_x and q_y, respectively. The line styles and symbols in the top and bottom rows follow the same convention as in Fig. 6.9.

Next, in Fig. 6.12, we report the collective excitation spectrum for the coupling parameters $(k_L, \Omega) = (4.0, 0.0)$ with interaction strengths $c_0 = 50.0$ and $c_2 = -2.5$. The

top panel displays the eigenvalue spectrum as a function of the quasi-momentum q_x, while the bottom panel exhibits the spectrum along the q_y direction. In Fig. 6.12(a i), the low-lying branch of the eigenspectrum exhibits the presence of multi-band imaginary eigenfrequencies for $q_x \in [0, 3.30]$ with band amplitude 2.93, and $q_x \in [6.26, 8.74]$ with band amplitude 4.74. In the first-excited branch of the eigenspectrum, we obtain the presence of a single band instability for quasi-momentum range $q_x \in [0, 3.30]$ with band amplitude 2.93, which emerges as a result of unstable avoided crossing between the low-lying and first-excited branches of the eigenspectrum [95, 115]. The location and amplitude are similar to those of the first band on the low-lying branch. The corresponding eigenvector components in Fig. 6.12(a ii) display the spin-like mode due to the presence of imaginary eigenfrequencies, following the criterion given in Eq. 6.15. At the point of unstable avoided crossing for $q_x \in [0, 3.30]$, the eigenvector components of low-lying and first-excited branches are out of phase among themselves as well as out of phase with each other. Similar to the previous case, a kink-like structure emerges in $|u_{+1}|^2_{ll}$ and $|v_{+1}|^2_{ll}$ at $q_x \approx 0$. The zeroth component of the low-lying and first-excited branches displays the density-like mode independently [Fig. 6.12(a iii)]. In the bottom row, Fig. 6.12(b i) presents the eigenspectrum along the quasi-momentum direction q_y. The spectrum exhibits only real eigenfrequencies for both the low-lying and first-excited branches. An avoided crossing appears between these two branches at $q_y = -1.09$, and the low-lying branch takes on negative eigenvalues. The presence of negative excitations leads to energetic instability of the condensate [21]. The corresponding eigenvector components in Fig. 6.12(b ii) display the density-like mode for low-lying and the first-excited branches. A kink-like structure emerges in $|u_{+1}|^2_{ll}$ and $|v_{+1}|^2_{ll}$ at $q_x \approx 0$. At the point of the avoided $q_y = -1.09$, eigenvector components undergo a flip for both branches. The zeroth component of the eigenvectors exhibits the density-like mode independently [Fig. 6.12(b iii)]. The region is dynamically unstable throughout; however, both energetically and dynamically unstable for higher SO coupling strength [Fig. 6.7(d)].

Numerical Simulation: In this section, we present numerical simulations for region III, focusing on the points: (k_L, Ω) = (2.0, 0.0) and (4.0, 0.0), with interaction strengths $c_0 = 50$ and $c_2 = -2.5$. Initially, in Fig. 6.13, we consider the case with (2.0, 0.0). In Fig. 6.13(a i-a iii), we obtain the stationary state density profile, which is a circularly highly asymmetric state. The stripe phase also exists for the above-mentioned SO coupling strength in the absence of Rabi coupling strength, which is an excited state of the condensate [100, 167]. We find that in the absence of SO coupling, finite Rabi coupling

stabilizes a zero momentum phase. When SO coupling is present without Rabi coupling, the single-particle spectrum exhibits a degenerate ring of minima and interaction determine the ground state: ferromagnetic interactions favour a circularly asymmetric plane-wave phase, while antiferromagnetic interactions allow stripe or superstripe phases as ground states. However, when both the SO and Rabi couplings are present, the degeneracy of the Rashba ring is lifted, leading to an anisotropic dispersion with minima at finite momentum. This explicitly favours plane-wave-type condensates and suppresses stripe formation [93, 169]. To study the quench dynamics, we abruptly reduce the trap strength to half its initial value. As the time evolves, the condensate shape deforms and breaks into several small domains across components at $t = 200$ and 500 units [Figs. 6.13(b i–b iii, c i–c iii)]. At a later time ($t = 1000$ units), as shown in Fig. 6.13(d i–d iii), the amplitudes of the densities $\rho_{\pm 1}$ decrease, and stripe-like patterns begin to appear across the components [125, 180].

Next, we examine the second point in region III with coupling parameters $(k_L, \Omega) = (4.0, 0.0)$. The initially obtained ground-state density profile is circularly asymmetric. Similar to the above case, the stripe phase also exists for SO coupling mentioned here in the absence of Rabi coupling, which is an excited state as well [100, 167]. As before, we abruptly change the trap strength by half to study the dynamics of the condensate. Since the eigenspectrum in Fig. 6.12(a i) contains the imaginary eigenfrequency, the condensate fragments into several smaller domains during evolution. By $t = 200$ units, fragmentation is already visible across all components, and it becomes more pronounced at later times ($t = 500$ units). At a later time, $t = 1000$ units, the density of the zero-component is reduced, and the system exhibits a strongly fragmented structure across components (not shown here).

We now report the total energy of the condensate during time evolution in region III for the point $(k_L, \Omega) = (2.0, 0.0)$. The energy starts with $E = -0.31$ at $t = 0$ units. During time evolution following the quench of the trap strength, the condensate energy relaxes to a lower value, reaching and maintaining $E = -0.64$ up to $t = 1000$ units. Since the collective excitation spectrum contains imaginary eigenfrequencies, it matches well with the dynamics of the condensate, revealing dynamical instability. The total energy of the condensate behaves differently at another point in the region, where we consider $(k_L, \Omega) = (4.0, 0.0)$. The energy of the condensates starts with a value $E = -6.3$ at $t = 0$ units. It starts to decrease similarly to the previous point and reaches $E = -6.5$ at $t = 112.25$ units, rises again and reaches a higher value $E = 18.78$ at $t = 1000$ units (not shown here).

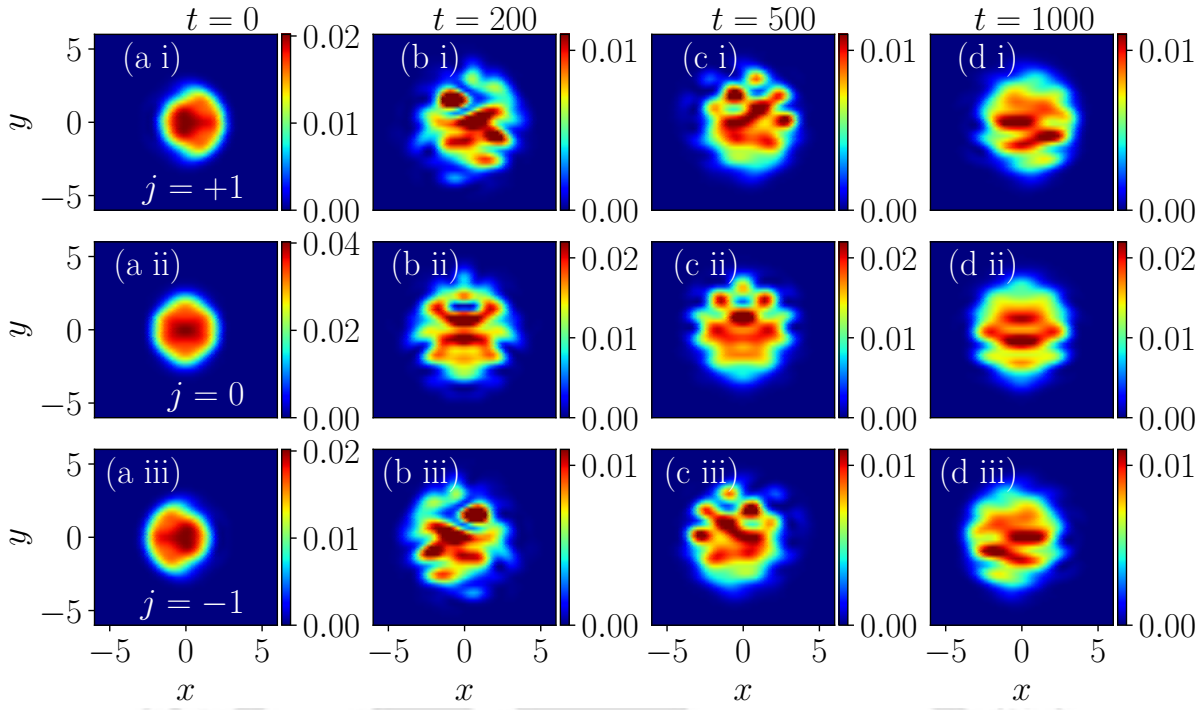


Figure 6.13: Pseudocolor plots of the stationary state and time-evolved densities. (a) The circularly asymmetric density profile of the ground state. (b–d) The density evolution at times $t = 200, 500$, and 1000, respectively. Columns (i)–(iii) correspond to the spinor components $j = +1, 0$, and -1, respectively. Parameters: lattice coupling $(k_L, \Omega) = (2.0, 0.0)$ and interaction strengths $c_0 = 50$, $c_2 = -2.5$.

6.6 Collective Excitations for Anti-ferromagnetic interactions

So far, we have focused on the stability analysis in the presence of ferromagnetic interactions across the $k_L - \Omega$ plane, where we identified stable region I and unstable region II, subdivided into IIa and IIb. We also designated the line corresponding to zero Rabi coupling ($\Omega \sim 0$) as region III, which remains unstable throughout. For $\Omega \sim 0$ we have recently reported the emergence of the superstripe in one-dimensional SO coupled spin-1 BECs [101]. Here we extend the work to 2D spin-1 BECs. For the case of antiferromagnetic interactions, we now examine the scenario with zero Rabi coupling for two different SO coupling strengths, $k_L = 2.0$ and 4.0, with interaction strengths $c_0 = 50$ and $c_2 = 2.5$. These parameter choices correspond to antiferromagnetic interactions, where the ground state at $\Omega = 0$ forms a superstripe (supersolid-like) phase [100]. Since a finite Rabi coupling tends to suppress this phase, restricting our analysis to $\Omega = 0$ allows us to emphasize the intrinsic behavior of the system without Rabi-induced mixing.

TH-4102_206121026

Case (i): $k_L = 2.0, \Omega = 0.0$

We begin by considering the antiferromagnetic regime with interaction strengths $c_0 = 50$, $c_2 = 2.5$. We first focus on the SO coupling strength $k_L = 2.0$ in the absence of the Rabi coupling ($\Omega = 0.0$), and present the corresponding collective excitation spectrum and condensate dynamics.

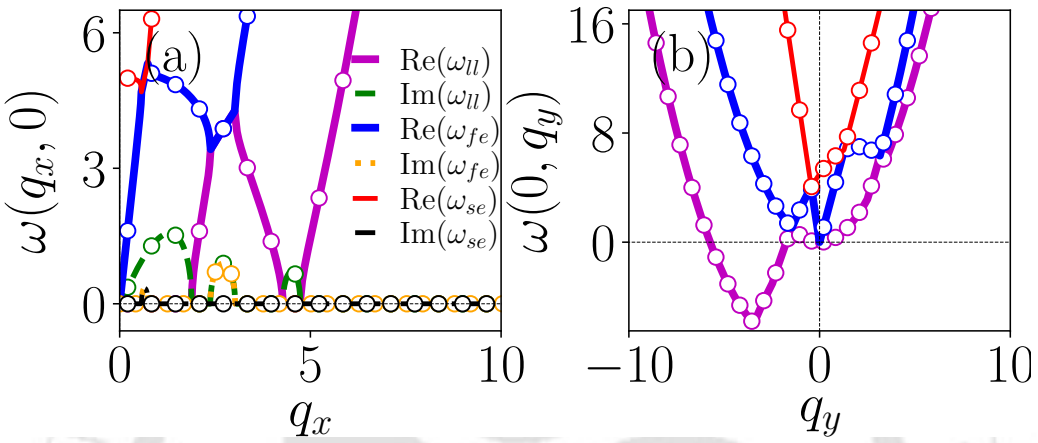


Figure 6.14: Collective excitation spectrum as a function of (a) quasi-momentum q_x and (b) quasi-momentum q_y. Parameters are SO coupling strength $k_L = 2.0$, Rabi frequency $\Omega = 0.0$, and interaction strengths $c_0 = 50$, $c_2 = 2.5$. Solid magenta, solid blue, and thin red lines represent Re(ω_{ll}), Re(ω_{fe}), and Re(ω_{se}), respectively; dashed green, dotted orange, and dash-dotted black lines show the corresponding magnitude of the imaginary part $|\text{Im}(\omega)|$. A multiband instability with a roton minimum appears along q_x, while negative excitation frequencies are observed along q_y.

Collective excitations: In Fig. 6.14, we report the eigenvalue spectrum for the first point considering coupling parameters $(k_L, \Omega) = (2.0, 0.0)$, with interaction strengths $c_0 = 50$, $c_2 = 2.5$. In Fig. 6.14(a), we present the excitation spectrum along the quasi-momentum direction q_x. The eigenspectrum reveals multi-band instabilities in the low-lying branch, with locations and amplitudes $(q_x, \omega) = (1.29, 1.578)$, $(2.70, 0.920)$, and $(4.50, 0.715)$. Among the three imaginary frequencies, the third band represents roton instability, where $\text{Re}(\omega_{ll}) \approx 0$ and $\text{Im}(\omega_{ll}) \neq 0$ [169, 181]. In the first-excited branch of the eigenspectrum, we obtain two-band instability at $q_x = 0.67, 2.70$ with amplitude $\omega = 0.352, 0.920$. The second instability band emerges as a result of overlap between the low-lying and first-excited branch of the eigenspectrum, which is also discussed above in ferromagnetic interactions, and we define it as an unstable avoided crossing. The first instability band appears as a result of the overlap between the first-excited and second-excited branches of the eigenspectrum. Hence, the second-excited branch exhibits only a single instability band, which is located at $q_x = 0.67$, with ampli-

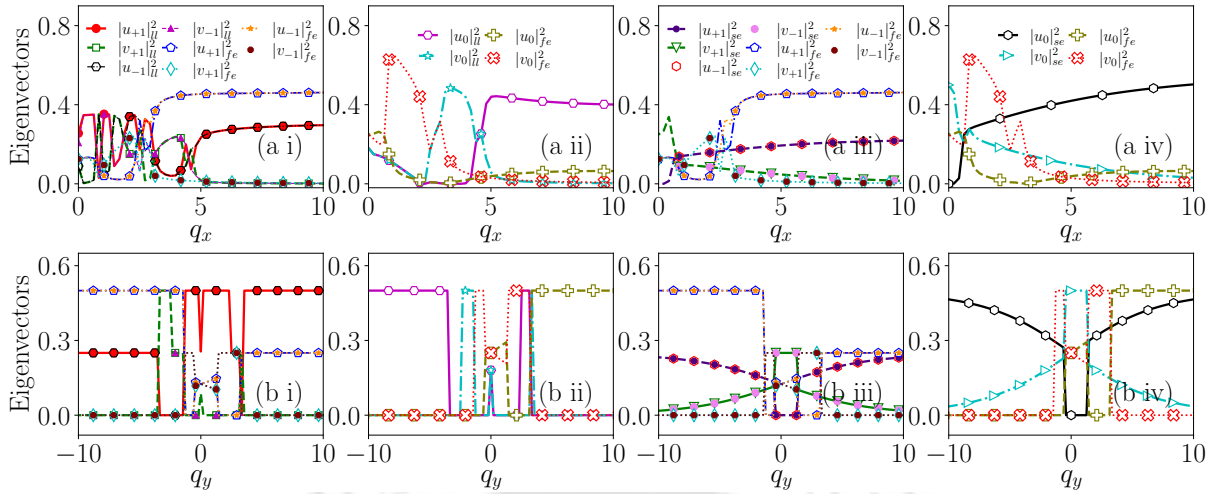


Figure 6.15: Eigenvector components for the excitation branches along the quasi-momentum directions (a i–a iv) q_x and (b i–b iv) q_y, corresponding to the eigenvalues in Fig. 6.14. For each branch, squared amplitudes $|u_m|^2$ and $|v_m|^2$ (with $m = 0, \pm 1$) are shown using distinct markers. Low-lying branch: $|u_{+1}|^2_{ll}$ (red open circles), $|u_{-1}|^2_{ll}$ (black diamonds), $|u_0|^2_{ll}$ (magenta open hexagons), $|v_0|^2_{ll}$ (cyan open stars), $|v_{+1}|^2_{ll}$ (green open squares), $|v_{-1}|^2_{ll}$ (magenta triangles). First-excited branch: $|u_{+1}|^2_{fe}$ (blue open pentagons), $|u_{-1}|^2_{fe}$ (orange stars), $|u_0|^2_{fe}$ (olive open pluses), $|v_0|^2_{fe}$ (red open crosses, dotted line), $|v_{+1}|^2_{fe}$ (cyan open diamonds), $|v_{-1}|^2_{fe}$ (maroon dots). Second-excited branch: $|u_{+1}|^2_{se}$ (indigo dots), $|u_{-1}|^2_{se}$ (red hexagons), $|u_0|^2_{se}$ (black hexagons), $|v_0|^2_{se}$ (cyan left-pointing triangles), $|v_{+1}|^2_{se}$ (green open downward triangles), $|v_{-1}|^2_{se}$ (violet dots).

tude $\omega = 0.352$. The overlap between the first-excited and second-excited branches is defined as a second unstable avoided crossing [90, 116]. The presence of the instability bands in the eigenspectrum is symmetric about q_x.

In Fig. 6.14(b), we present the collective excitation spectrum along the quasi-momentum direction q_y. We obtain only real eigenfrequencies; however, the gap among the branches closes at several points. The gap between the low-lying and first-excited branch closes at $q_y = -1.44$ and 3.16, while it closes between the first-excited and second-excited at $q_y = -0.43$ and 1.26. The low-lying branch develops a negative eigenfrequency with the magnitude of $\omega = -5.95$ at $q_y = -3.45$, which is responsible for the energetic instability of the condensate [21].

In Fig. 6.15, we present the eigenvectors corresponding to the eigenvalue spectrum given in Fig. 6.14. In the top row, we exhibit the eigenvectors corresponding to Fig. 6.14(a) along the quasi-momentum direction q_x, and in the bottom row corresponding to Fig. 6.14(b) along the quasi-momentum direction q_y. Along q_x, in Fig. 6.15(a i), the eigenvectors of the low-lying and first-excited branches exhibit the spin-like mode and satisfy the criterion given in Eq. 6.15, owing to the presence of the imaginary eigenfrequencies in the eigenspectrum. The low-lying branch exhibits the spin-

like mode for the quasi-momentum range $q_x \in [0.0, 1.87], [2.37, 3.04]$, $[4.27, 4.72]$, and the first-excited branch depicts the spin-like mode $q_x \in [0.56, 0.77], [2.37, 3.04]$. At the point of unstable avoided crossing $q_x \in [2.37, 3.04]$, the eigenvector components are out of phase among themselves as well as with the other involved branch. In Fig. 6.15(a ii), the zeroth component of the low-lying and first-excited branches exhibits the density-like modes independently. Since the eigenspectrum shows the presence of imaginary eigenfrequencies in the second-excited branch as a result of the unstable avoided crossing with the first-excited, we report the eigenvectors of both branches. In Fig. 6.15(a iii), at the point of unstable avoided crossing for quasi-momentum range $q_x \in [0.56, 0.77]$, the eigenvector components exhibit the spin-like mode, due to the presence of the imaginary eigenfrequency in the eigenspectrum, which follows the criterion,

$$\begin{aligned} |u_{+1}|^2_{se} - |u_{-1}|^2_{se} \neq 0, \quad |v_{+1}|^2_{se} - |v_{-1}|^2_{se} \neq 0, \\ |u_{+1}|^2_{fe} - |u_{-1}|^2_{fe} \neq 0, \quad |v_{+1}|^2_{fe} - |v_{-1}|^2_{fe} \neq 0. \end{aligned} \tag{6.16}$$

In Fig. 6.15(a iv), the zeroth component of the low-lying and first-excited branches exhibits the density-like modes independently. Along the q_y direction, in Fig. 6.15(b i), a flip occurs in the eigenvector components at the point of avoided crossings at $q_y = -1.46$ and $q_y = 3.16$ for both low-lying and first-excited branches of the eigenspectrum [152]. However, due to the presence of real eigenfrequencies, the eigenvector components exhibit the density-like mode, following the criterion given in Eq. 6.13. In Fig. 6.15(b ii), the zeroth component of the eigenvector depicts the density-like mode independently. Similar to the q_x direction, here also, we report eigenvectors of the second-excited and first-excited branches separately, owing to the avoided crossing between them. A flip occurs in the eigenvector components at the point of avoided crossing $q_y = -0.43$, and 1.26 [Fig. 6.15(b iii)] for both first-excited and second-excited branches of the eigenspectrum [152]. However, due to the presence of real eigenfrequencies only, the eigenvector components exhibit the density-like mode, following the relation,

$$\begin{aligned} |u_{+1}|^2_{se} - |u_{-1}|^2_{se} = 0, \quad |v_{+1}|^2_{se} - |v_{-1}|^2_{se} = 0, \\ |u_{+1}|^2_{fe} - |u_{-1}|^2_{fe} = 0, \quad |v_{+1}|^2_{fe} - |v_{-1}|^2_{fe} = 0. \end{aligned} \tag{6.17}$$

The zeroth component of the eigenvector depicts the density-like mode independently [Fig. 6.15(b iv)].

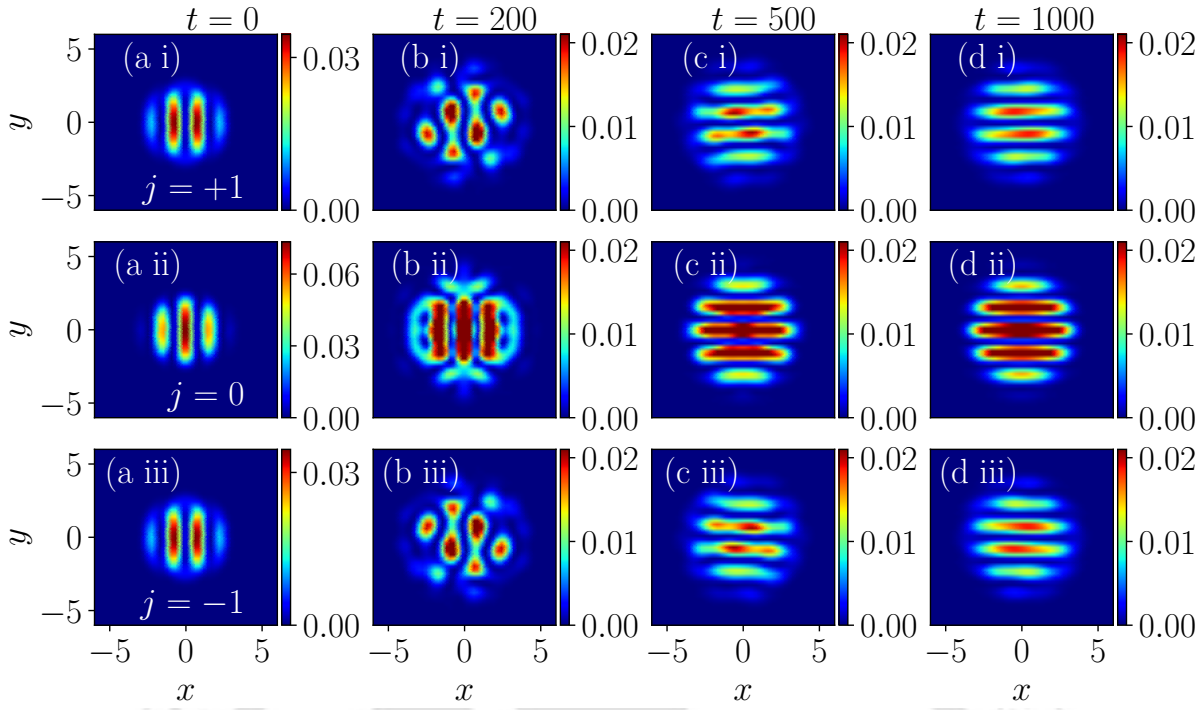


Figure 6.16: Pseudocolor plots of the condensate density for the spin-1 system. Plot of (a) the stationary state density profile exhibiting a superstripe phase and (b–d) density profiles during dynamical evolution at times $t = 200$, 500, and 1000 (in arbitrary units), respectively. In each subfigure, columns (i), (ii), and (iii) correspond to the $m_F = +1$, 0, and -1 spinor components. The system parameters are fixed at $k_L = 2.0$, $\Omega = 0.0$, and interaction strengths $c_0 = 50$, $c_2 = 2.5$.

Numerical Simulation: In this section, we present the numerical simulation generating stationary state density profile and performing quench dynamics of the condensate for coupling strengths $(k_L, \Omega) = (2.0, 0.0)$, with interaction strengths $c_0 = 50$, $c_2 = 2.5$.

In Fig. 6.16(a i-a iii), we show the stationary state density profile, which corresponds to a superstripe phase in a Rashba-type SO coupled condensate. All three spinor components namely $m_F = +1, 0, -1$, participate in this phase. The $m_F = \pm 1$ components exhibit overlapping behaviour, while the $m_F = 0$ fill in the maxima and minima, leading to observed density modulation [78, 70, 100]. To perform the quench dynamics, we quenched the trap strength (λ) to half ($\lambda/2$) of its original value. In Fig. 6.16(b i-b iii), at t = 200 units, modulations appear inside the condensate density, and the profile starts to split into several bright spots. The originally smooth shape is now broken into multiple localized peaks. At $t = 500$ units, the state has reorganized, with an increased number of stripes in the zeroth component of the condensate [Fig. 6.16(c i-c iii)]. At a later time, $t = 1000$ units, in Fig. 6.16(d i-d iii), the state has fully reorganized.

In Fig. 6.17, we report the line plots of the density profiles shown in Fig. 6.16. The top row presents the profile along the spatial x-direction at $y = 0$, while the bottom

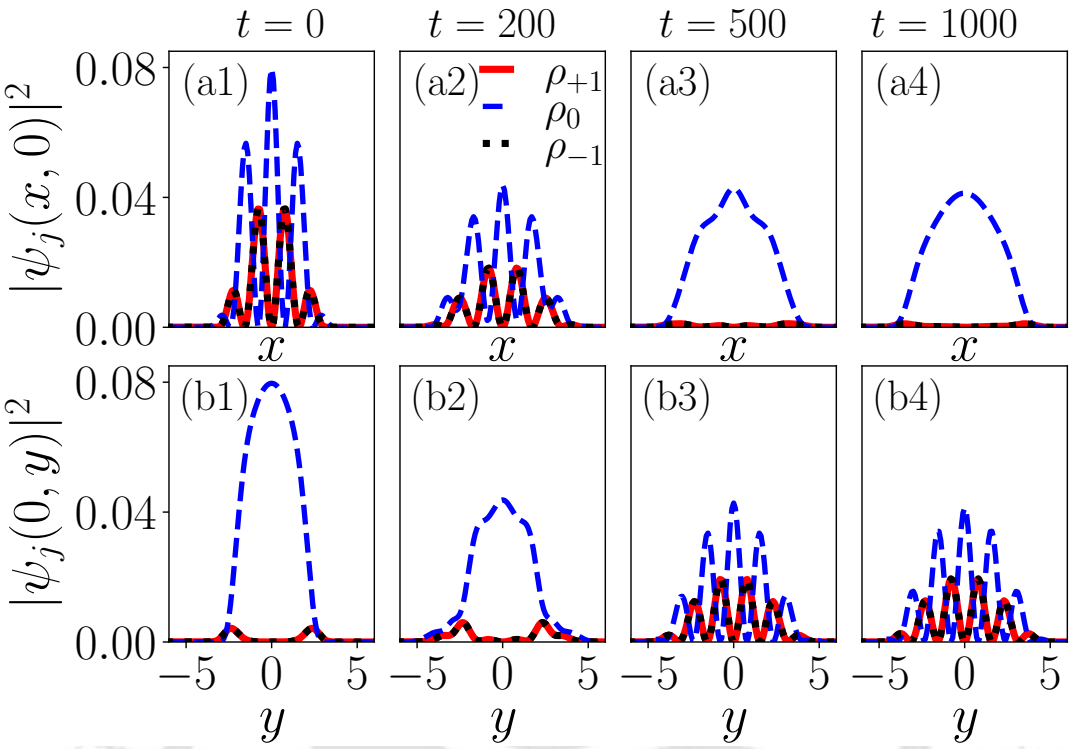


Figure 6.17: (a1, b1) Stationary state density profiles. (a2–a4, b2–b4) Density profiles at evolution times $t = 200$, 500, and 1000 (arb. units). The top row shows the density along the spatial x-direction at $y = 0$, and the bottom row shows the density along the y-direction at $x = 0$. Coupling parameters and interaction strengths are the same as in Fig. 6.16. The solid red line represents $|\psi_{+1}|^2$, the dashed blue line $|\psi_0|^2$, and the dotted black line $|\psi_{-1}|^2$.

row depicts it along the y-direction at $x = 0$. Along the x-direction, Fig. 6.17(a1) shows the ground-state density profile, which corresponds to a superstripe phase with density modulations produced by all three spinor components $m_F = +1, 0, -1$. During the time evolution, the density begins to distort; the superstripe pattern disappears, forming a stripe-like phase by $t = 200$ units [Fig. 6.17(a2)]. At $t = 500$ units, the $m_F = \pm 1$ components vanish, while the $m_F = 0$ component develops a single-peak structure with filament-like shape [Fig. 6.17(a3)]. At a later time, $t = 1000$ units, similar features appear in the density profile, including $m_F = 0$ component with a single-peak structure, but no filament-like structure [Fig. 6.17(a4)]. Along the y-direction, Fig. 6.17(b1) shows the ground-state profile, where the $m_F = 0$ component has a single-peak structure, and the $m_F = \pm 1$ components exhibit two symmetric humps. During the dynamics, at $t = 200$ units, a spatially extended density profile emerges similar to the initial profile; however, the zeroth component develops a filament-like shape [Fig. 6.17(b2)]. The superstripe phase appears in all components, with a higher stripe density than the initial state in the $m_F = 0$ component at $t = 500$ units [Fig. 6.17(b3)]. By $t = 1000$ units,

TH-4102_206121026

the superstripe phase has fully reorganized. These line plots confirm the alteration of the condensate configuration due to the growth of unstable modes.

We also analyze the total energy of the condensate in the antiferromagnetic regime for the interaction strengths $c_0 = 50$, $c_2 = 2.5$. We find that for $k_L = 2.0$ and $\Omega = 0$, during the time evolution, the total energy initially has a value of $E = -0.26$ at $t = 0$ units. It begins to decrease following the abrupt change of the trap strength and reaches $E = -0.60$ at $t = 512.50$ units. Beyond this point, the energy of the condensate gets saturated (not shown here).

6.6.1 Case (ii): $k_L = 4.0, \Omega = 0.0$

In this part, considering interaction strengths $c_0 = 50$, $c_2 = 2.5$ with SO coupling strength $k_L = 4.0$ in the absence of Rabi coupling ($\Omega \sim 0.0$), we present the collective excitations and corresponding post-quench dynamics for the antiferromagnetic regime. To scan the condensate behaviour for the above-mentioned point, we present the collective excitation spectrum and quench dynamics.

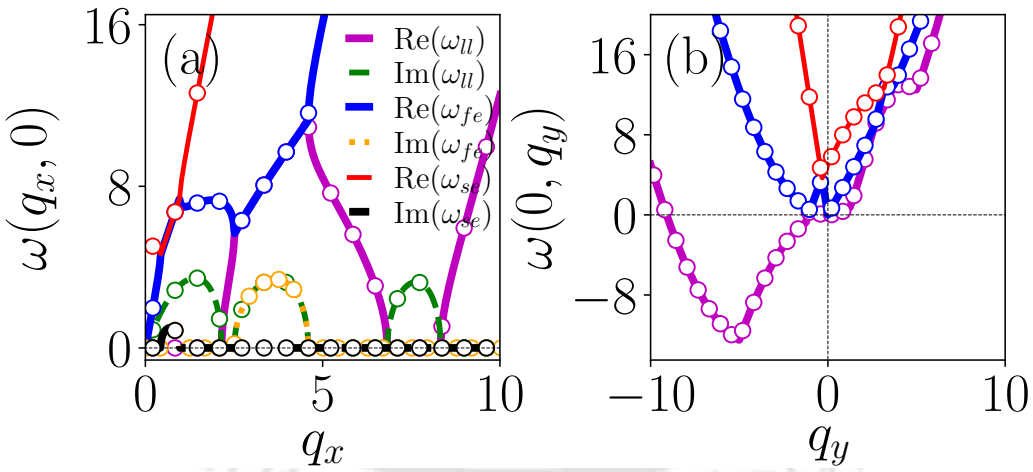


Figure 6.18: Eigenvalue spectrum along the quasi-momentum directions (a) q_x and (b) q_y. The coupling parameters are $k_L = 4.0$ and $\Omega = 0.0$, with interaction strengths $c_0 = 50$ and $c_2 = 2.5$. Line styles and symbols have the same meaning as in Fig. 6.14.

Collective excitations: Fig. 6.18 presents the collective excitation spectrum for SO coupling strength $k_L = 4.0$, in absence of Rabi coupling with interaction strengths $c_0 = 50$, $c_2 = 2.5$ along the quasi-momentum direction q_x, and q_y, separately. Along the quasi-momentum direction q_x, in Fig. 6.18(a), we obtain three instability bands in the low-lying branch with location and amplitude (q_x, ω) = (1.42, 3.44), (3.62, 3.44), and

(7.61, 3.27). The second instability band arises from the overlap with the first-excited branch, exhibiting an unstable avoided crossing. At this point, the first-excited branch also develops an instability band of the same amplitude. In the first-excited branch, the second instability in the first-excited branch arises when it overlaps with the second-excited branch, located at $q_x = 0.68$, with amplitude $\omega = 1.01$. This band is shared by both the first- and second-excited branches and corresponds to the double unstable avoided crossing [90]. This is the only instability band that appears in the second excited branch of the eigenspectrum.

Along quasi-momentum direction q_y, in Fig. 6.18(b), we obtain only real eigenfrequencies in all three branches of the eigenspectrum. However, avoided crossings emerge among low-lying, first-excited, and second-excited branches of the eigenspectrum. The avoided crossings between the low-lying and first-excited branches at $q_y = -1.02, 2.63, 3.77$; between first-excited and second-excited branches at $q_y = -0.33, 3.14$. The low-lying branch develops the negative contribution to the excitation spectrum with amplitude $\omega = -12.54$ at $q_y = -5.05$. This negative excitation leads to energetic instability of the condensate [21].

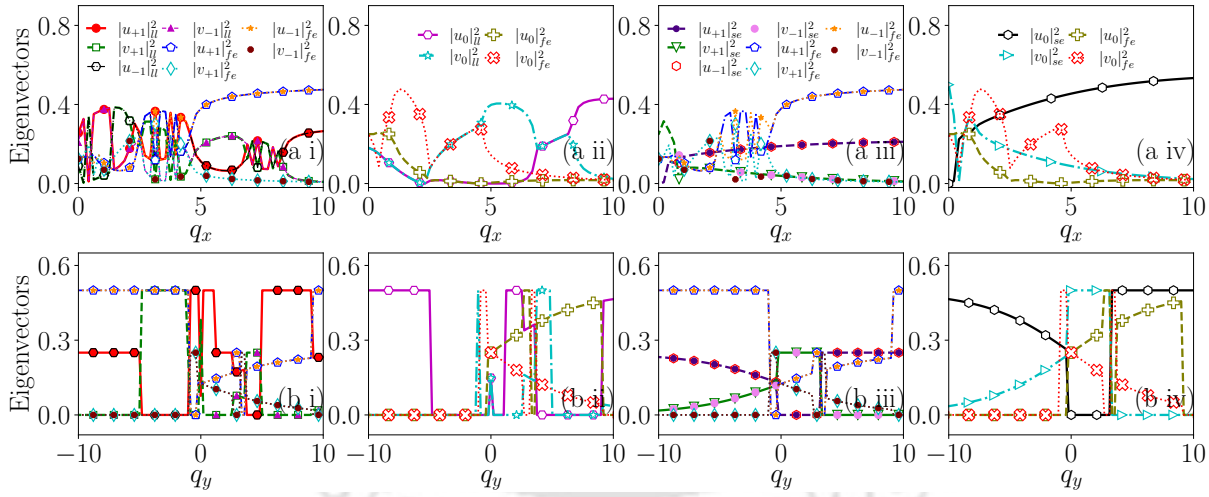


Figure 6.19: Eigenvectors corresponding to Fig. 6.18; (a i-a iv) along the quasi-momentum direction q_x, and (b i-b iv) along the quasi-momentum direction q_y. The lines and symbols have the similar meaning as in Fig. 6.15.

In Fig. 6.19, we present the eigenvectors corresponding to the eigenvalue spectrum given in Fig. 6.18. In the top row, we exhibit the eigenvectors along the quasi-momentum direction q_x, while in the bottom row, along the quasi-momentum direction q_y. Along q_x direction, in Fig. 6.19(a i), we obtain spin-like modes in the low-lying and first-excited branches in eigenvector components following the criterion given in Eq. 6.15. In the low-lying branch, the eigenvectors depict the spinlike mode

TH-4102_206121026

for quasi-momentum range $q_x \in [0, 2.14], [2.5, 4.60], [6.80, 8.33]$. For the first-excited branch, instability emerges at the point of overlap between the low-lying and first-excited branch, which is $q_x \in [2.5, 4.60]$ (second band in low-lying branch). At the point of unstable avoided crossing, the eigenvectors are out of phase with each other as well as with the other branch. The zeroth component of the eigenvectors exhibits the density-like mode independently [Fig. 6.19(a ii)]. Since the first and second excited branches show unstable avoided crossings in the eigenspectrum, we also present the corresponding eigenvectors for these two branches. In Fig. 6.19(a iii), the eigenvector components depict spin-like modes for quasi-momentum range $q_x \in [0.41, 0.98]$ in the first-excited and second-excited branches of the spectrum, following the criterion given in Eq. 6.16. At the point of unstable avoided crossings, the eigenvector components are out of phase within the branch as well as with other branches. The zeroth component of the eigenvectors depicts density-like mode independently [Fig. 6.19(a iv)] [116].

Along the q_y direction, in Fig. 6.19(b i), the eigenvector components of the low-lying and first-excited branches exhibit in-phase behavior (density-like modes), following the criterion given in Eq. 6.13. A flip occurs in the eigenvector components at the point of avoided crossings between the branches, located at $q_y = -1.02, 2.63, 3.77$ [152]. The zeroth component of the eigenvector depicts density-like mode independently [Fig. 6.19(b ii)]. Here, we also obtain the avoided crossings between the first-excited and second-excited branches of the eigenspectrum and report the eigenvectors separately. In Fig. 6.19(b iii), the eigenvector components of the first-excited and second-excited branches exhibit the density-like modes, following the criterion given in Eq. 6.17. A flip appears in the eigenvector components at the point of avoided crossings between the branches at points $q_y = -0.33, 3.14$ [152]. The zeroth component of the eigenvector depicts density-like mode independently [Fig. 6.19(b iv)].

Numerical Simulation: In this part of the study, we perform numerical simulation considering the SO coupling strength $k_L = 4.0$ in the absence of Rabi coupling ($\Omega = 0$) with interaction strengths $c_0 = 50$, $c_2 = 2.5$. Initially, we generate the stationary state density profile, which is the superstripe wave phase [Fig. 6.20(a i-a iii)]. Similar to the previous point regarding antiferromagnetic interactions, this superstripe wave phase also exhibits density modulation combining all three spinor components of the condensate. The $m_F = \pm 1$ components largely overlap, while the $m_F = 0$ component fills in the maxima and minima [78, 100]. To study the dynamics of the condensate, we quench the trap strength to half of its original value, i.e., $\lambda \to \lambda/2$. At t =200 units, small fluctuations start to appear on top of the main density peaks, marking the onset

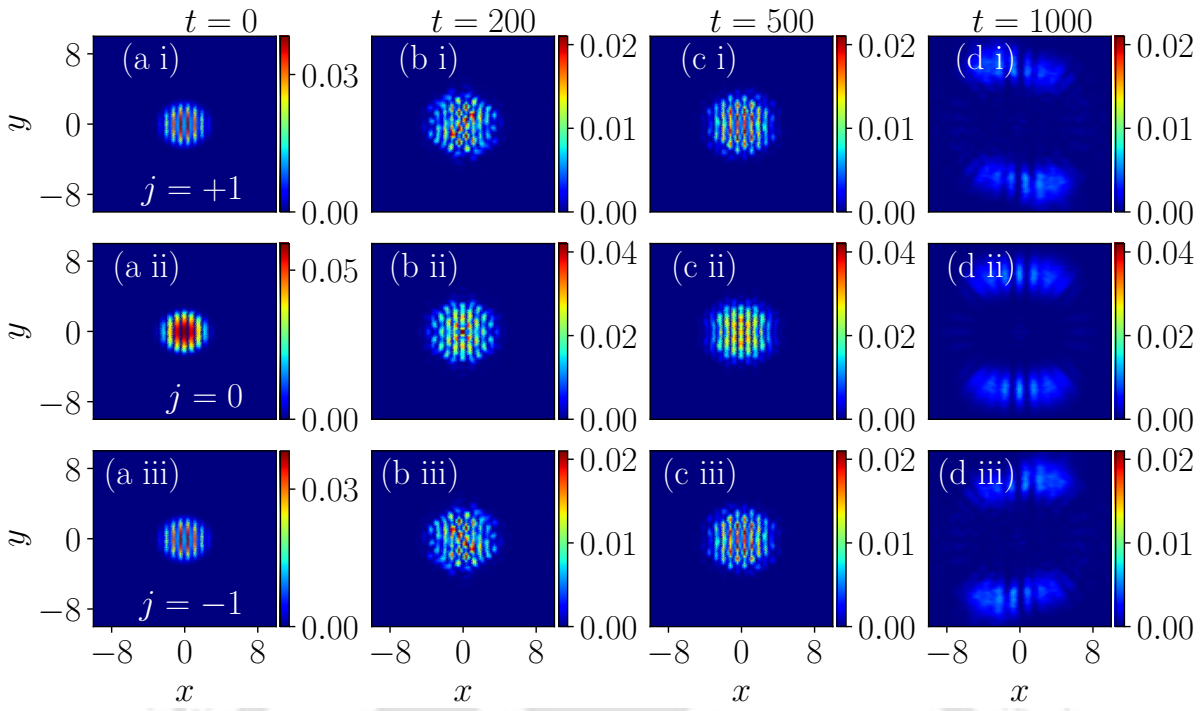


Figure 6.20: Density profiles of a spin-1 condensate. (a) The initial stationary state profile, showing the superstripe phase. (b–d) Dynamical density profiles at evolution times $t = 200$, 500, and 1000 (in simulation units), respectively. For each state (a–d), the three columns (i), (ii), and (iii) correspond to the spinor components $m_F = +1$, 0, and -1. The system parameters are $k_L = 4.0$, $\Omega = 0.0$, $c_0 = 50$, and $c_2 = 2.5$.

of fragmentation [Fig. 6.20(b i-b iii)]. At $t = 500$ units, the density profile loses its clean shape. Fragmentation grows due to the growth of unstable modes in the condensate [Fig. 6.20(c i-c iii)]. At a later time, at $t = 1000$ units, in Fig. 6.20(b i-b iii), the condensate is fully fragmented, leaving only two vertical lobes in the density profile, which reflects the dynamically unstable nature of the condensate [90].

In Fig. 6.21, we depict the line plots of the density profile corresponding to Fig. 6.20. In the top row, we consider the variation along the spatial x-direction keeping $y = 0$, while in the bottom row, we present it along the spatial y-direction keeping $x = 0$. In the top row, in Fig. 6.21(a1), we obtain the density profile with the multi-peak, where $m_F = \pm 1$ components overlap largely, and zeroth components fill in for maxima and minima, producing a density modulation, which corresponds to the superstripe phase. During time evolution at $t = 200$ units, the density profile starts to deform and shrink in spatially [Fig. 6.21(a2)]. Further, it keeps shrinking and fragmented at t= 500 units [Fig. 6.21(a3)]. At a later time $t = 1000$ units in Fig. 6.21(a4), all components of the density profile disappear along the spatial direction x. In the bottom row, in Fig. 6.21(b1), we obtain the stationary state along the spatial y-direction, where the $m_F = 0$ has a sin-

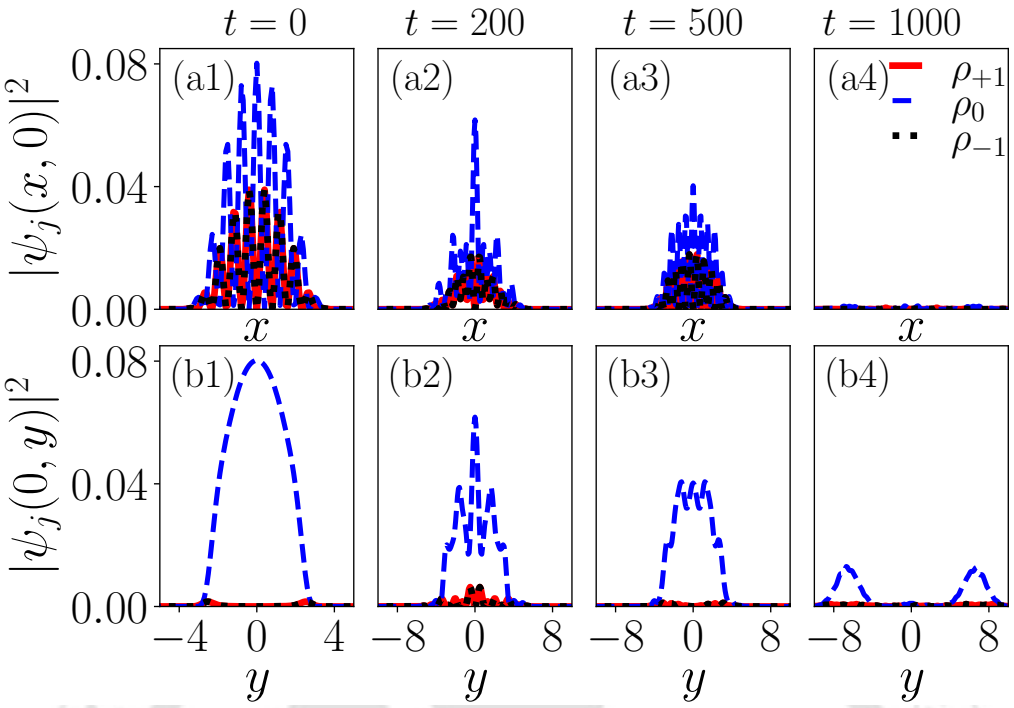


Figure 6.21: (a) shows the ground-state density profile, while (b–d) display the density profiles during time evolution at $t = 200, 500$, and 1000 units, respectively. The top row shows densities along the x-direction at $y = 0$, and the bottom row along the y-direction at $x = 0$. The coupling parameters and interaction strengths are the same as in Fig. 6.20. Line styles indicate the spinor components: solid red for $|\psi_{+1}|^2$, dashed blue for $|\psi_0|^2$, and dotted black for $|\psi_{-1}|^2$.

gle peak density profile, while the $m_F = \pm 1$ depicts the negligible two hump density profile. During the dynamics at $t = 200$ units, deformation begins, and all three components develop the multi-peak density profile [Fig. 6.21(b2)]. Density profile keeps deforming, and the number of peaks reduces at $t = 500$ units [Fig. 6.21(b3)]. At a later time $t = 1000$ units, in Fig. 6.21(b4), the zeroth component develops two hump in the density profile peaks at $y \approx 8$, while $m_F = \pm 1$ vanishes. The evolving behavior of the condensate density profile along spatial directions confirms the dynamically unstable nature of the condensate [90, 180].

The total energy of the condensate with anti-ferromagnetic interactions ($c_0 = 50$, $c_2 = 2.5$) for $k_L = 4.0$, in the absence of Rabi coupling, exhibits a gradual evolution following a quench in the trap strength. Starting from $E = -6.26$ (in non-dimensional units) at $t = 0$, the energy relaxes to a lower value of $E = -6.5$ by $t = 213.50$ (data not shown), reflecting the adjustment of the condensate during its dynamical evolution.

6.7 Summary and Conclusions

In this Chapter, we have presented the collective excitation spectrum and dynamical stability of quasi-two-dimensional Rashba spin-orbit and Rabi-coupled spin-1 Bose-Einstein condensates. Using Bogoliubov-de Gennes analysis complemented by quench dynamics, we systematically analyzed the interplay between spin-orbit coupling and interaction for the ferromagnetic and antiferromagnetic cases.

We first examined the single-particle spectrum and showed that the Rabi coupling opens gaps between the three branches of the excitation spectrum, with the gap magnitude set by Ω between $\omega_{\pm1}$ and ω_0 and 2Ω between ω_- and ω_+. The lowest energy (ω_-) branch undergoes a transition from a single minimum to a double minimum structure when $\Omega < k_L^2$. While this transition generally occurs along the q_x direction, along the q_y direction it requires the simultaneous presence of both spin–orbit and Rabi couplings, highlighting their nontrivial interplay.

For ferromagnetic interactions, the collective excitation spectrum reveals a rich structure in the $k_L - \Omega$ parameter space, which can be classified into three distinct regions characterized by their dynamical and energetic stability. Region I is fully stable and supports well-defined phonon modes with density-like character. Regions II and III exhibit various forms of dynamical instabilities, including single-band and multi-band instabilities, unstable avoided crossings, and maxon–roton features. These instabilities are accompanied by characteristic changes in the eigenvector structure, including density–spin mixing, spin-like modes, and mode flipping at avoided crossings. Notably, Region III differs from Region II by supporting instabilities that coexist with phonon modes in the low-lying and first-excited branches.

We also analyzed the collective excitations and dynamics for antiferromagnetic interactions. In this case, the spectrum exhibits multiple unstable avoided crossings involving low-lying, first-excited, and second-excited branches, leading to both multi-band and single-band instabilities. The corresponding eigenmodes are predominantly spin-like and display characteristic phase reversals at avoided crossings. Dynamically, in the absence of Rabi coupling, the system supports a supersolid-like phase with density modulations arising from all three spin components. With increasing spin–orbit coupling, instabilities strongly modify the density profile, leading to enhanced stripe formation at intermediate coupling strengths and fragmentation into spatially separated lobes at larger coupling.

Taken together, the analysis performed in our work establishes a unified picture of how Rashba spin-orbit coupling, Rabi coupling, and spin-dependent interaction jointly

TH-4102_206121026

shape the excitation spectrum and non-equilibrium dynamics of the spin-1 condensates. Across both the ferromagnetic and antiferromagnetic interactions, dynamical instabilities are shown to be intimately connected to the structure of avoided crossings in the excitation spectrum and to the evolving characteristics of the corresponding eigenmodes. The real-time dynamics consistently indicate these spectral features, with unstable modes seeding the pattern formation, density modulation, and fragmentation on experimentally accessible timescales. In particular, for the antiferromagnetic cases, we have demonstrated how the enhanced instability amplitude and extended unstable momentum ranges can lead to the emergence of a supersolid-like structure.

TH-4102_206121026

Chapter 7

Conclusions and future scope

7.1 Main conclusions of the thesis

This thesis presents a comprehensive analytical and numerical investigation of spin-orbit (SO) coupled spin-1 Bose-Einstein condensates (BECs) under the influence of SO coupling, Rabi coupling, and spin-dependent interactions. Using a combination of mean-field Gross-Pitaevskii simulations, Bogoliubov-de Gennes (BdG) analysis, and quench dynamics, the thesis systematically explores ground-state phases, excitation spectra, and non-equilibrium dynamics in both quasi-one and quasi-two-dimensional geometries. Across four studies presented in this thesis, a unified picture emerges showing how the competition between SO coupling, Rabi coupling, and interaction parameters governs the stability, excitation spectrum, and dynamical evolution of spin-1 condensates.

In **Chapter 3**, we investigated the ground-state phases and quench dynamics of quasi-one-dimensional (quasi-1D) SO coupled spin-1 condensates with ferromagnetic and anti-ferromagnetic interactions. Our numerical calculations revealed a rich phase diagram arising from the interplay among the density-density interaction, the spin-exchange interaction, the SO coupling, and the Rabi coupling. For ferromagnetic interactions at weak Rabi coupling, we identified four distinct phases, namely zero-momentum (ZM), elongated zero-momentum of first type (EZM I), stripe-wave (SW), and superstripe-wave (SSW), while the SSW phase disappeared once the Rabi coupling becomes finite. In contrast, antiferromagnetic interactions supported ZM, elongated zero momentum of second type (EZM II), and SSW phases at vanishing Rabi coupling, which gradually evolved into ZM, EZM I, and SW phases as the Rabi coupling strength increased. A systematic analysis of the interaction parameters demonstrated that the

TH-4102_206121026

ZM phase remains largely insensitive to interaction variations, whereas the SW and SSW phases transition to the EZM phases for strong attractive interaction strengths. The miscibility properties and the root-mean-square size of the condensate further supported the phase classification. Dynamical studies based on sudden quenches of SO and Rabi couplings revealed a variety of nonequilibrium behaviours, including the revival of spin components, breather-like dynamics, and complex domain formation. These results highlighted the dynamical sensitivity of modulated phases and provided experimentally relevant signatures for the creation and control of stripe configurations.

In **Chapter 4**, we studied the collective excitation spectrum of quasi-1D SO coupled spin-1 ferromagnetic BECs with linear Rabi coupling using the BdG theory together with numerical simulations. We first analyzed the single-particle dispersion for different values of the SO coupling (k_L) and the Rabi coupling (Ω). The results show that the Rabi coupling opens the gap between the branches of the dispersion, leading to a separation between the negative (ω_-) and positive (ω_+) branches of the eigenspectrum, with ω_- possessing the lowest minimum. For the parameter regime $\Omega < k_L^2$, the lowest branch develops a double minimum, which signals the emergence of stripe-wave phases. Based on the collective excitation calculations, we divided the $k_L - \Omega$ phase plane into three regions with distinct dynamical characteristics. Region I corresponds to the stable regime where the excitation spectrum exhibits only real eigenfrequencies together with phonon modes, confirming both dynamical and energetic stability. Regions II and III represent the unstable regimes where complex eigenfrequencies appear in the spectrum. Region II is subdivided into two parts. Region IIa, characterized by the emergence of gapped modes and region IIb, characterized by gapless modes (unstable avoided crossings) between the low-lying and first-excited branches. The presence of multiband instabilities led to mixed-spin-density modes in eigenvector components. Owing to imaginary eigenfrequencies, this region exhibited dynamically unstable stripe configuration, resulted in complex pattern formation. Region III, corresponding to the $\Omega \approx 0$ line, exhibits gapless, unstable avoided crossings (UACs) together with phonon modes, and numerical simulations indicate the presence of a superstripe ground-state phase whose dynamics exhibit unstable nonlinear patterns. Overall, this study provides a comprehensive understanding of the stability and instability mechanisms in SO coupled spin-1 ferromagnetic condensates and offers useful guidance for the experimental realization of stable and unstable spinor BEC phases.

In **Chapter 5**, we investigated the stability and excitation spectrum of SO coupled spin-1 BECs with both ferromagnetic and antiferromagnetic interactions using the BdG formalism together with Gross-Pitaevskii simulations. The excitation spectrum re-

TH-4102_206121026

vealed distinct stability regimes governed by the competition between the SO coupling (k_L) and Rabi coupling (Ω). For weak SO coupling ($k_L^2 < \Omega$), the eigenspectrum exhibited real eigenfrequencies with phonon modes, dynamical stable nature of the condensate. In contrast, for strong SO coupling ($k_L^2 > \Omega$), multiband imaginary eigenfrequencies appeared in the excitation spectrum, signaling the onset of dynamical instability. In this regime, UACs between excitation branches played a crucial role in generating I_o-type instabilities, and mixed spin-density modes in eigenvector components. While ferromagnetic interaction primarily exhibited a single UAC, antiferromagnetic condensates displayed double UAC features together with multiband instabilities, leading to fragmentation of the condensate density profile during time evolution. The instability regions were found to be symmetric with respect to SO coupling, while asymmetric for the Rabi coupling. Dynamical evolution of the condensate matches well the BdG calculations: stable breather dynamics were observed in the weak SO coupling regime, the strong SO coupling regime produced a dynamically unstable striped condensate with fragmentation and complex domain formation. These results provide a detailed understanding of the instability mechanisms of the SO coupled spin-1 condensates and highlight the role of interactions in determining their dynamical behaviour.

In **Chapter 6**, we investigated the collective excitation spectrum and dynamical stability of quasi-two-dimensional (quasi-2D) Rashba SO coupled spin-1 BECs using Bogoliubov-de Gennes analysis complemented by quench dynamics. The single-particle dispersion revealed that the Rabi coupling opens gaps among the three branches of the spectrum, while the lowest branch undergoes a transition from a single minimum to the double minimum when $\Omega < k_L^2$, indicating the onset of stripe-like configurations only when $\Omega \approx 0$. For finite Ω, asymmetric behaviour emerges in the spectrum along the q_y, leading to the appearance of a plane wave phase. For ferromagnetic interactions, the collective excitation spectrum in the SO-Rabi plane is classified into three distinct regions based on dynamical and energetic stability. Region I corresponds to the stable regime where the excitation spectrum exhibited real eigenfrequencies with phonon modes. Region II and III represent the dynamically unstable regimes characterized by single and multiband instabilities, unstable avoided crossings, and the emergence of maxon-roton features in the excitation spectrum. These instabilities are accompanied by significant changes in the eigenvector components, including spin-density mixed modes and mode flipping near avoided crossings. For antiferromagnetic interactions, the excitation spectrum exhibited double UACs involving the low-lying, first-excited, and second-excited branches, leading to both single and multiband instabilities with predominantly spinlike modes. Numerical simulations further re-

TH-4102_206121026

vealed that in the absence of Rabi coupling, the condensate supports a supersolid-like ground state with density modulation across all three spin components for antiferromagnetic interactions. Quench dynamics further confirmed these stability properties: the stable regime exhibited no change in the density profile during time evolution, whereas the unstable regimes led to changes in shape, stripe formation, and fragmentation of the density profile.

Overall, the studies presented in this thesis established a unified understanding of ground-state phases, collective excitations, and dynamical instabilities in SO coupled spin-1 Bose-Einstein condensates. The results demonstrate that the interplay among the SO coupling, Rabi coupling, and spin-dependent interactions not only determines exotic ground-state phases, including the stripe-wave phase and the supersolid-like configuration, but also controls instability-driven pattern formation. The combined BdG analysis and real-time simulations provide consistent evidence that the unstable excitation modes play a crucial role in triggering complex domain formation and fragmentation in spinor condensates.

7.2 Future outlook

The results presented in this thesis open several promising directions for further investigation of SO coupled spin-1 Bose-Einstein condensates.

For the quasi-1D configurations studied in this thesis, several extensions can be explored to further understand the interplay among SO coupling, Rabi coupling, and spin-dependent interactions. One natural direction is to investigate additional external parameters that may modify the excitation spectrum and phase stability of the condensate. For instance, anisotropic forms of SO coupling or the presence of long-range dipolar interactions may give rise to new stability mechanisms and emergent quantum phases, including supercurrent-carrying supersolid states [182–184]. Furthermore, recent studies suggest that the quadratic Zeeman interaction can serve as an effective tuning parameter to control the gap between roton-like minima and drive transitions between plane-wave and stripe phases in spin-1 SO-coupled condensates [185]. Exploring the influence of such parameters on the modulational instabilities and collective excitations discussed in this thesis may provide deeper insight into phase engineering and nonlinear dynamics in low-dimensional spinor condensates.

The quasi-2D condensate investigated in this thesis also presents several interesting directions for future study. Extending these analyses to fully two and three-dimensional

TH-4102_206121026

geometries could reveal a richer variety of phenomena such as topological excitations, vortex lattices, and supersolid phases arising from interplay between SO coupling and interatomic interactions [65, 186]. In addition, the dynamical control of SO and Rabi couplings offers a promising route for studying nonequilibrium phenomena in spin-1 condensates. Techniques such as Floquet engineering, where system parameters are periodically modulated in time, can generate effective Hamiltonians with tunable properties and may enable the realization of novel nonequilibrium phases and dynamical phase transitions in SO coupled spinor condensates [187].

Finally, extending the present theoretical framework beyond the zero-temperature mean-field approximation would be important for establishing closer connections with experiments. Effects such as finite temperature fluctuations, higher order interactions including three-body processes, and beyond mean-field corrections may significantly influence the collective excitation spectrum and stability of stripe and supersolid-like phases [169, 185, 188]. Investigating these effects would provide a more comprehensive understanding of the many body physics of SO coupled spin-1 BECs and further strengthen their role as versatile platforms for exploring complex quantum phenomena.



TH-4102_206121026

Appendix A

Appendix related to Chapters 4 and 5

A.1 Relevant terms of the BdG matrix of collective excitations

In this appendix, we provide explicit expressions for the matrix elements of the BdG matrix used in Chapters 4 and 5 of the thesis. In particular, we list the Eq. (4.10) used in Section 4.4 and Eq. (5.6) used in Section 5.3. The explicit expressions of these matrix elements are given below.

$$H_+ = \frac{q_x^2}{2} + c_0(2\phi_{+1}^2 + \phi_0^2 + \phi_{-1}^2) + c_2(2\phi_{+1}^2 + \phi_0^2 - \phi_{-1}^2)\,, \tag{A.1a}$$

$$H_0 = \frac{q_x^2}{2} + c_0(\phi_{+1}^2 + 2\phi_0^2 + \phi_{-1}^2) + c_2(\phi_{+1}^2 + \phi_{-1}^2)\,, \tag{A.1b}$$

$$H_- = \frac{q_x^2}{2} + c_0(\phi_{+1}^2 + \phi_0^2 + 2\phi_{-1}^2) + c_2(2\phi_{-1}^2 + \phi_0^2 - \phi_{+1}^2)\,. \tag{A.1c}$$

$$\mu_+\phi_{+1} = c_0(\phi_{+1}^2 + \phi_0^2 + \phi_{-1}^2)\phi_{+1} + c_2(\phi_{+1}^2 + \phi_0^2 - \phi_{-1}^2)\phi_{+1} + c_2\phi_0^2\phi_{-1}^* + \frac{\Omega}{\sqrt{2}}\phi_0\,, \tag{A.1d}$$

$$\mu_0\phi_0 = c_0(\phi_{+1}^2 + \phi_0^2 + \phi_{-1}^2)\phi_0 + c_2(\phi_{+1}^2 + \phi_{-1}^2)\phi_0 + 2c_2\phi_0^*\phi_{+1}\phi_{-1} + \frac{\Omega}{\sqrt{2}}(\phi_{+1} + \phi_{-1})\,, \tag{A.1e}$$

$$\mu_-\phi_{-1} = c_0(\phi_{+1}^2 + \phi_0^2 + \phi_{-1}^2)\phi_{-1} + c_2(\phi_{-1}^2 + \phi_0^2 - \phi_{+1}^2)\phi_{-1} + c_2\phi_0^2\phi_{+1}^* + \frac{\Omega}{\sqrt{2}}\phi_0\,, \tag{A.1f}$$

TH-4102_206121026

where,

$$\mu_{+1} = \mu_0 = \mu_{-1} \equiv \mu \, .$$

$$\mathcal{L}_{12} = C^{+}\phi_{+1}^{2};\ \ \mathcal{L}_{13} = C^{+}\phi_0^{*}\phi_{+1} - \frac{k_L}{\sqrt{2}} i q_x + 2c_2\phi_0\phi_{-1}^{*} + \frac{\Omega}{\sqrt{2}};\ \ \mathcal{L}_{14} = C^{+}\phi_0\phi_{+1};$$

$$\mathcal{L}_{15} = C^{-}\phi_{-1}^{*}\phi_{+1}\ \ \mathcal{L}_{16} = C^{-}\phi_{-1}\phi_{+1} + c_2\phi_0^{2};\ \ \mathcal{L}_{21} = -C^{+}\phi_{+1}^{*2};\ \ \mathcal{L}_{23} = -C^{+}\phi_0^{*}\phi_{+1}^{*};$$

$$\mathcal{L}_{24} = -C^{+}\phi_0\phi_{+1}^{*} + \frac{k_L}{\sqrt{2}} i q_x - 2c_2\phi_0^{*}\phi_{-1} - \frac{\Omega}{\sqrt{2}};\ \ \mathcal{L}_{25} = -C^{-}\phi_{-1}^{*}\phi_{+1}^{*} - c_2\phi_0^{*2};$$

$$\mathcal{L}_{26} = -C^{-}\phi_{-1}\phi_{+1}^{*};\ \ \mathcal{L}_{31} = C^{+}\phi_{+1}^{*}\phi_0 + 2c_2\phi_0^{*}\phi_{-1} + \frac{k_L}{\sqrt{2}} i q_x + \frac{\Omega}{\sqrt{2}};\ \ \mathcal{L}_{32} = C^{+}\phi_{+1}\phi_0;$$

$$\mathcal{L}_{34} = c_0\phi_0^{2} + 2c_2\phi_{+1}\phi_{-1};\ \ \mathcal{L}_{35} = C^{+}\phi_{-1}^{*}\phi_0 + 2c_2\phi_0^{*}\phi_{+1} - \frac{k_L}{\sqrt{2}} i q_x + \frac{\Omega}{\sqrt{2}};\ \ \mathcal{L}_{36} = C^{+}\phi_{-1}\phi_0;$$

$$\mathcal{L}_{41} = -C^{+}\phi_{+1}^{*}\phi_0^{*};\ \ \mathcal{L}_{42} = -C^{+}\phi_{+1}\phi_0^{*} - \frac{k_L}{\sqrt{2}} i q_x - 2c_2\phi_0\phi_{-1}^{*} - \frac{\Omega}{\sqrt{2}};\ \ \mathcal{L}_{43} = -c_0\phi_0^{*2} - 2c_2\phi_{+1}^{*}\phi_{-1}^{*};$$

$$\mathcal{L}_{45} = -C^{+}\phi_{-1}^{*}\phi_0^{*};\ \ \mathcal{L}_{46} = -C^{+}\phi_{-1}\phi_0^{*} + \frac{k_L}{\sqrt{2}} i q_x - 2c_2\phi_0\phi_{+1}^{*} - \frac{\Omega}{\sqrt{2}};\ \ \mathcal{L}_{51} = C^{-}\phi_{+1}^{*}\phi_{-1};$$

$$\mathcal{L}_{52} = C^{-}\phi_{+1}\phi_{-1} + c_2\phi_0^{2};\ \ \mathcal{L}_{53} = C^{+}\phi_0^{*}\phi_{-1} + \frac{k_L}{\sqrt{2}} i q_x + 2c_2\phi_0\phi_{+1}^{*} + \frac{\Omega}{\sqrt{2}};\ \ \mathcal{L}_{54} = C^{+}\phi_0\phi_{-1};$$

$$\mathcal{L}_{56} = C^{+}\phi_{-1}^{2};\ \ \mathcal{L}_{61} = -C^{-}\phi_{+1}^{*}\phi_{-1}^{*} - c_2\phi_0^{*2}; \mathcal{L}_{62} = -C^{-}\phi_{+1}\phi_{-1}^{*};\ \ \mathcal{L}_{63} = -C^{+}\phi_0^{*}\phi_{-1}^{*};$$

$$\mathcal{L}_{64} = -C^{+}\phi_0\phi_{-1}^{*} - \frac{k_L}{\sqrt{2}} i q_x - 2c_2\phi_0^{*}\phi_{+1} - \frac{\Omega}{\sqrt{2}};\ \ \mathcal{L}_{65} = -C^{+}\phi_{-1}^{*2}.$$

Also,

$$C^{+} \equiv c_0 + c_2,\ C^{-} \equiv c_0 - c_2 \, .$$

The coefficients for the BdG characteristic equations, Eq. (4.12) in Chapter 4 and

TH-4102_206121026

Eq.(5.8) in Chapter 5, are given as follows:

$$b = -5\Omega^2 - 4c_2^2 - (2k_L^2 + 3\Omega + c_0)q_x^2 - \frac{3}{4}q_x^4 + c_2(8\Omega + q_x^2), \tag{A.2}$$

$$\begin{aligned} c =& 4\Omega^4 + \Omega\left[(2\Omega(k_L^2 + 3\Omega) - (k_L^2 - 5\Omega)c_0\right]q_x^2 + 4c_2^3 q_x^2 \\ &+ \frac{1}{2}\left[2k_L^4 + 9\Omega^2 + (k_L^2 + 6\Omega)c_0\right]q_x^4 + \frac{1}{2}(3\Omega + c_0)q_x^6 + \frac{3}{16}q_x^8 + 4c_2^2\left[\Omega^2 + (k_L^2 - \Omega + c_0)q_x^2\right] \\ &- \frac{1}{2}c_2\left[16\Omega^3 + 2\Omega(7k_L^2 + 5\Omega + 8c_0)q_x^2 + (k_L^2 + 6\Omega + 4c_0)q_x^4 + q_x^6\right], \end{aligned} \tag{A.3}$$

$$\begin{aligned} d =& -\frac{1}{64}q_x^2\left[(4k_L^2 - 4\Omega - q_x^2)(2\Omega + q_x^2) + c_2(-8k_L^2 + 8\Omega + 4q_x^2)\right]\Bigg[-4c_0\Big(8\Omega^2 - 2(k_L^2 - 3\Omega)q_x^2 \\ &+ q_x^4 - 4c_2(2\Omega + q_x^2)\Big) + (2\Omega + q_x^2)\Big(-16\Omega c_2 + 16c_2^2 - q_x^2(-4k_L^2 + 4\Omega + q_x^2)\Big)\Bigg]. \end{aligned} \tag{A.4}$$

TH-4102_206121026

Appendix B

Appendix related to Chapter 6

B.1 Relevant terms of the BdG matrix of collective excitations

In this appendix, we provide an explicit form of the matrix elements of the BdG matrix Eq. (6.9) used in Chapter 6, Section 6.4.

The matrix elements of Eq. (6.9) read as

$$H_+ = \frac{q_x^2+q_y^2}{2} + c_0(2\phi_{+1}^2+\phi_0^2+\phi_{-1}^2) + c_2(2\phi_{+1}^2+\phi_0^2-\phi_{-1}^2)\,, \tag{B.1a}$$

$$H_0 = \frac{q_x^2+q_y^2}{2} + c_0(\phi_{+1}^2+2\phi_0^2+\phi_{-1}^2) + c_2(\phi_{+1}^2+\phi_{-1}^2)\,, \tag{B.1b}$$

$$H_- = \frac{q_x^2+q_y^2}{2} + c_0(\phi_{+1}^2+\phi_0^2+2\phi_{-1}^2) + c_2(2\phi_{-1}^2+\phi_0^2-\phi_{+1}^2)\,. \tag{B.1c}$$

$$\mu_+\phi_{+1} = c_0(\phi_{+1}^2+\phi_0^2+\phi_{-1}^2)\phi_{+1} + c_2(\phi_{+1}^2+\phi_0^2-\phi_{-1}^2)\phi_{+1} + c_2\phi_0^2\phi_{-1}^* + \frac{\Omega}{\sqrt{2}}\phi_0\,, \tag{B.1d}$$

$$\mu_0\phi_0 = c_0(\phi_{+1}^2+\phi_0^2+\phi_{-1}^2)\phi_0 + c_2(\phi_{+1}^2+\phi_{-1}^2)\phi_0 + 2c_2\phi_0^*\phi_{+1}\phi_{-1} + \frac{\Omega}{\sqrt{2}}(\phi_{+1}+\phi_{-1})\,, \tag{B.1e}$$

$$\mu_-\phi_{-1} = c_0(\phi_{+1}^2+\phi_0^2+\phi_{-1}^2)\phi_{-1} + c_2(\phi_{-1}^2+\phi_0^2-\phi_{+1}^2)\phi_{-1} + c_2\phi_0^2\phi_{+1}^* + \frac{\Omega}{\sqrt{2}}\phi_0\,, \tag{B.1f}$$

where,

$$\mu_{+1} = \mu_0 = \mu_{-1} \equiv \mu\,.$$

TH-4102_206121026

$$\mathcal{L}_{12} = C^{+}\phi_{+1}^{2};\ \ \mathcal{L}_{13} = C^{+}\phi_{0}^{*}\phi_{+1} + \frac{k_L}{\sqrt{2}}(iq_x + q_y) + 2c_2\phi_0\phi_{-1}^{*} + \frac{\Omega}{\sqrt{2}};\ \ \mathcal{L}_{14} = C^{+}\phi_0\phi_{+1};$$
$$\mathcal{L}_{15} = C^{-}\phi_{-1}^{*}\phi_{+1};\ \ \mathcal{L}_{16} = C^{-}\phi_{-1}\phi_{+1} + c_2\phi_0^2;\ \ \mathcal{L}_{21} = -C^{+}\phi_{+1}^{*2};\ \ \mathcal{L}_{23} = -C^{+}\phi_0^{*}\phi_{+1}^{*};$$
$$\mathcal{L}_{24} = -C^{+}\phi_0\phi_{+1}^{*} + \frac{k_L}{\sqrt{2}}(-iq_x + q_y) - 2c_2\phi_0^{*}\phi_{-1} - \frac{\Omega}{\sqrt{2}};\ \ \mathcal{L}_{25} = -C^{-}\phi_{-1}^{*}\phi_{+1}^{*} - c_2\phi_0^{*2};$$
$$\mathcal{L}_{26} = -C^{-}\phi_{-1}\phi_{+1}^{*};\ \ \mathcal{L}_{31} = C^{+}\phi_{+1}^{*}\phi_0 + 2c_2\phi_0^{*}\phi_{-1} + \frac{k_L}{\sqrt{2}}(-iq_x + q_y) + \frac{\Omega}{\sqrt{2}};\ \ \mathcal{L}_{32} = C^{+}\phi_{+1}\phi_0;$$
$$\mathcal{L}_{34} = c_0\phi_0^2 + 2c_2\phi_{+1}\phi_{-1};\ \ \mathcal{L}_{35} = C^{+}\phi_{-1}^{*}\phi_0 + 2c_2\phi_0^{*}\phi_{+1} + \frac{k_L}{\sqrt{2}}(iq_x + q_y) + \frac{\Omega}{\sqrt{2}};\ \ \mathcal{L}_{36} = C^{+}\phi_{-1}\phi_0;$$
$$\mathcal{L}_{41} = -C^{+}\phi_{+1}^{*}\phi_0^{*};\ \ \mathcal{L}_{42} = -C^{+}\phi_{+1}\phi_0^{*} + \frac{k_L}{\sqrt{2}}(iq_x + q_y) - 2c_2\phi_0\phi_{-1}^{*} - \frac{\Omega}{\sqrt{2}};$$
$$\mathcal{L}_{43} = -c_0\phi_0^{*2} - 2c_2\phi_{+1}^{*}\phi_{-1}^{*};\ \ \mathcal{L}_{45} = -C^{+}\phi_{-1}^{*}\phi_0^{*};$$
$$\mathcal{L}_{46} = -C^{+}\phi_{-1}\phi_0^{*} + \frac{k_L}{\sqrt{2}}(-iq_x + q_y) - 2c_2\phi_0\phi_{+1}^{*} - \frac{\Omega}{\sqrt{2}};\ \ \mathcal{L}_{51} = C^{-}\phi_{+1}^{*}\phi_{-1};$$
$$\mathcal{L}_{52} = C^{-}\phi_{+1}\phi_{-1} + c_2\phi_0^2;\ \ \mathcal{L}_{53} = C^{+}\phi_0^{*}\phi_{-1} + \frac{k_L}{\sqrt{2}}(-iq_x + q_y) + 2c_2\phi_0\phi_{+1}^{*} + \frac{\Omega}{\sqrt{2}};$$
$$\mathcal{L}_{54} = C^{+}\phi_0\phi_{-1};\ \ \mathcal{L}_{56} = C^{+}\phi_{-1}^{2};\ \ \mathcal{L}_{61} = -C^{-}\phi_{+1}^{*}\phi_{-1}^{*} - c_2\phi_0^{*2};$$
$$\mathcal{L}_{62} = -C^{-}\phi_{+1}\phi_{-1}^{*};\ \ \mathcal{L}_{63} = -C^{+}\phi_0^{*}\phi_{-1}^{*};\ \ \mathcal{L}_{64} = -C^{+}\phi_0\phi_{-1}^{*} + \frac{k_L}{\sqrt{2}}(iq_x + q_y) - 2c_2\phi_0^{*}\phi_{+1} - \frac{\Omega}{\sqrt{2}};$$
$$\mathcal{L}_{65} = -C^{+}\phi_{-1}^{*2}.$$

Also,

$$C^{+} \equiv c_0 + c_2,\ C^{-} \equiv c_0 - c_2\ .$$

The coefficients for the BdG characteristic equation (6.11) are given as follows:

$$b = 0, \tag{B.2}$$
$$c = \frac{1}{16}\Big(-4(q_x^2+q_y^2)(3(q_x^2+q_y^2)+8k_L^2) - 48(q_x^2+q_y^2)\Omega - 80\Omega^2 + 4c_0^2 + 4c_2(q_x^2+q_y^2+26\Omega)$$
$$- 61c_2^2 - 8c_0(q_x^2+q_y^2-2\Omega+c_2)\Big)\ , \tag{B.3}$$
$$d = \frac{1}{2}k_L q_y\Big(-8\Omega(q_x^2+q_y^2+2\Omega) - 2c_0^2 + c_0(4(q_x^2+q_y^2+\Omega)-3c_2) + (12(q_x^2+q_y^2)+26\Omega-7c_2)c_2\Big)\ , \tag{B.4}$$

TH-4102_206121026

$$
\begin{aligned}
e =& \frac{1}{32}\Big(2(3(q_x^2+q_y^2)^4+16(q_x^2+q_y^2)^2k_L^4+24(q_x^2+q_y^2)^3\Omega+8(9(q_x^2+q_y^2)^2\\
&-4(q_y-q_x)(q_y+q_x)k_L^2)\Omega^2+96(q_x^2+q_y^2)\Omega^3+64\Omega^4)+4c_0^3(q_x^2+q_y^2+2\Omega-2c_2)\\
&-4((q_x^2+q_y^2)^3-2(q_y^2-5q_x^2)(q_x^2+q_y^2)k_L^2+6(q_x^2+q_y^2)^2\Omega+4(-13q_y^2+17q_x^2)k_L^2\Omega\\
&+10(q_x^2+q_y^2)\Omega^2+52\Omega^2)c_2-(15q_y^4+15q_x^4-236\Omega^2+4q_x^2(-32k_L^2+29\Omega)\\
&+2q_y^2(15q_x^2+52k_L^2+58\Omega))c_2^2+(71(q_x^2+q_y^2)-210\Omega)c_2^3+96c_2^4\\
&-4c_0^2(3q_y^4+(q_x^2+4\Omega)(3q_x^2+4\Omega)+2q_y^2(3q_x^2-2k_L^2+8\Omega)+2c_2(-6(q_x^2+q_y^2+2\Omega)+5c_2))\\
&+c_0(8((q_x^2+q_y^2)^3-2(q_y^2-2q_x^2)(q_x^2+q_y^2)k_L^2+2(3(q_x^2+q_y^2)^2+2q_y^2k_L^2)\Omega\\
&+10(q_x^2+q_y^2)\Omega^2-4\Omega^3)+c_2(-4(9q_y^4+9q_x^4+42q_x^2\Omega-6\Omega^2+2q_y^2(9q_x^2+5k_L^2+21\Omega))\\
&+c_2(85(q_x^2+q_y^2)-22\Omega+14c_2)))\Big), \qquad \text{(B.5)}
\end{aligned}
$$

$$
\begin{aligned}
f =& \frac{1}{8}q_yk_L\Big(8\Omega(q_x^2+q_y^2+2\Omega)^3+2(q_x^2+q_y^2+2\Omega)^2c_0^2-2(6(q_x^2+q_y^2)^3+(37(q_x^2+q_y^2)^2\\
&+8q_x^2k_L^2)\Omega+76(q_x^2+q_y^2)\Omega^2+52\Omega^3)c_2+(7q_y^4+7q_x^4+28\Omega^2+14q_y^2(q_x^2+2\Omega)\\
&+4q_x^2(8k_L^2+7\Omega))c_2^2-c_0(4((q_x^2+q_y^2)^3+(5(q_x^2+q_y^2)^2-4q_x^2k_L^2)\Omega\\
&+8(q_x^2+q_y^2)\Omega^2+4\Omega^2)-3(q_y^2+q_x^2+2\Omega)^2c_2)\Big), \qquad \text{(B.6)}
\end{aligned}
$$

TH-4102_206121026

$$
\begin{aligned}
g =& \frac{1}{256}\Big(-8(q_x^2+q_y^2+2\Omega)^2 c_0^3 (q_x^2+q_y^2+2\Omega-2c_2) \\
&+4(q_x^2+q_y^2+2\Omega)c_0^2((q_x^2+q_y^2+2\Omega)(5q_x^4+5q_y^4+28\Omega^2+4q_x^2(-4k_L^2+7\Omega) \\
&+2q_y^2(5q_x^2-4k_L^2+14\Omega))-8(3q_y^4+3q_x^4-4q_x^2(k_L^2-3\Omega)+12\Omega^2+6q_y^2(q_x^2+2\Omega))c_2 \\
&+20(q_x^2+q_y^2+2\Omega)c_2^2)-2c_0(4(q_x^2+q_y^2+2\Omega)((q_x^2+q_y^2)(q_y^2+q_x(q_x-2k_L)) \\
&\times(q_x^2+q_y^2-4k_L^2)(q_y^2+q_x(q_x+2k_L))+12(q_x^2+q_y^2)(q_y^2+q_x(q_x-2k_L)) \\
&\times(q_y^2+q_x(q_x+2k_L))\Omega+4(11(q_x^2+q_y^2)^2+4(q_y^2-3q_x^2)k_L^2)\Omega^2+48(q_x^2+q_y^2)\Omega^3) \\
&+c_2(8(-5(q_x^2+q_y^2)^4-(5q_y^2-22q_x^2)(q_x^2+q_y^2)^2k_L^2-16q_x^4k_L^4-(q_x^2+q_y^2)(43(q_x^2+q_y^2)^2 \\
&+4(5q_y^2-22q_x^2)k_L^2)\Omega-(111(q_x^2+q_y^2)^2+4(5q_y^2-22q_x^2)k_L^2)\Omega^2-88(q_x^2+q_y^2)\Omega^3+4\Omega^4) \\
&+(q_x^2+q_y^2+2\Omega)c_2(85(q_x^2+q_y^2)^2-160q_x^2k_L^2+148(q_x^2+q_y^2)\Omega-44\Omega^2 \\
&+14(q_x^2+q_y^2+2\Omega)c_2)))+(q_x^2+q_y^2+2\Omega)(-4(q_x^2+q_y^2+2\Omega)((q_x^2+q_y^2)(q_x^2+q_y^2-4k_L^2) \\
&+4(q_x^2+q_y^2-2q_yk_L)\Omega)((q_x^2+q_y^2)(q_x^2+q_y^2-4k_L^2)+4(q_x^2+q_y^2-2q_yk_L)\Omega) \\
&+c_2(4(q_x^2+q_y^2)(q_x^2+q_y^2-4k_L^2)((q_x^2+q_y^2)^2-8q_x^2k_L^2)-64(q_x^2+q_y^2)((q_x^2+q_y^2)^2 \\
&+(7q_y^2-3q_x^2)k_L^2)\Omega-16(31(q_x^2+q_y^2)^2+4(13q_y^2-11q_x^2)k_L^2)\Omega^2-704(q_x^2+q_y^2)\Omega^3 \\
&+c_2(91(q_x^2+q_y^2)^3+16(13q_y^2-22q_x^2)(q_x^2+q_y^2)k_L^2 \\
&+658(q_x^2+q_y^2)^2\Omega+32(13q_y^2-38q_x^2)k_L^2\Omega+724(q_x^2+q_y^2)\Omega^2-456\Omega^3 \\
&+2c_2(-71q_y^4-142q_y^2q_x^2-71q_x^4+256q_x^2k_L^2+68(q_x^2+q_y^2)\Omega+420\Omega^2 \\
&-96(q_x^2+q_y^2+2\Omega)c_2))))\Big)\,. \qquad \text{(B.7)}
\end{aligned}
$$

TH-4102_206121026

Bibliography

[1] M. Z. Hasan and C. L. Kane, "Colloquium: Topological insulators," *Rev. Mod. Phys.*, vol. 82, pp. 3045–3067, Nov 2010.

[2] T. Jungwirth, J. Wunderlich, and K. Olejník, "Spin Hall effect devices," *Nat. Mat.*, vol. 11, no. 5, pp. 382–390, 2012.

[3] I. Žutić, J. Fabian, and S. Das Sarma, "Spintronics: Fundamentals and applications," *Rev. Mod. Phys.*, vol. 76, pp. 323–410, Apr 2004.

[4] Y.-J. Lin, K. Jiménez-García, and I. B. Spielman, "Spin–orbit-coupled Bose–Einstein condensates," *Nature (London)*, vol. 471, no. 7336, pp. 83–86, 2011.

[5] Y. A. Bychkov and E. I. Rashba, "Oscillatory effects and the magnetic susceptibility of carriers in inversion layers," *J. Phys. C Solid State Phys.*, vol. 17, pp. 6039–6045, Nov. 1984.

[6] G. Dresselhaus, "Spin-orbit coupling effects in zinc blende structures," *Phys. Rev.*, vol. 100, pp. 580–586, Oct 1955.

[7] J. Ruseckas, G. Juzeliūnas, P. Öhberg, and M. Fleischhauer, "Non-abelian gauge potentials for ultracold atoms with degenerate dark states," *Phys. Rev. Lett.*, vol. 95, p. 010404, Jun 2005.

[8] S.-L. Zhu, H. Fu, C.-J. Wu, S.-C. Zhang, and L.-M. Duan, "Spin Hall effects for cold atoms in a light-induced gauge potential," *Phys. Rev. Lett.*, vol. 97, p. 240401, Dec 2006.

[9] X.-J. Liu, X. Liu, L. C. Kwek, and C. H. Oh, "Optically induced spin-Hall effect in atoms," *Phys. Rev. Lett.*, vol. 98, p. 026602, Jan 2007.

TH-4102_206121026

[10] D. Campbell, R. Price, A. Putra, A. Valdés-Curiel, D. Trypogeorgos, and I. Spielman, "Magnetic phases of spin-1 spin–orbit-coupled Bose gases," *Nat. Commun.*, vol. 7, no. 1, p. 10897, 2016.

[11] X. Luo, L. Wu, J. Chen, Q. Guan, K. Gao, Z.-F. Xu, L. You, and R. Wang, "Tunable atomic spin-orbit coupling synthesized with a modulating gradient magnetic field," *Scient. Rep.*, vol. 6, no. 1, p. 18983, 2016.

[12] L. Landau, "Theory of the superfluidity of Helium II," *Phys. Rev.*, vol. 60, pp. 356–358, Aug 1941.

[13] N. Bogoliubov, "On the theory of superfluidity," *J. Phys*, vol. 11, no. 1, p. 23, 1947.

[14] M. H. Anderson, J. R. Ensher, M. R. Matthews, C. E. Wieman, and E. A. Cornell, "Observation of Bose-Einstein condensation in a dilute atomic vapor," *Science*, vol. 269, no. 5221, pp. 198–201, 1995.

[15] K. B. Davis, M.-O. Mewes, M. R. Andrews, N. J. van Druten, D. S. Durfee, D. Kurn, and W. Ketterle, "Bose-Einstein condensation in a gas of sodium atoms," *Phys. Rev. Lett.*, vol. 75, no. 22, p. 3969, 1995.

[16] D. S. Jin, J. R. Ensher, M. R. Matthews, C. E. Wieman, and E. A. Cornell, "Collective excitations of a Bose-Einstein condensate in a dilute gas," *Phys. Rev. Lett.*, vol. 77, pp. 420–423, Jul 1996.

[17] M.-O. Mewes, M. R. Andrews, N. J. van Druten, D. M. Kurn, D. S. Durfee, C. G. Townsend, and W. Ketterle, "Collective excitations of a Bose-Einstein condensate in a magnetic trap," *Phys. Rev. Lett.*, vol. 77, pp. 988–991, Aug 1996.

[18] D. M. Stamper-Kurn, A. P. Chikkatur, A. Görlitz, S. Inouye, S. Gupta, D. E. Pritchard, and W. Ketterle, "Excitation of phonons in a Bose-Einstein condensate by Light scattering," *Phys. Rev. Lett.*, vol. 83, pp. 2876–2879, Oct 1999.

[19] J. Stenger, S. Inouye, A. P. Chikkatur, D. M. Stamper-Kurn, D. E. Pritchard, and W. Ketterle, "Bragg spectroscopy of a Bose-Einstein condensate," *Phys. Rev. Lett.*, vol. 82, pp. 4569–4573, Jun 1999.

[20] E. V. Goldstein and P. Meystre, "Quasiparticle instabilities in multicomponent atomic condensates," *Phys. Rev. A*, vol. 55, no. 4, p. 2935, 1997.

TH-4102_206121026

[21] T. Ozawa, L. P. Pitaevskii, and S. Stringari, "Supercurrent and dynamical instability of spin-orbit-coupled ultracold Bose gases," *Phys. Rev. A*, vol. 87, p. 063610, Jun 2013.

[22] M. A. Khamehchi, Y. Zhang, C. Hamner, T. Busch, and P. Engels, "Measurement of collective excitations in a spin-orbit-coupled Bose-Einstein condensate," *Phys. Rev. A*, vol. 90, p. 063624, Dec 2014.

[23] Z.-Q. Yu, "Phase transitions and elementary excitations in spin-1 Bose gases with Raman-induced spin-orbit coupling," *Phys. Rev. A*, vol. 93, p. 033648, Mar 2016.

[24] K. Sun, C. Qu, Y. Xu, Y. Zhang, and C. Zhang, "Interacting spin-orbit-coupled spin-1 Bose-Einstein condensates," *Phys. Rev. A*, vol. 93, p. 023615, Feb 2016.

[25] Y. Chen, H. Lyu, Y. Xu, and Y. Zhang, "Elementary excitations in a spin–orbit-coupled spin-1 Bose–Einstein condensate," *New J. Phys.*, vol. 24, no. 7, p. 073041, 2022.

[26] B. M. Caradoc-Davies, "Vortex dynamics in Bose-Einstein condensates," *Doctor of Philosophy*, 2000.

[27] C. J. Pethick and H. Smith, *Bose–Einstein Condensation in dilute gases*. Cambridge: Cambridge University Press, 2 ed., 2008.

[28] R. Corgier, "Engineered atomic states for precision interferometry," 2019.

[29] C. J. Myatt, E. A. Burt, R. W. Ghrist, E. A. Cornell, and C. E. Wieman, "Production of two overlapping Bose-Einstein condensates by sympathetic cooling," *Phys. Rev. Lett.*, vol. 78, pp. 586–589, Jan 1997.

[30] E. A. Cornell, D. Hall, M. Matthews, and C. Wieman, "Having it both ways: Distinguishable yet phase-coherent mixtures of Bose-Einstein condensates," *Jour. Low Temp. Phys.*, vol. 113, no. 3, pp. 151–165, 1998.

[31] D. M. Stamper-Kurn, M. R. Andrews, A. P. Chikkatur, S. Inouye, H.-J. Miesner, J. Stenger, and W. Ketterle, "Optical confinement of a Bose-Einstein condensate," *Phys. Rev. Lett.*, vol. 80, pp. 2027–2030, Mar 1998.

[32] J. Stenger, S. Inouye, D. Stamper-Kurn, H.-J. Miesner, A. Chikkatur, and W. Ketterle, "Spin domains in ground-state Bose–Einstein condensates," *Nature*, vol. 396, no. 6709, pp. 345–348, 1998.

TH-4102_206121026

[33] H.-J. Miesner, D. M. Stamper-Kurn, J. Stenger, S. Inouye, A. P. Chikkatur, and W. Ketterle, "Observation of metastable states in spinor Bose-Einstein condensates," *Phys. Rev. Lett.*, vol. 82, pp. 2228–2231, Mar 1999.

[34] D. M. Stamper-Kurn, H.-J. Miesner, A. P. Chikkatur, S. Inouye, J. Stenger, and W. Ketterle, "Quantum tunneling across spin domains in a Bose-Einstein condensate," *Phys. Rev. Lett.*, vol. 83, pp. 661–665, Jul 1999.

[35] M.-S. Chang, *Coherent spin dynamics of a spin-1 Bose-Einstein condensate*. Georgia Institute of Technology, 2006.

[36] T.-L. Ho, "Spinor Bose condensates in optical traps," *Phys. Rev. Lett.*, vol. 81, pp. 742–745, Jul 1998.

[37] T. Ohmi and K. Machida, "Bose-Einstein condensation with internal degrees of freedom in alkali atom gases," *Jour. Phys. Soc. Jpn.*, vol. 67, no. 6, pp. 1822–1825, 1998.

[38] C. K. Law, H. Pu, and N. P. Bigelow, "Quantum spins mixing in spinor Bose-Einstein condensates," *Phys. Rev. Lett.*, vol. 81, pp. 5257–5261, Dec 1998.

[39] Y. Kawaguchi and M. Ueda, "Spinor Bose–Einstein condensates," *Phys. Rep.*, vol. 520, no. 5, pp. 253–381, 2012.

[40] N. N. Klausen, J. L. Bohn, and C. H. Greene, "Nature of spinor Bose-Einstein condensates in rubidium," *Phys. Rev. A*, vol. 64, p. 053602, Oct 2001.

[41] E. G. M. van Kempen, S. J. J. M. F. Kokkelmans, D. J. Heinzen, and B. J. Verhaar, "Interisotope determination of ultracold rubidium interactions from three high-precision experiments," *Phys. Rev. Lett.*, vol. 88, p. 093201, Feb 2002.

[42] L. Landau and E. Lifshitz, "Quantum mechanics pergamon press," 1977.

[43] L. Tao and E. Y. Tsymbal, "Persistent spin texture enforced by symmetry," *Nat. commun.*, vol. 9, no. 1, p. 2763, 2018.

[44] X.-L. Qi and S.-C. Zhang, "Topological insulators and superconductors," *Rev. Mod. Phys.*, vol. 83, pp. 1057–1110, Oct 2011.

[45] Y. K. Kato, R. C. Myers, A. C. Gossard, and D. D. Awschalom, "Observation of the spin Hall effect in semiconductors," *Science*, vol. 306, no. 5703, pp. 1910–1913, 2004.

TH-4102_206121026

[46] M. Johanning, A. F. Varón, and C. Wunderlich, "Quantum simulations with cold trapped ions," *Journal of Physics B: Atomic, Molecular and Optical Physics*, vol. 42, p. 154009, jul 2009.

[47] I. Bloch, J. Dalibard, and S. Nascimbene, "Quantum simulations with ultracold quantum gases," *Nature Physics*, vol. 8, no. 4, pp. 267–276, 2012.

[48] T. D. Stanescu and V. Galitski, "Spin relaxation in a generic two-dimensional spin-orbit coupled system," *Phys. Rev. B*, vol. 75, p. 125307, Mar 2007.

[49] J. D. Koralek, C. P. Weber, J. Orenstein, B. A. Bernevig, S.-C. Zhang, S. Mack, and D. Awschalom, "Emergence of the persistent spin helix in semiconductor quantum wells," *Nature*, vol. 458, no. 7238, pp. 610–613, 2009.

[50] R. Ravisankar, D. Vudragović, P. Muruganandam, A. Balaž, and S. K. Adhikari, "Spin-1 spin–orbit-and rabi-coupled Bose–Einstein condensate solver," *Comput. Phys. Commun.*, vol. 259, p. 107657, 2021.

[51] R. Ozeri, N. Katz, J. Steinhauer, and N. Davidson, "Colloquium: Bulk Bogoliubov excitations in a Bose-Einstein condensate," *Rev. Mod. Phys.*, vol. 77, pp. 187–205, Apr 2005.

[52] F. Dalfovo, S. Giorgini, L. P. Pitaevskii, and S. Stringari, "Theory of Bose-Einstein condensation in trapped gases," *Rev. Mod. Phys.*, vol. 71, pp. 463–512, Apr 1999.

[53] I. Bloch, J. Dalibard, and W. Zwerger, "Many-body physics with ultracold gases," *Rev. Mod. Phys.*, vol. 80, pp. 885–964, Jul 2008.

[54] I. M. Georgescu, S. Ashhab, and F. Nori, "Quantum simulation," *Rev. Mod. Phys.*, vol. 86, pp. 153–185, Mar 2014.

[55] M. S. Safronova, D. Budker, D. DeMille, D. F. J. Kimball, A. Derevianko, and C. W. Clark, "Search for new physics with atoms and molecules," *Rev. Mod. Phys.*, vol. 90, p. 025008, June 2018.

[56] L. Chomaz, I. Ferrier-Barbut, F. Ferlaino, B. Laburthe-Tolra, B. L. Lev, and T. Pfau, "Dipolar physics: a review of experiments with magnetic quantum gases," *Rep. Progr. Phys.*, vol. 86, p. 026401, Dec. 2022.

[57] P. Krantz, M. Kjaergaard, F. Yan, T. P. Orlando, S. Gustavsson, and W. D. Oliver, "A quantum engineer's guide to superconducting qubits," *Appl. Phys. Rev.*, vol. 6, p. 021318, June 2019.

TH-4102_206121026

[58] A. M. Kaufman and K.-K. Ni, "Quantum science with optical tweezer arrays of ultracold atoms and molecules," *Nat. Phys.*, vol. 17, pp. 1324–1333, Nov. 2021.

[59] M. Konig, S. Wiedmann, C. Brune, A. Roth, H. Buhmann, L. W. Molenkamp, X.-L. Qi, and S.-C. Zhang, "Quantum spin Hall insulator state in HgTe quantum wells," *Science*, vol. 318, no. 5851, pp. 766–770, 2007.

[60] Z. Wu, L. Zhang, W. Sun, X.-T. Xu, B.-Z. Wang, S.-C. Ji, Y. Deng, S. Chen, X.-J. Liu, and J.-W. Pan, "Realization of two-dimensional spin-orbit coupling for Bose-Einstein condensates," *Science*, vol. 354, no. 6308, pp. 83–88, 2016.

[61] W. Sun, B.-Z. Wang, X.-T. Xu, C.-R. Yi, L. Zhang, Z. Wu, Y. Deng, X.-J. Liu, S. Chen, and J.-W. Pan, "Highly controllable and robust 2d spin-orbit coupling for quantum gases," *Phys. Rev. Lett.*, vol. 121, p. 150401, Oct 2018.

[62] C. Qu, C. Hamner, M. Gong, C. Zhang, and P. Engels, "Observation of Zitterbewegung in a spin-orbit-coupled Bose-Einstein condensate," *Phys. Rev. A*, vol. 88, p. 021604, Aug 2013.

[63] C. Hamner, C. Qu, Y. Zhang, J. Chang, M. Gong, C. Zhang, and P. Engels, "Dicke-type phase transition in a spin-orbit-coupled Bose–Einstein condensate," *Nat. Commun.*, vol. 5, no. 1, p. 4023, 2014.

[64] T.-L. Ho and S. Zhang, "Bose-Einstein condensates with spin-orbit interaction," *Phys. Rev. Lett.*, vol. 107, p. 150403, Oct 2011.

[65] J.-R. Li, J. Lee, W. Huang, S. Burchesky, B. Shteynas, F. v. Top, A. O. Jamison, and W. Ketterle, "A stripe phase with supersolid properties in spin–orbit-coupled Bose–Einstein condensates," *Nature (London)*, vol. 543, no. 7643, pp. 91–94, 2017.

[66] G. I. Martone and S. Stringari, "Supersolid phase of a spin-orbit-coupled Bose-Einstein condensate: A perturbation approach," *SciPost Phys.*, vol. 11, no. 5, p. 092, 2021.

[67] H. Zhang, S. Liu, and Y.-S. Zhang, "Faraday patterns in spin-orbit-coupled Bose-Einstein condensates," *Phys. Rev. A*, vol. 105, p. 063319, Jun 2022.

[68] T. Kawakami, T. Mizushima, M. Nitta, and K. Machida, "Stable skyrmions in su(2) gauged Bose-Einstein condensates," *Phys. Rev. Lett.*, vol. 109, no. 1, p. 015301, 2012.

TH-4102_206121026

[69] X.-W. Luo and C. Zhang, "Tunable spin-orbit coupling and magnetic superstripe phase in a Bose-Einstein condensate," *Phys. Rev. A*, vol. 100, p. 063606, Dec 2019.

[70] C. S. Chisholm, S. Hirthe, V. B. Makhalov, R. Ramos, R. Vatré, J. Cabedo, A. Celi, and L. Tarruell, "Probing supersolidity through excitations in a spin-orbit–coupled Bose-Einstein condensate," *Science*, vol. 391, no. 6784, pp. 480–484, 2026.

[71] L. P. Pitaevskii and S. Stringari, *Bose-Einstein Condensation*. Oxford: Oxford University Press, 2003.

[72] P. Muruganandam and S. K. Adhikari, "Fortran programs for the time-dependent Gross–Pitaevskii equation in a fully anisotropic trap," *Comput. Phys. Commun.*, vol. 180, no. 10, pp. 1888–1912, 2009.

[73] W. Bao and F. Y. Lim, "Computing ground states of spin-1 Bose–Einstein condensates by the normalized gradient flow," *SIAM J. Sci. Comput.*, vol. 30, no. 4, pp. 1925–1948, 2008.

[74] V. Achilleos, D. Frantzeskakis, P. Kevrekidis, and D. Pelinovsky, "Matter-wave bright solitons in spin-orbit coupled Bose-Einstein condensates," *Phys. Rev. Lett.*, vol. 110, no. 26, p. 264101, 2013.

[75] Y. Xu, Y. Zhang, B. Wu, *et al.*, "Bright solitons in spin-orbit-coupled Bose-Einstein condensates," *Phys. Rev. A*, vol. 87, no. 1, p. 013614, 2013.

[76] S. K. Adhikari, "Symbiotic solitons in quasi-one- and quasi-two-dimensional spin-1 condensates," *Phys. Rev. E*, vol. 104, p. 024207, Aug 2021.

[77] S. K. Adhikari, "Stable multi-peak vector solitons in spin–orbit coupled spin-1 polar condensates," *Physica E*, vol. 118, p. 113892, 2020.

[78] S. K. Adhikari, "Multiring, stripe, and superlattice solitons in a spin-orbit-coupled spin-1 condensate," *Phys. Rev. A*, vol. 103, p. L011301, Jan 2021.

[79] S. Mardonov, M. Modugno, and E. Y. Sherman, "Dynamics of spin-orbit coupled Bose-Einstein condensates in a random potential," *Phys. Rev. Lett.*, vol. 115, p. 180402, Oct 2015.

[80] S. Mardonov, V. V. Konotop, B. A. Malomed, M. Modugno, and E. Y. Sherman, "Spin-orbit-coupled soliton in a random potential," *Phys. Rev. A*, vol. 98, p. 023604, Aug 2018.

TH-4102_206121026

[81] S. Mardonov, M. Modugno, E. Y. Sherman, and B. A. Malomed, "Rabi-coupling-driven motion of a soliton in a Bose-Einstein condensate," *Phys. Rev. A*, vol. 99, p. 013611, Jan 2019.

[82] G. I. Martone, Y. Li, L. P. Pitaevskii, and S. Stringari, "Anisotropic dynamics of a spin-orbit-coupled Bose-Einstein condensate," *Phys. Rev. A*, vol. 86, p. 063621, Dec 2012.

[83] L. Chen, H. Pu, Z.-Q. Yu, and Y. Zhang, "Collective excitation of a trapped Bose-Einstein condensate with spin-orbit coupling," *Phys. Rev. A*, vol. 95, p. 033616, Mar 2017.

[84] K. Kasamatsu and M. Tsubota, "Multiple domain formation induced by modulation instability in two-component Bose-Einstein condensates," *Phys. Rev. Lett.*, vol. 93, p. 100402, Sep 2004.

[85] K. Kasamatsu and M. Tsubota, "Modulation instability and solitary-wave formation in two-component Bose-Einstein condensates," *Phys. Rev. A*, vol. 74, p. 013617, Jul 2006.

[86] N. P. Robins, W. Zhang, E. A. Ostrovskaya, and Y. S. Kivshar, "Modulational instability of spinor condensates," *Phys. Rev. A*, vol. 64, p. 021601, Jul 2001.

[87] W. Zhang, D. L. Zhou, M.-S. Chang, M. S. Chapman, and L. You, "Dynamical instability and domain formation in a spin-1 Bose-Einstein condensate," *Phys. Rev. Lett.*, vol. 95, p. 180403, Oct 2005.

[88] M. Matuszewski, T. J. Alexander, and Y. S. Kivshar, "Spin-domain formation in antiferromagnetic condensates," *Phys. Rev. A*, vol. 78, p. 023632, Aug 2008.

[89] M. Matuszewski, "Rotonlike instability and pattern formation in spinor Bose-Einstein condensates," *Phys. Rev. Lett.*, vol. 105, p. 020405, Jul 2010.

[90] J. Kronjäger, C. Becker, P. Soltan-Panahi, K. Bongs, and K. Sengstock, "Spontaneous pattern formation in an antiferromagnetic quantum gas," *Phys. Rev. Lett.*, vol. 105, p. 090402, Aug 2010.

[91] I. A. Bhat, T. Mithun, B. A. Malomed, and K. Porsezian, "Modulational instability in binary spin-orbit-coupled Bose-Einstein condensates," *Phys. Rev. A*, vol. 92, p. 063606, Dec 2015.

TH-4102_206121026

[92] S. Bhuvaneswari, K. Nithyanandan, P. Muruganandam, and K. Porsezian, "Modulation instability in quasi-two-dimensional spin–orbit coupled Bose–Einstein condensates," *J. Phys. B: At. Mol. Opt. Phys.*, vol. 49, no. 24, p. 245301, 2016.

[93] R. Ravisankar, H. Fabrelli, A. Gammal, P. Muruganandam, and P. K. Mishra, "Effect of Rashba spin-orbit and Rabi couplings on the excitation spectrum of binary Bose-Einstein condensates," *Phys. Rev. A*, vol. 104, p. 053315, Nov 2021.

[94] Z. Pu, J. Zhang, S. Yi, D. Wang, and W. Zhang, "Magnetic-field-induced dynamical instabilities in an antiferromagnetic spin-1 Bose-Einstein condensate," *Phys. Rev. A*, vol. 93, p. 053628, May 2016.

[95] N. R. Bernier, E. G. Dalla Torre, and E. Demler, "Unstable avoided crossing in coupled spinor condensates," *Phys. Rev. Lett.*, vol. 113, p. 065303, Aug 2014.

[96] R. K. Kumar and P. Muruganandam, "Numerical studies on vortices in rotating dipolar Bose-Einstein condensates," in *J. Phys. Conf. Ser.*, vol. 497, p. 012036, 2014.

[97] R. K. Kumar, L. E. Young-S, D. Vudragović, A. Balaž, P. Muruganandam, and S. K. Adhikari, "Fortran and c programs for the time-dependent dipolar Gross–Pitaevskii equation in an anisotropic trap," *Comput. Phys. Commun.*, vol. 195, pp. 117–128, 2015.

[98] S. Koonin and D. Meredith, "Computational physics art (fortran version)," 1990.

[99] W. F. Ames, *Numerical methods for partial differential equations*. Academic press, 2014.

[100] S. Adhikari, "Supersolid-like states in a two-dimensional trapped spin–orbit-coupled spin-1 condensate," *J. Phys.: Condens. Matter*, vol. 33, no. 26, p. 265402, 2021.

[101] S. K. Gangwar, R. Ravisankar, P. Muruganandam, and P. K. Mishra, "Emergence of spin-mixed superstripe phases in spin-orbit-coupled spin-1 condensates," *Phys. Rev. A*, vol. 113, p. 023311, Feb 2026.

[102] L. Huang, Z. Meng, P. Wang, P. Peng, S.-L. Zhang, L. Chen, D. Li, Q. Zhou, and J. Zhang, "Experimental realization of two-dimensional synthetic spin–orbit coupling in ultracold Fermi gases," *Nat. Phys.*, vol. 12, no. 6, pp. 540–544, 2016.

TH-4102_206121026

[103] E. N. Bulgakov and A. F. Sadreev, "Vortex phase diagram of $f = 1$ spinor Bose-Einstein condensates," *Phys. Rev. Lett.*, vol. 90, p. 200401, May 2003.

[104] A. Kato, Y. Nakano, K. Kasamatsu, and T. Matsui, "Vortex formation of a Bose-Einstein condensate in a rotating deep optical lattice," *Phys. Rev. A*, vol. 84, p. 053623, Nov 2011.

[105] S. K. Adhikari, "Vortex-lattice formation in a spin–orbit coupled rotating spin-1 condensate," *J. Phys.: Conden. Matter*, vol. 33, p. 065404, nov 2020.

[106] G. Katsimiga, S. Mistakidis, P. Schmelcher, and P. Kevrekidis, "Phase diagram, stability and magnetic properties of nonlinear excitations in spinor Bose–Einstein condensates," *New J. Phys.*, vol. 23, no. 1, p. 013015, 2021.

[107] J. Yang and Y. Zhang, "Spin-orbit-coupled spinor gap solitons in Bose-Einstein condensates," *Phys. Rev. A*, vol. 107, p. 023316, Feb 2023.

[108] S. Gautam and S. K. Adhikari, "Mobile vector soliton in a spin–orbit coupled spin-1 condensate," *Laser Phys. Lett.*, vol. 12, no. 4, p. 045501, 2015.

[109] S. Gautam and S. K. Adhikari, "Phase separation in a spin-orbit-coupled Bose-Einstein condensate," *Phys. Rev. A*, vol. 90, p. 043619, Oct 2014.

[110] E. M. Bookjans, A. Vinit, and C. Raman, "Quantum phase transition in an antiferromagnetic spinor Bose-Einstein condensate," *Phys. Rev. Lett.*, vol. 107, p. 195306, Nov 2011.

[111] H.-X. Yang, T. Tian, Y.-B. Yang, L.-Y. Qiu, H.-Y. Liang, A.-J. Chu, C. B. Dağ, Y. Xu, Y. Liu, and L.-M. Duan, "Observation of dynamical quantum phase transitions in a spinor condensate," *Phys. Rev. A*, vol. 100, p. 013622, Jul 2019.

[112] S. Liu and Y. Zhang, "Quench dynamics in a trapped Bose-Einstein condensate with spin-orbit coupling," *Phys. Rev. A*, vol. 99, p. 053609, May 2019.

[113] T.-S. Deng, W. Zhang, W. Yi, and G.-C. Guo, "Quench dynamics of a Bose-Einstein condensate under synthetic spin-orbit coupling," *Phys. Rev. A*, vol. 93, p. 053621, May 2016.

[114] R. Ravisankar, T. Sriraman, L. Salasnich, and P. Muruganandam, "Quenching dynamics of the bright solitons and other localized states in spin–orbit coupled Bose–Einstein condensates," *J. Phys. B: At. Mol. Opt. Phys.*, vol. 53, p. 195301, aug 2020.

TH-4102_206121026

[115] S. K. Gangwar, R. Ravisankar, H. Fabrelli, P. Muruganandam, and P. K. Mishra, "Emergence of unstable avoided crossing in the collective excitations of spin-1 spin-orbit-coupled Bose-Einstein condensates," *Phys. Rev. A*, vol. 109, p. 043306, Apr 2024.

[116] S. K. Gangwar, R. Ravisankar, H. Fabrelli, P. Muruganandam, and P. K. Mishra, "Double unstable avoided crossings and complex-domain-pattern formation in spin-orbit-coupled spin-1 condensates," *Phys. Rev. A*, vol. 111, p. 063303, Jun 2025.

[117] D. M. Stamper-Kurn and M. Ueda, "Spinor Bose gases: Symmetries, magnetism, and quantum dynamics," *Rev. Mod. Phys.*, vol. 85, pp. 1191–1244, Jul 2013.

[118] R. Ravisankar, T. Sriraman, R. K. Kumar, P. Muruganandam, and P. K. Mishra, "Influence of Rashba spin–orbit and Rabi couplings on the spin-mixing and ground state phases of binary Bose–Einstein condensates," *J. Phys. B: At. Mol. Opt. Phys.*, vol. 54, p. 225301, dec 2021.

[119] S. K. Sarkar, S. Mardonov, E. Y. Sherman, P. Muruganandam, and P. K. Mishra, "Spin-dependent localization of spin-orbit and Rabi-coupled Bose-Einstein condensates in a random potential," *New J. Phys.*, vol. 27, p. 023018, Feb 2024.

[120] S. Inouye, M. Andrews, J. Stenger, H.-J. Miesner, D. M. Stamper-Kurn, and W. Ketterle, "Observation of Feshbach resonances in a Bose–Einstein condensate," *Nature (London)*, vol. 392, no. 6672, pp. 151–154, 1998.

[121] A. Marte, T. Volz, J. Schuster, S. Dürr, G. Rempe, E. G. M. van Kempen, and B. J. Verhaar, "Feshbach Resonances in Rubidium 87: Precision Measurement and Analysis," *Phys. Rev. Lett.*, vol. 89, p. 283202, Dec 2002.

[122] C. Chin, R. Grimm, P. Julienne, and E. Tiesinga, "Feshbach resonances in ultracold gases," *Rev. Mod. Phys.*, vol. 82, pp. 1225–1286, Apr 2010.

[123] K. Rajaswathi, S. Bhuvaneswari, R. Radha, and P. Muruganandam, "Dispersion engineering in spin-orbit-coupled spinor $F = 1$ condensates driven by negative masses," *Phys. Rev. A*, vol. 108, p. 033317, Sep 2023.

[124] D. Ma and C. Jia, "Soliton oscillation driven by spin-orbit coupling in spinor condensates," *Phys. Rev. A*, vol. 100, p. 023629, Aug 2019.

TH-4102_206121026

[125] T. Mithun and K. Kasamatsu, "Modulation instability associated nonlinear dynamics of spin–orbit coupled Bose–Einstein condensates," *J. Phys. B*, vol. 52, no. 4, p. 045301, 2019.

[126] L. Zhou, H. Pu, H. Y. Ling, K. Zhang, and W. Zhang, "Spin dynamics and domain formation of a spinor Bose-Einstein condensate in an optical cavity," *Phys. Rev. A*, vol. 81, no. 6, p. 063641, 2010.

[127] Y. Zhang, M. E. Mossman, T. Busch, P. Engels, and C. Zhang, "Properties of spin–orbit-coupled Bose–Einstein condensates," *Front. Phys.*, vol. 11, pp. 1–28, 2016.

[128] D. Jacob, L. Shao, V. Corre, T. Zibold, L. De Sarlo, E. Mimoun, J. Dalibard, and F. Gerbier, "Phase diagram of spin-1 antiferromagnetic Bose-Einstein condensates," *Phys. Rev. A*, vol. 86, p. 061601, Dec 2012.

[129] K. Kasamatsu, M. Tsubota, and M. Ueda, "Vortices in multicomponent Bose–Einstein condensates," *Int. J. Mod. Phys. B*, vol. 19, no. 11, pp. 1835–1904, 2005.

[130] K. Fujimoto and M. Tsubota, "Counterflow instability and turbulence in a spin-1 spinor Bose-Einstein condensate," *Phys. Rev. A*, vol. 85, p. 033642, Mar 2012.

[131] G. I. Martone, F. V. Pepe, P. Facchi, S. Pascazio, and S. Stringari, "Tricriticalities and quantum phases in spin-orbit-coupled spin-1 Bose gases," *Phys. Rev. Lett.*, vol. 117, p. 125301, Sep 2016.

[132] G.-Q. Li, G.-D. Chen, P. Peng, Z. Li, and X.-D. Bai, "Modulation instability of a spin-1 Bose–Einstein condensate with spin–orbit coupling," *J. Phys. B: At. Mol. Opt. Phys.*, vol. 50, no. 23, p. 235302, 2017.

[133] B. A. Malomed, "Creating solitons by means of spin-orbit coupling," *EPL*, vol. 122, no. 3, p. 36001, 2018.

[134] P. Peng, G.-Q. Li, L.-C. Zhao, W.-L. Yang, and Z.-Y. Yang, "Magnetized vector solitons in a spin-orbit coupled spin-1 Bose-Einstein condensate with Zeeman coupling," *Phys. Lett. A*, vol. 383, no. 24, pp. 2883–2890, 2019.

[135] S. K. Adhikari, "Phase separation of vector solitons in spin-orbit-coupled spin-1 condensates," *Phys. Rev. A*, vol. 100, p. 063618, Dec 2019.

[136] S. Gautam and S. Adhikari, "Solitons in a spin-orbit-coupled spin-1 Bose-Einstein condensate," *Braz. J. Phys.*, vol. 51, pp. 298–307, 2021.

TH-4102_206121026

[137] J. Cabedo, J. Claramunt, and A. Celi, "Dynamical preparation of stripe states in spin-orbit-coupled gases," *Phys. Rev. A*, vol. 104, p. L031305, Sep 2021.

[138] Q.-L. Zhu, L. Pan, and J. An, "Spin-orbit-coupled spin-1 Bose-Einstein condensate flow past an obstacle in the presence of a Zeeman field," *Phys. Rev. A*, vol. 102, p. 053320, Nov 2020.

[139] L. Pitaevskii and S. Stringari, *Bose-Einstein Condensation and Superfluidity*. Oxford University Press, 01 2016.

[140] Y. Li, G. I. Martone, L. P. Pitaevskii, and S. Stringari, "Superstripes and the excitation spectrum of a spin-orbit-coupled Bose-Einstein condensate," *Phys. Rev. Lett.*, vol. 110, p. 235302, Jun 2013.

[141] J. He and J. Lin, "Stationary and moving bright solitons in Bose–Einstein condensates with spin–orbit coupling in a Zeeman field," *New J. Phys.*, vol. 25, p. 093041, sep 2023.

[142] G. C. Katsimiga, S. I. Mistakidis, K. Mukherjee, P. G. Kevrekidis, and P. Schmelcher, "Stability and dynamics across magnetic phases of vortex-bright type excitations in spinor Bose-Einstein condensates," *Phys. Rev. A*, vol. 107, p. 013313, Jan 2023.

[143] Rajat, A. Roy, and S. Gautam, "Collective excitations in cigar-shaped spin-orbit-coupled spin-1 Bose-Einstein condensates," *Phys. Rev. A*, vol. 106, p. 013304, Jul 2022.

[144] M. C. Cross and P. C. Hohenberg, "Pattern formation outside of equilibrium," *Rev. Mod. Phys.*, vol. 65, pp. 851–1112, Jul 1993.

[145] L. Salasnich, A. Parola, and L. Reatto, "Effective wave equations for the dynamics of cigar-shaped and disk-shaped Bose condensates," *Phys. Rev. A*, vol. 65, p. 043614, Apr 2002.

[146] L. Wen, Q. Sun, H. Q. Wang, A. C. Ji, and W. M. Liu, "Ground state of spin-1 Bose-Einstein condensates with spin-orbit coupling in a Zeeman field," *Phys. Rev. A*, vol. 86, p. 043602, Oct 2012.

[147] C. Wang, C. Gao, C.-M. Jian, and H. Zhai, "Spin-orbit coupled spinor Bose-Einstein condensates," *Phys. Rev. Lett.*, vol. 105, p. 160403, Oct 2010.

TH-4102_206121026

[148] Q. Zhu, C. Zhang, and B. Wu, "Exotic superfluidity in spin-orbit coupled Bose-Einstein condensates," *EPL*, vol. 100, no. 5, p. 50003, 2012.

[149] E. Anderson, Z. Bai, C. Bischof, L. S. Blackford, J. Demmel, J. Dongarra, J. Du Croz, A. Greenbaum, S. Hammarling, A. McKenney, *et al.*, *LAPACK users' guide*. Philadelphia: SIAM, 1999.

[150] L. E. Young-S, D. Vudragović, P. Muruganandam, S. K. Adhikari, and A. Balaž, "Openmp fortran and c programs for solving the time-dependent Gross–Pitaevskii equation in an anisotropic trap," *Comput. Phys. Commun.*, vol. 204, pp. 209–213, 2016.

[151] R. S. Tasgal and Y. B. Band, "Sound waves and modulational instabilities on continuous-wave solutions in spinor Bose-Einstein condensates," *Phys. Rev. A*, vol. 91, p. 013615, Jan 2015.

[152] M. Abad and A. Recati, "A study of coherently coupled two-component Bose-Einstein condensates," *Eur. Phys. J. D*, vol. 67, pp. 1–11, 2013.

[153] H. Lyu and Y. Zhang, "Spin-orbit-coupling-assisted roton softening and super-stripes in a Rydberg-dressed Bose-Einstein condensate," *Phys. Rev. A*, vol. 102, p. 023327, Aug 2020.

[154] W.-L. Xia, L. Chen, T.-T. Li, Y. Zhang, and Q. Zhu, "Metastable supersolid in spin-orbit-coupled Bose-Einstein condensates," *Phys. Rev. A*, vol. 107, p. 053302, May 2023.

[155] J. Radić, T. A. Sedrakyan, I. B. Spielman, and V. Galitski, "Vortices in spin-orbit-coupled Bose-Einstein condensates," *Phys. Rev. A*, vol. 84, p. 063604, Dec 2011.

[156] H. Wang, "A time-splitting spectral method for computing dynamics of spinor F=1 Bose–Einstein condensates," *Comput. Math.*, vol. 84, no. 6, pp. 925–944, 2007.

[157] F. Y. Lim and W. Bao, "Numerical methods for computing the ground state of spin-1 Bose-Einstein condensates in a uniform magnetic field," *Phys. Rev. E*, vol. 78, p. 066704, Dec 2008.

[158] Y.-K. Liu and S.-J. Yang, "Exact solitons and manifold mixing dynamics in the spin-orbit–coupled spinor condensates," *Europhys. Lett.*, vol. 108, no. 3, p. 30004, 2014.

TH-4102_206121026

[159] A. L. Fetter, "Ground state and excited states of a confined condensed Bose gas," *Phys. Rev. A*, vol. 53, pp. 4245–4249, Jun 1996.

[160] M. Edwards, P. A. Ruprecht, K. Burnett, R. J. Dodd, and C. W. Clark, "Collective excitations of atomic Bose-Einstein condensates," *Phys. Rev. Lett.*, vol. 77, pp. 1671–1674, Aug 1996.

[161] K. G. Singh and D. S. Rokhsar, "Collective excitations of a confined Bose Condensate," *Phys. Rev. Lett.*, vol. 77, pp. 1667–1670, Aug 1996.

[162] S. Stringari, "Collective excitations of a trapped Bose-condensed gas," *Phys. Rev. Lett.*, vol. 77, pp. 2360–2363, Sep 1996.

[163] N. P. Proukakis, "A century of Bose-Einstein condensation," *Commun. Phys.*, vol. 8, p. 264, July 2025.

[164] S.-C. Ji, L. Zhang, X.-T. Xu, Z. Wu, Y. Deng, S. Chen, and J.-W. Pan, "Softening of roton and phonon modes in a Bose-Einstein condensate with spin-orbit coupling," *Phys. Rev. Lett.*, vol. 114, p. 105301, Mar 2015.

[165] Rajat, P. Banger, and S. Gautam, "Collective excitations and universal coarsening dynamics of a spin-orbit-coupled spin-1 Bose-Einstein condensate," *Phys. Rev. A*, vol. 111, p. 033316, Mar 2025.

[166] P. Kaur, S. Gautam, and S. Adhikari, "Supersolid-like solitons in two-dimensional nonmagnetic spin-orbit coupled spin-1 and spin-2 condensates," *Phys. Lett. A*, vol. 455, p. 128507, Dec. 2022.

[167] S. Adhikari, "Spontaneous spatial order in two-dimensional ferromagnetic spin-orbit coupled uniform spin-1 condensate solitons," *Phys. Lett. A*, vol. 388, p. 127042, Feb. 2021.

[168] J. Higbie and D. M. Stamper-Kurn, "Periodically dressed Bose-Einstein condensate: A superfluid with an anisotropic and variable critical velocity," *Phys. Rev. Lett.*, vol. 88, p. 090401, Feb 2002.

[169] R. Ravisankar, S. K. Gangwar, H. Fabrelli, Y. Zhang, P. Muruganandam, P. K. Mishra, E. Kengne, G. Xianlong, and B. A. Malomed, "Stable supersolids and boselets in spin-orbit-coupled Bose-Einstein condensates with three-body interactions," *Phys. Rev. Research*, vol. 7, p. 023317, June 2025.

TH-4102_206121026

[170] R. Ravisankar, K. Rajaswathi, R. Radha, P. Muruganandam, and X. Gao, "Instability-driven dynamics of spin–orbit and Rabi-coupled Bose-Einstein condensates," *Chaos, Solitons & Fractals*, vol. 195, p. 116287, 2025.

[171] T. Ozawa and G. Baym, "Stability of ultracold atomic bose condensates with Rashba spin-orbit coupling against quantum and thermal fluctuations," *Phys. Rev. Lett.*, vol. 109, p. 025301, Jul 2012.

[172] S. Sahu and D. Majumder, "Collective excitation of two-dimensional Bose–Einstein condensate in liquid phase with spin–orbit coupling," *J. Phys. B: At. Mol. Opt. Phys.*, vol. 53, p. 095301, mar 2020.

[173] W. Zheng and Z. Li, "Collective modes of a spin-orbit-coupled Bose–Einstein condensate: A hydrodynamic approach," *Phys. Rev. A*, vol. 85, no. 5, p. 053607, 2012.

[174] Y.-C. Zhang, Z.-Q. Yu, T. K. Ng, S. Zhang, L. Pitaevskii, and S. Stringari, "Superfluid density of a spin-orbit-coupled Bose gas," *Phys. Rev. A*, vol. 94, p. 033635, Sep 2016.

[175] V. I. Yukalov, "Dipolar and spinor bosonic systems," *Laser Phys.*, vol. 28, p. 053001, apr 2018.

[176] K. Fujimoto and M. Tsubota, "Spin turbulence in a trapped spin-1 spinor Bose-Einstein condensate," *Phys. Rev. A*, vol. 85, p. 053641, May 2012.

[177] C. W. Beenakker, "Search for Majorana fermions in superconductors," *Annu. Rev. Condens. Matter Phys.*, vol. 4, no. 1, pp. 113–136, 2013.

[178] L.-C. Ha, L. W. Clark, C. V. Parker, B. M. Anderson, and C. Chin, "Roton-maxon excitation spectrum of Bose condensates in a shaken optical lattice," *Phys. Rev. Lett.*, vol. 114, p. 055301, Feb 2015.

[179] H. Lyu, Y. Zhang, and T. Busch, "Detection of roton and phonon excitations in a spin-orbit-coupled Bose-Einstein condensate with a moving barrier," *Phys. Rev. A*, vol. 106, p. 013302, Jul 2022.

[180] L. Sadler, J. Higbie, S. Leslie, M. Vengalattore, and D. Stamper-Kurn, "Spontaneous symmetry breaking in a quenched ferromagnetic spinor Bose-Einstein condensate," *Nature (London)*, vol. 443, no. 7109, pp. 312–315, 2006.

TH-4102_206121026

[181] R. M. Wilson, C. Ticknor, J. L. Bohn, and E. Timmermans, "Roton immiscibility in a two-component dipolar Bose gas," *Phys. Rev. A*, vol. 86, p. 033606, Sep 2012.

[182] Y. Li, L. P. Pitaevskii, and S. Stringari, "Quantum tricriticality and phase transitions in spin-orbit coupled Bose-Einstein condensates," *Phys. Rev. Lett.*, vol. 108, p. 225301, May 2012.

[183] M. Lewkowicz, T. Karpiuk, M. Gajda, and M. Brewczyk, "Supersolidity of dipolar Bose-Einstein condensates induced by coupling to fermions," *Phys. Rev. A*, vol. 111, p. L011301, Jan 2025.

[184] H. Lyu, Y. Chen, Q. Zhu, and Y. Zhang, "Supercurrent-carrying supersolid in spin-orbit-coupled Bose-Einstein condensates," *Phys. Rev. Res.*, vol. 6, p. 023048, Apr 2024.

[185] Ritu, Rajat, A. Roy, and S. Gautam, "Thermal amplification and melting of phases in spin–orbit-coupled spin-1 Bose–Einstein condensates," *New J. Phys.*, vol. 27, p. 043005, apr 2025.

[186] A. Putra, F. Salces-Cárcoba, Y. Yue, S. Sugawa, and I. Spielman, "Spatial coherence of spin-orbit-coupled Bose gases," *Phys. Rev. Lett.*, vol. 124, no. 5, p. 053605, 2020.

[187] N. Goldman and J. Dalibard, "Periodically driven quantum systems: Effective Hamiltonians and engineered gauge fields," *Phys. Rev. X*, vol. 4, p. 031027, Aug 2014.

[188] S. Gangwar, R. Ravisankar, P. Muruganandam, and P. K. Mishra, "Dynamics of quantum solitons in Lee-Huang-Yang spin-orbit-coupled Bose-Einstein condensates," *Phys. Rev. A*, vol. 106, p. 063315, Dec 2022.

TH-4102_206121026